Quantifying Present-Day Overpressure and its Development Through Time in Active and Passive Sedimentary Basins

ERIKA ELIZABETH CALDERON-MEDINA

Quantifying Present-Day Overpressure and its Development Through Time in Active and Passive Sedimentary Basins

Volume 1 of 1

Erika Elizabeth Calderon Medina

Thesis submitted for the degree of Doctor of Philosophy

Earth Sciences Department

Durham University

2023

Abstract

Pore fluid pressure is a critical variable that needs to be assessed for many geological applications, including hydrocarbon exploration and exploitation, geothermal energy, carbon capture and storage, H_2, and nuclear waste storage. To further understand and mitigate the uncertainty of unexpected overpressured intervals or areas, this research assesses the occurrence of and the controls on pore fluid pressure in three geologically distinct regions: the East Coast Basin of New Zealand (ECB), the Magnolia Field in the Gulf of Mexico, and an Atlantic margin of the West African basin. The factors that contribute to overpressure generation, maintenance, and dissipation are assessed, as are the geological and geomechanical approaches used to identify the overpressure-generating mechanisms that contributed to the present-day overpressure.

Simple approaches to overpressure evaluation, such as analytical equations and log-based well interpretations, were applied to the data; however, they are insufficient to explain the distribution of overpressure in areas with complex geological histories (e.g., erosive events, changes in sedimentation rates, tectonic compression, active tectonism). Geological data from each area were therefore used to construct 1D and 2D geomechanical (thermo-hydro-mechanical and hydro-mechanical) models that provide the evolution of porosity, stresses, and pore fluid pressure through time and facilitate the evaluation of each overpressure mechanism separately.

Present-day overpressure in the three sedimentary basins results from different mechanisms acting at different periods of time. Overpressure dissipation occurs during erosive events and where lateral pressure drainage is present; the most recent events (e.g., <2 Ma) have the greatest influence on porosity and pore fluid pressure. Overpressure maintenance occurs when thick (>1,000 m) intervals of shale or thin (e.g., <85 m) successions of exceptionally low-permeability intervals are present. In tectonic active settings, tectonic compression acting during the most recent geological events (e.g., <6 Ma) has the greatest impact on porosity and pore fluid pressure; in the context of salt tectonics, this impact depends on the shape of the developing salt wall. Early geological clay diagenesis can locally reduce porosity and generate high overpressures due to the reduction of sediment permeability caused by a combination of chemical compaction (smectite to illite transformation) and mechanical compaction (post-diagenesis sedimentation). Finally, low (200 m/Ma) and high (3,000 m/Ma) sedimentation rates can generate overpressure when low-permeability intervals are present, also resulting in the preservation of high porosities.

A detailed geological interpretation used as an input for the construction of geomechanical models can provide more realistic results, and consequently a better understanding of the present-day overpressure distribution within a basin. In addition, this information can be used to mitigate the level of uncertainty in seal failure of sites with the potential to store CO_2, H_2, and nuclear waste.

Table of Contents

Declaration

I declare that this thesis, which I submit for the degree of Doctor of Philosophy at Durham University, is my own work, except where acknowledgement is made in the text, and not substantially the same as any work which has previously been submitted at this or any other university for any degree, diploma or other qualification.

Statement of Copyright

Acknowledgements

This research was conducted as part of the GeoPOP4 an industry supported research consortium funded by BP and Petrobras together with Durham University and the University of Newcastle.

I would like to thank to both companies for the financial support and the data provided which are part of one of the projects assessed in this research.

Also, I would like to thank you to my tutors; Prof. Andrew Aplin, Joshua Obradors-Prats, Dr Stuart Jones, and Dr Mohamed Rouainia, first for giving me the opportunity to carry out this research and then for their continued guidance and support.

Finally, a special thank you to my two daughters Daniela and Mia and my lovely husband Richard for their support, inspiration, and motivation during this stage.

Chapter 1: Introduction

Pore pressure prediction is crucial during well planning as it can reduce costs and mitigate risks while drilling (Dickinson, 1953; Dutta, 1987). There have been several cases in recent history where problems during drilling caused by a lack of understanding of the pore fluid pressure changes along the sedimentary column have resulted in wells being abandoned without reaching their targets, as well as cases where wells have blown out. This includes the E. N. Ross No. 2 well, Mississippi, 1985, and the Macondo well, Mississippi Canyon, 2010. As more geologically complex locations are considered during hydrocarbon exploration and as sites are increasingly considered for the storage of waste products such as CO_2, H_2, and nuclear waste, the need for more accurate pore pressure calculations has never been more essential.

The main overpressure-generating mechanism in young passive basins has been determined to be disequilibrium compaction or undercompaction, due to the sedimentation of low-permeability, mud-rich lithologies at high sedimentation rates (>1,000 m/Ma) in the relatively recent geological past (e.g., Late Miocene (~12 Ma) to present-day) in the Gulf of Mexico. Undercompaction results from increases in pore pressure due to increases in vertical stress during rapid loading, combined with the inability of the sediments to reduce the pore pressure at the same rate by fluid flow (Dickinson, 1953; Bredehoeft and Hanshaw, 1968; Audet, 1996; Osborne and Swarbrick, 1997).

In active basins, such as subduction margins, tectonic compression has been suggested to have more impact on the overpressure generation. Yassir and Addis (2002) suggested that the overpressure generated by tectonic compression is higher than the generated by disequilibrium compaction because the sediments are exposed to shearing which change the structure of the sediments without fluid flow. A variation of pore pressures through time in these systems has also been suggested and has been related to the change of the subduction rates and angle of the tectonic plates (Palciauskas and Domenico, 1989). High overpressure generation due to tectonic compression related to salt wall growth has also been suggested (e.g., Luo et al., 2017; Nikolinakou et al., 2018). In this case, the amount of overpressure generated depends on the horizontal stress generated during the salt growth.

Overpressure related to clay diagenesis (chemical compaction) could be associated with basins with high geothermal gradients (>39 °C/km) where the sediments have smectite content and reach the required temperature to start diagenesis processes. Temperatures between 50 and 150 °C have been suggested to start the smectite to illite transformation (e.g., O'Connor et al., 2011, Lahann, 2002; Bruce, 1984). During this process, water is released partially or completely, and the expandable clay smectite dehydrates to the non-expandable illite clay increasing pore pressure (Audet, 1995). An increase in pore pressure during the transformation has also been related to the arrangement of the grains and the release of bound water in the system (Powers, 1967). In addition, during the smectite to illite transformation, an increase in fluid pressure can be generated due to the transfer from the load of the grain system to the pore fluid (Osborne and Swarbrick, 1997; Lahann and Swarbrick, 2011). Swarbrick et al. (2002) also suggested that the overpressure generated is due to the baffles and barriers created during the smectite to illite transformation.

Fluid expansion has been also suggested to generate overpressure. It has been related to hydrocarbon generation in source rock intervals with kerogen type II (Meissner, 1978), oil cracking

to gas (Barker, 1990; Swarbrick and Hills, 1999), and aquathermal pressure. Although aquathermal pressure has been quantified to have a minimum effect on overpressure generation (e.g., Luo and Vasseur, 1992; Swarbrick et al., 2002), Barker (1972) suggested that isolated intervals could be affected by the variation of the geothermal gradient and salinity of the system, resulting in overpressure generation by this mechanism.

Lateral pressure transfer has also been suggested as an overpressure mechanism. In this mechanism the high pore fluid pressures encountered at shallow depths are interpreted to have been transferred through faults, fractures, or any high permeability interval from deep and overpressured intervals that at one time could be connected (Osborne and Swarbrick, 1997).

While the mechanisms that generate overpressure have been analysed over multiple decades, resulting in different methods, equations, and workflows for overpressure calculation, these approaches can only be applied when the right data are available, and a good geological understanding of the area is acquired. For instance, analytical equations proposed almost 100 years ago have been commonly used to interpret pore pressure based on well log data (e.g., Athy, 1930; Dickinson, 1953; Wyllie, 1956; Eaton, 1975; Hamilton, 1976; Plumley, 1980; Raymer et al., 1980; Issler, 1992; Bowers, 1995; Tingay et al., 2009). Whilst practical and important, these simple log-based methods have limited predictive power because they are not effective at unravelling contributions from multiple overpressure generation mechanisms, nor the individual contribution of a single mechanism. Recently, more sophisticated methods such as 1D, 2D, and 3D geomechanical models have been developed to explore, quantitatively, the range of physical and chemical processes that can contribute to and dissipate fluid pressure. These models can capture stresses, strains, porosities, and pore pressures during basin evolution (Ge and Garven, 1992; Audet, 1995; Darby and Ellis, 2001; Crook et al., 2006; Vidal-Royo et al., 2011; Crook et al., 2018; Nikolinakou et al., 2014; Obradors-Prats et al., 2016, 2017a and 2017b; Luo et al., 2017; Heidari et al., 2021).

This study aims to identify the present-day overpressure-generating mechanisms and their contribution to three projects located in different basins with different geological histories, by establishing the factors needed to preserve the overpressure through time and understanding the evolution of porosity, stresses, and pore pressure. To achieve this, different data sets were created for each project. A regional evaluation was conducted, including well data and tectono-stratigraphic revision. Seismic interpretation was performed on 2D and 3D seismic data. Lithology, facies, and formation interpretation with stratigraphic and structural correlations. 3D static models were created to represent the sedimentary column investigated. These models contain the geological structures of the studied region and the distribution of continuous (e.g., porosity, pore pressure) and discrete properties (e.g., lithologies, formations, sediment ages). An assessment of pore pressure data with well logs and analytical equations was performed together with an interpretation of measured pressure data. As part of this research, 1D and 2D geomechanical models were constructed, and the input considered the geological assessment performed in each project.

1.1 Thesis Outline

This thesis consists of seven chapters. Chapter one consists of a general introduction to overpressure and the generating mechanisms. Chapter two focuses on the data and methods used during this research. Chapter three corresponds to the East Coast Basin Project, which is located along the eastern margin of the North Island of New Zealand. The East Coast Basin (ECB) is a tectonically active basin due to the subduction of the Pacific Plate underneath the Australian Plate. Chapter four corresponds to the Gulf of Mexico Project, which is located in a passive basin with active salt tectonics. Chapter five corresponds to the West Africa Project, which is located in a passive basin with high temperatures. Chapter six is a general discussion of the three projects, and Chapter seven corresponds to conclusions and further research.

1.2 References

Athy, L. F. (1930). Density, porosity, and compaction of sedimentary rocks. *AAPG Bulletin*, 14(1), 1-24.

Audet, D. M. (1995). Mathematical modeling of gravitational compaction and clay dehydration in thick sediment layers, *Geophysics Journal International*, 122, 283–298.

Audet, S. M. (1996). Compaction and overpressuring in Pleistocene sediments on the Louisiana Shelf, Gulf of Mexico, *Marine and Petroleum Geology*, *13*(5), 467-474.

Bachu, S. (2008). CO2 storage in geological media: Role, means, status and barriers to deployment, *Progress in Energy and Combustion Science*, 34(2), 254-273.

Barker, C. (1972). Aquathermal Pressuring – Role of Temperature in Development of Abnormal – Pressure Zones, *AAPG Bulletin*, 56(10), 2068-2071.

Barker, C. (1990). Calculated Volume and Pressure Changes During the Thermal Cracking of Oil to Gas in Reservoirs, *AAPG Bulletin*, 74, 1254-1261.

Bowers, G. L. (1995). Pore pressure Estimation from Velocity Data: Accounting for Overpressure Mechanisms Besides Undercompaction, *SPE Drilling and Completion,* 89-95.

Bredehoeft, J. D. and Hanshaw, B.B. (1968). On the Maintenance of Anomalous Fluid Pressures: Thick Sedimentary Sequences, *Geological Society of America Bulletin*, 79, 1097–1106.

Bruce, C. H. (1984). Smectite Dehydration – Its Relation to Structural Development and Hydrocarbon Accumulation in Northern Gulf of Mexico Basin, *AAPG Bulletin,* 68, 673-683.

Chenrai, P. and Huuse, M. (2017). Pockmark formation by porewater expulsion during rapid progradation in the offshore Taranaki Basin, New Zealand, *Marine and Petroleum Geology,* 82, 399-413.

Crook, A. J. L., Willson, S. M., Yu, J. G., and Owen, D. R. J. (2006). Predictive modelling of structure evolution in sandbox experiments, *Journal of Structural Geology*, 28(5), 729-744.

Crook, A. J. L., Obradors-Prats, J., Somer, D., Peric, D., Lovely, P. and Kacewicz, M. (2018). Towards an integrated restoration/forward geomechanical modelling workflow for basin evolution prediction. Oil and Gas Science and Technology – Rev. *IFP Energies Nouvelles*, 73, 1-19.

Darby, D. and Funnell, R. H. (2001). Overpressure associated with a convergent plate margin: East Coast Basin, New Zealand. *Petroleum Geoscience,* 7, 291-299.

Deming, D. (1994). Factors Necessary to Define a Pressure Seal, *AAPG Bulletin*, 78(6), 1005-1009.

Dickinson, G. (1953). Geological Aspects of Abnormal Reservoir Pressures in Gulf Coast Louisiana, *The American Association of Petroleum Geologist*, 37, 410-432.

Dutta, N. C. (1987). Shale compaction, burial diagenesis, and geopressures: a dynamic model, solution, and some results, in Burrus, J. (ed.) *Thermal Modeling in Sedimentary Basins.* Paris, 149-172.

Eaton, B. A. (1975). The Equation for Geopressure Prediction from Well Logs, *SPE,* 1-11.

Erdi, A., Huuse, M. and Bachtiar, A. (2018). Tectonic Evolution and Hydrocarbon Prospectively of East Coast Basin, Offshore Hawke Bay, New Zealand, *Offshore Technology Conference,* 1-18.

Hamilton, E. L. (1976). Variations of Density and Porosity with Depth in Deep-Sea Sediments, *Journal of Sedimentary Petrology*, 46(2), 280-300.

Hart, B. S., Flemings, P. B. and Desphpande, A. (1995). Porosity and pressure: Role of compaction disequilibrium in the development of geopressures in a Gulf Coast Pleistocene basin. *AAPG Bulletin,* 23, 45-48.

Heidari, M., Nikolinakou, M. A., Hudec, M. R. And Flemings, P. B. (2021). Impacts of vertical salt welding on pore pressure, stresses, and deformation near the weld. *Marine and Petroleum Geology*, 133, 1-18.

Heinemann, N., Booth, M. G., Haszeldine, R. S., Wilkinson, M., Scafidi, J. and Edlmann, K. (2018). Hydrogen storage in porous geological formations – onshore play opportunities in the midland valley (Scotland, UK), *International Journal of Hydrogen Energy*, 43, 20861-208774.

Ingram, G. M., Urai, J. L. And Naylor, M. A. (1997). Sealing processes and top seal assessment, in Møller-Pedersen, P. and Koestler, A. G. (ed.), *Hydrocarbon Seals: Importance for Exploration and Production*. Singapore: Norwegian Petroleum Society, 165-174.

Issler, D. R. (1992). A new approach to shale compaction and the stratigraphic restoration, Beaufort-Mackenzie Basin and Mackenzie Corridor, Northern Canada. *AAPG Bulletin*, 76(8), 1170-1189.

Lahann, R. W. (2002). Impact of Smectite Diagenesis on Compaction Modeling and Compaction Equilibrium, in Huffman, A. R. and Bowers, G. L. (eds.), *Pressure regimes in sedimentary basins and their prediction*: AAPG Memoir, 76, 61–72.

Lahann, R. W. and Swarbrick, R. E. (2011). Overpressure generation by load transfer following shale framework weakening due to smectite diagenesis, *Geofluids*, 11, 362-375.

Luo, X. and Vasseur, G. (1992). Contributions of Compaction and aquathermal Pressuring to Geopressure and the Influence of Environmental Conditions, *AAPG Bulletin*, 76, 1550-1559.

Luo, G., Hudec, M. R., Flemings, P. B. and Nikolinakou, M. A. (2017). Deformation, stress, and pore pressure in an evolving suprasalt basin, *Journal of Geophysical Research: Solid Earth*, 122, 5663-5690.

Mazzini, A. and Etiope, G. (2017). Mud volcanism: An updated review, *Earth-Science Reviews, 81*-112.

McCartney, J. S., Sánchez, M. and Tomac, I. (2016). Energy geotechnics: Advances in subsurface energy recovery, storage, exchange, and waste management, *Computers and Geotechnics*, 75, 244-256.

Meissner, F. F. (1978). Petroleum Geology of the Bakken Formation Williston Basin, North Dakota, and Montana, in Demaison, D and Murris, R. J. (eds.) *Petroleum Geochemistry and Basin Evaluation.* AAPG Memoir, 159-179.

Nikolinakou, M. A., Flemings, P. B. and Hudec, M. R. (2014). Modeling stress evolution around a rising salt diapir. *Marine and Petroleum Geology*, 51, 230-238.

Nikolinakou, M. A., Heidari, M., Hudec, M. R. and Flemings, P. B. (2018). Stress and pore pressure in mudrocks bounding salt systems. *Rock Mechanics and Rock Engineering*, 51, 3883-3894.

Obradors-Prats, J., Rouainia, M., Aplin, A. C. and Crook, A. J. L. (2016). Stress and pore pressure in complex tectonic settings predicted with coupled, 3D geomechanical-fluid flow models. *Marine and Petroleum Geology*, 76, 464-477.

Obradors-Prats, J., Rouainia, M., Aplin, A. C. and Crook, A. J. L. (2017a). Assessing the implications of tectonic compaction on pore pressure using a coupled geomechanical approach. *Marine and Petroleum Geology*, 79, 31-43.

Obradors-Prats, J., Rouainia, M., Aplin, A. C. and Crook, A. J. L. (2017b). Hydromechanical modeling of stress, pore pressure, and porosity evolution in fold-and-thrust belt systems. *Journal of Geophysical Research: Solid Earth*, 122(11), 9383-9403.

O'Connor, S., Swarbrick, R. and Lahann, R. (2011). Geologically-driven pore fluid pressure models and their implications for petroleum exploration. Introduction to thematic set, *Geofluids,* 11 343-348.

Osborne, M. J. and Swarbrick, R. E. (1997). Mechanisms for Generating Overpressure in Sedimentary Basins: A Reevaluation, *AAPG Bulletin,* 81, 1023-1041.

Palciauskas, V. V. and Domenico, P. A. (1989). Fluid Pressures in Deforming Porous Rocks, *Water Resources Research*, 25(2), 203-213.

Plaza-Faverola, A., Klaeschen, D., Barnes, P., Pecher, I., Henrys, S. and Mountjoy, J. (2012). Evolution of fluid expulsion and concentrated hydrate zones across the southern Hikurangi subduction margin, New Zealand: An analysis from depth migrated seismic data, *Geochemistry, Geophysics, Geosystems,* 13, 1-21.

Plumley W. J. (1980). Abnormal High Fluid Pressure: Survey of Some Basic Principles, *AAPG Bulletin*, 64, 414-430.

Powers, M. C. (1967). Fluid-Release Mechanisms in Compacting Marine Mudrocks and their Importance in oil Exploration, *AAPG Bulletin*, 51(7), 1240-1254.

Raymer, L. L., Hunt, E. R. and Gardner, J. S. (1980). An improved sonic transit time-to-porosity transform, *OnePetro*, 1-13.

Ridd, M. F. (1970). Mud Volcanoes in New Zealand, *The American Association of Petroleum Geologist Bulletin,* 54, 601-616.

Strout, J. M. and Tjelta, T. I. (2005). In situ pore pressures: What is their significance and how can they be reliably measured?, *Marine and Petroleum,* 22, 275-285.

Swarbrick, R. E. and Hillis, R. R. (1999). The Origin and Influence of Overpressure with Reference to the North West Shelf, Australia, *The APPEA Journal,* 39, 64-72.

Swarbrick, R. E., Osborne, M. O. and Yardley, G. S. (2002). Comparison of Overpressure Magnitude Resulting from the Main Generating Mechanisms, in Huffman, A. R. and Bowers, G. L. (eds.) *Pressure regimes in sedimentary basins and their prediction.* AAPG Memoir 76, 1-12.

Tingay, M. R. P., Hillis, R. R., Swarbrick, R. E., Morley, C. K. and Damit, A. R. (2009). Origin of overpressure and pore-pressure prediction in the Baram province, Brunei. *AAPG Bulletin,* 93, 51-74.

Vidal-Royo, O., Hardy, S., and Muñoz, J. A. (2011). The roles of complex mechanical stratigraphy and syn-kinematic sedimentation in fold development: insights from discrete-element modelling and application to the Pico del Aguila anticline (External Sierras, Southern Pyrenees) in Poblet, J. and Lisle, R. J. (eds.) *Kinematic Evolution and Structural Styles of Fold-and Thrust Belts*. Geological Society, London, 349, 45-60.

Yassir, N. and Addis, M. A. (2002). Relationships between Pore Pressure and Stress in Different Tectonic Settings, in Huffman, A. R. and Bowers G. L. (eds.) *Pressure regimes in sedimentary basins and their prediction*: AAPG Memoir 76, 79–88.

Wyllie, M. R. J., Gregory, A. R. and Gardner, L. W. (1956). Elastic wave velocities in heterogeneous and porous media. *Geophysics*, 21, 41-70.

Zivar, D., Kumar, S and Foroozesh, J. (2021). Underground hydrogen storage: A comprehensive review, *International Journal of Hydrogen Energy*, 46, 23436-23462.

Chapter 2: Data and Methods

Data were collected from diverse sources, including government websites such as the New Zealand Petroleum and Mine Online Exploration Database (NZPAM) and the New Zealand Crown Research Institute (GNS), as well as the private datasets of oil and gas companies. The projects outlined in chapters 3, 4, and 5 each had individual data sets, and, depending on the study location and availability of data, different workflows were constructed for each. All the data used were uninterpreted primary data, aside from the interpretations already contained within the well reports. Qualitative and quantitative methods were used to analyse the data.

There was a scarcity of direct pressure measurements available for use across the three projects. Where direct pressure measurements were available, these were obtained in high-permeability intervals (reservoirs) in some wells. Measured pressure data were not registered along the overburden in any of the wells used within the projects. For this reason, mud weight data were used, which were obtained from well reports (e.g., the East Coast Basin and the Magnolia Field projects).

The geomechanical model results were compared to mud weight and measured pressure data when available (e.g., reservoir intervals). Well log data were also scarce for the overburden sections used within the three projects. When well log data had a short, shallow section missing (< 300 m), analytical equations to extrapolate the well log to the mud line were applied. In cases where the missing section was >300 m, the well logs were not used.

Mud weight data (ppg; pounds per gallon), which were taken along the sedimentary column, were converted to pore fluid pressure (MPa or psi), was compared to the results obtained from the geomechanical models. Measured pressure data obtained from drill stem test (DST), modular formation dynamic tester (MDT) and repeat formation tester (RFT), were also used; however, these data are scarce along the sedimentary column as these tests are generally taken in reservoir intervals with high permeabilities (e.g., sandstones). Depending on the equipment used during the pressure tests, other information such as reservoir productivity, permeability, connectivity, and skin can also be obtained.

The overpressure mechanisms that were investigated in each project depended on the geological characteristics of the study region. In this research, disequilibrium compaction, tectonic compression, clay diagenesis (chemical compaction), lateral pressure transfer, and fluid expansion (hydrocarbon generation) were investigated. A number of models were created throughout the research to facilitate the interpretation of the results. It should be noted that the numbering adopted to identify the models within this thesis is not always consecutive because only the models that are most representative of the geology in each study region are presented.

The software Petrel (versions 2019 to 2022) was used for seismic interpretation, structural framework, well-correlation, lithology interpretation, and 3D static model construction with property characterisation (e.g., porosity, pore pressure, and lithology distribution). In addition, analytical equations were applied to the well data of each project. Data and interpretations generated in the software Petrel, supported the generation of the 1D and 2D geomechanical models. Petromod (version 2021.2) was used for 1D basin modelling in chapter 5.

Geomechanical modelling was performed with the software ParaGeo (version 3.9.3). The visualisation of the results of each model was performed in the software ParaView (version 5.9.1). The models' results are presented in plots generated in Excel. Core and pore pressure data analysis was achieved using both the software Petrel and Excel.

Results are presented in metres (m), feet (ft), kilometres (km), and milliseconds (ms) for distances, thicknesses, and depths; mega Pascal (MPa) and pound per square inch (psi) for pore pressure; squared meters (m^2) and milli Darcy (mD) for permeabilities; fraction or percentage (%) for porosity; square kilometres (km^2) for areas; Celsius grades (°C) for temperatures; pound per square inch divided by feet (psi/ft) and mega Pascal divided by meters (MPa/m) for pore pressure gradients.

2.1 Geomechanical Models Equations

The software used was ParaGeo, which works with finite geological elements. The geomechanical models used a staggered two-way coupling approach, where generally 200 to 1,000 (depending on the model) mechanical steps are solved per each flow step with the coupling performed at every flow step. The governing equations are described below (equation 2.1 to 2.6). For the constitutive equations (e.g., yield surface, hardening law, and photoelasticity) please refer to the paper published during this research for Chapter 2 (Obradors-Prats et al., 2023*)* in addition to Obradors-Prats et al. 2017a.

For the mechanical field, ParaGeo solves the linear momentum balance equation for a saturated porous medium of a single phase, as described in Lewis and Schrefler (1998). Equation 2.1 is written in a continuum mechanics sign convention.

$$L^T\left(\sigma' - \alpha(\emptyset) m P_f\right) + \rho_b g = 0 \quad (2.1)$$

with:

$$\sigma' = \left\{\sigma'_x \;\; \sigma'_y \;\; \sigma'_z \;\; \tau_{xy} \;\; \tau_{yz} \;\; \tau_{zx}\right\}^T \quad (2.2)$$

$$m = [1 \;\; 1 \;\; 1 \;\; 0 \;\; 0 \;\; 0]^T \quad (2.3)$$

$$\rho_b = (1 - \emptyset)\rho_s + \emptyset\rho_f \quad (2.4)$$

Where L is the standard continuum mechanics differential operator, σ' is the effective stress tensor, σ'_x σ'_y and σ'_2 are the normal effective stresses to orthogonal planes *x*, *y*, and *z* respectively, τ_{xy} τ_{yz} and τ_{zx} are the tangential stresses acting in planes *x*, *y*, and *z* respectively, $\alpha(\emptyset)$ is the Biot's coefficient as a function of porosity (for the models in this thesis it is assumed a constant value of $\alpha = 1$), P_f is the pore fluid pressure, m is the hydrostatic unit tensor, ρ_b is the saturated bulk mass density, g is the gravitational vector, ρ_s is the solid grain density, and ρ_f is the fluid density (1,000).

The effective stress, which is the stress exerted on the matrix is represented by equation 2.5. This equation is written in geomechanical sign convention for convenience.

2.5 $\sigma' = \sigma - \alpha(\emptyset)\, mP_f$

Where σ' is the effective stress and σ is the total stress tensor.

Fluid transport is modelled by the single phase Darcy's flow equation as defined in Lewis and Schrefler (1998).

2.6 $div\left(\frac{k(\emptyset)}{u_f}\left(\nabla P_f - \rho_f g\right)\right) = \left(\frac{\emptyset}{K_f} + \frac{(\propto(\emptyset) - \emptyset)}{K_s}\right)\frac{\partial P_f}{\partial t} + \frac{\alpha(\emptyset)}{1-\emptyset}\frac{\partial_\emptyset}{\partial t}$

Where $k(\emptyset)$ is the permeability tensor, which is function of porosity, u_f is the fluid viscosity (3.17101E-23) MPa*Ma, K_f is the fluid stiffness (2,000) MPa, K_s is the solid grain stiffness, and $\frac{\alpha(\emptyset)}{1-\emptyset}\frac{\partial_\emptyset}{\partial t}$ represents the fluid flow due to a change in porosity and provides the coupling between the mechanical and flow fields.

The properties of clastic sediments used in the three projects is presented in Table 2.1.

Table 2.1.- Properties and values for clastic sediments used in the geomechanical models of the three projects (East Coast Basin, Magnolia, and West Africa), which were modelled with the critical-state SR4 model.

Property	Symbol (Units)	Mudstone	Siltstone	Sandstone	Carbonate (with clay content)	Carbonate Low Permeability
Grain stiffness	K_{g} (MPa)	70,000	70,000	70,000	70,000	70,000
Grain density	ρ_s (Kg/m3)	2,700	2,700	2,700	2,700	2,7000
Depositional Porosity	fraction	0.54	0.50	0.45	0.42.5	0.35
Biot constant	α	1.0	1.0	1.0	1.0	1.0
Poisson's Ratio	v	0.3	0.25	0.2	0.3	0.3
Kappa	K	0.008	0.0075	0.007	0.002	0.002
Tensile intercept	P_{t0} (MPa)	0.05	0.05	0.05	0.05	0.05
Depositional pre-consolidation pressure	P_{c0} (MPa)	-0.5	-0.5	-0.5	-0.5	-0.5
Friction angle	$\emptyset_{cs}$ (Deg)	24	30	32	38	38
Friction parameter	β (Deg)	62	67.4	68.8	72.1	72.1
Dilatation parameter	φ (Deg)	57	62.4	63.8	68	68

Table 2.2.- Properties and values used for the salt, which was modelled using the Hershel-Bulkley viscoplastic law.

Property	Symbol (Units)	Salt
Grain stiffness	K_g (MPa)	30,000
Grain density	ρ_s (Kg/m3)	2,140
Young's Modulus	E (MPa)	5,000
Poisson's Ratio	v	0.3
Yield strength	q_y (MPa)	0.1
Viscoplastic constant	K_{visc} (MPa*Ma)	3.2E-3
Viscoplastic exponent	n_{visc}	1.0

2.2 Models Description, Boundary Conditions and Properties

The models developed during this research, were used to investigate the influence of different geological events (e.g., sedimentation, erosion, hiatus, tectonic compression, clay diagenesis) on overpressure development. In this manuscript, the term "1D model" is used for models involving a column-shaped geometry with 1 element across the column, while the term "2D model" is used for those models that account for basin-like geometric shapes (e.g., geological sections). For the 1D models that investigated the effect of sedimentation, erosion, pots-erosion sedimentation, a roller boundary condition was applied to the base side boundaries. For the models that incorporate tectonic compression, a prescribed displacement was applied to the eastern boundary (Figure 2.1a). For the 2D models, roller boundary conditions to the base side boundaries in conjunction with spatially varying sedimentation were used (Figure 2.1b).

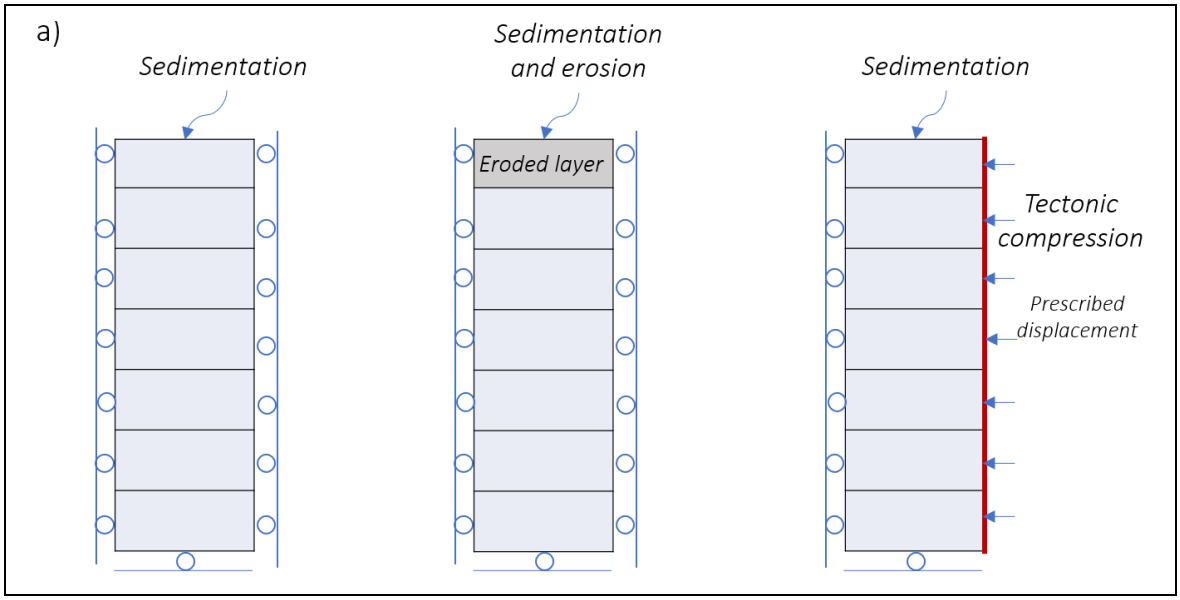

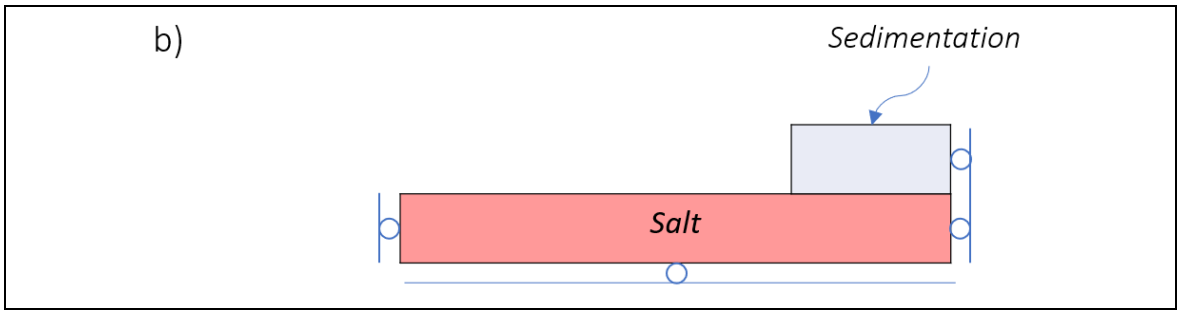

Figure 2.1.- Sketch of the 1D and 2D models showing the boundary conditions applied.

2.3 References

Lewis, R. W. and Schrefler, B. A. (1998). The finite element method in the static and dynamic deformation and consolidation of porous media. Chichester: John Wiley and Sons, Inc.

Obradors-Prats, J., Rouainia, M., Aplin, A. C. and Crook, A. J. L. (2017a). Assessing the implications of tectonic compaction on pore pressure using a coupled geomechanical approach. *Marine and Petroleum Geology*, 79, 31-43.

Obradors-Prats, J., Calderon, M. E. E., Jones S. J., Rouainia, M., Aplin, A. C. and Crook, A. J. L. (2023). Integrating Petrophysical, Geological and Geomechanical Modelling to Assess Stress States, Overpressure Development and Compartmentalisation Adjacent to a Salt Wall, Gulf of Mexico, *Marine and Petroleum Geology*, 155, 1-22.

Chapter 3: Overpressure Development in Sediments with Complex Geological Histories, East Coast Basin, New Zealand

*Part of this chapter has been presented at the Offshore Technology Conference, Houston, 2023 and a published paper titled "**1D Hydro-geomechanical Modelling of Pore Pressure on an Active Convergent Margin: East Coast Basin, New Zealand**" for the Offshore Technology Conference (doi.org/10.4043/32406-MS).*

The contribution made by Erika Calderon Medina (PhD student) to this paper was 80% and formed part of wider scoping research within the GeoPOP4 research consortium.

Abstract

This chapter is focused on the East Coast Basin (ECB) of New Zealand, an active convergent margin where near to lithostatic pore fluid pressures have been encountered at shallow depths as 300 m. This study aims to identify the generating overpressure mechanisms through the analysis of geological data and geomechanical modelling.

A regional investigation, which included analysis of the Cretaceous to Pleistocene tectono-stratigraphy was combined with seismic and well-log interpretation to understand the structural and sedimentation history of the basin and thus the main factors that have contributed to overpressure generation or dissipation. 1D geomechanical models were built to undertake parametric studies to investigate the effect different sedimentation and erosion rates, hiatus periods, different erosion thicknesses, and tectonic compression have on porosity and pore pressure evolution.

Results from the parametric models show that, depending on sediment permeability, high overpressures can be preserved during rapid erosion events due to the small timeframe for its dissipation. Furthermore, it was shown that only recent erosive events are relevant to present-day overpressure. High levels of tectonic compression (from 8 to 12.5%) applied to recent events can produce both high pore pressure values and significant porosity reduction if the sedimentary column was under-compacted prior to the tectonic compression.

Findings from the parametric models were used as a starting point to understand controls on the pore pressure and porosity in five wells located in the onshore area of the ECB. Results show that the high pore pressure registered at shallow depths (< 1 km) is significantly driven by tectonic compression as a result of the high convergence rates (20 to 60 mm/yr) of the Pacific Plate towards the Australian Plate. Disequilibrium compaction generated mild overpressure due to high sedimentation rates (up to ~3,000 m/Ma). However, most of this overpressure was dissipated during uplift, hiatus, and erosion.

Factors such as (a) thick (up to 1 km) mudstone packages deposited from the Cretaceous to Pleistocene, (b) thin low-permeability layers of limestone deposited during the Miocene to Pliocene, and (c) intervals with high smectite content are shown to be important seals for overpressure retention. Nevertheless, if these seals have been eroded or the layers are connected to the surface, the overpressure generated would dissipate, and the dissipation time depends on the petrophysical properties of the layers, the time of exposure to the surface, and the existence of a recent active overpressure mechanism.

3.1 Introduction

This project is focused on the East Coast Basin (ECB) of New Zealand, an active tectonic basin where unanticipated, shallow, near-lithostatic pore pressures have been encountered during exploration and drilling (Barnes, 1997; Darby and Ellis, 2001). The reasons for such high pressures have not been completely identified because of the geological and structural complexity of the ECB. However, manifestations such as mud volcanoes, oil and gas seeps, gas chimneys, seep-carbonates, and pockmarks have been identified along this basin and have been related to overpressure dissipation (e.g., Ridd, 1970; Campbell et al., 2008; Barnes et al., 2010; Plaza-Faverola et al., 2012; Erdi et al., 2018; Watson et al., 2019).

It has been proposed that disequilibrium compaction and tectonic compression both play a role in the generation of overpressure; first due to the sedimentation of bathyal mudstone lithologies over the Miocene Epoch and second due to the subduction of the Pacific Plate underneath the Australian Plate from the Cretaceous to the present-day (Darby and Funnell, 2001; Darby and Ellis, 2001; Sibson et al., 2003; Burgreen-Chan et al., 2016). On the other hand, fluid expansion due to gas generation and clay diagenesis have been determined to not have any contribution to overpressure in this basin (Field et al., 1997) due to the fact that the ECB is a cold basin with a geothermal gradient of ~23 °C/km (Funnell et al., 1999). Two formations (Wanstead and Weber Formations; Figure 3.2) have been identified to have high smectite contents (Fergusson, 1985; Field et al., 1997; Hines et al., 2013; McArthur et al., 2020), but these intervals do not reach the necessary temperature and depth to begin clay diagenesis (Darby and Funnell, 2001). The source rocks identified in this basin are the Waipawa and Whangai Formations (Rogers et al., 1999; Figure 3.2); however, in the studied area, these source rocks do not have high organic content and have been determined to be immature to expel gas (Funnell and Benchilla, 2005).

The contribution of each overpressure generation mechanism has not fully been established, as this basin has a complex geological history from the Cretaceous to the present-day, with multiple periods of erosion, tectonic events, and changes in sedimentation and erosion rates. This means that it is difficult to evaluate potentially multiple controls on present-day pore pressure as well as the evolution of pore pressure through geological time (Brown, 1998, 1999; Darby and Funnell, 2001; Burgreen-Chan et al., 2016; Jiao et al., 2017).

The aim of this study is to apply 1D hydro-geomechanical modelling (these are coupled models that use finite elements) to identify and quantify the contribution of two overpressure mechanisms: disequilibrium compaction and tectonic compression. To achieve this, a regional evaluation, including data selection, a tectono-stratigraphy revision, 2D seismic data interpretation, well log analysis, and a 3D static model construction was undertaken. The findings of this assessment were later considered in the construction of the hydro-mechanical models. These hydro-mechanical models are presented first with a step-by-step models where different variables were addressed separately (e.g., sedimentation and erosion rates, erosive events, hiatus periods, low-permeability layers, and tectonic compression) and then with 1D hydro-mechanical models constructed for five key wells located in the ECB.

3.1.1 Geological Background

The ECB is located to the east of the North Island, New Zealand. It has an area of ~100,000 km^2, which includes both onshore and offshore regions (Field et al., 1997). This basin is positioned on the active Hikurangi subduction margin, where the Pacific Plate (10 to 15 km of oceanic crust) subducts beneath the Australian Plate (>40 km of continental crust) (Field et al., 1997) at a convergence rate of 20 to 60 mm/yr along the Northern Island (Wallace et al., 2004 and 2009) (Figure 3.1a). The subduction process has caused earthquakes with high magnitudes (e.g., 1855 with a magnitude of 8.2, 1931 with a magnitude of 7.4, and 2016 with a magnitude of 7.8) (Eiby, 1968; Ansell and Bannister, 1996). The paleo-relief of the ECB has also been changing from the Oligocene to the present-day by ridges and seamounts (Lewis et al., 1998; Barnes et al., 2010; Pedley et al., 2010; Burgreen and Graham, 2014) formed during accretion.

The deposits of the ECB are mainly deep-water turbidites described as either sea-plain sheets or lobes, deposited in trench-slope basins developed by the subduction process, that have been redeposited in some areas by contourites (Bailleul et al., 2007; Lewis and Kohn, 1973; Lewis, 1980; Burgreen and Graham, 2014; McArthur et al., 2020; Bailey et al., 2021; Sloss et al., 2021).

Petroleum exploration started around the 1870s with primitive, short-depth wells. In 1910, the well Waitangi-1 was drilled in the Hawkes Bay region (Gisborne Oil Co., 1910; Figure 3.1a) and reported an increase in pore fluid pressure at ~200 m depth. Most of the wells in this basin have registered high overpressure values at different depths and formations (e.g., (a) Kauhauroa-3 around 3 MPa at ~315 m, (b) Mangaone-1 around 3.6 MPa at ~825 m, and (c) Kiakia-1 around 4.5 MPa at ~900 m; for reference see Figure 3.1a).

The hydrocarbon traps in the ECB are anticlines (hanging wall folds) related to thrust and strike-slip faults with a stratigraphic component (Figure 3.1b). The target reservoirs are clastic (e.g., Tunanui Sandstone), with potential in carbonate intervals (e.g., Kiakia Limestone). The identified hydrocarbon seals are thick mudstone intervals (e.g., Pindari, Tangihau, and Waingaromia mudstones) and smectite-rich intervals of marls and calcareous mudstones (Wanstead and Weber Formations) (Field et al., 1997; Davies et al., 2000) (Figure 3.2 and Appendix 3.9.1).

The main source rocks are shales of the Palaeocene and Late Cretaceous (Waipawa and Whangai Formations; Figure 3.2) (Rogers et al., 1999), which have been interpreted to be immature to expel gas (Funnell and Benchilla, 2005). In the ECB, the Waipawa Formation has a total organic carbon (TOC) value of ~5% (Rogers et al., 2001; Naeher et al., 2019), while the Whangai Formation has up to 1.5% with common values of 0.5% in a few intervals of the Opoutama-1 well (Figure 3.2). However, other deposits from the Late Cretaceous can also be excellent source rocks due to the thick successions of turbidites and shallow marine clastic deposits as described in the East Coast, Taranaki, and Pegasus Basins (Figure 3.1a) (Killops et al., 1994; Funnell and Benchilla, 2005; Uruski and Bland, 2011; Campbell et al., 2008; O'Neil et al., 2023).

Around nine source rock kitchens have been identified, with the biggest located offshore around the northern part of Hawke Bay (1) to the western part of Mahia Peninsula (2) (Figure 3.1a). The expulsion time has been debated; Funnell et al. (1999) determined that expulsion from this source

began in the Early Oligocene, while Brown (2002) and Erdi et al. (2018), in studies performed around the Hawkey Bay proposed a migration path during an extensional phase in the Late Miocene.

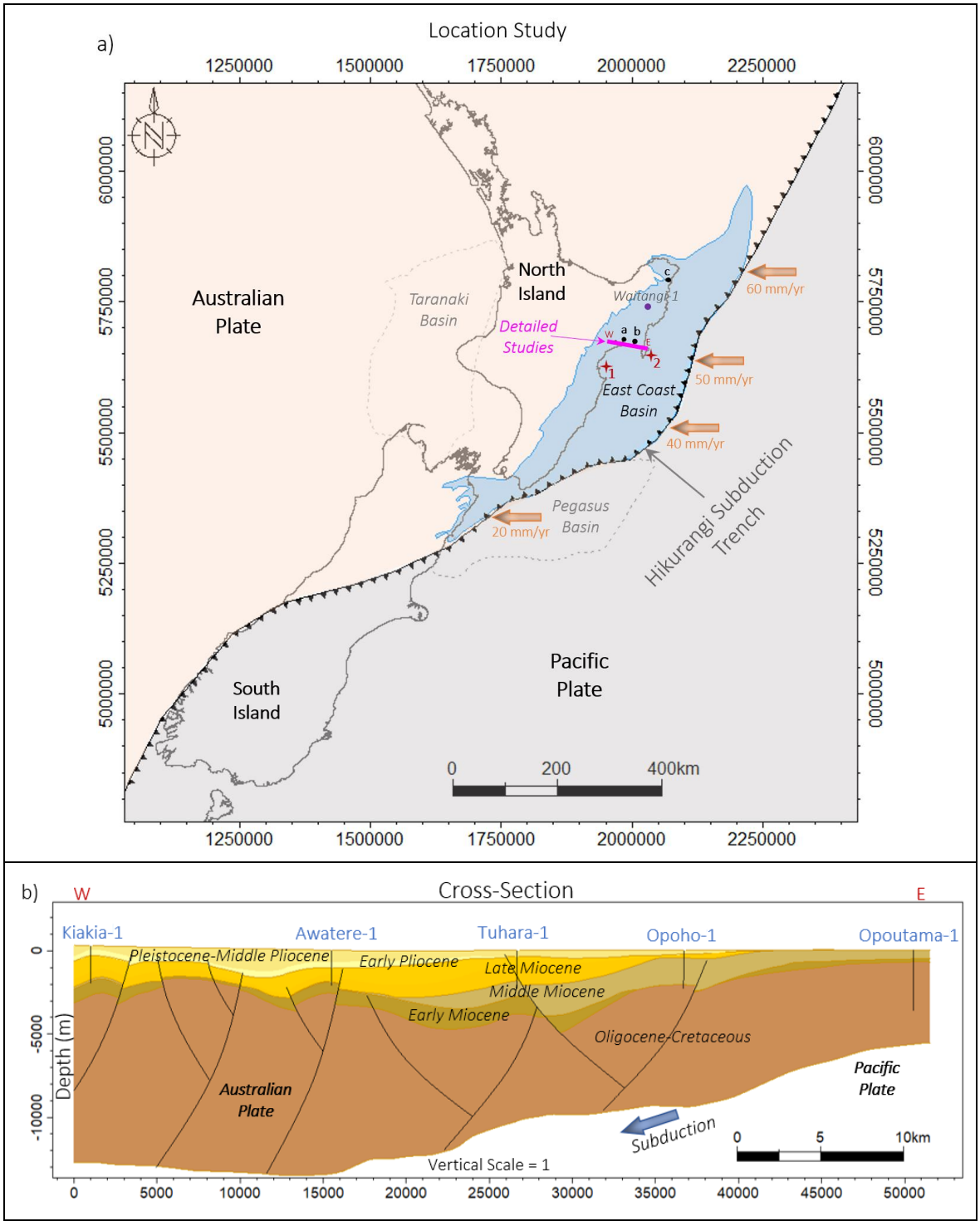

Figure 3.1.- a) Project location map with the Taranaki, Pegasus, and East Cost Basins; the location of the main hydrocarbon kitchen areas: Hawke Bay (1) and Mahia Peninsula (2*); the location of three of the wells with shallow overpressures (a) Kauhauroa-3 at ~315 m, (b) Mangaone-1 at ~825 m, and (c) and Kiakia-1 at ~900 m. It is also highlighted the area selected for a detailed assessment, including the location of the five key wells and the current convergence rates along the Northern Island (Source: Wallace et al., 2004 and 2009). b) Cross-section showing the location of the five wells, the main faults, and the main periods interpreted during this research.*

The geological formations (Appendix 3.9.1) used in this study have been described in well reports, and the names are the most common in the area selected for a detailed study (NZ Aquitaine Petroleum Ltd., 1967; Field et al., 1997; Brown, 1998 and 1999; Raine et al., 2015) (Figure 3.2)

The tectonic-stratigraphic evolution of this basin (Figure 3.2) began during the Cretaceous, when New Zealand was part of the Gondwana Supercontinent (Mortimer, 2004; Balance, 2017). During the Middle Cretaceous, subduction was reduced, and a period of rifting started with the separation of New Zealand from Australia and Antarctica, which led to the formation of the ECB (Field et al., 1997; Funnel et al., 1999).

The Early Cretaceous sediments correspond to metamorphic and deformed strata known as the Torlesse Group (Figure 3.2). Over these sediments, a regional angular unconformity has been interpreted in the ECB which separates Early Cretaceous sediments from the upper sequences deposited during the Albian (J. A. R., 1985).

In the Late Cretaceous, a mixed clastic succession including mudstones, siltstones, and sandstones was deposited. The names of these sediments depend on the area where they were described. In the ECB, these sediments are recognised as the Mata-Raukumara Formation. Overlaying these sediments and in a relatively passive margin, a thick package of mudstones was deposited, which corresponds to the Whangai Formation (Lillie, 1953).

During the Palaeocene, in a widening area of the ECB, a thin section of poorly bedded, non-calcareous mudstone known as the Waipawa Formation was deposited (Field et al., 1997; Funnel et al., 1999) (Figure 3.2). Even though a passive margin has been established, signs of tectonism have been observed during the Paleogene that affected the deposition of the formations along the basin (Field et al., 1997).

During the Eocene, a thick interval of mudstone lithologies was deposited, named as the Wanstead Formation in the studied area of the ECB. The main characteristic of this formation is the amount of smectite (Lillie, 1953; Fergusson, 1985; Haskell, 2005). A transition of these sediments to more calcareous mudstones is represented by the Weber Formation, which was deposited from the Late Eocene to the Middle-Late Oligocene and represents the end of the passive margin (Figure 3.2). According to J. A. R. (1985) and Simpson et al. (1993), this formation represents a maximum transgression in the basin.

From the Late Eocene-Early Oligocene to the present-day, subduction has been reactivated (Jiao et al., 2017). Sedimentation of sandstone and mudstone lithologies and erosive events have been interpreted in this period (Funnel et al., 1999). In the Late Miocene, extensive erosion with an extensional component affected the sedimentation. During the Late Miocene, thin intervals of limestones (~10 to 85 m) described as strongly cemented bryozoan and thick intervals of shale lithologies were deposited (e.g., Kauhauroa and Kiakia Limestones and Pindari Mudstone) (Turner, 1989).

From the Pliocene to the present-day an inversion phase affected by a compressional component has been controlling the sedimentation and the structural framework in the ECB (Field et al., 1997; Erdi et al., 2018; McArthur et al., 2020).

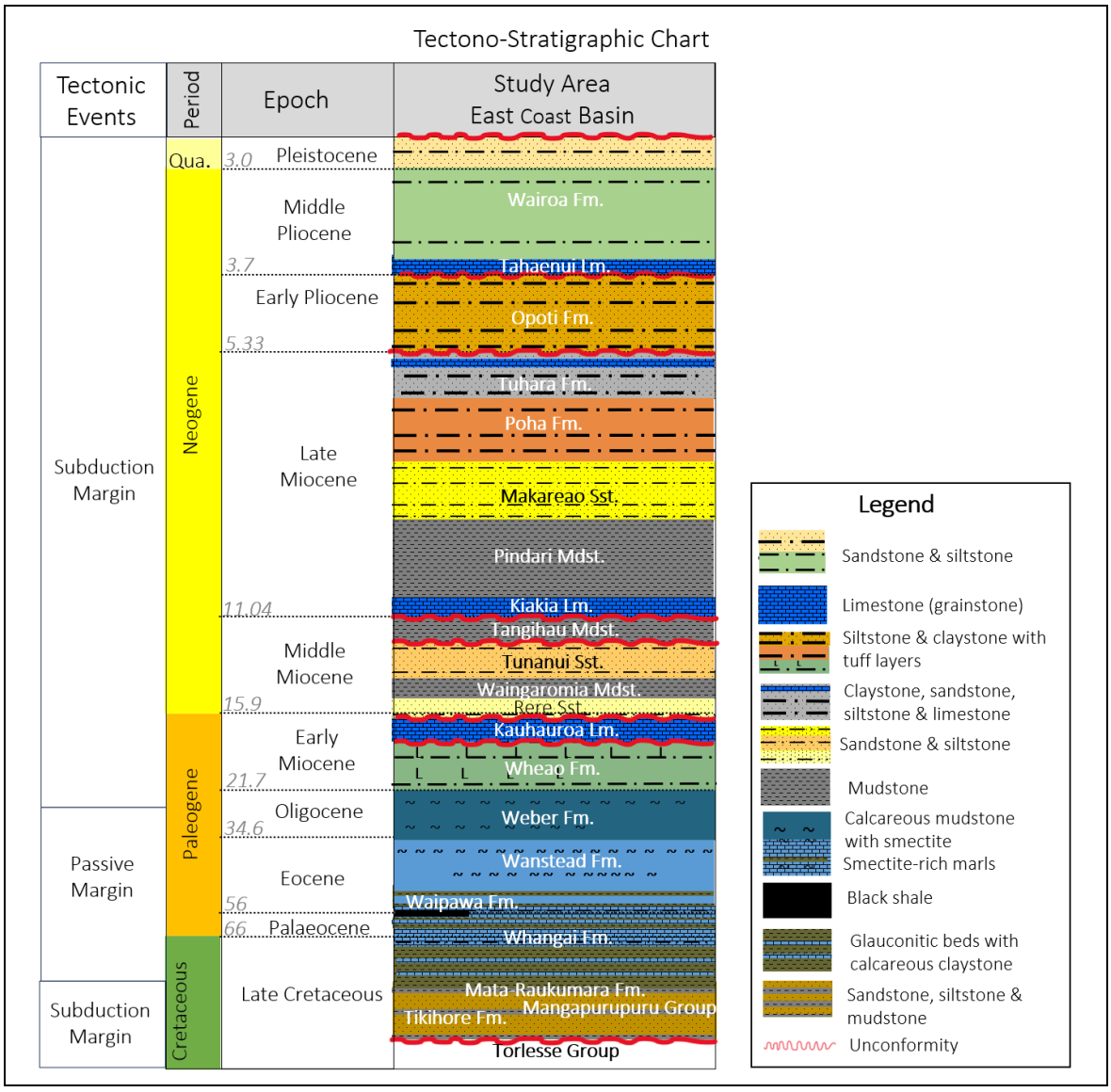

Figure 3.2.- Tectono-stratigraphic chart with the main formations and tectonic events described in the ECB research area. Source: ECB well reports and Raine et al. (2015). As the formations in the ECB are often referred to under different names, the names in this report will refer to the most commonly used by oil companies and academic studies. The most representative lithology was chosen in each formation.

3.2 Data and Methods

Data for the ECB were obtained through the New Zealand Petroleum and Mine Online Exploration Database (NZPAM), the New Zealand Crown Research Institute (GNS), and the General Bathymetric Chart of the Oceans (GEBCO).

The primary data for this study are from seismic surveys and well reports. The data consist of twenty-two well log sets (GR, RHOB, DT, and resistivity), twenty wells with mud weight values, nine wells with RFT, MDT or DST, ninety-eight well reports, one 3D seismic survey, and approximately two hundred 2D seismic lines in time with two 2D seismic lines in depth.

These data were assessed to understand the regional geology of the area, and from that, a small area (~337 km^2) that has five wells and two seismic sections in depth was chosen for a more detailed

assessment (Figure 3.3). This area is almost perpendicular to the Hikurangi subduction trench, and the wells reached different depths and formations, which allowed to investigate the overpressure along the whole sedimentary column of the area.

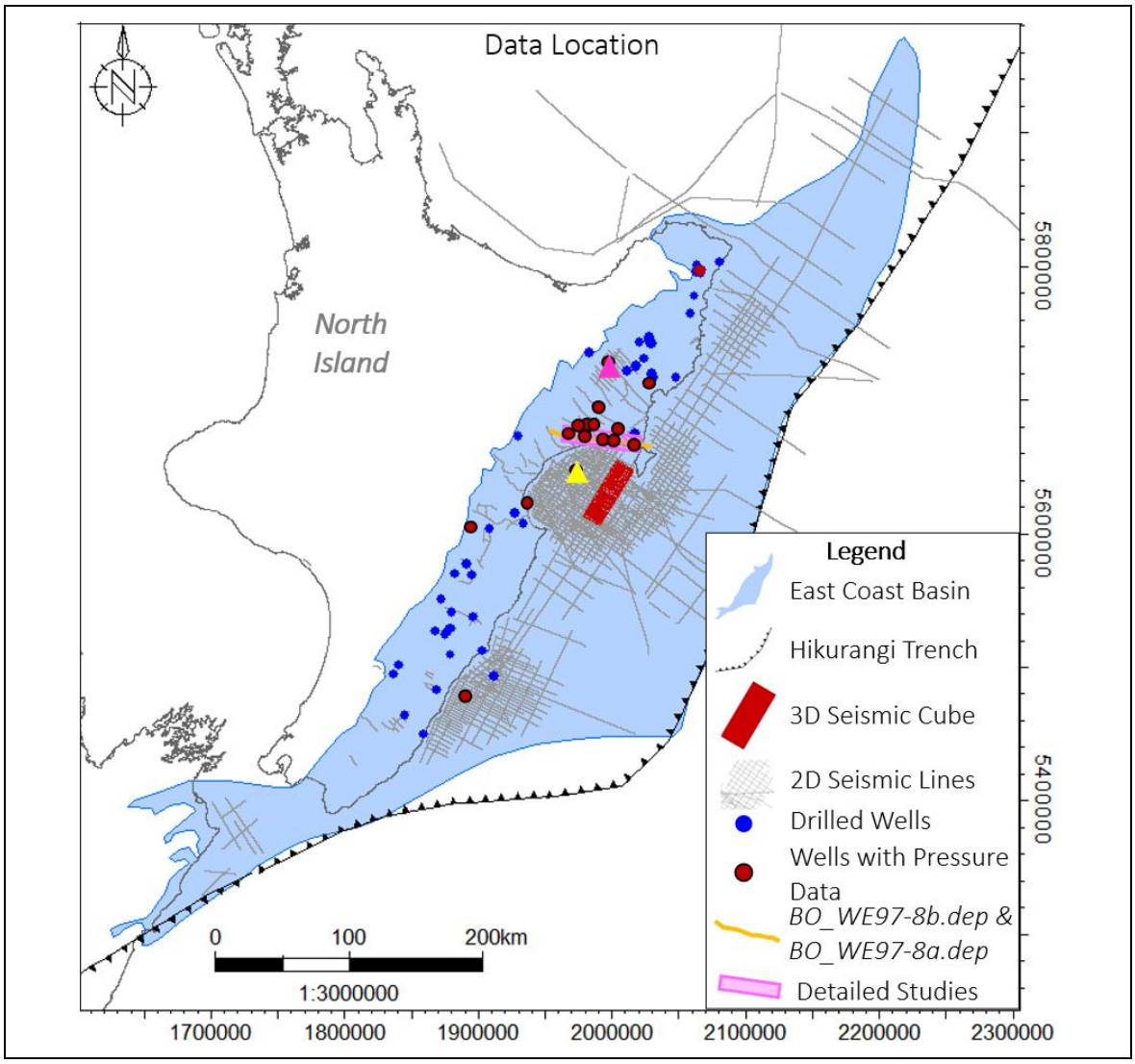

Figure 3.3.- Location map with 2D and 3D seismic data, drilled well locations, wells with pressure data, 2D seismic lines in depth and the area selected for a more detailed studies. It is also presented the two wells with check shots Rere-1 (pink triangle) and Hawke Bay-1 (yellow triangle). The data are from a mix of onshore and offshore wells in the ECB.

3.3 Pore Pressure Analysis of Geological Data

A review of well logs, seismic data, and petrographic reports available for the ECB (110,000 km^2), followed by a detailed assessment in the 337 km^2, was performed to understand the evolution of the fluid pore pressure in the ECB. Five key wells (Kiakia-1, Awatere-1, Tuhara-1, Opoho-1, and Opoutama-1) located almost perpendicular to the subduction margin and with different sedimentary successions were chosen for the detailed analysis. The objectives of these wells were clastic and carbonate intervals. However, only some hydrocarbon shows with a few intervals with high gas levels were registered, making these wells uneconomic. These wells crossed different periods of time and discovered high pore pressure values at different depths and lithologies (Figures 3.1b and 3.8).

Seismic interpretation was conducted on several 2D seismic lines and one 3D seismic cube. Most of the interpretation was performed in time with two 2D seismic lines in depth (BO_WE97-8b.dep and BO_WE97-8a.dep) (Figure 3.4). Check shots from two wells, Rere-1 and Hawke Bay-1, were used to calibrate the well tops (Figure 3.3). One-way time (OWT) was created in wells with good sonic logs (DT). In this study, horizons interpreted in time were first converted to depth and then adjusted with the horizons interpreted in depth. The time-depth conversion was performed with analytical equations created by Funnell et al. (1999), as in this study a velocity model was not created. Equation 3.1 adjusts better for shallow horizons, while equation 3.2 works better for deep horizons.

3.1 $$Depth\,(m) = 0.0005 * (TWT)2 + 0.4629 * TWT + 95$$

3.2 $$Depth\,(m) = 0.0002 * (TWT)2 + 0.8733 * TWT$$

A total of eight horizons were mapped during this study, considering previous interpretations (Topographic Surface, Early Pliocene, Late Miocene, Pindari Mudstone, Middle Miocene, Early Miocene, Late Oligocene, and Basement). The horizon named Basement represents the boundary between the Pacific Plate and the Australian Plate. In most cases, these horizons represent unconformities (e.g., erosive events).

The main structures identified in this basin are anticlines with an N 20° E orientation with thrust and back-thrust faults. The reflectors in the detailed area reach high dips of ~70°, which was also interpreted in nearby areas by Watson (1962). The dip angle of the faults varies along the plane of the fault; at shallow depths, the angles are between 10 and 15° while at deep depths, the angles increase to ~65°. Thrust faults are the most common faults in this basin. In the detailed studied area, the thrust faults start from the horizon named Basement and dip towards the west, while the back-thrust faults start from the trust faults and dip towards the east.

As the seismic resolution from 2,000 ms (~4,000 m) to 4,000 ms (~10,000 m) is not clear and there are no deep wells available to calibrate this interpretation, the horizons mapped in this research could differ from other studies. In general, the quality of the seismic data is variable; there are some areas where the reflectors are clear and others where the quality is poor.

In the detailed area (~337 km^2), the section from the Late Oligocene to the Basement contains a mixture of different lithologies (e.g., sandstone, clay, breccia-conglomerate, igneous rocks, calcareous concretions, gneiss, and mudstone) (Moore and Speden, 1979; Field et al., 1997; Mortimer, 2004). These lithologies could not be identified within the seismic data during this research.

Mud-dominated lithologies of the Early and Middle Miocene were observed on seismic data as blurry reflectors (Figure 3.4a). The thickest interval recognised was the Pindari Mudstone (Late Miocene), with a thickness varying from ~200 to ~1000 m in the small area. This formation has most recently been related to deep ocean currents (contourites), where the originally deposited sediments were transported to a different location, leaving very fine accumulations of sediments (e.g., Bailey et al., 2021; Ballance et al., 2017). The influence of thick mud-dominated lithologies on overpressure generation was investigated through 1D mechanical modelling in this research.

Other lithologies recognised within the seismic data were the thick smectite-rich marls and calcareous mudstone intervals of the Wanstead and Weber Formations (Eocene and Late Oligocene) and the thin limestone intervals of the Kiakia, Kauhauroa, and Tahaenui Formations (Early Miocene to Pliocene) (Figure 3.4a). The thin limestone lithologies were interpreted as non-continuous thin bright reflectors (~10 to 85 m interpreted on well logs) present in the forelimb and back-limb of the trench-slope structures. Their distribution is not continuous, which has also been identified in other studies (e.g., Bailleul et al., 2013; Claussmann et al., 2021).

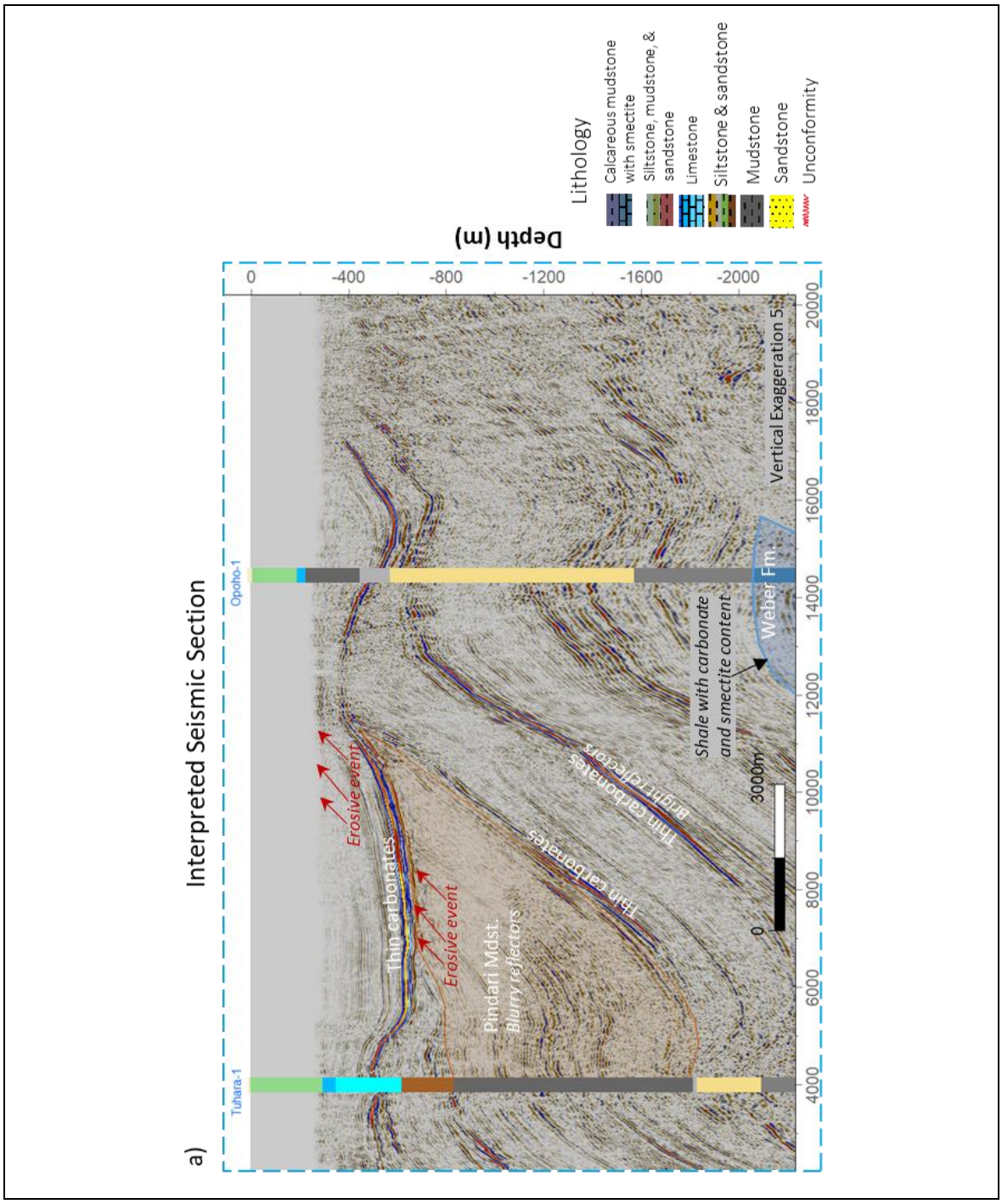

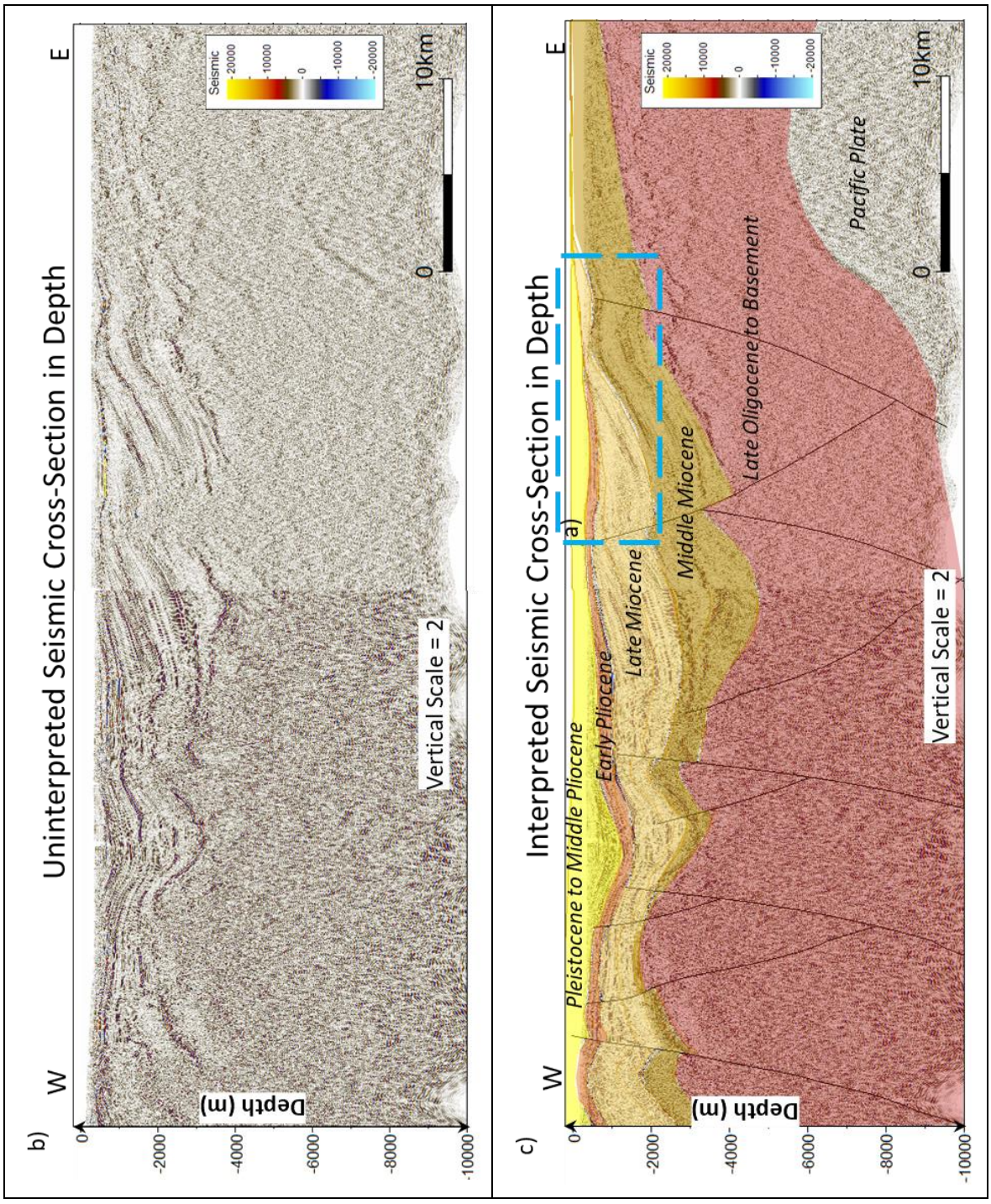

Figure 3.4.- (a) Seismic section showing the bright discontinuous thin carbonate intervals, erosive events, and blurry reflectors of the Pindari Mdst. b) Uninterpreted seismic section and (c) interpreted seismic section with horizons and faults. This location of this cross-section is presented in Figures 3.1. The blue rectangle represents Figure 3.4a.

To identify any relationship between overpressure and the lithologies of this basin, samples of the Kauhauroa limestone were analysed as this formation is interpreted to have low porosities (e.g., low sonic values) similar to the other thin limestone intervals (Tuhara carbonate section, Tahaenui and Kiakia Limestones). The Kauhauroa Limestone is highly calcite-cemented and contains skeletons of bryozoans, echinoderms, and foraminifers with grains of quartz (1) and glauconite (2). The parallel lines in the calcite crystals were interpreted to be due to tectonic compaction (3) (Longman, 1998 in

Brown, 1999; Figure 3.5). In addition, core reports and thin sections of wells located in the ECB (e.g., Awatere-1, Tuhara-1A) highlight the existence of elongated and irregular contacts between grains related to mechanical compaction (Brown, 1998 and 1999; Martin, 1995; Watters, 1990).

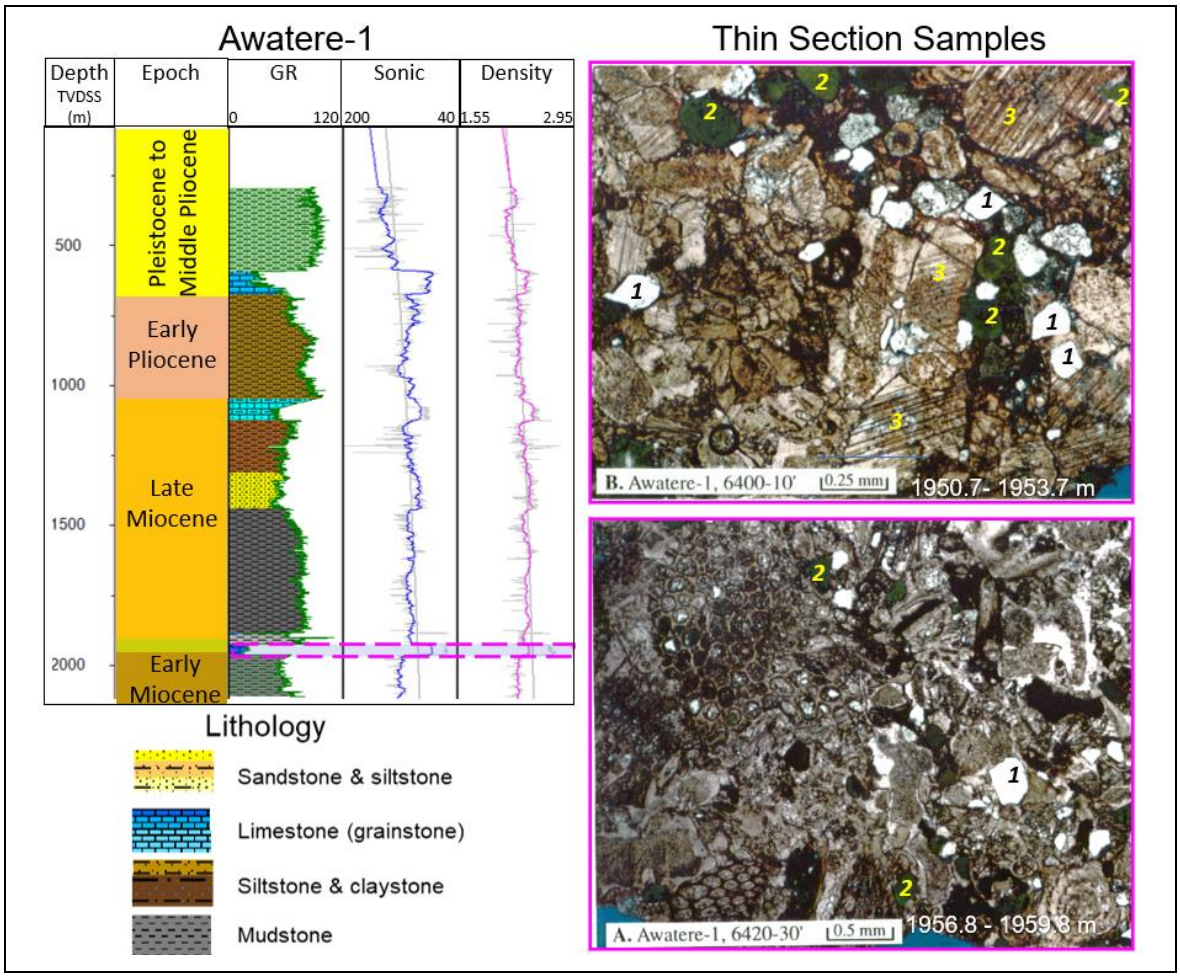

Figure 3.5.- Summary of the photos of the thin sections selected to show the Kauhauroa Limestone. The location of these intervals has been highlighted in pink on the Awatere-1 well. This interval has low sonic values, indicating low porosities. The thin section photos and description were taken from the study performed by Longman (1998) in Brown (1999).

A 3D static model was also built to better understand the general distribution of fluid pore pressures and their relationship with lithologies. The structural framework was based on the seismic interpretation (2D lines) performed in this research. Formations, which represent the main lithologies (Figure 3.6a), were distributed in this model using a truncated Gaussian simulator and pore pressures used a sequence Gaussian simulator without any dependent variable (Figure 3.6b).

From this distribution, it is observed that pore pressure values increased with depth and below limestone intervals (Early Miocene to Pleistocene) and thick mudstone sections (Late Miocene). The faults are interpreted to be sealed and the intervals with exposure to the surface with a potential lateral pressure drainage. It is also observed that the wells located to the east (offshore area) have larger eroded sections than the wells located to the west (onshore area).

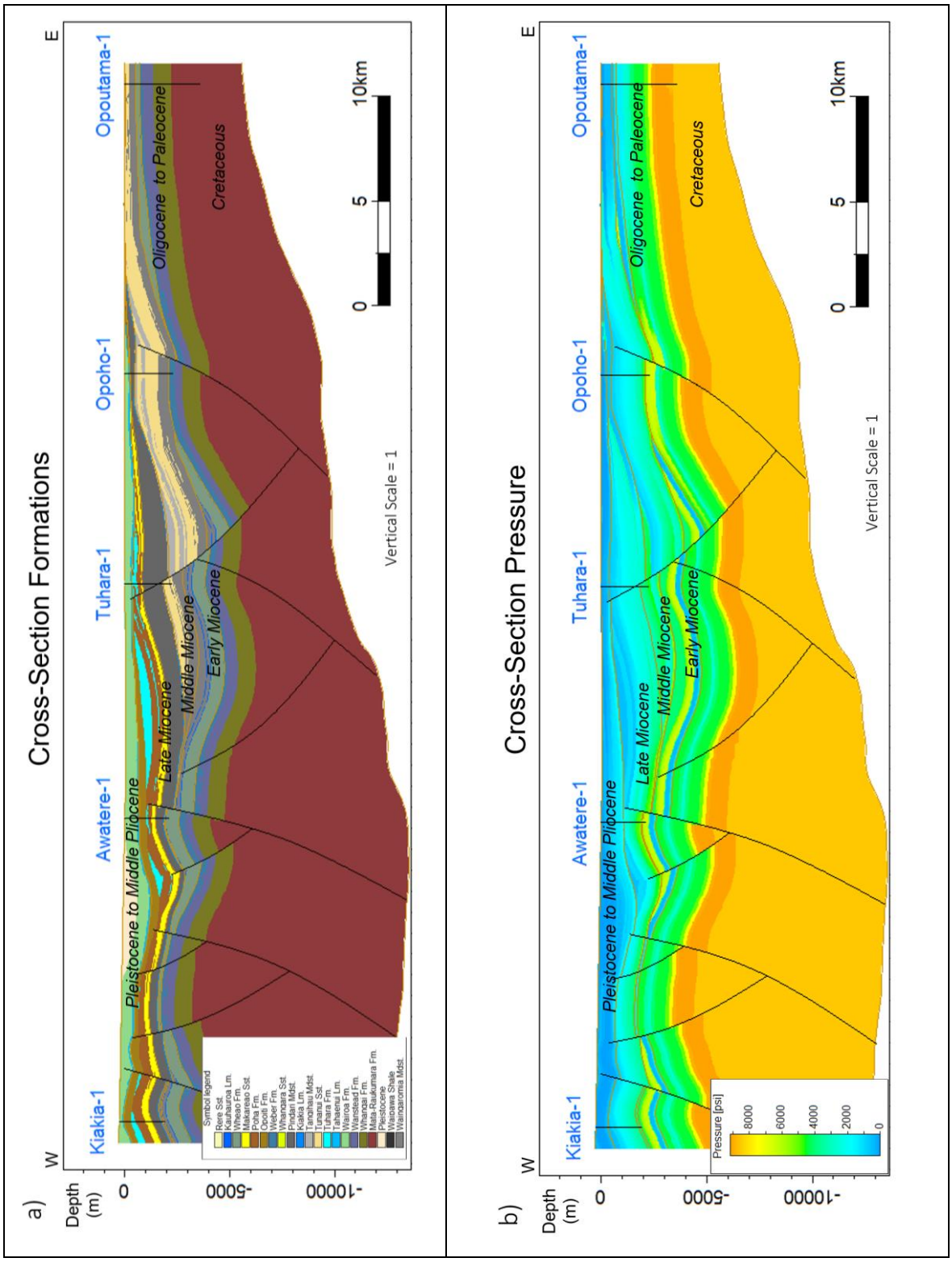

Figure 3.6.- Cross-sections of the 3D static model constructed in the detailed area. a) Formations distribution represented by the main lithology. Yellow colours represent sandstone lithologies, blue colours represent carbonate lithologies, grey colours represent mudstone lithologies, and green and brown siltstone lithologies. b) Pore pressure distribution of the mud weight data.

A well correlation (Figure 3.7) with the five key wells (Kiakia-1, Awatere-1, Tuhara-1, Opoho-1, and Opoutama-1) shows the thickness variation of the sedimentary successions in the ECB (e.g., Middle Miocene, Late Miocene). The thin carbonate intervals (~10 to 85 m) have low DT and low GR

readings from the Middle Miocene to the Holocene. These thin intervals were eroded or not deposited in the Opoutama-1 well.

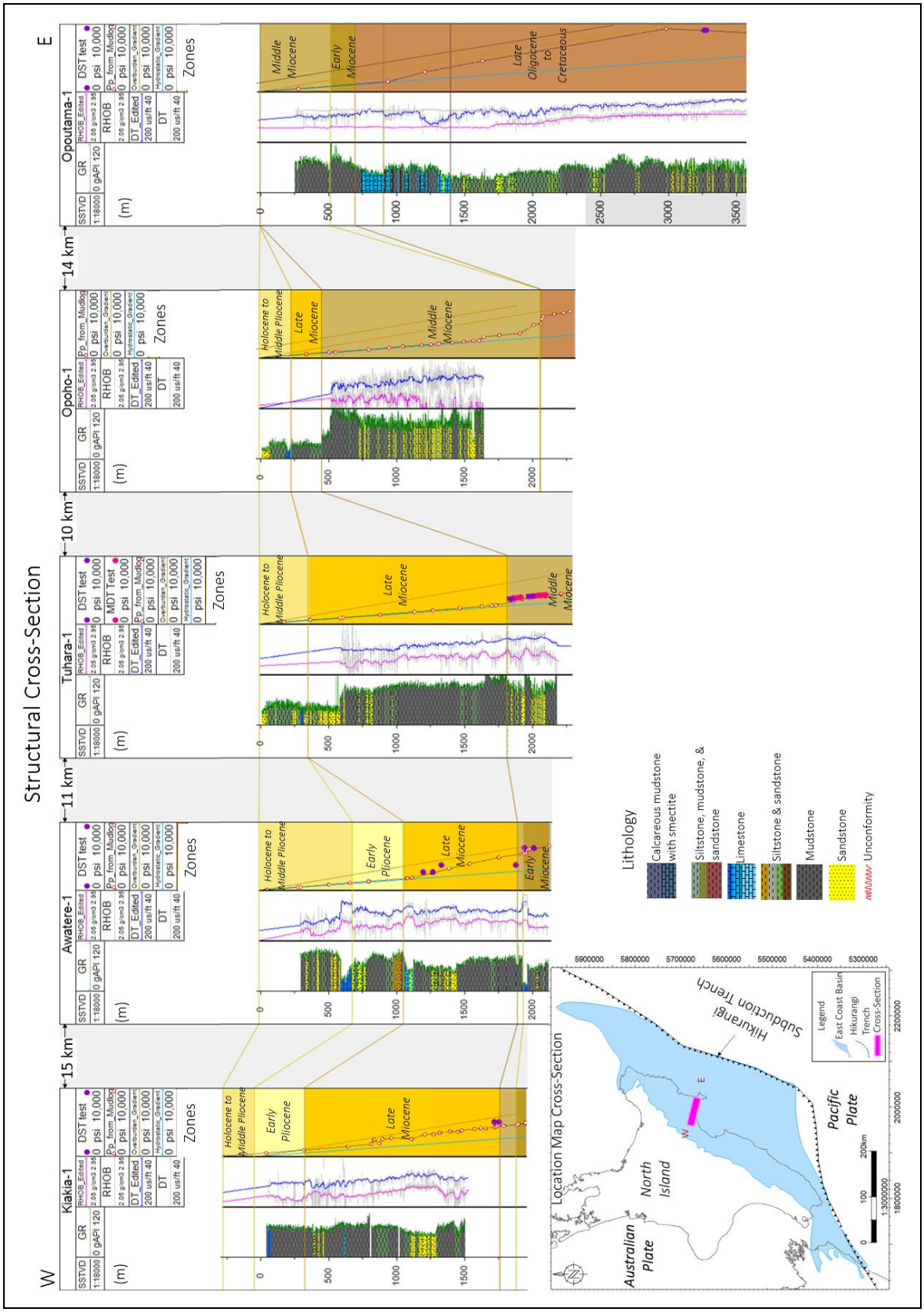

Figure 3.7.- Well correlation of the five key wells located in the onshore area of the ECB, showing depth (TVDSS), GR with lithologies, density (RHOB), and sonic (DT) logs. Pore pressure values with hydrostatic and lithostatic gradients are presented with the interpreted periods.

In the ECB, pressure data are scarce and have been taken in sandstone intervals. An analysis of the measured data was performed on nine drill stem tests (DST), one repeat formation tester (RFT), one modular formation dynamics tester (MDT) and mud weights of twenty wells (see Figure 3.3 for the location of the twenty wells with mud weight data). Data show that overpressure is not related to a depth, region, or formation, which was also previously noted by Darby and Funnell (2001). Nevertheless, during this study, it has been observed that overpressure also increases below thin layers of limestone in addition to the thick intervals of mudstone and formations with high smectite contents. The intervals with smectite are considered to be low-permeability units (e.g., Fergusson, 1985; Field et al., 1997; Darby, 2002; Lothe et al., 2023) as smectite is a very fined-grained clay that can be identified on well logs due to its relatively low density and high Poisson's ratio when compared to other clays (e.g., Mondol et al., 2008; Beloborodov et al., 2019) (Figures 3.8a and 3.8b).

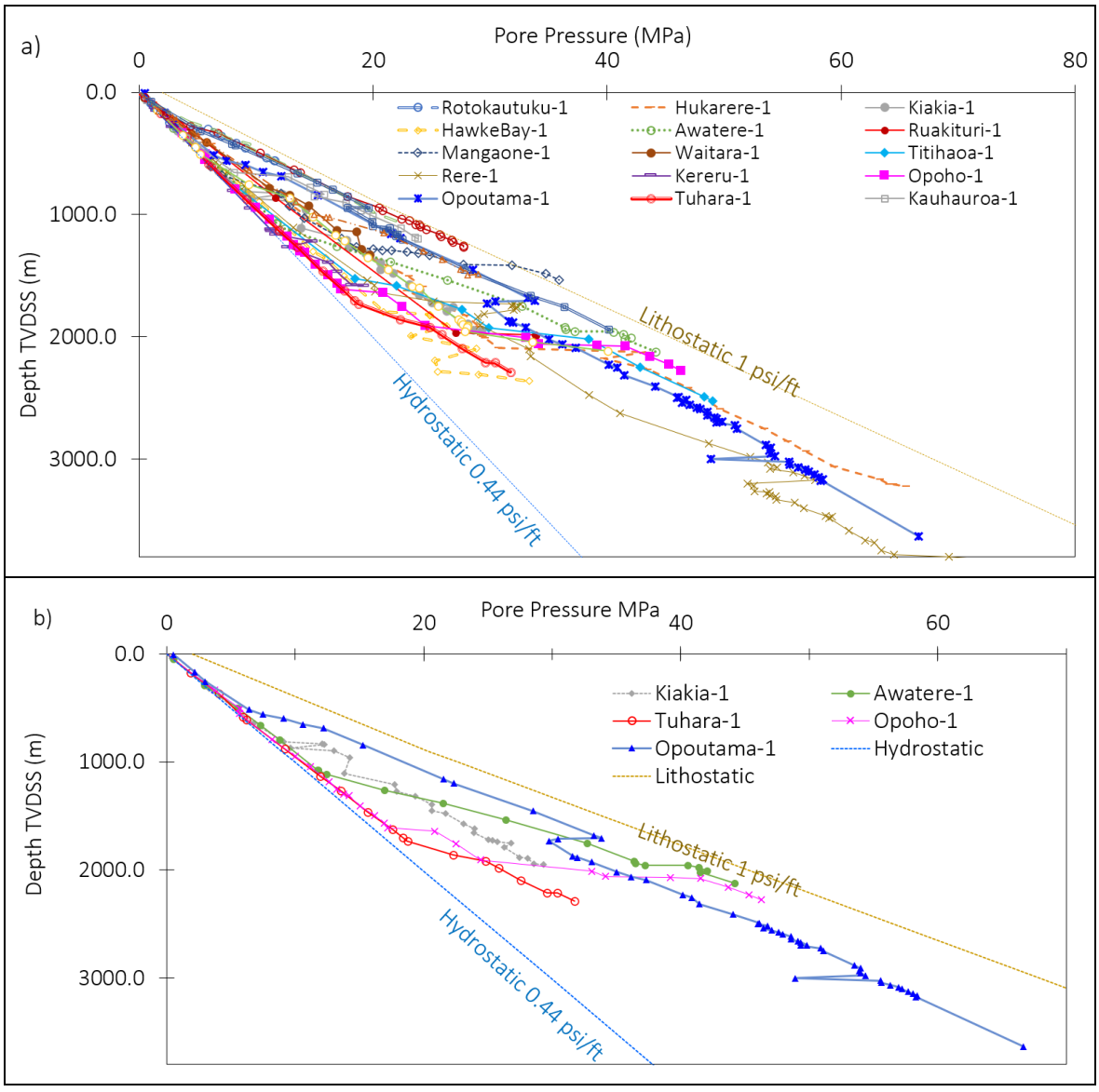

Figure 3.8.- a) Pore pressure vs. depth plot of twenty wells located in the ECB. b) Pore pressure vs. depth of the five wells selected to study in depth, with the hydrostatic pressure gradient of 0.00995 MPa/m (0.44 psi/ft) and lithostatic gradient of 0.0226 MPa/m (1 psi/ft); reference hydrostatic gradients between 0.433 and 0.45 psi/ft have been determined previously (Watson, 1962; Brown, 1960).

3.3.1 Pore Pressure Log-Based Assessment

Analytical equations can be used to estimate the eroded thickness during the last erosive event. However, the effect of pore pressure, effective stress, and other erosive intervals (e.g., regional and local unconformities interpreted on seismic and wells) along the sedimentary column cannot be accurately determined (e.g., Bailleul et al., 2007); therefore, geomechanical modelling was used.

Overpressure interpretation is not straightforward in the ECB due to its complex geological evolution. Normal compaction trends (hydrostatic trends) were obtained from sonic and density logs using Wyllie's (1956) and Athy's (1930) equations (3.3 and 3.4). To match these trends with the well data, an eroded interval (ei), which varies in each well location, was calculated qualitatively, and used in the analytical equations. The eroded thickness investigated ranged from 0 m (no erosion) to 2,000 m, and the best fit was selected.

$$\Delta t_{NC} = \Delta t_{ma} + (\Delta t_{ml} - \Delta t_{ma}) * e^{c*(-Z-ei)} \quad 3.3$$

$$\rho_{NC} = \rho_{ma} + (\rho_{ml} - \rho_{ma}) * e^{c*(-Z-ei)} \quad 3.4$$

Where Δt_{NC} is the transit time for normal compaction (hydrostatic trends), Δt_{ma} is the matrix transit time (67 us/ft), Δt_{ml} is the mudline transit time (188 us/ft), z is the depth below sea level (m), c is the compaction coefficient (0.0005 m^{-1}) after Hansen (1996) and Tingay et al. (2009), ei is the eroded interval, ρ_{NC} is the density of the normal compaction, ρ_{ma} is the matrix density (2.67 gr/cm^3) and ρ_{ml} is the density at the mudline (1.8 g/cm^3) (Couzens-Schultz and Azbel, 2014).

The normal compaction trends for porosity were obtained with Athy's (1930) equation. This equation was previously used by Funnell et al. (1996) in other New Zealand basins. This approach calculates the porosity at normal compaction and subtracts a value that represents the eroded thickness. In this research, the missing section was represented by (ei) (equations 3.5 and 3.6).

$$\emptyset_{NC\ mudstones\ and\ carbonates} = \emptyset_{mud} * e^{c*(-z-ei)} \quad 3.5$$

$$\emptyset_{NC\ sandstones} = \emptyset_{sst} * e^{c*(-z-ei)} \quad 3.6$$

Where $\emptyset_{NC\ mudstones}$ is the porosity of mudstones, $\emptyset_{NC\ sandstones}$ is the porosity of sandstones, $\emptyset_{mud}$ and $\emptyset_{sst}$ is the porosity at mudline (e.g., 0.54 for mudstones and 0.45 for sandstones), (z) is the depth in metres below sea level, and c is the compaction constant (e.g., 0.0005 for mudstones and 0.000333 for sandstones). The initial porosities and compaction values in these equations were determined using New Zealand data (Funnell et al., 1996).

Porosities were obtained from the sonic and density logs using equations 3.7 and 3.8.

$$\emptyset_{DTx} = 1 - \left(\frac{\Delta tma}{\Delta t}\right)^{1/x} \quad 3.7$$

$$\emptyset_{density} = \frac{\rho_{ma} - \rho_b}{\rho_{ma} - \rho_f} \quad 3.8$$

Where $Ø_{DTx}$ is the corrected porosity from the sonic log, x is the acoustic formation factor considered to be 2.19 after Hart et al. (1995) and Issler (1992), Δt_{ma} is the matrix transit time (67 us/ft), Δt is the measured transit time (us/ft), $Ø_{density}$ is the porosity from density log, ρ_{ma} is the matrix density (2.67 gr/cm^3), ρ_b is the bulk density measured (g/cm^3) and ρ_f is the fluid density (1.03 g/cm^3).

To show the results, the well Awatere-1 was selected as it has pressure tests and mud weight values for almost the whole sedimentary column. This well also crossed all the thin limestone intercalations (Tahaenui, Kiakia, and Kauhauroa Limestones and the carbonate section of the Tuhara Formation) (Figure 3.9) and the Pindari Mudstone, which has low permeability values. An interpretation based on log reversals (sonic and density) could imply that disequilibrium compaction might have some contribution to overpressure. The first reversal starts below a thin carbonate interval at ~700 m depth. The second reversal starts within the thick mudstone package (Pindari Mdst.) at ~1,625 m depth. This interpretation does not account for all the erosive events, hiatus, and tectonic compression periods, and it cannot be compared with the rest of the wells as each well has a different sedimentary column with overpressures that start at different depths (for reference see Figure 3.8).

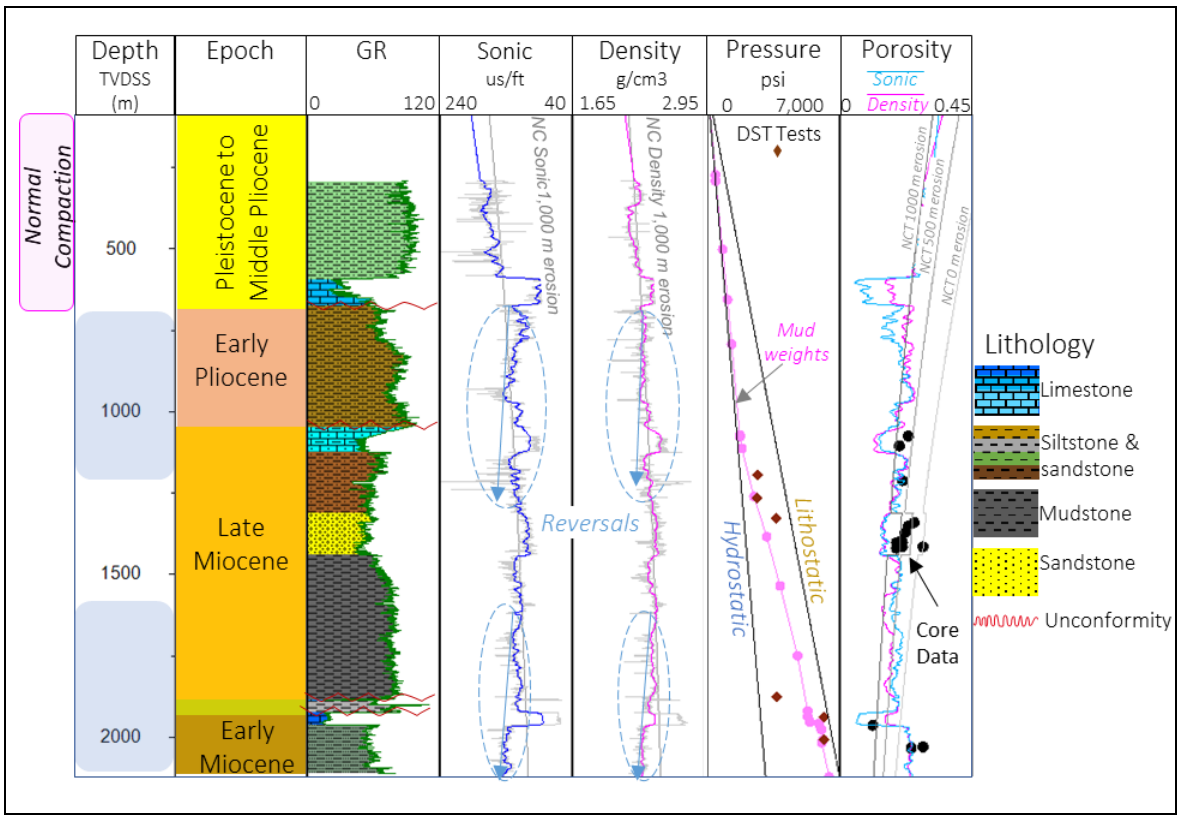

Figure 3.9.- Log-based pore pressure interpretation showing depth, periods, GR with the lithologies, sonic (DT), density (RHOB), pore pressure values and calculated porosity with core data. The porosity track also shows three normal compaction trends, which represent different eroded thickness intervals.

3.4 Geomechanical Modelling Assessment

To illustrate the effect of sedimentation, erosion, hiatus, and tectonic compression on the pore pressure and porosity evolution of the ECB, 1D models with simplified geological histories were

created. These models facilitate the understanding of the effect of different parameters on pore pressure evolution. Similar models have been used to understand sediment behaviour and to calibrate parameters such as porosity-permeability relationships and compaction trends (e.g., Darby and Ellis, 2001; Obradors-Prats et al., 2017b). Obrador-Prats et al. (2017a) created geomechanical models to understand the effect of tectonic compaction on sediments that experience different sedimentation rates and different tectonic shortenings, including post-tectonic sedimentation.

This research used 1D parametric geomechanical models to investigate first the factors (e.g., sedimentation rates, low-permeability sediments, hiatus periods, erosive events, tectonic shortening compactions) that affect overpressure generation and then incorporate additional geological events to examine the roles of additional overpressure generation mechanisms and the role of overpressure dissipation.

The second part of the geomechanical modelling assessment was to apply the findings from the parametric models to the five key wells (Kiakia-1, Awatere-1, Tuhara-1, Opoho-1, and Opoutama-1), located on the onshore area of the ECB, creating 1D column coupled models that aim to capture the stratigraphic and geological history of this basin, to better understand the potential of a range of geological processes on pore pressure development in the region.

The software used for the geomechanical modelling was ParaGeo, a finite element code capable of solving the physics involved in complex geological histories, capturing stresses, strain tensors, pore pressure, and temperature, among other parameters, to predict the evolution of sedimentary basins (Crook et al., 2018).

This software encompasses the critical state poro-elasto-plastic Soft Rock 4 model, which can capture the plastic strain hardening or the plastic strain softening depending on the stress path yielding location (e.g., hardening on the compression side of yield and softening on the tensile side of yield surface). The critical state poro-elasto-plastic model continues shearing without changes in volume or effective stresses (Wood, 1990). The equations for mechanical and fluid flow fields are the linear momentum for a saturated medium with a single fluid phase, which in these models was water using Darcy's single-phase flow equation. The models constructed in this study do not account for plastic deformation.

3.4.1 1D Parametric Column Models

The dimensions of all the models are 20 m wide. The lithology used in all the layers of the parametric models is mudstone (shale). Each layer that was deposited has a thickness of 300 m. The model begins with one layer deposited (300 m), followed by the sedimentation of fourteen additional layers (4,200 m).

The normal compaction trend (hydrostatic trend) used is based on Schneider's model (1996), which is a variant of Athy's model, but it has more flexibility to define the compaction curve shape (Figure 3.10a). The porosity-permeability relationship used in the parametric models (Parametric Models in Figure 3.10b) is a modification of the Kozeny-Carmen's mudstone relationship (K-C Shale in Figure 3.10b), which depends on the porosity and pore throat size of each lithology.

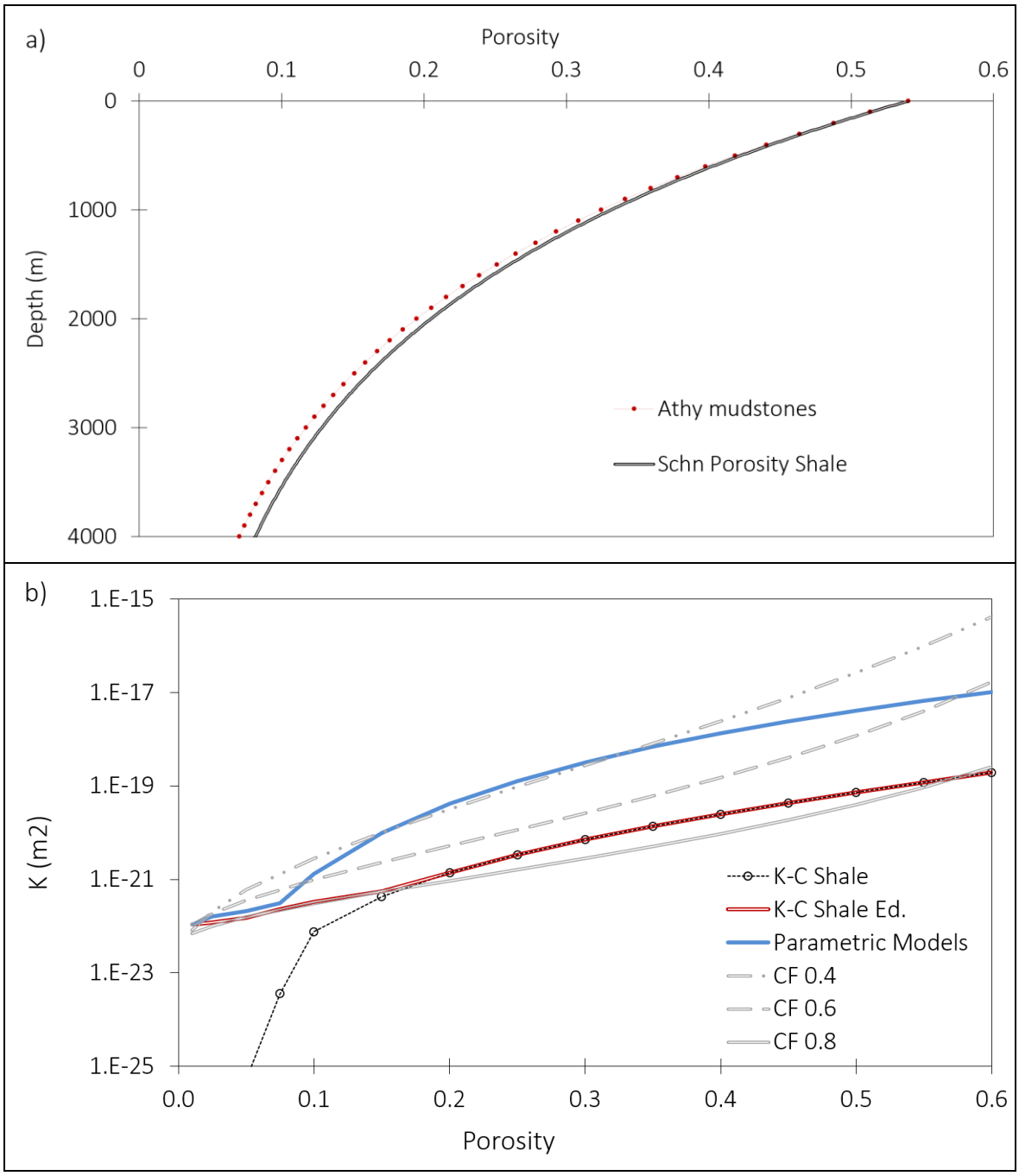

Figure 3.10.- a) Schneider's normal compaction trend for mudstones (hydrostatic trend) with Athy's normal compaction trend for mudstone for reference. b) Porosity-permeability relationship for mudstone based on Kozeny-Carmen's mudstone relationship. The parametric relationship for mudstone lithologies used in all the parametric models, and the K-S Shale Ed. relationship used in five models (Section 3.4.2). The porosity-permeability relationships (CF 0.4, CF 0.6, and CF 0.8) suggested by Yang and Aplin (2010) are presented as references. A minimum cut-off value for permeability was set to 1.E-22 m^2 (a value adopted after Yang and Aplin, 2007). CF is the clay content (e.g., 0.6 has 60% clay content).

3.4.2 Sedimentation Rates

The sedimentation rates considered in the parametric study are summarised in Table 3.1 and are based on studies performed in the ECB and other basins around the world (e.g., Audet, 1996;

Swarbrick and Hillis, 1999; Swarbrick et al., 2002; Darby and Funnell, 2001; Neef, 1992). The models 2, 3, 4, 1, and 36 used the Parametric Models porosity-permeability relationship (Figure 3.10b).

The effect of low-permeability intervals was investigated with the same sedimentation rates but with a porosity-permeability relationship (K-C Shale Ed.) 23 times lower than the porosity-permeability relationship named Parametric Models (Figure 3.10b) with models 2a, 3a, 4a, 1a, and 36a.

Table 3.1.- Inputs of the sedimentation rates used in the models.

Model	Sed. rate (m/Ma)	Sed. duration per layer (Ma)
2 and 2a	200	1.5
3 and 3a	500	0.6
4 and 4a	1,000	0.3
1 and 1a	2,000	0.15
36 and 36a	3,000	0.1

Results from the models show that the faster the sedimentation rate, the higher the predicted pore pressure, as the pressure is unable to dissipate. For instance, a pore pressure of 44 MPa is observed at 3 km when the sedimentation rate is 3,000 m/Ma, whereas a pore pressure of 32 MPa is observed at the same depth with a sedimentation rate of 200 m/Ma (Figure 3.11b).

Porosity is preserved due to overpressure reducing the vertical effective stress. For example, at 3 km, a porosity of 0.29 is observed with a sedimentation rate of 3,000 m/Ma, while a porosity of 0.18 is seen at the same depth with a sedimentation rate of 200 m/Ma (Figure 3.11a). While it could be argued that porosity is preserved due to undercompaction, there is only a thickness difference of 200 m between the models with the fastest and slowest sedimentation rates, suggesting the influence of compaction is minimal.

Models 36a, 1a, 4a, 3a, and 2a correspond to 3,000, 2,000, 1,000, 500, and 200 m/Ma respectively show that a lower porosity-permeability relationship, which is ~23 times lower than the one used in models 36, 1, 4, 3, and 2, will generate greater pore pressure values. However, porosity values were preserved in most of the sedimentary columns due to the overpressure generated during sedimentation (Figures 3.11c and 3.11d).

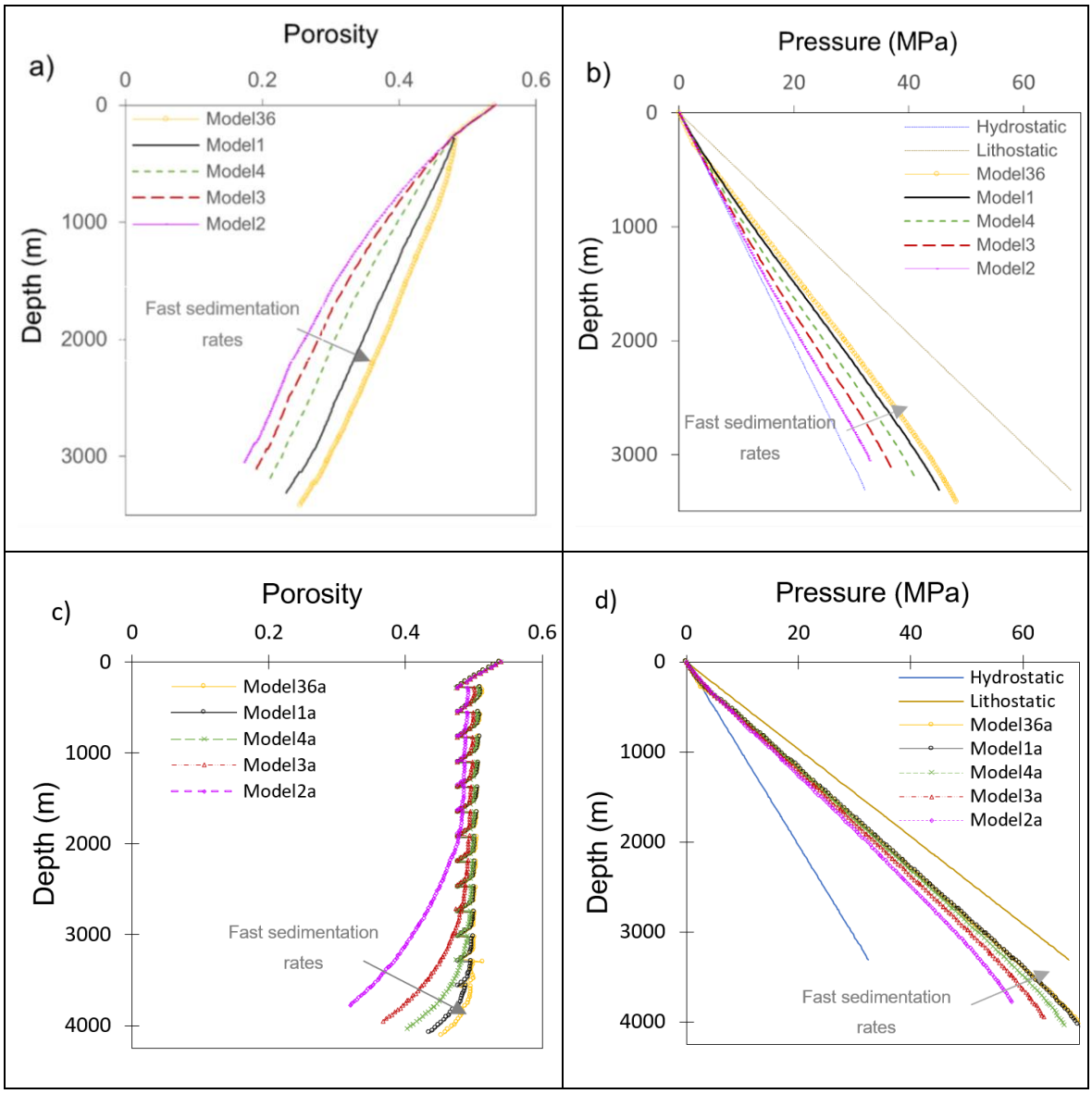

Figure 3.11.- a) and c) porosity vs. depth plots with five cases each, showing different sedimentation rates (model2 = 200 m/Ma, model3 = 500 m/Ma, model4 = 1,000 m/Ma, model1 = 2,000 m/Ma, and model36 = 3,000 m/Ma), and b) and d) pore pressure vs. depth plots showing how pore pressure increases as sedimentation rates increase. A water gradient (hydrostatic) of 0.0099 MPa/m and a lithostatic gradient of 0.0226 MPa/m are presented for reference.

3.4.3 Erosion

During erosion, there are two factors that contribute to the evolution of pore pressure and porosity. First, the exhumation and removal of sediments, with the consequent reduction in the mechanical load associated with the weight of the eroded sediments; and second, fluid flow during erosion, which leads to overpressure dissipation. Porosity can reduce due to an increase in effective stresses as a result of overpressure dissipation and increase due to elastic unloading attributed to the eroded thickness.

To evaluate the effect of erosive events on the sediments, four scenarios were investigated, which consider different eroded thicknesses, erosion rates, erosion at different times followed by sedimentation post-erosion, and erosion at the last event followed by sedimentation post-erosion.

3.4.3.1 Eroded Thicknesses

Models that factored in a deposition phase at a constant sedimentation rate of 2,000 m/Ma (fifteen layers of 300 m each) followed by an erosion event were generated. The thicknesses of the erosion events varied in each of the four models (Table 3.2).

Table 3.2.- Models with one to four eroded layers that have the same erosion time. The total erosion time was maintained constant to minimise different effects due to fluid flow between the cases.

Model	Sed. rate (m/Ma)	Sed. time per layer (Ma)	Thickness eroded (m)	Total erosion time (Ma)
40	2,000	0.15	1,200	0.15
39	2,000	0.15	900	0.15
38	2,000	0.15	600	0.15
8	2,000	0.15	300	0.15

Figures 3.12a and 3.12b show that there is a noticeable pore pressure difference between Model 1 (a model without erosion) and the remaining models, which is related to overpressure dissipation due to fluid flow. The slight pressure differences between models 8, 38, 39, and 40 are because all models were constructed using the same erosion time frame (0.15 Ma), and therefore the overpressure dissipation due to fluid flow is similar in all the models.

The pressure changes can therefore be attributed to the differences in the mechanical load reduction that lead to unloading and flow pathway lengths in each model as a result of the different eroded thicknesses.

The porosity figure shows a greater difference between all the models, which is related to the exhumation of previously deeper buried, more highly compacted sediments. This shift in the vertical porosity due to the thickness removal could also present an unloading percentage due to the reduction of stresses that could lead to a porosity increase and an overpressure reduction.

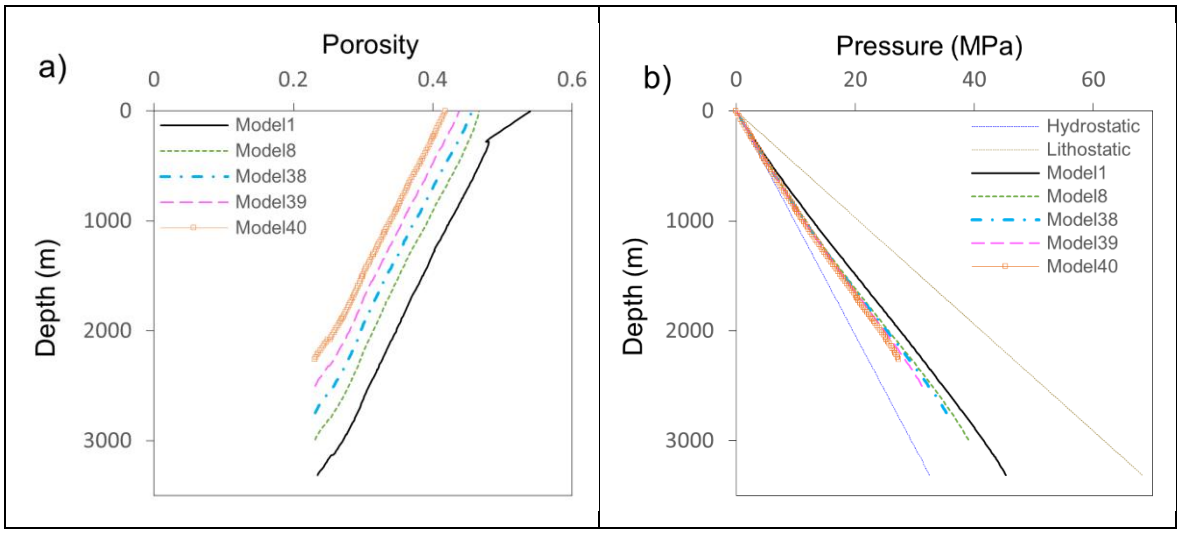

Figure 3.12.- a) Porosity vs. depth plot with the five models, where model40 = 4 eroded layers, model39 = 3 eroded layers, model38 = 2 eroded layers, model8 = 1 eroded layer and model1 does not have any eroded layer, and b) fluid pore pressure vs. depth plot showing the reduction of pore pressure due to erosion of the models 8, 38, 39, and 40. Model1 has a complete sedimentary column without erosion events.

3.4.3.2 Erosion Rates

The effects of different erosion rates were assessed with models 8 to 11. These models consider an initial phase of sedimentation with a constant sedimentation rate of 2,000 m/Ma (fifteen layers of 300 m each) followed by an erosion event where one layer is eroded at different erosion rates. The input is presented in Table 3.3, and the results are shown in Figures 3.13a and 3.13b.

Table 3.3.- These models test different erosion rates in one layer.

Model	Sed. rate (m/Ma)	Sed. time per layer (Ma)	Number of eroded layers	Total erosion time (Ma)
8	2,000	0.15	1	0.15
9	2,000	0.15	1	0.3
10	2,000	0.15	1	0.45
11	2,000	0.15	1	0.6

Results show that erosion rates slightly affect pore pressure values. The fast erosion rates result in less overpressure dissipation as there is less time for the fluid to flow. On the other hand, excess pore pressure will dissipate when the erosion rates are low (Figure 3.13b), as there is more time for the fluid to flow. Porosity values were slightly reduced, and this is due to overpressure dissipation, which results in increased stress and more compaction (Figure 3.13a).

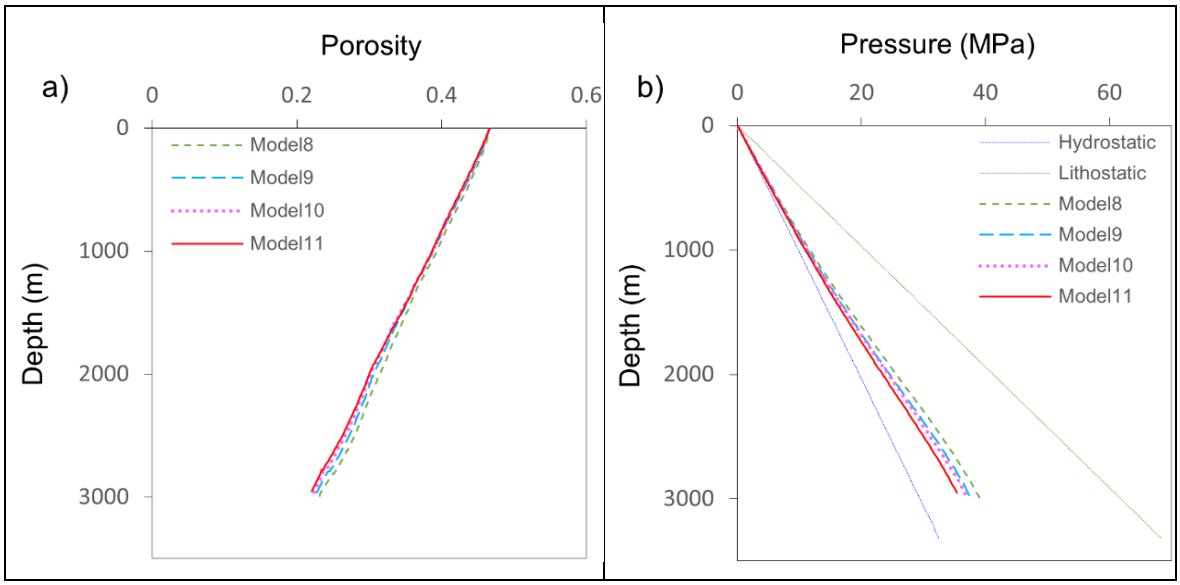

Figure 3.13.- a) Porosity vs. depth plot and b) pore pressure vs. depth plot showing the results of models testing the influence of different erosion rates on the most recently deposited sediments. Model1 has the same sedimentation rate (2,000 m/Ma) but without erosion or additional sedimentation and is shown for comparison. A water gradient (hydrostatic) of 0.0099 MPa/m and a lithostatic gradient of 0.0226 MPa/m are presented for reference.

3.4.3.3 Sedimentation Post-Erosion

Models A, B, and C were constructed to investigate erosive events at different times, followed by sedimentation post-erosion. Model-A started with six layers deposited (1,800 m), followed by the erosion of one layer (300 m eroded thickness) and the sedimentation of ten more layers (3,000 m) deposited with a constant sedimentation rate of 2,000 m/Ma. Model-B started with eleven layers deposited (3,300 m) followed by the erosion of one layer (300 m eroded thickness) and the sedimentation of five more layers (1,500 m) deposited with a constant sedimentation rate of 2,000 m/Ma. Model-C started with sixteen layers (4,800 m) deposited with a constant sedimentation rate of 2,000 m/Ma, followed by the erosion of one layer (300 m). Model inputs are presented in Table 3.4, and the results are shown in Figures 3.14a and 3.14b.

Models 1H, 3H, and 5H were used to investigate the effect of sedimentation after erosion on porosity and pore pressure. After the initial sedimentation phase, in which 4,500 m of sediments (fifteen layers of 300 m each) were deposited with a constant sedimentation rate of 2,000 m/Ma, five layers were eroded (removed thickness 1,500 m) with a constant erosion rate (10,000 m/Ma). This is followed by another sedimentation phase with a constant sedimentation rate of 2,000 m/Ma, in which the models deposited different thicknesses. For instance, after erosion in Model-1H was deposited 300 m of sediments, in Model-3H was deposited 900 m of sediments, and in Model-5H was deposited 1,500 m of sediment. Model inputs are presented in Table 3.4, and the results are shown in Figures 3.14c and 3.14d.

Table 3.4.- The main input of the models that investigated sedimentation post-erosion. At the end of models A, B, and C a total of 15 layers remain deposited while Model-1H has 11 layers, Model-3H has 13 layers, and Model-5H has 15 layers. The time when erosion occurred is presented in column six (Erosive Event Time).

Model	Sed. rate (m/Ma)	Sed. time per layer (Ma)	Thickness eroded (m)	Total erosion time (Ma)	Erosive Event Time (Ma)	Post-erosion sedimentation (m)
A	2,000	0.15	300	0.15	0.9	3,000
B	2,000	0.15	300	0.15	1.65	1,500
C	2,000	0.15	300	0.15	2.4	0
1H	2,000	0.15	1,500	0.15	2.25	300
3H	2,000	0.15	1,500	0.15	2.25	900
5H	2,000	0.15	1,500	0.15	2.25	1,500

Results from models A, B, and C, which investigated erosive events at different times, show that only the last erosive event had an impact on pore pressure. This is due to the removal of thickness (300 m or one layer) and the exhumation of deep intervals to shallow depths (Figure 3.14b). Porosity was reduced by <1 unit in Model-B and by 2 units in Model-C. This reduction is related to the exhumation of compacted sediments to shallow depths (Figure 3.14a).

In models 1H, 3H, and 5H (Figures 3.14c and 3.14d), the erosion of five layers (1,500 m) led to a reduction in the overpressure generated during the sedimentation phase and the exhumation of the deep, more highly compacted sedimentary column to shallower levels.

During the next sedimentation phase, a discontinuity is observed in the porosity plot model 1-H at 300 m between the first sedimentation phase and the subsequent one, as the exhumed sediments are over-consolidated. Therefore, these sediments will not develop any further plastic compaction until the previous maximum stress is overcome, leaving the possibility of only elastic porosity reduction.

Consequently, the potential for overpressure generation during sedimentation after erosion is low in comparison to the overpressure that is generated during the first sedimentation. It is noticed that model 5-H, which has reached the same thickness before erosion, predicts lower porosity and lower pressure than model 1 (sedimentation with no erosion). This is a result of the overpressure dissipation due to fluid flow during erosion and subsequent sedimentation above over-consolidated sediments.

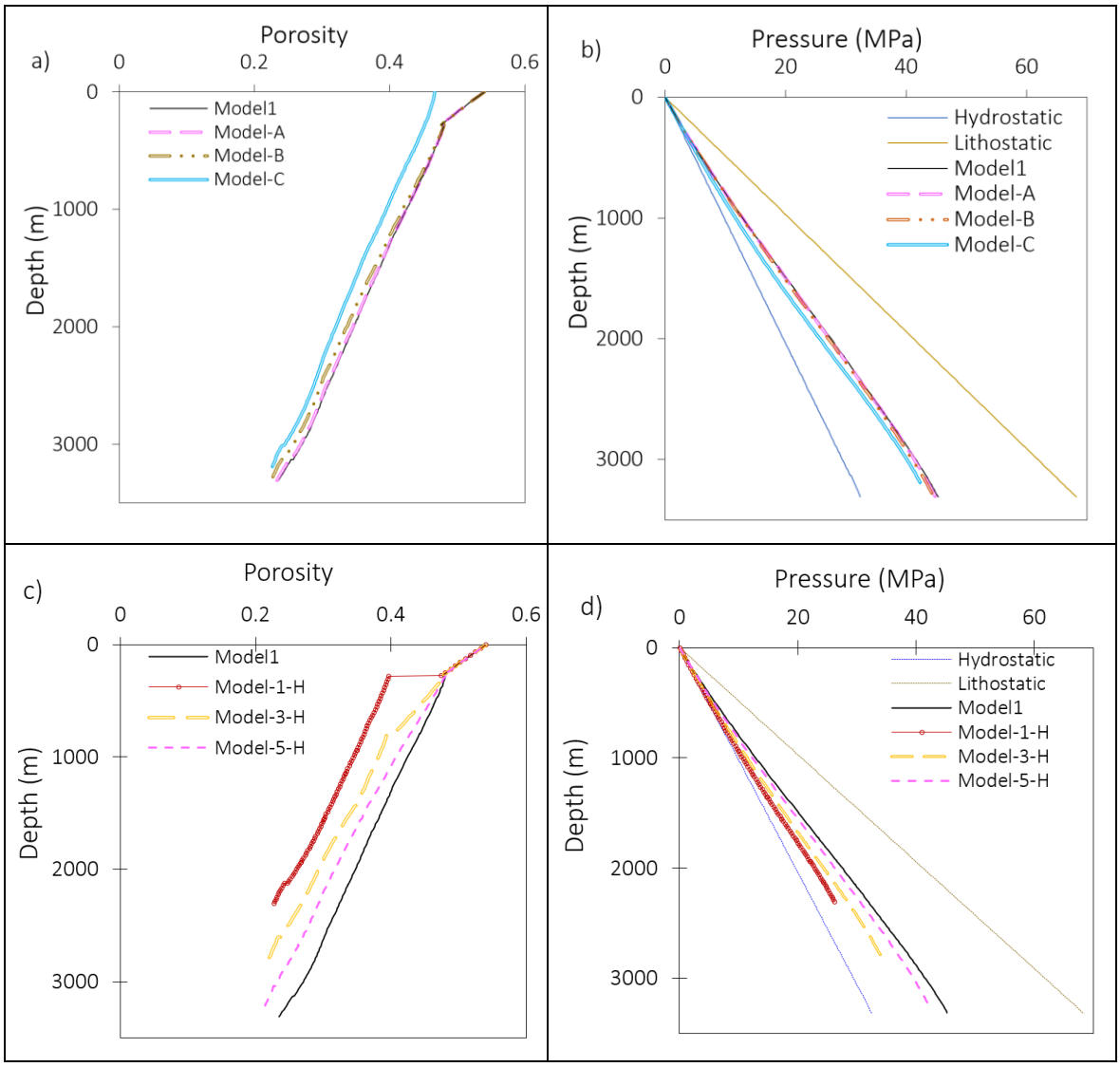

Figure 3.14.- a) Porosity vs. depth plot and b) pore pressure vs. depth plot with the results of the models that investigated erosion at different times followed by sedimentation post-erosion. c) Porosity vs. depth plot, and d) pore pressure vs. depth plot with the results of models that investigated the influence of different additional sedimentation thicknesses post-erosion. Model1 has the same sedimentation rate (2,000 m/Ma) but without erosion or additional sedimentation and is shown for comparison. At the end of models A, B, and C a total of 15 layers remain deposited while Model-1H has 11 layers, Model-3H has 13 layers, and Model-5H has 15 layers. A water gradient (hydrostatic) of 0.0099 MPa/m and a lithostatic gradient of 0.0226 MPa/m are presented for reference.

3.4.4 Hiatus Periods

Models 21 to 24 investigated overpressure dissipation during different hiatus periods that follow the sedimentation of fifteen layers of 300 m, each at a sedimentation rate of 500 m/Ma. Model inputs are presented in Table 3.5, and results are shown in Figures 3.15a and 3.15b.

In the absence of a very low permeability sealing layer or any other overpressure mechanism acting on the sediments, previously generated overpressure dissipates due to fluid flow during a hiatus period. The longer the hiatus period, the larger the overpressure dissipation and, consequently, the lower the predicted overpressure and porosities.

Table 3.5.- The main input of models that investigated the effect of hiatus periods on porosity and pore pressure.

Model	Sed. rate (m/Ma)	Sed. time per layer (Ma)	Number of hiatus events	Hiatus time (Ma)
21	500	0.6	1	0.6
22	500	0.6	1	1.2
23	500	0.6	1	1.8
24	500	0.6	1	2.4

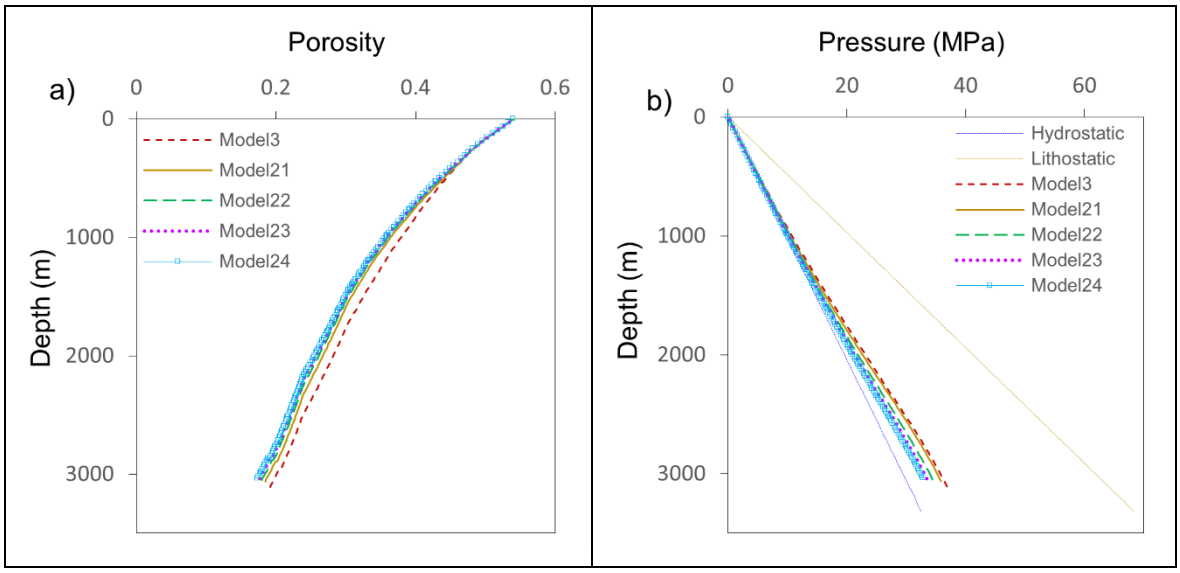

Figure 3.15.- a) Porosity vs. depth plot with models that represent different hiatus periods, and b) pore pressure vs. depth showing how pore pressure is dissipated through time without any further sedimentation. Model3, which has the same sedimentation rate (500 m/Ma) but without a hiatus, is used to compare porosity and pore pressure. A water gradient (hydrostatic) of 0.0099 MPa/m and a lithostatic gradient of 0.0226 MPa/m are presented for reference.

3.4.5 Tectonic Compression with Constant Shortening Applied at the Last Events

Models 12, 13, 14, and 15 assessed disequilibrium compaction and tectonic compression together. An analysis of the shortening values was described in previous studies in the ECB (e.g., Nicol et al., 2002; Bailleul et al., 2013; Reyners, 2013). However, these values were calculated considering fault displacements and deformation and were obtained from restorations on seismic sections. Therefore, those restorations neglected tectonic compaction.

Studies such as Butler and Paton (2010) and Dalton et al. (2015) have compared restored displacements in the extensional and contractional domains on gravitational thrust belt systems

(Orange Basin, offshore Namibia), where the recovered displacements in the extensional domain are larger than the displacements recovered in the compressional structures, attributing the missing strain component to tectonic compaction (shortening values from 5 to 12.5%).

Due to the lack of well-constrained tectonic strain estimates for the ECB, shortening values between 5 and 12.5% were adopted to investigate its effect on pore pressure, porosity, and effective stresses.

Models 12 to 15 include a single shortening value of 5% with a constant sedimentation rate of 500 m/Ma set to occur during the deposition of the last one to four layers or a thickness of 300 to 1,200 m respectively (Table 3.6). The shortening distance is dependent on the width of the model and the shortening percentage; models in this study are 20 m wide.

Table 3.6.- Input of models that investigated the effect of shortening applied during the deposition of the last one to four layers.

Model	Sed. rate (m/Ma)	Sed. time per layer (Ma)	Number of layers deposited during tectonic compression	Shortening % applied	Tectonic compression rate (m/Ma)
12	500	0.6	1	5	0.33
13	500	0.6	2	5	0.16
14	500	0.6	3	5	0.11
15	500	0.6	4	5	0.0825

Modelled pore pressures increase with the shortening rate. If the shortening is only applied during the last depositional event, tectonic-induced overpressure can only dissipate during this period (e.g., Model12). If the same amount of shortening is applied during the deposition of the last four layers, the time for overpressure dissipation is four times greater (e.g., Model15).

Another contributing factor to overpressure dissipation is the sediment thickness before the onset of tectonic compaction. Model 12 (one layer) has a longer pathway than Model 15 (four layers) from the bottom of the column to the surface to dissipate and accommodate the tectonic load (Figure 3.16b). Porosity reduction is also a result of tectonic compression, and this reduction varies with depth (e.g., from 1 to 1.5 units at different depths) (Figure 3.16a).

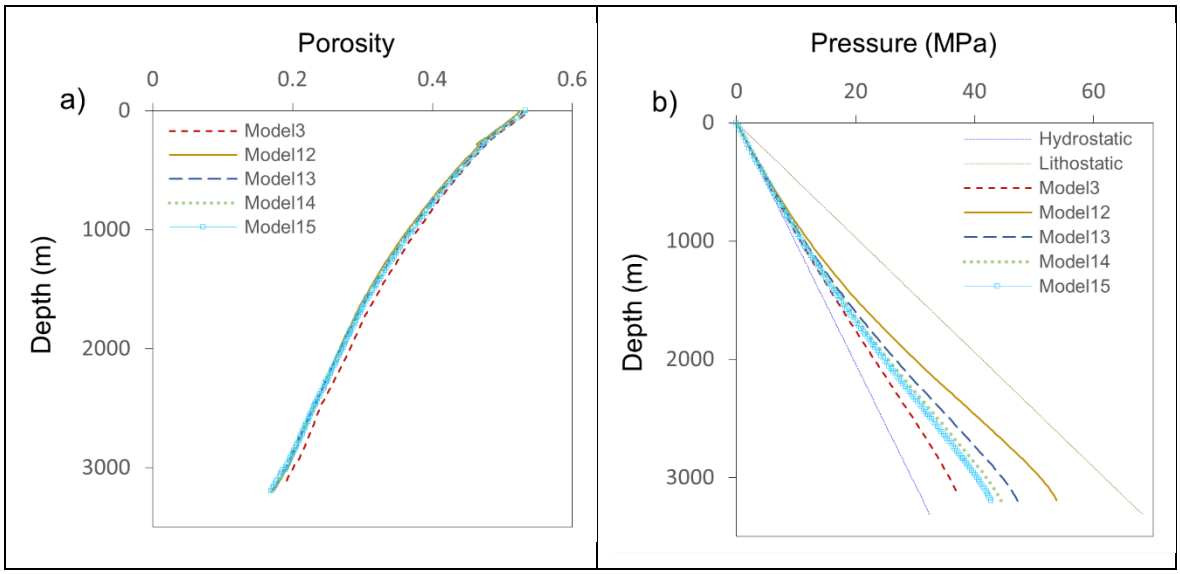

Figure 3.16.- a) Porosity vs. depth plot showing the reduction of porosity due to tectonic compression applied for different lengths of time; b) pore pressure vs. depth showing that the period over which tectonic compression is applied influences the pore pressure throughout the whole depositional sequence. The greatest effect is when tectonic compression is restricted to the latest depositional event, as shown in Model12. For references to the model inputs, see Table 3.6. A water gradient (hydrostatic) of 0.0099 MPa/m and a lithostatic gradient of 0.0226 MPa/m are presented for reference.

3.4.6 Tectonic Compression with Different Amounts of Shortening

Disequilibrium compaction and the effect of different shortening percentages applied only during the last depositional event were also evaluated. To represent tectonic compression, shortening distances (also termed shortening percentages) are used. These models have a sedimentation rate of 500 m/Ma with a shortening percentage between 5 and 12.5% (Table 3.7).

Table 3.7.- The main input of models that investigated different amounts of tectonic compression (shortening distance) that was applied during the deposition of the last deposited sediment layer.

Model	Sed. rate (m/Ma)	Sed. time per layer (Ma)	Number of layers deposited during tectonic compression	Shortening % applied	Tectonic compression rate (m/Ma)
16	500	0.6	1	1	0.333
12	500	0.6	1	5	1.665
17	500	0.6	1	10	3.333
18	500	0.6	1	12.5	4.167

From the results, it is observed that pore pressure is directly related to the amount of shortening: the greater the shortening, the higher the pore pressure (Figure 3.17b). The maximum shortening applied to the models was 12.5% (Model18) which is consistent with the maximum estimated tectonic compaction value (e.g., Butler and Paton, 2010; Dalton et al., 2015).

Tectonic compression can result in porosity reduction. For instance, a reduction of 2.5 units at 1,000 m depth was obtained during modelling in models 12, 16, 17, and 18 (Figure 3.17a).

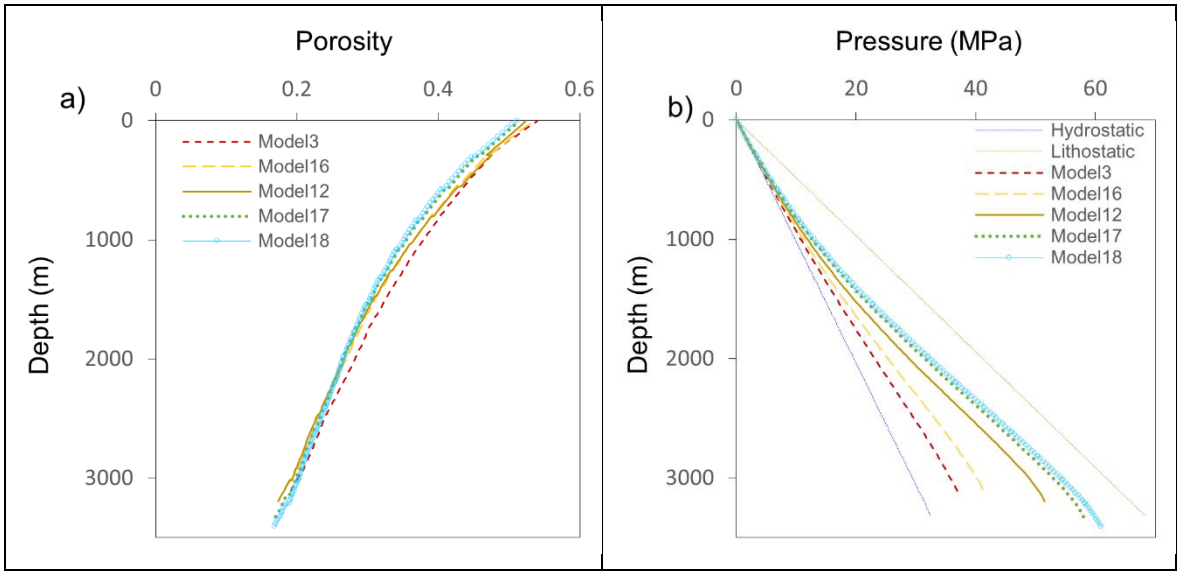

Figure 3.17.- a) Porosity vs. depth plot showing the porosity reduction as a result of tectonic compression that was applied during the sedimentation of the last layer; b) pore pressure vs. depth plot showing that increased shortening during the deposition of the most recent sediment layer results in increased pore pressure. Model3 has the same sedimentation rate (500 m/Ma) without tectonic compression, and it is shown for comparison.

3.4.7 Summary of the Results Obtained with the Parametric Models

- High sedimentation rates of low-permeability units result in high pore pressures. However, high porosity values similar to the initial deposited porosities would be preserved at those intervals.
- Hiatus periods result in overpressure dissipation. The longer the period, the more overpressure dissipation would occur in the absence of another overpressure mechanism. The sediments will continue compacting which results in porosity reduction.
- The models show that only the most recent erosive events have the most impact on porosity and pore pressure.
- The thicknesses of earlier eroded sediments do not have a significant impact on porosity and pore pressure. However, if a previous erosive event removed a section higher than the section deposited post-erosion, two effects can be observed. A drift on porosity (low porosity at shallow depths) as the sediments were already compacted prior to the erosion, and pore pressures will not be higher than the values prior to the erosion.
- Tectonic compression applied during the last events has a greater impact on porosity and pore pressure. High percentages of tectonic shortening can result in high overpressure.

3.5 Geomechanical Modelling Applied to Wells of the ECB

Due to the complex geological histories interpreted in the ECB, pressure estimations based on well logs and analytical equations are not sufficient to identify the parameters and mechanisms required to generate the large overpressure values encountered at shallow depths. Therefore, geomechanical modelling was used to gain additional insights.

The insights obtained from the parametric models enabled the identification of factors that could play a role in overpressure generation in geologically complex regions such as the ECB. This included eroded sediment thickness, sedimentation rates, hiatus periods, and the extent and rate of tectonic shortening. The maximum shortening applied was 12.5%, which corresponds to the maximum value estimated in previous studies (e.g., Butler and Paton, 2010; Dalton et al., 2015). The shortening was applied during the last events (from 3 to 5.7 Ma) considering the results of the parametric models and studies showing the increase of shortening from the Miocene to the present-day (e.g., Walcott, 1987; Barnes, 1997; Bailleul et al., 2007 and 2013; Jiao et al., 2017). The shortening value of 8% was chosen as it fit better with the data of the five key wells.

1D column models were constructed for the five key wells: Opoutama-1, Opoho-1, Tuhara-1, Awatere-1, and Kiakia-1, located in the ECB, onshore New Zealand.

For the well models, normal compaction trends (hydrostatic trends) and porosity-permeability relationships were created to represent the ECB lithologies. Similar to the parametric models, the normal compaction trends are modifications of Schneider et al. (1996), while the porosity-permeability relationships are modifications of the Kozeny-Carmen relationships for different lithologies (Figures 3.18a and 3.18b).

As there is high uncertainty on sedimentation and erosion rates, eroded thicknesses, periods of non-deposition, and the amount of tectonic compaction, numerous models were created. From all these models, only those that corresponded with the geology of the area and could be matched to the measured data are presented.

The erosive events were considered in the models constructed for the five key wells, but the thicknesses were assumed as they did not have any impact on the results. Only the last erosive event (eroded thickness) was investigated with different models.

In the ECB, different seals to petroleum accumulations have been identified; there are both mudstone intervals (e.g., Pindari, Tangihau, and Waingaromia mudstones) and the smectite-rich marls and calcareous mudstones of the Wanstead and Weber Formations (Field et al., 1997; Darby, 2002). In addition to these seals, the thin low-permeability intervals of limestones of the Early Miocene to Middle Pliocene (Kauhauroa, Kiakia, and Tahaenui Limestones) and the carbonate interval of the Tuhara Formation have been identified during this study to have low permeabilities and were also investigated in the geomechanical models (Figure 3.3). The thin limestone and the smectite content intervals were changed to a low permeability relationship (Carb. Tight; Figure 3.18a) to investigate the effect on pore fluid pressure generation. The models that do not investigate the thin limestone and the smectite content intervals as pore pressure seals, used the porosity-permeability relationship named Carb. (Figure 3.18a).

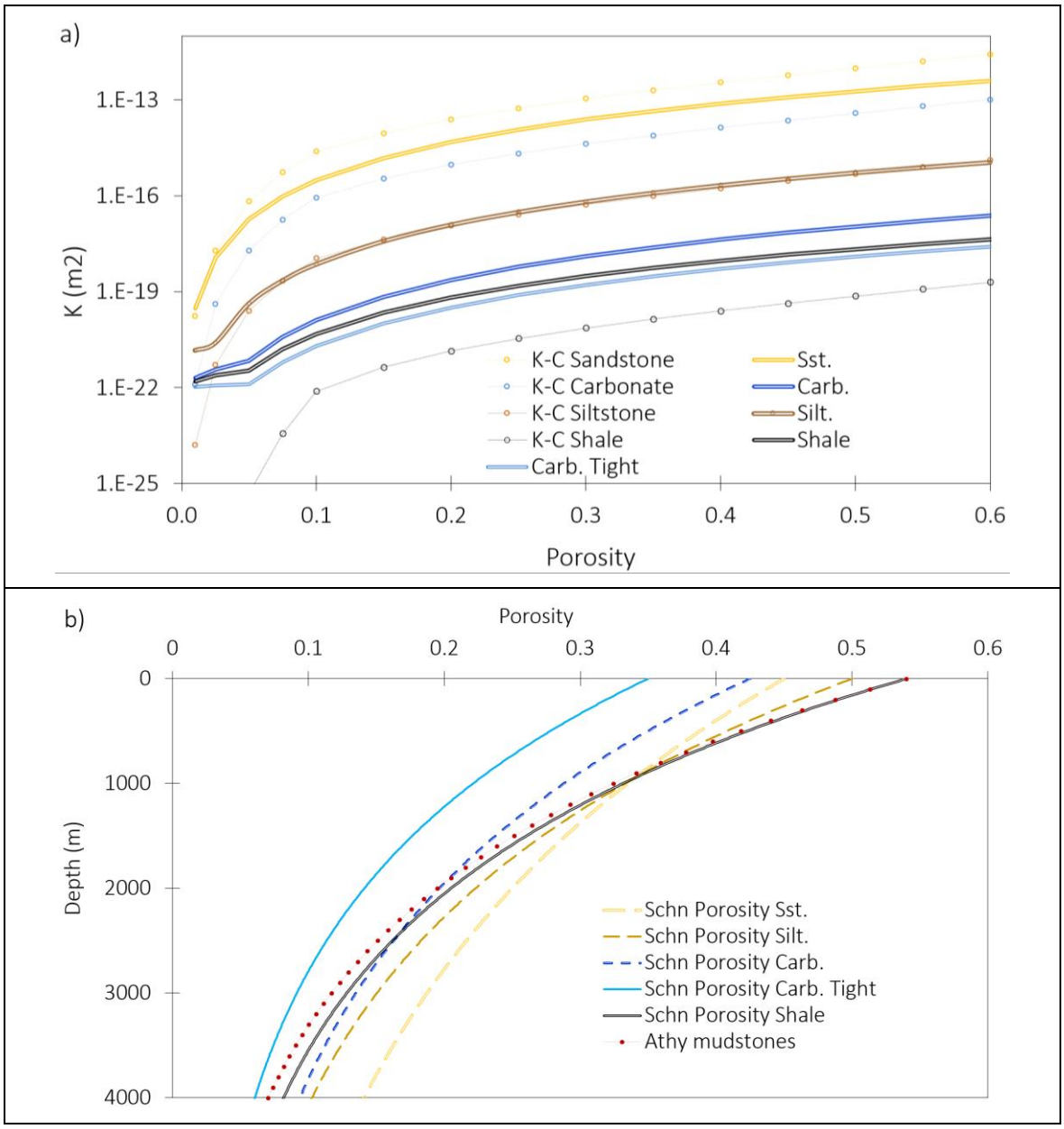

Figure 3.18.- a) Porosity-permeability relationships were created for the different lithologies interpreted in the ECB. For reference, the Kozeny-Carmen relationships as defined in Hantschel and Kauerauf (2009) are provided. The minimum permeability used in the models was 1.E-22 m^2, adopted after Yang and Aplin (2007). b) Normal compaction trends (hydrostatic trends) were created for each lithology using Shneider's trends. Athy's compaction trend for mudstones is presented as a reference.

The models investigated sediments from the Cretaceous to the Pleistocene. A width of 20 m was used for all the models, while the length varied for each well. The present-day thickness and porosity of each lithology were derived from well-log analysis. Then, with assumed depositional porosities, the depositional thicknesses were calculated to input into the models. The colours used to present the model results represent different lithologies (e.g., Figure 3.19a). For example, yellow colours represent sandstone lithologies (Makareao Sst.) blue represents carbonate lithologies (Wanstead, Weber, Kiakia, Kauhauroa, Tahaenui and an interval of the Tuhara Formation), light black represents mudstone lithologies (Pindari, Waingaromia, Wheao, and Whangai Formations), and brown and grey represent siltstone lithologies (Wairoa, Opoti, Tuhara, and Poha).

3.5.1 Opoutama-1 Column Model

The total depth of this well is 3,657 m, and it penetrated sediments from the Cretaceous (72.08 Ma) to the Middle Miocene (11.04 Ma). Two regional unconformities identified in seismic data, well logs, and well reports were considered in the geomechanical models: one during the Early Miocene and a second which possibly eroded Pleistocene, Middle Pliocene, and Early Pliocene sediments. All the models constructed for this well have the same configuration until the Late Miocene (blue cells in Table 3.8), which includes sedimentation and erosion events. Above the Late Miocene, the models also investigated hiatus periods and tectonic compression.

The events with the letter a or b (third column in all the tables used for each well (e.g., 3.8, 3.10, 3.12, 3.14, and 3.16) represent the layers that were eroded in the models. The eroded thickness of these layers was calculated from other nearby wells where these intervals are present and adjusted within the models.

Table 3.8.- Opoutama-1 well 1D column models with depositional and erosional settings. All the models constructed for this well have the same configuration until the Late Miocene (highlighted in blue).

Period	Duration (Ma)	Event	Lithology	Init. Porosity	Init. Thickness (m)
Pleistocene	3	Erosion2			
		11b	Siltstone	0.50	128
		11a	Shale	0.54	139
Middle Pliocene	0.7	10b	Shale	0.54	739
		10a	Siltstone	0.50	680
Early Pliocene	1.63	9b	Shale	0.54	848
		9a	Siltstone	0.50	780
Late Miocene	5.71	8b	Shale	0.54	891
		8a	Siltstone	0.50	820
Middle Miocene	4.86	7	Sandstone	0.45	342

Period	Duration (Ma)	Event	Lithology	Init. Porosity	Init. Thickness (m)
Middle Miocene		6	Shale	0.54	443
Early Miocene	5.8	Erosion1			
		5a	Shale	0.54	413
		5	Shale	0.54	282
Oligocene	12.9	4	Shale with smectite and carbonate content (represented as carbonate)	0.43	328
Eocene	21.4	3	Shale with smectite and carbonate content (represented as carbonate)	0.43	639
Paleocene	10	2	Shale	0.54	1236
Cretaceous	6.1	1	Shale and Sand	0.54 and 0.45	2629

In the Opoutama-1 well, pore pressure (from mud weights) increases steadily below the Waingaromia Mdst. at ~400 to ~1,730 m depth, where the values reduce ~4 MPa. After this depth, pore pressures continue increasing to the total depth of this well. Porosity values calculated from sonic logs (for reference, this curve is highlighted in blue; Figure 3.19a) start around 0.30 at the surface and continue reducing with depth, except for the high porosities (up to 0.34) at the base of the Wanstead Formation (Figures 3.19a, 3.19c, and 3.19e). This increase in porosity does not present any change in the mud weight readings (pore pressure) nor GR readings (Figure 3.6); however, well reports indicated an increase in montmorillonite clay and a decrease in kaolinite, chlorite, and illite, indicating a change in lithology. The organic matter is >1% in this interval. Pore pressure tests (DST in purple; Figures 3.19b, 3.19d, and 3.19f), and pore pressure from mud weights (in black) are presented in Figures 3.19b, 3.19d, and 3.19f and were used as references.

The Weber and Wanstead Formations in the models were investigated as carbonate lithologies, as these formations have a high content of carbonate intercalations. The capacity of these two formations to act as overpressure seals was investigated with a low porosity-permeability relationship (Carb. Tight), which is 6.8 times lower than the porosity-permeability relationship used for these two formations (Carb.). The other seal intervals, such as the Pindari Mudstone and the thin, low-permeability carbonate intervals, were either not deposited or were eroded. According to well reports (NZ Aquitaine Petroleum Ltd., 1967), the Wanstead and Weber Formations in this well contain high

smectite clays, which could result in excellent seals. However, a fracture system has also been identified in some of the intervals of the Wanstead Formation, which could result in overpressure dissipation. This possibility was investigated during this research, and the results are presented in section 3.6.2.

The 1D models built for the Opoutama-1 well represent the geological events identified in this well (Table 3.9). Seismic and well-data registered sediments from the Middle Miocene (Tunanui Sst.) to the Cretaceous (Mata Formation); therefore, it has been interpreted that sediments above the Middle Miocene were not deposited or have been eroded. Model Opoutama-1_M-1 considers sedimentation, after the Middle Miocene during the events labelled as 8a, 8b, 9a, 9b, 10a, 10b, 11a, and 11b. This model finishes with an erosive event (erosion2), which considers the removal of 5,025 m of sediments, which is the sum of the uncompacted thicknesses of events 8a to 11b in Table 3.8; the results are presented in Figure 3.19.

The low porosity-permeability relationship (Carb. Tight) was used in the models Opoutama-1_M-7 and M-5 in two intervals (Weber and Wanstead Formations).

Table 3.9.- Scenarios investigated in the Opoutama-1 well.

Model	Disequilibrium Compaction	Tectonic Compression	Low-Permeability Layers
Opoutama-1_M-1	Yes, with an eroded thickness of 5,025 m	No	No
Opoutama-1_M-3	Yes, with an eroded thickness of 1,711 m and hiatus from Early Pliocene to Pleistocene	No	No
Opoutama-1_M-7	Yes, with an eroded thickness of 1,711 m and hiatus from Early Pliocene to Pleistocene	No	Weber + Wanstead Formations
Opoutama-1_M-4	Yes, with an eroded thickness of 1,711 m and hiatus from Early Pliocene to Pleistocene	Yes, 8%	No
Opoutama-1_M-5	Yes, with an eroded thickness of 1,711 m and hiatus from Early Pliocene to Pleistocene	Yes, 8%	Weber +Wanstead Formations

Results show that disequilibrium compaction is not sufficient to generate the present-day overpressure (models Opoutama-1_M-1, M-3, and M-7) (Figures 3.19b and 3.19d). This mechanism contributed to the overpressure. However, it dissipated due to the erosive events and hiatus periods. Tectonic compression (models Opoutama-1_M-4 and M-5) is shown to have a significant impact on pore pressure.

The Opoutama-1 well is located in the eastern part of this research and crosses a small interval of Miocene sediments and a thick section of Cretaceous, Oligocene, and Eocene sediments. Different eroded thicknesses were investigated to match porosity and pore pressure.

For example, in the model Opoutama-1_M-1, 5,025 m of sediments were deposited and eroded, which resulted in over-compacted sediments with low porosities (Figure 3.19a). The best-matched data were obtained when only two layers (8a and 8b) were deposited and later eroded by the event erosion2 (eroded thickness of 1,711 m). The rest of the layers (from 9a to 11b were not deposited; Table 3.8) in models Opoutama-1_M-3, M-4, M-5, and M-7 were represented as hiatus periods as opposed to being deposited and later eroded (Figure 3.19).

Model Opoutama-1_M-7 preserved slightly high porosities below the low-permeability intervals (Weber and Wanstead Formations) in comparison to models M-1 and M-3, due to the slight overpressure generated during sedimentation. However, this overpressure is low in comparison to the observed data (Figure 3.19d).

Model Opoutama-1_M-5 accounts for the same depositional, hiatus, and erosional configuration as model Opoutama-1_M-7, but this model also considers tectonic compression.

Porosities further decreased in the models M-4 and M-5 due to tectonic compaction, and pore pressure almost reached the lithostatic when the Weber and Wanstead Formations were changed to a low porosity-permeability relationship (model Opoutama-1_M-5) (Figures 3.19e and 3.19f).

It is noted that due to the simplification of the geology considered in the models (e.g., no faults or structural shapes), and although two mechanisms were applied (disequilibrium compaction and tectonic compression), the results do not properly match porosity nor pore pressure data.

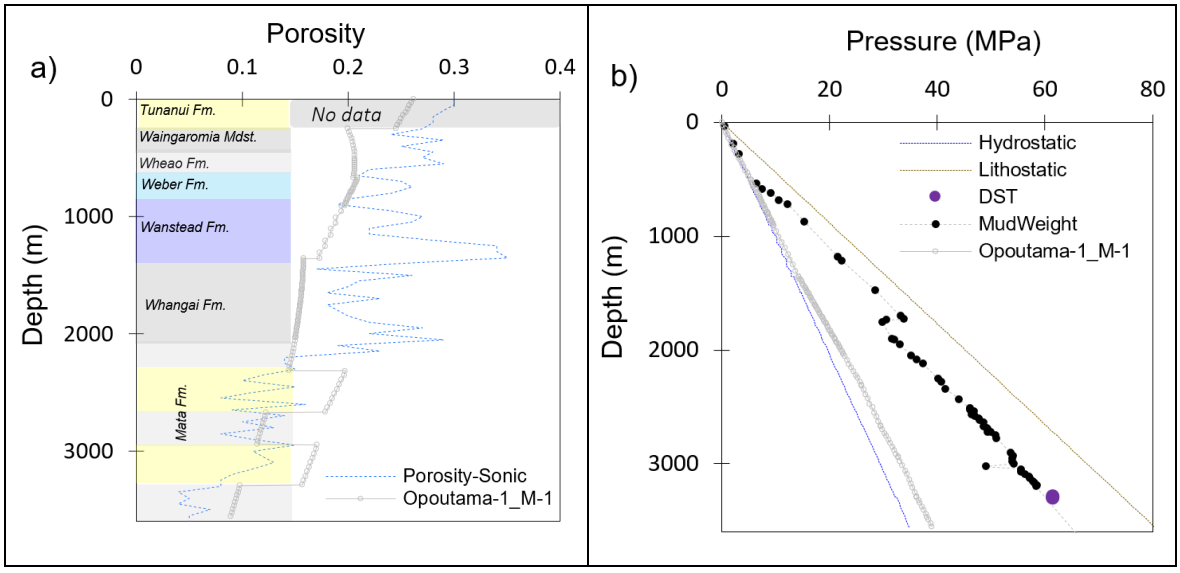

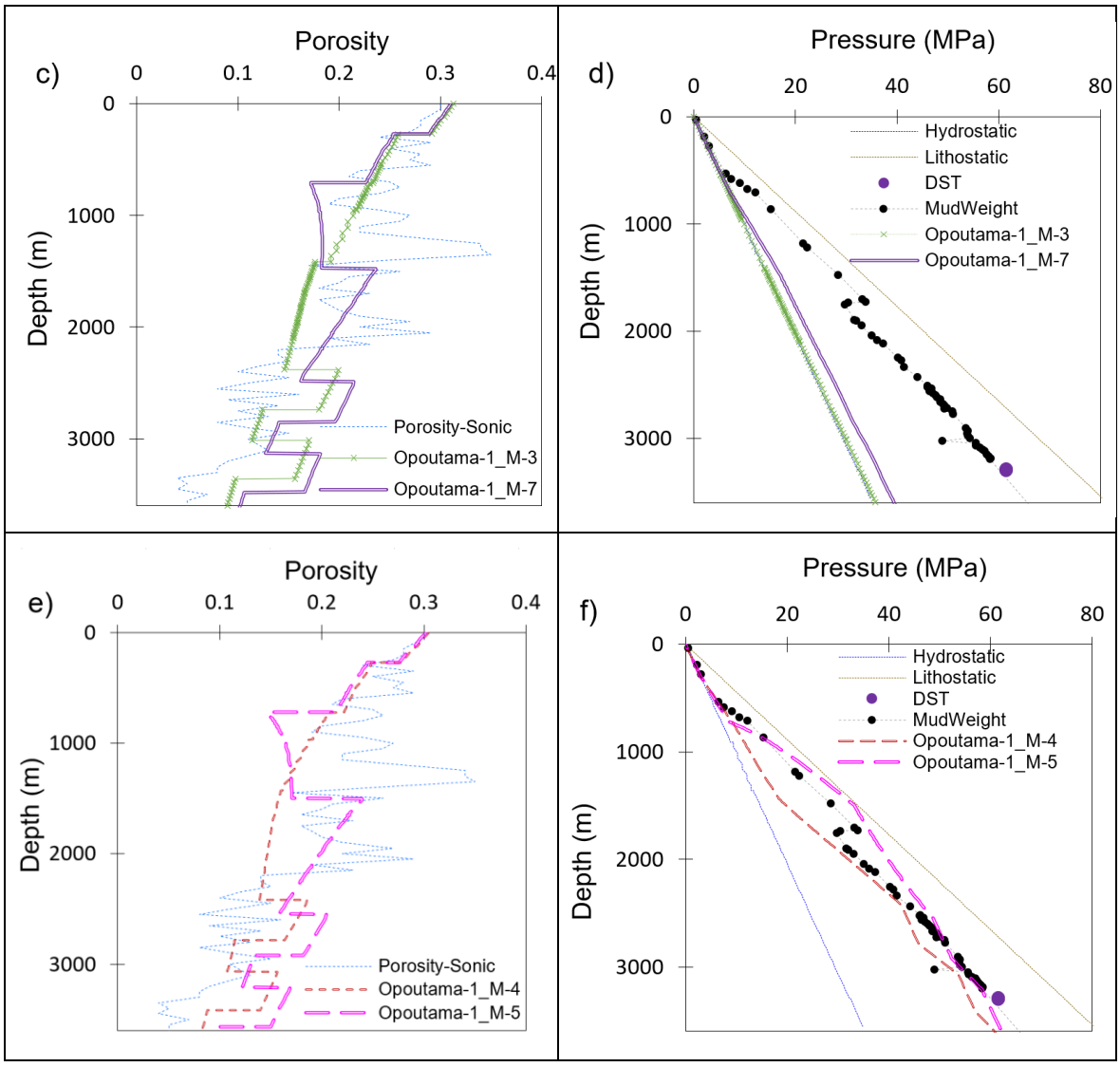

Figure 3.19.- Summary of the scenarios investigated in the Opoutama-1 well. a), c), and e) are porosity vs. depth plots, while b), d), and f) are pressure vs. depth plots. The hydrostatic and lithostatic gradients considered were 0.00995 MPa/m (0.44 psi/ft) and 0.0226 MPa/m (1 psi/ft), respectively. Models Opoutama-1_M-1, M-3, and M-7 investigated disequilibrium compaction, while Models Opoutama-1_M-4 and M-5 investigated disequilibrium compaction and tectonic compression.

3.5.2 Opoho-1 Column Model

This well penetrated 2,320 m of sediments from the Oligocene (34 Ma) to the Pleistocene, and it is located 13,825 m from the Opoutama-1 well towards the west. It is positioned between two regional faults, one dipping towards the west and the other dipping towards the east, as interpreted in the 2D seismic section in depth (for reference see Figure 3.1b). Three regional and three local unconformities identified in seismic data, well logs, and well reports were considered in the geomechanical models: one during the Early Miocene, two during the Middle Miocene, one in the Late Miocene, one during the Early Pliocene, and one during the Pleistocene. The total thickness modelled for this well was 4,984 m (2,320 m drilled + 2667 m obtained from other wells, which included sediments from the Eocene (Wanstead Formation), Paleocene (Whangai Formation), and Cretaceous (Mata Formation)) (highlighted in orange; Table 3.10).

Table 3.10.- Opoho-1 well 1D column models with depositional and erosional settings. The thickness and porosity of sediments for the Cretaceous, Paleocene, and Eocene were obtained from other wells.

Period	Duration (Ma)	Event	Lithology	Init. Porosity	Init. Thickness (m)
Pleistocene	3	Erosion6			
		15b	Siltstone	0.50	320
		15a	Siltstone	0.50	320
		14	Sandstone	0.45	77
Middle Pliocene	0.7	13	Siltstone	0.50	178
		12	Carbonate	0.35	43
Early Pliocene	1.63	Erosion5			
		11b	Shale	0.54	848
		11a	Siltstone	0.50	780
Late Miocene	5.71	Erosion4			
		10b	Siltstone	0.50	136
		10a	Shale	0.54	1283
		9	Shale	0.54	336
Middle Miocene	4.86	Erosion3			
		8a	Shale	0.54	19
		8	Shale	0.54	187

Period	Duration (Ma)	Event	Lithology	Init. Porosity	Init. Thickness (m)
		Erosion2			
		7a	Sandstone	0.45	518
		7-2	Sandstone	0.45	616
		7-sh	Shale	0.54	74
		7-1	Sandstone	0.45	616
		6	Shale	0.54	801
Early Miocene	5.8	Erosion1			
		5b	Shale	0.54	282
		5a	Shale	0.54	282
Oligocene	12.9	4	Shale with smectite and carbonate content (represented as carbonate)	0.43	354
Eocene	21.4	3	Shale with smectite and carbonate content (represented as carbonate)	0.43	639
Paleocene	10	2	Shale	0.54	1236
Cretaceous	6.1	1	Shale and Sand	0.54 and 0.45	2629

Mud weights and well drilling reports registered overpressure values of ~42 MPa from the Waingaromia Mdst at ~1,600 m depth, which increased with depth up to 47 MPa at the Weber Formation around 2,260 m depth (Figure 3.20b). The low permeability preserved intervals above this formation in this well are the Tahaenui Limestone and the Pindari Mudstone, with a current thickness of ~32 and ~224 m, respectively. According to the structural interpretation performed during this research, these two formations are exposed to the surface at the present-day, which could result in overpressure dissipation (Figure 3.8). To investigate lateral pressure drainage, a high porosity-

permeability relationship (Sandstone relationship; Figure 3.18a) was used in the layers of the Middle Miocene to Pleistocene (1,438 m) of the model Opoho-1_M-11.

Density and sonic logs were registered from ~600 m depth, and the shallow section was extrapolated to the mudline (188 us/ft and 1.8 g/cm^3) (Figure 3.20a). There is a difference between the porosity calculated with sonic and density logs. This difference could be related to a change in lithology (not identified by the GR), poor well data, and/or hydrocarbon residual content in the Tunanui Formation as described in the well reports.

The geomechanical models generated for the Opoho-1 well investigated disequilibrium compaction and tectonic compression. In addition, three models (Opoho-1_M-7, M-4, and M-11) investigated low permeability intervals (Table 3.11). Hiatus periods were not considered in the models as the shallow sections have been reported and were interpreted to be present in this well (Figure 3.8).

Table 3.11.- Scenarios investigated in the Opoho-1 well.

Model	Disequilibrium Compaction	Tectonic Compression	Low-Permeability Layers
Opoho-1_M-1	Yes, with an eroded thickness of 640 m	No	No
Opoho-1_M-7	Yes, with an eroded thickness of 640 m	No	Tahaenui Fm. + Wanstead + Weber Fms.
Opoho-1_M-4	Yes, with an eroded thickness of 640 m	Yes, 8%	Tahaenui Fm. + Wanstead + Weber Fms.
Opoho-1_M-11	Yes, with an eroded thickness of 640 m + intervals that drain fluid laterally to the surface from the Middle Miocene (events 7-2 to Pleistocene; Table 3.10).	Yes, 8%	Wanstead + Weber Fms.

Results show that disequilibrium compaction alone (Opoho-1_M-1) even with low-permeability intervals (Opoho-1_M-7) does not generate enough overpressure in comparison to the observed data (Figures 3.20b, 3.20d, and 3.20f). The overpressure generated due to this mechanism preserved high porosity values, which do not match with the data (Figures 3.20a and 3.20c).

Models Opoho-1_M-4 and M-11 were constructed to investigate tectonic compression in addition to disequilibrium compaction. In the model, Opoho-1_M-4 overpressures started slightly increasing from shallow depths (~200 m depth), and they ramped just below the top of the Weber Formation at ~2,100 m depth from 23 to 31 MPa, reaching 47 MPa at ~2,300 m depth, almost matching the data (Figure 3.20f). To avoid the generation of overpressures from shallow depths, the formations interpreted to be exposed to the surface at the present-day (from the first interval above the thin shale layer of the Tunanui Sst. to the Pleistocene and Wairoa Formations; Middle Miocene events 7-2 to present; Table 3.10) were represented with a high porosity-permeability relationship in the model Opoho-1_M-11. (Figures 3.20e and 3.20f).

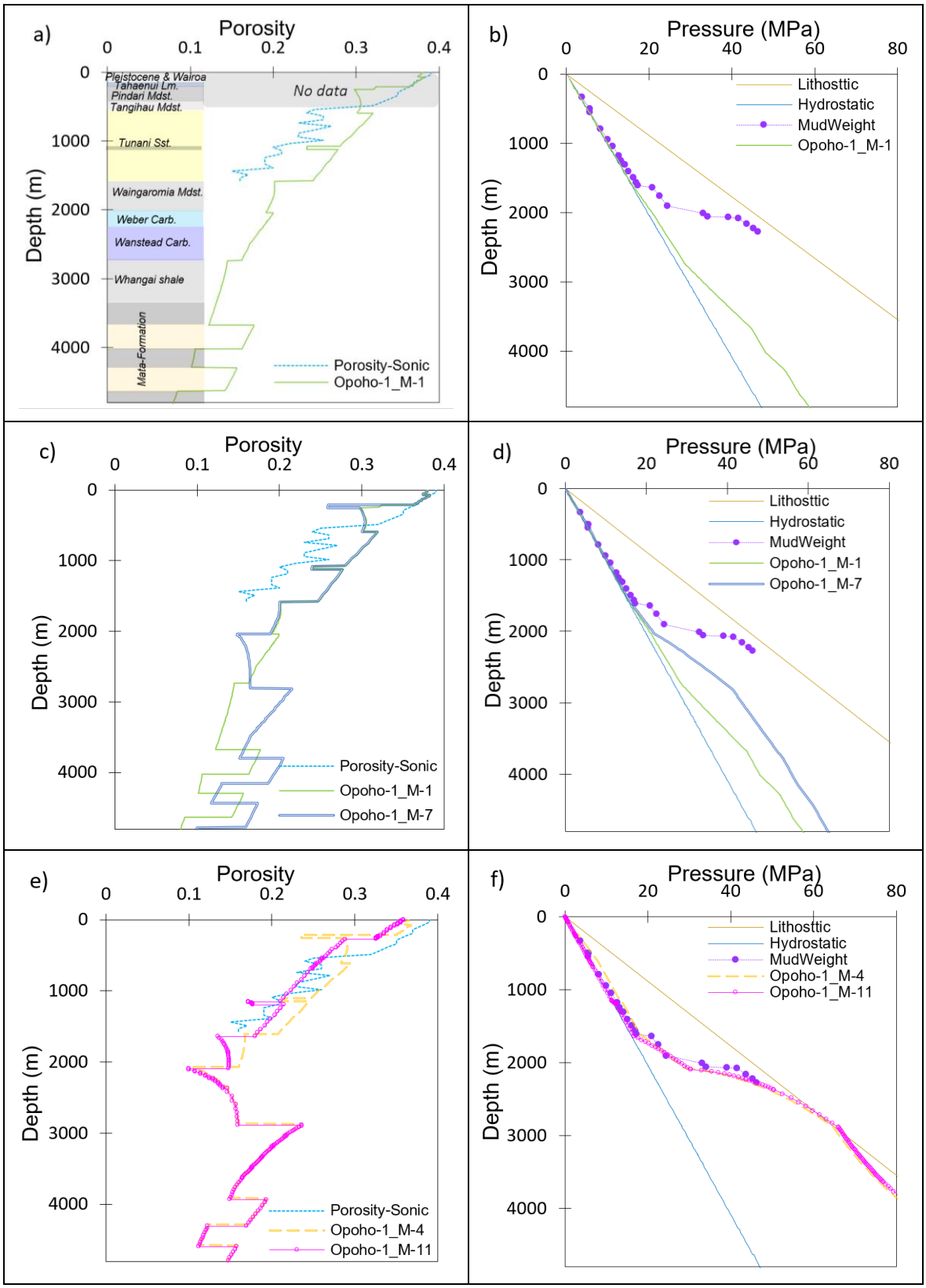

Figure 3.20.- Summary of the scenarios investigated in the Opoho-1 well. a), c), and e) are porosity vs. depth plots, while b), d), and f) are pressure vs. depth plots. The hydrostatic and lithostatic gradients considered were 0.00995 MPa/m (0.44 psi/ft) and 0.0226 MPa/m (1 psi/ft), respectively. Models Opoho-1_M-1 and M-7 investigated disequilibrium compaction while, models Opoho-1_M-4 and M-11 investigated disequilibrium compaction and tectonic compression.

3.5.3 Tuhara-1 Column Model

This well is located 10,018 m from the Opoho-1 well towards the west, in the onshore area of the ECB. The total depth reached was 2,297 m, crossing sediments from the Middle Miocene (15.9 Ma) to the Pleistocene. The seismic interpretation reveals that this well is in an area with both small and regional-scale faults. This well crossed a regional fault at approximately 2,000 m depth at the Tunanui Formation (Figures 3.1b and 3.8). Three regional and three local unconformities that were used in the geomechanical models were interpreted in seismic and well data: one during the Early Miocene, two during the Middle Miocene, one in the Late Miocene, one during the Early Pliocene, and one during the Pleistocene. The total thickness investigated for this well was 5,399 m (2,297 m from drilled data, and the remainder thickness, which corresponds to Oligocene, Eocene, Paleocene, and Cretaceous sediments, was obtained from other wells; Table 3.12).

Table 3.12.- Tuhara-1 well 1D column models with the depositional and erosional settings. The thickness and porosity of sediments for the Cretaceous, Paleocene, Eocene, Oligocene, and Early Miocene were obtained from near wells and were used in the models (highlighted in orange).

Period	Duration (Ma)	Event	Lithology	Init. Porosity	Init. Thickness (m)
Pleistocene	3	Erosion6			
		16b	Siltstone	0.50	896
		16a	Siltstone	0.50	896
		16	Sandstone	0.45	30
Middle Pliocene	0.7	15	Siltstone	0.50	371
		14	Carbonate	0.35	68
Early Pliocene	1.63	Erosion5			
		13b	Shale	0.54	848
		13a	Siltstone	0.50	780
		12a	Siltstone	0.50	45
		12-2	Shale	0.54	244

Period	Duration (Ma)	Event	Lithology	Init. Porosity	Init. Thickness (m)
Late Miocene	5.71	12-1	Carbonate	0.35	173
		11	Siltstone	0.50	282
		Erosion4			
		10a	Sandstone	0.45	141
		9	Shale	0.54	1685
Middle Miocene	4.86	Erosion3			
		8a	Shale	0.54	213
		8	Shale	0.54	19
		Erosion2			
		7a	Sandstone	0.45	613
		7-2	Sandstone	0.45	161
		7-sh	Shale	0.54	102
		7-1	Sandstone	0.45	161
		6	Shale	0.54	353
Early Miocene	5.8	Erosion1			
		5a	Shale	0.54	28
		5	Shale	0.54	282

Period	Duration (Ma)	Event	Lithology	Init. Porosity	Init. Thickness (m)
Oligocene	12.9	4	Shale with smectite and carbonate content (represented as carbonate)	0.43	354
Eocene	21.4	3	Shale with smectite and carbonate content (represented as carbonate)	0.43	639
Paleocene	10	2	Shale	0.54	1343
Cretaceous	6.1	1	Shale and Sand	0.54 and 0.45	2629

In the Tuhara-1 well, pore pressure increases to 26 MPa in the middle of the Tunanui Formation at ~1,860 m depth. This formation consists of intercalations of sandstone, siltstone, and claystone with an interval of mudstone lithologies of ~53 m in the middle of this formation (Figure 3.21b).

The values from the DST tests are ~2 MPa higher than the mud weights registered in this section (Figure 3.21b). According to the structural interpretation performed during this research, the intervals above the Tunanui Formation (Middle Miocene, event 7-2; Table 3.12) are currently exposed to the surface (for reference see Figures 3.1b and 3.8).

Porosity curves were calculated from the sonic and density logs, which start at ~300 m. Above this depth, sonic and density values were extrapolated to the mudline (188 us/ft and 1.8 g/cm^3). Both porosity curves from density and sonic logs show similar values until the middle of the Pindari Mudstone at ~1,340 m depth, where the density-porosity values start increasing (Figure 3.21a). This difference could be related to the poor quality of the density log or a change in lithology.

The low-permeability intervals identified in this well are the Tahaenui Limestone, the carbonate interval of the Tuhara Formation, the thick section of the Pindari Mudstone, and the Weber and Wanstead Formations.

Geomechanical modelling was used to investigate both disequilibrium compaction and tectonic compression. To investigate the effect of low-permeability layers, the porosity-permeability relationship of the carbonate intervals was changed to a 6.8 times low porosity-permeability relationship (Carb. Tight; Figure 3.18a).

The Wanstead and Weber Formations were not investigated as having low permeability values in this well, as overpressures are above these formations and registered data only reached the Waingaromia Mdst. in this well (Figures 3.21a and 3.21b; Table 3.13).

Table 3.13.- Scenarios investigated in the Tuhara-1 well.

Model	Disequilibrium Compaction	Tectonic Compression	Low Permability Layers
Tuhara-1_M-7	Yes, with an eroded thickness of 1,792 m	No	No
Tuhara-1_M-1	Yes, with an eroded thickness of 1,792 m	No	Tahaenui Fm. + Tuhara interval
Tuhara-1_M-2	Yes, with an eroded thickness of 1,792 m + intervals that drain fluid laterally to the surface from Middle Miocene (event 7-2 to Pleistocene; Table 3.12).	No	No
Tuhara-1_M-6	Yes, with an eroded thickness of 1,792 m	Yes, 8%	No
Tuhara1_M-8	Yes, with an eroded thickness of 1,792 m	Yes, 8%	Tahaenui Fm. + Tuhara interval
Tuhara-1_M-3	Yes, with an eroded thickness of 1,792 m + intervals that drain fluid laterally to the surface from the Middle Miocene (events 7-2 to the Pleistocene; Table 3.12).	Yes, 8%	No

Pore pressure generated within the models Tuhara1_M-7, M-1, and M-2 could not replicate those registered in the field data through disequilibrium compaction alone (Figures 3.21b and 3.21d). For the models Tuhara1_M-6, M-8, and M-3 where tectonic compression was applied, pore pressure rose above the registered values (Figure 3.21f).

Models Tuhara-1_M-1 and M-8 investigated low-permeability intervals to generate overpressures similar to the registered data. These two models considered the low porosity-permeability relationship (Carb. Tight; Figure 3.18a) in the two thin carbonate intervals (Tahaenui Limestone and the carbonate interval of the Tuhara Formation). Both models generate overpressure from shallow depths due to these low-permeability intervals. In the Tuhara-1_M-8 model, pore pressure increased more below these two intervals due to further reduction of the permeabilities due to tectonic compression (Figures 3.21e and 3.21f).

To match better porosity and pressure data, some of the shallow intervals were investigated as being connected to the surface. This scenario considers the structural interpretation performed during this research, where intervals above the Tunanui Formation (Middle Miocene, event 7-2) seem to be currently exposed to the surface (Figures 3.1b and 3.8). The porosity and pore pressure values matched better with the models Tuhara-1_M-2 (Figures 3.21c and 3.21d) and M-3 (Figures 3.21e and 3.21f). In these two models pore fluid pressure dissipates through these intervals while the sediments continue compacting, resulting in a porosity reduction. There is a fault that separates the sediments connected to the surface from the sediments without connection. In this scenario, this fault is interpreted as sealing (for reference, see Figures 3.1 and 3.8).

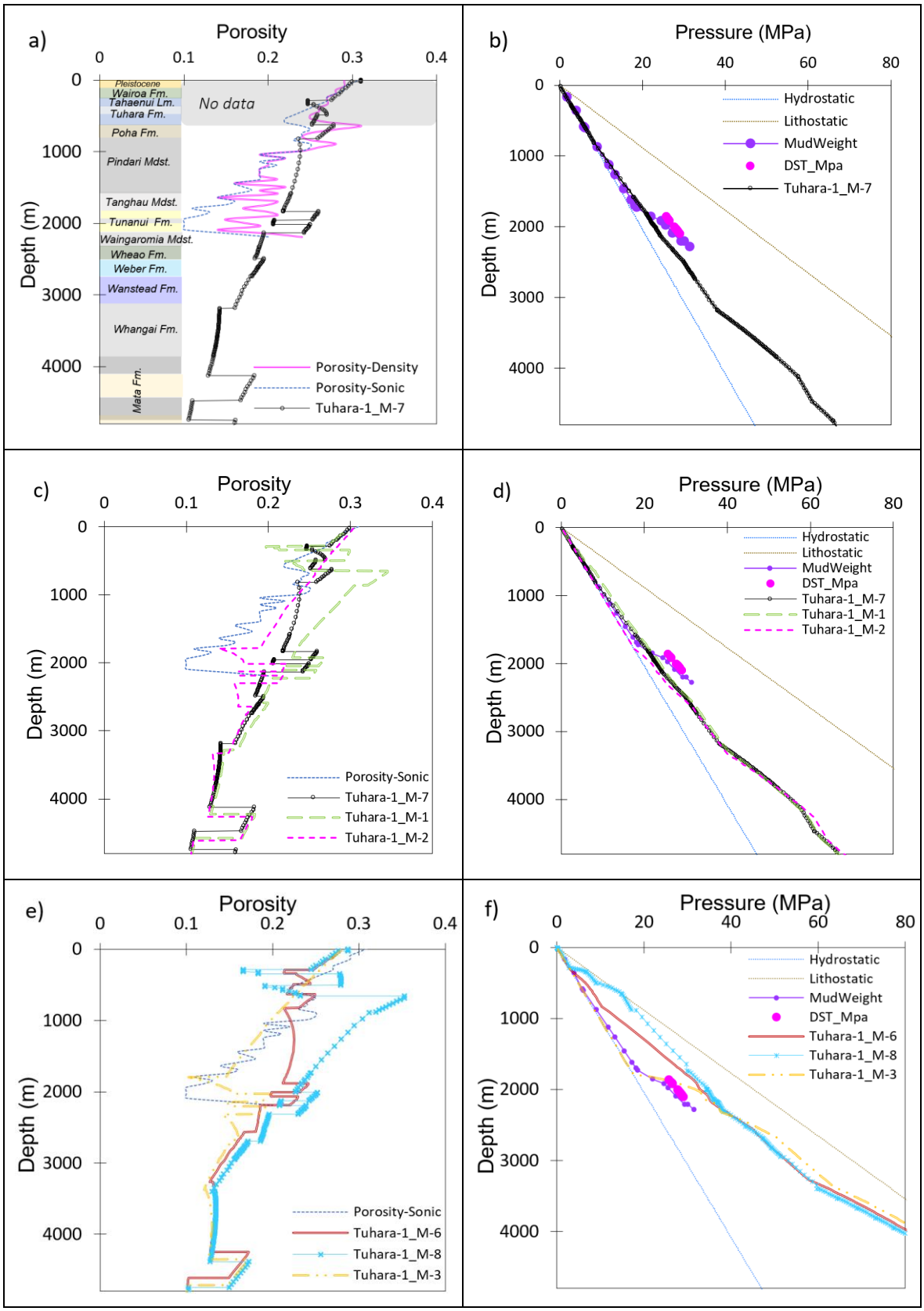

Figure 3.21.- Summary of the scenarios investigated in the Tuhara-1 well. a), c), and e) are porosity vs. depth plots, while b), d,) and f) are pressure vs. depth plots. The hydrostatic and lithostatic gradients considered were 0.00995 MPa/m (0.44 psi/ft) and 0.0226 MPa/m (1 psi/ft), respectively. Models Tuhara-1_M-7, M-1, and M-2 investigated disequilibrium compaction, while models Tuhara-1_M-6, M-8, and M-3 investigated disequilibrium compaction and tectonic compression.

3.5.4 Awatere-1 Column Model

Awatere is located 11,182 m from the Tuhara-1 well towards the west, in the onshore area of the ECB. The total depth reached for this well was 2,135.7 m, with sediments from the Early Miocene (21.7 Ma) to the Pleistocene. Six unconformities, three regional and three local, were identified within the seismic and well log data: two during the Early Miocene, one during the Middle Miocene, one in the Late Miocene, one in the Early Pliocene, and one during the Pleistocene.

The well model investigated a total thickness of 5,089 m constructed with 2,135.7 m of lithologies from drilled data, with the remainder of the thickness obtained from other wells (Table 3.14).

Table 3.14.- Awatere-1 well 1D column models with depositional and erosional settings. The thickness and porosity of sediments for the Cretaceous, Paleocene, Eocene, and Oligocene were obtained from other wells to use in the geomechanical models (highlighted in orange).

Period	Duration (Ma)	Event	Lithology	Init. Porosity	Init. Thickness (m)
Pleistocene	3.00	Erosion6			
		20b	Siltstone	0.50	427
		20a	Siltstone	0.50	427
		20	Sandstone	0.45	38
Middle Pliocene	0.70	19	Siltstone	0.50	772
		18	Carbonate	0.35	106
Early Pliocene	1.63	Erosion5			
		17a	Siltstone	0.50	59
		17	Siltstone	0.50	587
Late Miocene	5.71	Erosion4			
		16a	Siltstone	0.50	367
		16	Carbonate	0.35	46

Period	Duration (Ma)	Event	Lithology	Init. Porosity	Init. Thickness (m)
		15	Carbonate	0.35	47
		14	Siltstone	0.50	283
		13	Sandstone	0.45	202
		12	Shale	0.54	772
		11	Carbonate	0.35	50
Middle Miocene	4.86	Erosion3			
		10a	Shale	0.54	167
		10	Shale	0.54	65
		Erosion2			
		9a	Sandstone	0.45	576
		8a	Shale	0.54	916
		7a	Sandstone	0.45	44
Early Miocene	5.8	6a	Carbonate	0.35	58
		6	Carbonate	0.35	53
		Erosion1			
		5a	Shale	0.54	60
		5	Shale	0.54	283

Period	Duration (Ma)	Event	Lithology	Init. Porosity	Init. Thickness (m)
Oligocene	12.90	4	Shale with smectite and carbonate content (represented as carbonate)	0.43	367
Eocene	21.40	3	Shale with smectite and carbonate content (represented as carbonate)	0.43	679
Paleocene	10.0	2	Shale	0.54	1520
Cretaceous	6.10	1	Shale and sand	0.54 and 0.45	2840

In the Awatere-1 well, pore pressure increases at the Poha Formation around 1,200 m depth with pressure values of ~18 MPa and continues to increase to a value of ~42 MPa at the Wheao Formation around ~1,900 m (Figures 3.22a and 3.22b).

Both DST tests and mud weight values registered this increment. A value of 25 MPa was registered by the DST tests at 1,875 m (Figure 3.22b), which is lower than the identified trend. This value was not used to calibrate the geomechanical models as it could be poor quality data or lateral pressure drainage resulting in overpressure dissipation.

The low-permeability intervals identified in this well were the Tahaenui Limestone at ~600 m depth, the carbonate interval of the Tuhara Formation at ~1,200 m depth, the thick section of the Pindari Mudstone at ~1,600 m, the Kiakia Limestone at ~2025 m depth, and the Kauhauroa Limestone at ~2,125 m depth (Figure 3.22a).

The Weber and Wanstead Formations were not investigated with low porosity-permeability relationships within the well modelling as there is both a lack of well log data available to match the results and overpressure starts above these formations.

The calculated porosities from the density and sonic logs have similar values along the well. Low porosity values are observed where thin limestone intervals are present (Figure 3.22a).

The geomechanical models accounted for disequilibrium compaction (Awatere-1_M-1), disequilibrium compaction and tectonic compression (Awatere-1_M-2, Awatere-1_M-4), and disequilibrium compaction, tectonic compression, and intervals that drain fluid laterally to the surface (Awatere-1_M-3) (Table 3.15).

Table 3.15.- Scenarios investigated in the Awatere-1 well.

Model	Disequilibrium Compaction	Tectonic Compression	Low Peremability Layers
Awatere-1_M-1	Yes, with an eroded thickness of 854 m	No	Tahaenui Fm. + Tuhara carbonate interval + Kiakia and Kauhauroa Lms.
Awatere-1_M-2	Yes, with an eroded thickness of 854 m	Yes, 8%	Tahaenui Fm. + Tuhara carbonate interval + Kiakia and Kauhauroa Lms.
Awatere-1_M-3	Yes, with an eroded thickness of 854 m + intervals that drain fluid laterally to the surface from the Early Pliocene (events 17 to the Pleistocene; Table 3.14).	Yes, 8%	Tuhara carbonate interval + Kiakia and Kauhauroa Lms.
Awatere-1_M-4	Yes, with an eroded thickness of 854 m	Yes, 8%	Kiakia and Kauharoa Lms.

Results show that disequilibrium compaction with low-permeability layers is not sufficient to generate and keep high pore pressure values (Awatere-1_M-1). When tectonic compression is added (models Awatere-1_M-2, M-3, and M-4) pore pressure values increase; however, porosity values are high in the models Awatere-1_M-2 and M-3 due to the porosity preservation caused by the generation of overpressure (Figures 3.22c and 3.22d).

The Awatere-1_M-2 model generated high pore pressure values at different depths (e.g., ~700 m depth at the Tahaenui Limestone, ~1,185 m depth at the carbonate interval of the Tuhara Formation, ~2,000 m depth at the Kiakia Limestone, ~2,100 m depth at the Kauhauroa Limestone) (Figure 3.22d). Porosities could not be matched as they were preserved due to the overpressure generated as a result of the low-permeability intervals (Figure 3.22c).

The Awatere-1_M-4 model does not have any low-permeability intervals. Porosity values matched the porosity calculated from density and sonic logs. However, pore pressure started at the Pindari Mudstone (~1,500 m depth) instead of the Opoti Formation (~800 m depth) due to the lack of shallow low-permeability intervals (Figures 3.22c and 3.22d).

The Awatere-1_M-3 model included layers (Early Pliocene to Pleistocene) with high permeability values to mimic lateral flow drainage due to the exposure of these intervals to the surface. Porosity values matched the observed data in these intervals, but below Early Pliocene (intervals without high permeability values), porosities were preserved due to the overpressure generated as a result of the low porosity-permeability values of the carbonate interval of the Tuhara Formation (Figure 3.22c). Pore pressure values in this model fit better in the shallow section (above ~1,200 m depth) (Figure 3.22d). Below this section, pore pressures increased when low-permeability intervals were present

but remained slightly below the data registered in this well. For instance, the DST registered 42 MPa at ~2,000 m depth in comparison to 47 MPa at ~2,300 m depth within the models (Figure 3.22d).

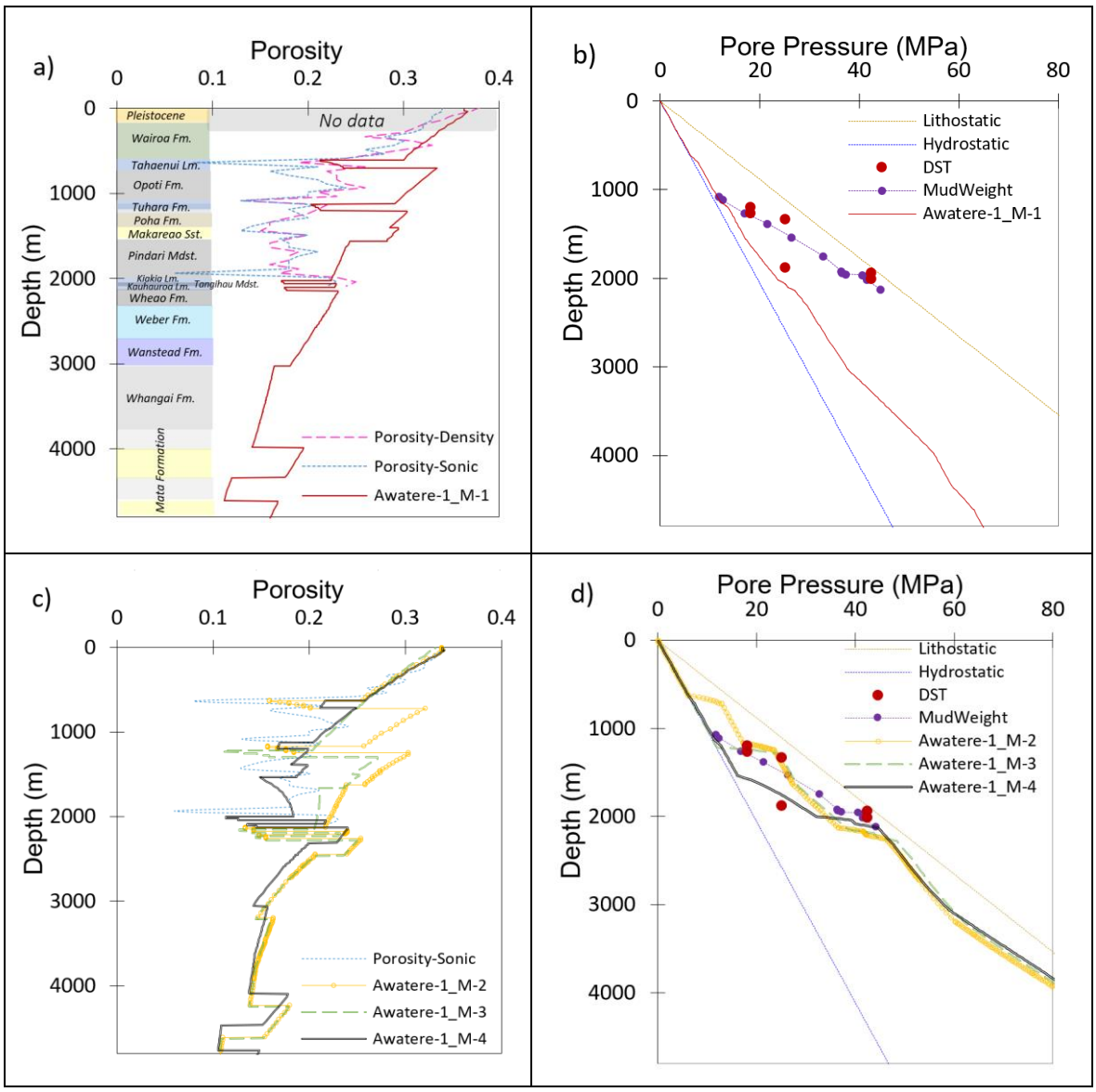

Figure 3.22.- Summary of the scenarios investigated in the Awatere-1 well. a) and c) are porosity vs. depth plots, while b) and d) are pressure vs. depth plots. The hydrostatic and lithostatic gradients considered were 0.00995 MPa/m (0.44 psi/ft) and 0.0226 MPa/m (1 psi/ft), respectively. Models Awatere-1_M-1 investigated disequilibrium compaction, while models Awatere-1_M-2, M-3, and M-4 investigated disequilibrium compaction and tectonic compression.

3.5.5 Kiakia-1 Column Model

Kiakia-1 is located 14,500 m from the Awatere-1 well towards the west of the onshore area of the ECB. This well reached a total depth of 2,014.7 m of sediments from the Early Miocene (17.2 Ma) to the Pleistocene. Six unconformities, three regional and three local, were interpreted on seismic and well logs. These include one during the Early Miocene, two during the Middle Miocene, one in the Late Miocene, one in the Early Pliocene, and one during the Pleistocene.

The geomechanical models created for this well have a total thickness of 5,258 m constructed with 2,014.7 m of lithologies from drilled data, with the remainder of the thickness obtained from other wells for the Cretaceous, Paleocene, Eocene, Oligocene, and part of the Early Miocene sediments (highlighted in orange in Table 3.16).

Table 3.16.- Kiakia-1 well 1D column models with depositional and erosional settings. The calculated thickness and porosity highlighted in orange belong to sediments of the Cretaceous, Paleocene, Eocene, Oligocene, and part of the Early Miocene from other wells.

Period	Total time (Ma)	Event	Lithology	Init. Porosity	Init. Thickness (m)
Pleistocene	3.00	Erosion6			
		20b	Siltstone	0.50	512
		20a	Siltstone	0.50	512
Middle Pliocene	0.70	19	Siltstone	0.50	291
		18	Carbonate	0.35	18
Early Pliocene	1.63	Erosion5			
		17a	Siltstone	0.50	55
		17	Siltstone	0.50	516
Late Miocene	5.71	Erosion4			
		16a	Siltstone	0.50	38
		16	Siltstone	0.35	219
		15	Carbonate	0.35	85
		14	Siltstone	0.50	613
		13	Sandstone	0.45	482

Period	Total time (Ma)	Event	Lithology	Init. Porosity	Init. Thickness (m)
		12	Shale	0.54	719
		11	Carbonate	0.35	19
Middle Miocene	4.86	Erosion3			
		10a	Shale	0.54	211
		Erosion2			
		9a	Sandstone	0.45	642
		8	Shale	0.54	149
		7	Sandstone	0.45	40
Early Miocene	5.8	6	Carbonate	0.35	53
		Erosion1			
		5a	Shale	0.54	31
		5	Shale	0.54	312
Oligocene	12.90	4	Shale with smectite and carbonate content (represented as carbonate)	0.43	367
Eocene	21.40	3	Shale with smectite and carbonate content (represented as carbonate)	0.43	679
Paleocene	10.0	2	Shale	0.54	1520
Cretaceous	6.10	1	Shale and sand	0.54 and 0.45	2840

In the Kiakia-1 well, pore pressures start increasing at the top of the Poha Formation at ~1,200 m depth reaching up to 18 MPa and continue to increase with depth (Figure 3.23b). Density and sonic calculated porosity decrease with depth, with the lowest porosity value of ~0.17 recorded at the Makareao Sandstone (Figure 3.23a).

The interpreted low-permeability intervals in this well are the Tahaenui Limestone at ~250 m depth, the carbonate interval of the Tuhara Formation at ~700 m depth, the thick section of the Pindari Mudstone at ~1,600 m, the Kiakia Limestone at ~2000 m depth, and the Kauhauroa Limestone at ~2,200 m depth (Figure 3.23a). The deep formations (Weber and Wanstead) were not investigated with low porosity-permeability relationships with the geomechanical models, as overpressure in this well starts at shallow depths.

The models investigated disequilibrium compaction and disequilibrium compaction with tectonic compression. Models Kiakia-1_M-1, M-2, and M-3 have low-permeability layers (Tahaenui Fm. + Tuhara carbonate interval + Kiakia Lm. + Kauhauroa Lm.). The Kiakia-1_M-4 model used the porosity-permeability relationship for carbonates (Carb.) for the Tahaenui Fm. and the Tuhara carbonate interval and the low permeability relationship (Carb. Tight) for the Kiakia and Kauhauroa Limestones (Figures 3.18a and 3.18.b) (Table 3.17).

Table 3.17.- Overpressure mechanisms investigated in the Kiakia-1 well. Model Kiakia-1_M-1 investigated only disequilibrium compaction, while models M-2, M-3, and M-4 investigated disequilibrium compaction and tectonic compression.

Model	Disequilibrium Compaction	Tectonic Compression	Low Permability Layers
Kiakia-1_M-1	Yes, with an eroded thickness of 1,024 m	No	Tahaenui Fm. + Tuhara interval + Kiakia Lm. + Kauhauroa Lm.
Kiakia-1_M-2	Yes, with an eroded thickness of 1,024 m	Yes, 8%	Tahaenui Fm. + Tuhara interval + Kiakia Lm. + Kauhauroa Lm.
Kiakia-1_M-3	Yes, with an eroded thickness of 1,024 m + intervals that drain fluid laterally to the surface from the Late Miocene (events 15 to the Pleistocene; Table 3.16).	Yes, 8%	Tuhara interval + Kiakia Lm. + Kauhauroa Lm.
Kiakia-1_M-4	Yes, with an eroded thickness of 1,024 m	Yes, 8%	Kiakia Lm. + Kauhauroa Lm.

Results show that disequilibrium compaction and low-permeability intervals (model Kiakia-1_M-1) are insufficient to generate the overpressure registered in this well. High pore pressure values were generated when tectonic compression was accounted for in the models Kiakia-1_M-2, M-3, and M-4. However, none of the models matched the pore pressure calculated from mud weights.

The Kiakia-1_M-1 model (Figure 3.23b) generated mild pore pressures below the carbonate interval of the Tuhara Formation (~830 m depth), and this continued to increase (~23 MPa) at the Pindari

Mudstone (~1,600 m depth), to ~24 MPa at the Kiakia Limestone (~2,063 m depth), and to ~28 MPa at Kauhauroa Limestone (~2,240 m depth). However, the values are lower than the pore pressure values registered within the well. Porosity values could not be matched as all the sediments below the low-permeability intervals were overpressured, resulting in porosity preservation (high porosity values) (Figure 3.23a).

The Kiakia-1_M-2 model generated high pore pressures, similar to the values registered in this well. Porosity values also matched better the calculated sonic porosities, as the values were reduced due to the tectonic compression applied in this model (Figures 3.23c and 3.23d).

The Kiakia-1_M-3 model investigated the exposure of shallow layers to the surface (from the siltstone interval of the Tuhara Formation ~900 m depth to the Pleistocene) (Figures 3.23c and 3.23d). Results from this model are similar to those produced by Kiakia-1_M-2, indicating that the intervals selected to have high permeability values, due to lateral flow drainage, have no impact on the pore pressure results. Porosity values do not match in the low-permeability layer (Tahaenui Lm.) due to the porosity-permeability relationship used in that layer.

The Kiakia-1_M-4 model shows a reduction of pore pressures at shallow depths as a result of the change in the petrophysical properties of the low-permeability intervals (Tahaenui and the carbonate interval of the Tuhara Fm.). This model used the normal compaction trend and porosity-permeability relationship of the carbonates (Carb.) instead of the tight carbonate curves. This model and the observed porosities were better adjusted with this model. However, pore pressures were not.

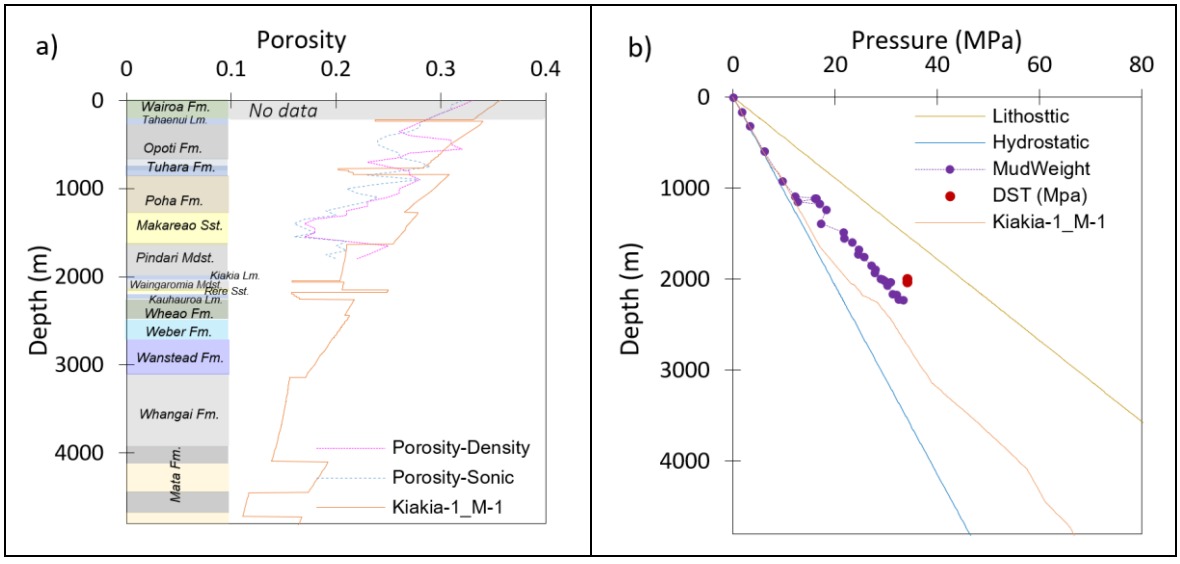

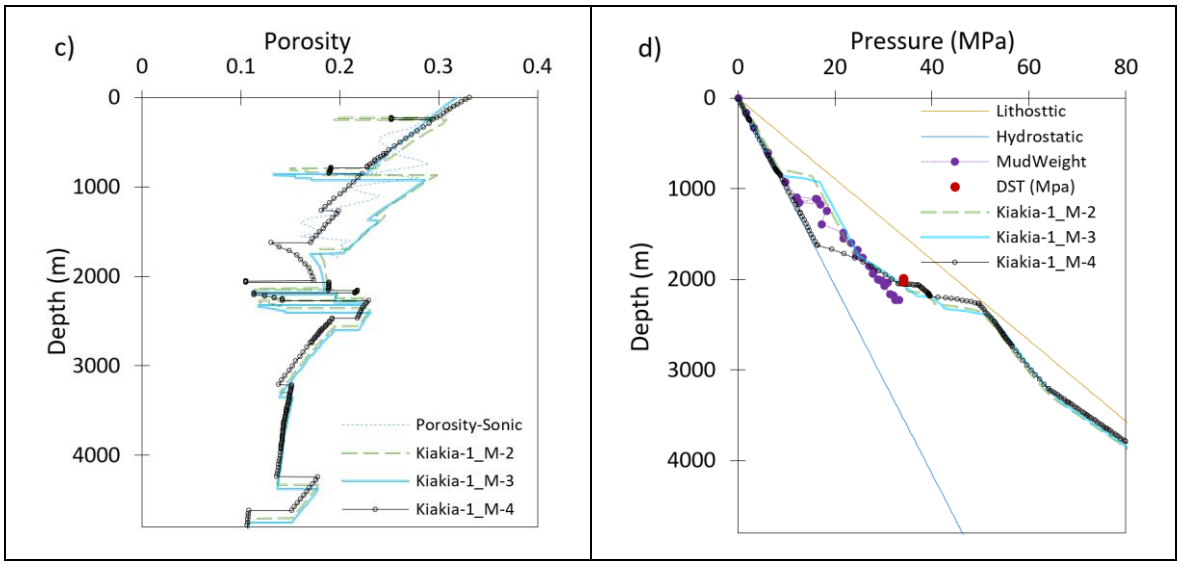

Figure 3.23.- Summary of the scenarios investigated in the Kiakia-1 well. a) and c) are porosity vs. depth plots, while b) and d) are pressure vs. depth plots. The hydrostatic and lithostatic gradients considered were 0.00995 MPa/m (0.44 psi/ft) and 0.0226 MPa/m (1 psi/ft), respectively. Models Kiakia-1_M-1 investigated disequilibrium compaction, while models Kiakia-1_M-2, M-3, and M-4 investigated disequilibrium compaction and tectonic compression.

3.6 Sediments Behaviour Through Time on Stress Paths

Stress paths were analysed during this research to understand how geological events (e.g., sedimentation, erosion, hiatus periods, and tectonic compression) influence the evolution of the stresses through time. This analysis was performed first on the parametric models and then on the Awatere-1 well.

The stress paths have been displayed in the mean effective stress vs. deviatoric stress (p' - q) plane. The mean effective stress is the average of the three principal stresses, while the deviatoric stress is a 3D formulation of shear stress and indicates the deviation from a hydrostatic stress state (Wood, 1990).

The software used was ParaGeo, a finite element code that captures the evolution of the 3D stress and strain tensors, pore pressure, and temperature, among other properties, through the simulated basin history (Crook et al., 2018; Obradors-Prats et al., 2017a and 2017b). This software encompasses the critical state poro-elasto-plastic Soft Rock 4 model, in which a yield surface defined in the stress space represents the material's strength (limit of elastic strains). When the stress path meets the yield surface, ongoing deformation will lead to the development of plastic strain, which induces a change in the material's strength. If the yielding occurs on the compression side of the yield surface (relatively high p' values), the plastic strain will be compressional (volume reduction), and the yield surface will expand (strength increase due to plastic hardening). On the other hand, yielding on the shear side of the yield surface (relatively low p' values) will lead to dilatational plastic strain (volume increase) and yield surface contraction (strength decrease due to plastic softening).

The point that divides the yield surface into two regions is known as the critical state, defined in soil mechanics as a state in which ongoing shear occurs at constant volume and constant stresses (e.g., Figure 3.24) (Wood, 1990).

3.6.1 Parametric Models

The stress paths show data from a monitoring point located at 270 m of sediment from the base in a 1D column model with a total thickness of 4,500 m.

3.6.1.1 Effect of sedimentation rates on stress paths

The models used were Model-3 (500 m/Ma) and Model-1 (2,000 m/Ma). The settings of these models are presented in section 3.4.2.

Results show that the mean stress (p') and the deviatoric stress (q) increase following a K_0 path (stress path in uniaxial burial conditions) from the beginning to the end (Figure 3.24). In Model-1, the monitored point reaches lower mean stress values compared to Model-3, as more overpressure is generated via disequilibrium compaction. In Model-3, compaction continues as the sedimentation of the 4,500m takes more time due to the low sedimentation rate. Consequently, the yield surface expands more than in Model-1 (Figure 3.24).

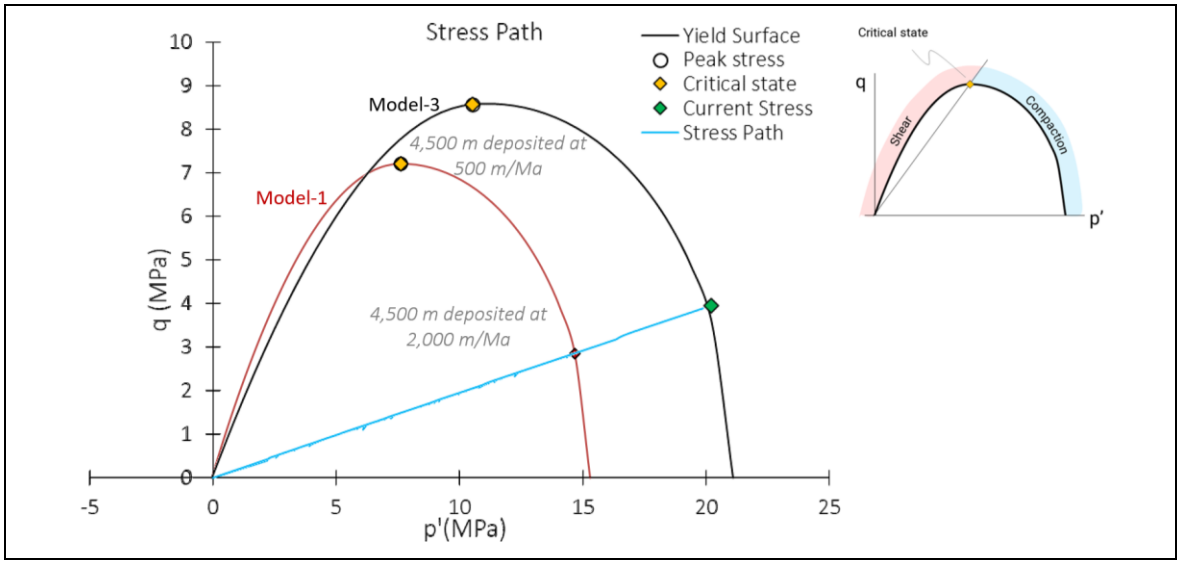

Figure 3.24.- Stress paths of the parametric models (shale lithology), which investigated different sedimentation rates. Model-1 investigated sediments deposited at 2,000 m/Ma, while Model-3 at 500 m/Ma. The mean effective stress vs. deviatoric stress (p' - q) plane is shown for reference. If the yielding occurs at the right side (blue colour) the sediments will compact, be more ductile, and their strength will increase. If the yielding occurs on the left side (red colour) the sediments will be brittle, the strength will decrease, and dilatation will occur.

3.6.1.2 Sedimentation Post-Erosion

Models A and B were constructed to investigate the effect of different erosive thicknesses occurring during the same time frame, followed by sedimentation post-erosion on the mean stress. The settings of Model-A are presented in section 3.4.3.3. Model-B has the same settings as Model-A, but in

Model-B, 900 m were eroded instead of 300 m. Model-A started with six layers deposited (1,800 m), followed by the erosion of one layer (300 m), and the sedimentation of ten more layers (3,000 m) deposited with a constant sedimentation rate of 2,000 m/Ma. Model-B started with six layers deposited (1,800 m), followed by the erosion of three layers (900 m) and the sedimentation of twelve more layers (3,600 m) deposited with a constant sedimentation rate of 2,000 m/Ma. The final thickness in both models is 4,500 m.

Results show that the mean stress (p') and the deviatoric stress (q) increase following a K_0 path (stress path in uniaxial burial conditions) from the beginning until the erosive event occurs (Figure 3.25).

The erosion of 300 m removed in Model-A did not lead to a deviation from the k0 path because the overpressure dissipated during erosion was larger or equal to the stress reduction due to the weight of the sediments removed. This leads to a stress increase and further compaction during erosion. The removal of 900 m in Model-B caused a decrease in both the mean stress (p') and the deviatoric stress (q) following an elastic unloading path. This is because the removal of the load associated with the weight of the eroded sediment was larger than the overpressure dissipated during erosion. In Model-B, with the sedimentation after erosion, the mean effective stress (p') and the deviatoric stress (q) start increasing following an elastic path until the previous pre-consolidation pressure is overcome and further consolidation plastic strains develop. The deviatoric stress (q) reaches zero values as the vertical stresses are equal to the horizontal stresses.

Even though the stress paths are different when the erosion occurs, the final pore pressure in both models is 42 MPa, indicating that the thicknesses eroded in previous events do not affect the present-day pore pressures.

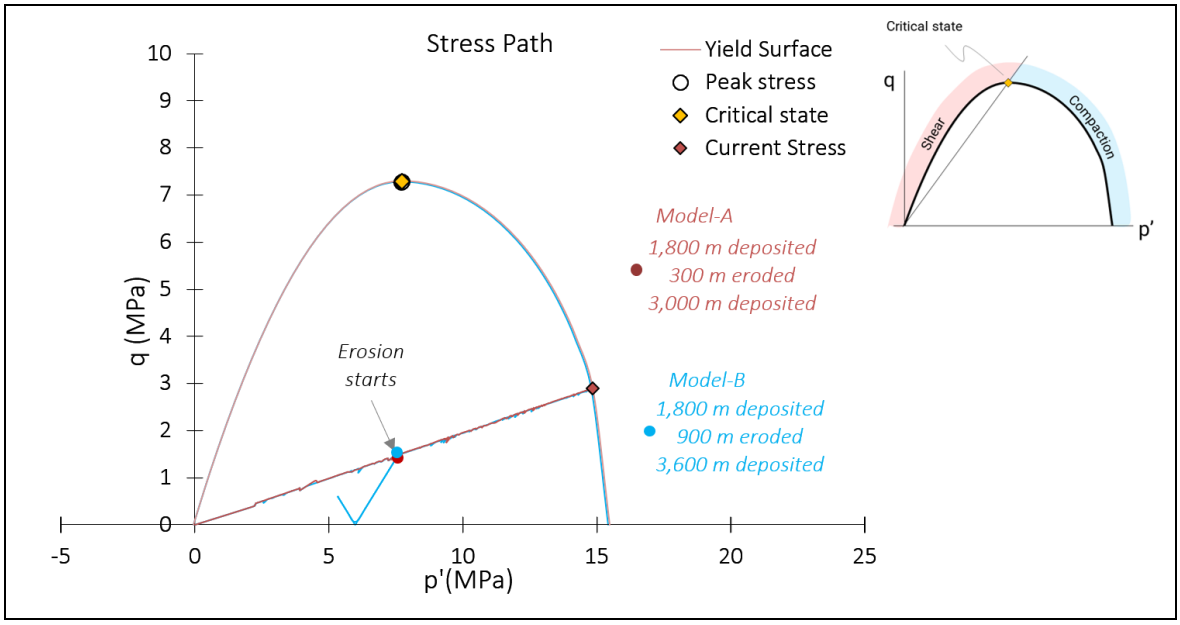

Figure 3.25.- Stress paths of the parametric models, which investigated different thicknesses eroded at the same time, followed by sedimentation. The sediments were deposited in both models at a constant sedimentation rate of 2,000 m/Ma. Model-A investigated an erosive event where 300 m of sediments were removed, while Model-B investigated an erosive event where 900 m of sediments were eroded.

3.6.1.3 Different Eroded Thickness at the Last Event

The models used to investigate different eroded thicknesses at the last event were 40 and 8. The settings of these models are presented in section 3.4.3.1. Both models have 4,500 m deposited before the erosion occurs. Model-40 has an erosive event where a thickness of 1,200 m was removed, while Model-8 has an erosive event where 300 m were removed.

Results show that the mean stress (p') and the deviatoric stress (q) increase following a K_0 path (stress path in uniaxial burial conditions) from the beginning to the end (Figure 3.26). Model-40 has a slightly higher p' than Model-8, as in Model-40 a thicker section of sediment was removed, reducing the overpressure generated during sedimentation.

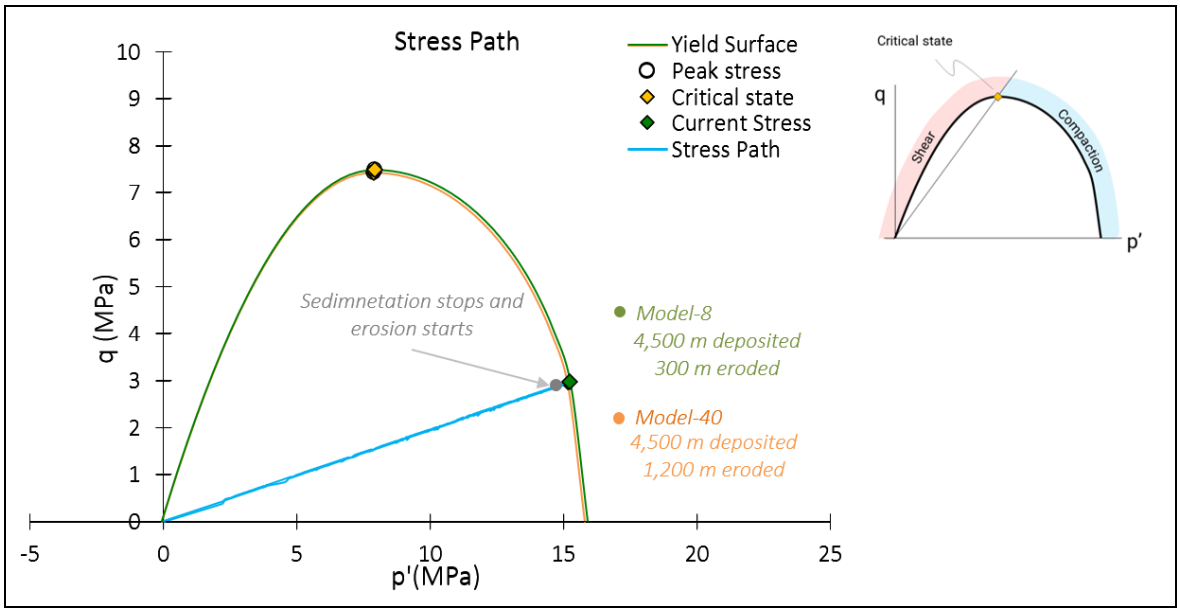

Figure 3.26.- Stress paths of the parametric models (shale lithology), which investigated erosion post-sedimentation at the last event. The sediments were deposited at a constant sedimentation rate of 2,000 m/Ma. The thickness eroded in Model-8 was 300 m, while in Model-40 it was 1,200 m.

3.6.1.4 Tectonic Compression

The models to investigate different horizontal shortenings at the last event were 18, 17, and 12. The settings of these models are presented in section 3.4.6. These three models had 4,200 m of sediment deposited at a constant sedimentation rate of 500 m/Ma before tectonic compression was applied when the last 300 m of sediments were deposited. Three horizontal shortenings were applied: 12% (Model-18), 10% (Model-17) and 5% (Model-5).

Results from these three models show that the current yielding is on the compaction side in all of them (Figure 3.27). The deviatoric stress (q) decreases when tectonic compression is applied as a result of the increase of the horizontal stress and the reduction of the vertical stress. The mean effective stress (p') slightly increases (<1 MPa). As tectonic compression and sedimentation continue, the mean effective stress (p') decreases.

The reduction of the mean effective stress (p') depends on the amount of the applied horizontal shortening. A shortening of 12% resulted in the highest reduction of the mean effective stress (p'),

or more overpressure generation. The deviatoric stress increases as the difference between the vertical and horizontal stresses continues increasing (Figure 3.27).

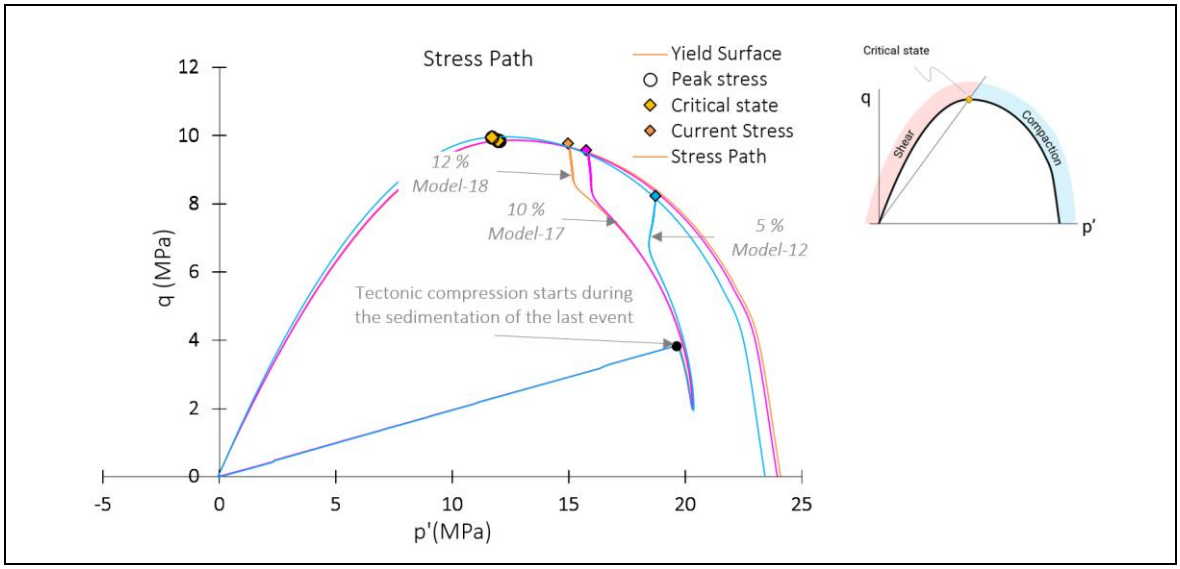

Figure 3.27.- Stress paths of the parametric models (shale lithology), which investigated tectonic compression during the last event, where 300 m of sediments were deposited. The whole sedimentary column was deposited at a constant sedimentation rate of 500 m/Ma. A 12% horizontal shortening was applied in Model-18, 10% horizontal shortening was applied in Model-17, and a 5% horizontal shortening was applied in Model-12.

3.6.2 New Zealand Models, Awatere-1 Well

Two formations with different properties were investigated on the Awatere-1 well: the shale interval modelled as carbonate due to the high carbonate and smectite content (Weber Formation) and the shale interval with little smectite or carbonate content (Wheao Formation) (Figure 3.28). These intervals were chosen as it has been suggested by Darby (2002) that the overpressure encountered in this basin could result in a failure of sealing integrity. The stress paths were plotted for the models of the Awater-1 well (models Awatere-1_M-1 and Awatere-1_M-2) previously presented in section 3.5.4 (Table 3.18).

Table 3.18.- Stress path settings. Two lithologies were investigated: Weber (high smectite and carbonate content) and Wheao (shale interval without smectite and carbonate content). Model M-1 investigated only disequilibrium compaction, and model M-2 investigated disequilibrium compaction and tectonic compression.

Model	Intervals Analysed	Disequilibrium Compaction	Tectonic Compression	Low Permability Layers
Awatere-1_M-1	Weber Formation	Yes	No	Tahaenui Fm. + Tuhara interval
	Wheao Formation			
Awatere-1_M-2	Weber Formation	Yes	Yes, 8%	Tahaenui Fm. + Tuhara interval
	Wheao Formation			

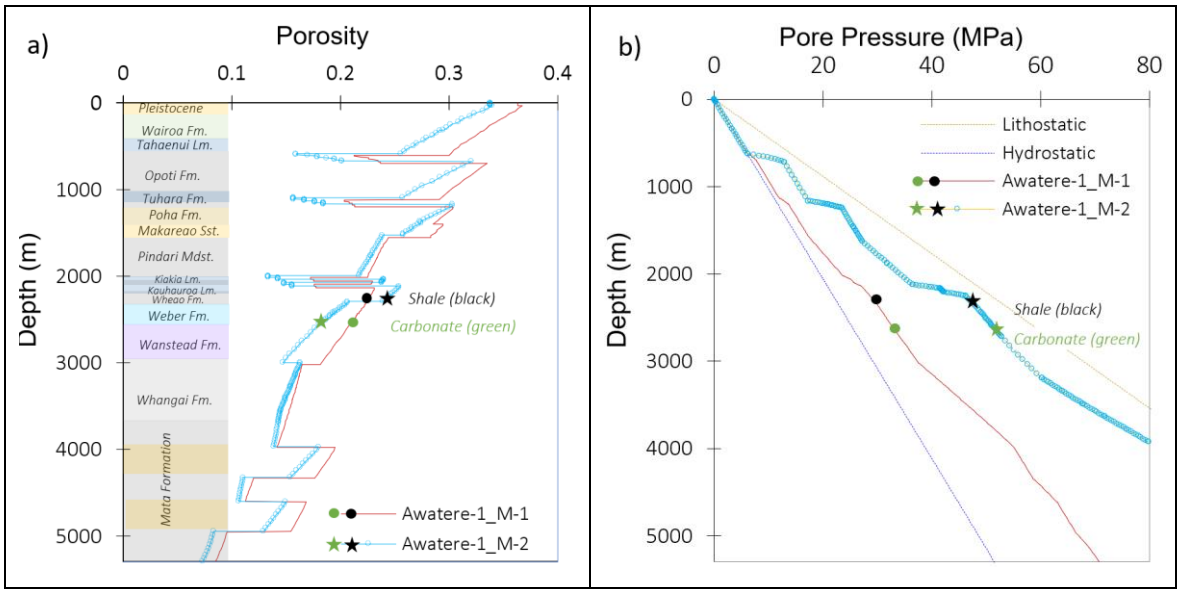

Figure 3.28.- a) Porosity vs. depth plot with the formations and the results of two models: Awatere-1 (disequilibrium compaction) and Awatere-1_M-2 (disequilibrium compaction + tectonic compression). b) Pore pressures vs. depth plot with the results of the two models Awatere-1_M-1 and M-2. Green markers represent the carbonate interval, while black markers represent the shale interval. The circles represent the locations from the model Awatere-1_M-1, and the stars represent the locations from the model Awatere-1_M-2. The depths on the plots of the two models have been rescaled to compare their values.

3.6.2.1 Stress Paths for the Model that Accounted Sedimentation and Erosion

3.6.2.1.1 Carbonate Lithology

The stress path within the carbonate interval (Figure 3.29a) started at point (a), which corresponds to the initial stress state after the carbonate interval was deposited. Then, the evolution of the stress path according to the subsequent events in the basin's history may be described as follows:

From point (a) to point (b), the sedimentation continues on top of this interval, and the mean effective stress (p') and the deviatoric stress (q) increase following a K_0 path (stress path in uniaxial burial conditions) (Figure 3.29a).

From point (b) to point (c), an erosional event occurred (thickness eroded 60 m; Erosion1; Table 3.14). This leads to a decrease in both the mean effective stress (p') and the deviatoric stress (q), with the stress path following an elastic unloading path.

From point (c) to point (d), post-erosion sedimentation results in an increase in both the mean effective stress (p') and the deviatoric stress (q). Initially, the path (c to d) follows an elastic path until the previous pre-consolidation pressure is overcome and further consolidation plastic strains develop between the points (b) to (d).

From point (d) to point (e), the erosive event (Erosion2, Table 3.14) leads to a decrease in both the mean effective stress (p') and the deviatoric stress (q). During this erosive event, 1,595 m of sediment were removed. The stress path follows an elastic unloading path.

From point (e) to point (f), post-erosion sedimentation resulted in an increase in both the mean effective stress (p') and the deviatoric stress (q). The stress path follows an elastic reloading path in the opposite direction of the previous unloading path.

From point (f) to point (g), the erosive event (Erosion3, Table 3.14) occurred with a thickness removal of 167 m. The mean effective stress (p') and the deviatoric stress (q) decrease with the stress path following an elastic unloading path.

From point (g) to point (h), post-erosion sedimentation results in an increase in both the mean effective stress (p') and the deviatoric stress (q). The stress path follows an elastic path until the previous pre-consolidation pressure is overcome and further consolidation plastic strains develop between the points (d) and (h).

From point (h) to point (i), a new erosive event occurred during which 367 m of sediments were removed with the stress path following an elastic unloading path (Erosion4; Table 3.14).

From point (i) to point (j), post-erosion sedimentation resumes, increasing the stresses. The path (i to j) follows an elastic path until the previous pre-consolidation pressure is overcome and further consolidation plastic strains develop between the points (h) and (j).

From point (j) to point (k), the erosive event (Erosion5) occurs, during which 59 m of sediments were removed, leading to a slight increase in the mean effective stress (p') and the deviatoric stress (q) as the overpressure dissipated, which was higher than the load removed.

From point (k) to point (l), post-erosion sedimentation resumes and results in an increase in both the mean effective stress (p') and the deviatoric stress (q). Between these points (k and l) a thickness of 1,771 m was deposited before the last erosive event occurred (Erosion6, Table 3.14). This last erosive event removed 854 m of sediments and did not cause a reduction in the mean effective stress (p') or the deviatoric stress (q), as the pore pressure reduction was larger than the reduction in stress caused by the thickness removed. (Figures 3.29a and 3.29b).

3.6.2.1.2 Shale Lithology

Similar to the carbonate interval, the stress path within the shale interval (Figure 3.29c) started at point (a), which corresponds to the initial stress state after the shale interval was deposited. This interval was deposited on top of the carbonate interval previously described. The stress path for this interval may be described as follows:

From point (a) to point (b), the sedimentation continues on top of this interval, and the mean stress (p') and the deviatoric stress (q) increase following a K_0 path (stress path in uniaxial burial conditions) (Figure 3.29dc).

From point (b) to point (c), an erosional event occurred (thickness eroded 60 m, Erosion1, Table 3.14). This leads to a decrease in both the effective mean stress (p') and the deviatoric stress (q), with the stress path following an elastic unloading path.

From point (c) to point (d), post-erosion sedimentation results in an increase in both the mean effective stress (p') and the deviatoric stress (q). Initially, the path (c to d) follows an elastic path until

the previous pre-consolidation pressure is overcome and further consolidation plastic strains develop between the points (b) to (d).

From point (d) to point (e), the erosive event (Erosive2) occurs, which removed 1,595 m of sediment, causing two behaviours: first, the deviatoric stress (q) reduces to almost zero and the mean effective stress (p') reduces to ~6.3 MPa; and second, the deviatoric stress (q) begins to increase to ~2 MPa while the mean effective stress (p') continues decreasing to ~4.3 MPa. The reason behind this behaviour is observed in Figure 3.29d, where the vertical stress decreases due to the thick section of sediment removed during this event, reaching values lower than the horizontal stress. The stress path follows an elastic unloading path.

From point (e) to point (f) post-erosion sedimentation results in an increase in the mean effective stress (p') and a reduction in the deviatoric stress (q). Between these points, the vertical stress increases with the new sedimentation, but it is still lower than the horizontal stress (Figure 3.29d). The stress path continues following the elastic unloading path.

From point (f) to point (g), the erosive event Erosion 3 (Table 3.14) occurs, removing a thickness of 167 m. This erosion results in a reduction of the mean effective stress (p') and an increase in the deviatoric stress (q). The stress path continues following the elastic unloading path.

From point (g) to point (h), post-erosion sedimentation results in an increase in both the mean effective stress (p') and the deviatoric stress (q). The stress path follows an elastic path until the previous pre-consolidation pressure is overcome and further consolidation plastic strains develop between the points (d) and (h).

From point (h) to point (i), a new erosive event occurred (Erosion4, Table 3.14). During this event, 367 m of sediment were removed. This erosion leads to a decrease in both the mean effective stress (p') and the deviatoric stress (q), with the stress path following an elastic unloading path.

From point (i) to point (j), post-erosion sedimentation resumes and results in an increase in both the mean effective stress (p') and the deviatoric stress (q). The path (i to j) follows an elastic path until the previous pre-consolidation pressure is overcome and further consolidation plastic strains develop between the points (h) to point (j).

From point (j) to point (k), the erosive event (Erosion5) occurs, during which 59 m of sediments were removed, leading to a slight increase in the mean effective stress (p') and the deviatoric stress (q) as the overpressure dissipated, which was higher than the load removed.

From point (k) to point (l), post-erosion sedimentation resumes and results in an increase in both the mean effective stress (p') and the deviatoric stress (q). Between these points (k and l) a thickness of 1,771 m was deposited before the last erosive event occurred (Erosion6, Table 3.14 with a removal of 854 m). This last erosive event did not cause a reduction in the mean effective stress (p') or the deviatoric stress (q), as the pore pressure reduction is larger than the reduction in stress caused by the thickness removed (Figures 3.29c and 3.29d).

The stress paths of both the carbonate and the shale lithologies were inside the yield surface through time, implying elastic and plastic behaviour in both lithologies. The shale stress path reaches slightly

higher mean stress values (p') (~18.3 MPa) than the carbonate mean effective stress values (p') (~16.8 MPa). This is due to the characteristics of each lithology (e.g., Poisson Ratio, Young's modulus, Bulk modulus, hardening modulus).

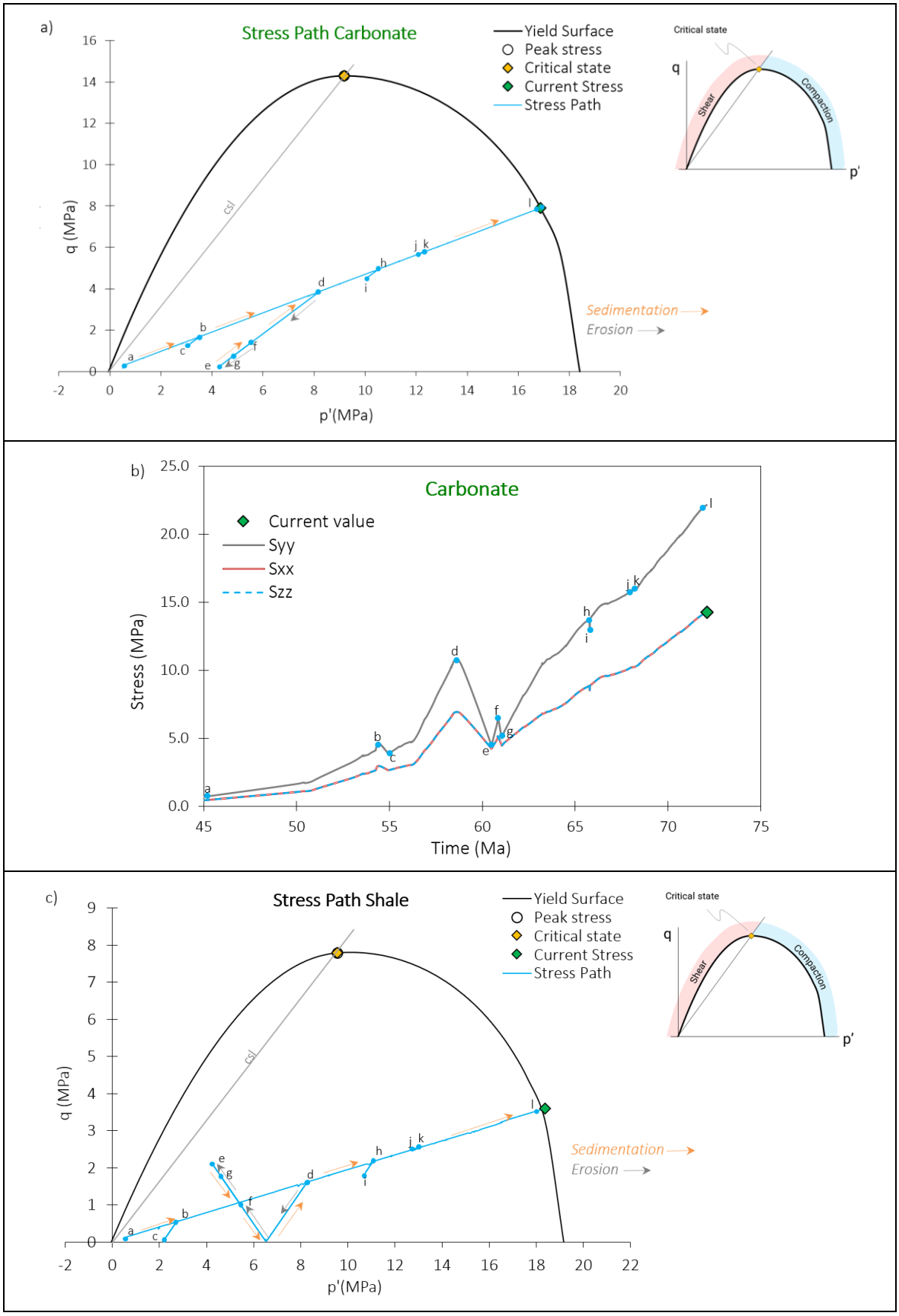

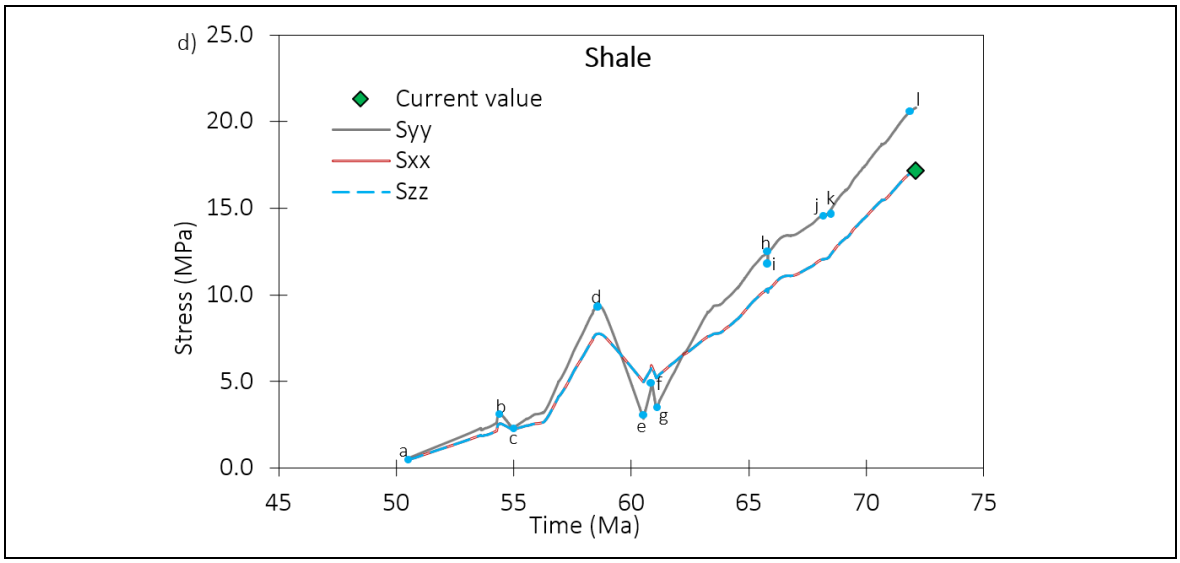

Figure 3.29.- Disequilibrium compaction results (Awatere-1_ M-1model). a) Carbonate and c) shale stress paths. b) Carbonate and d) shale cross-plots of the evolution of the stresses through time (x, y, and z). The sedimentation and erosion events have been highlighted with letters. Erosive events (total of six events).

3.6.2.2 Stress Paths for the Model that Accounted for Sedimentation, Erosion and Tectonic Compression

3.6.2.2.1 Carbonate and Shale Lithologies

The stress paths of each lithology are similar until point (k); after this point, post-erosion sedimentation resumes until tectonic compression is applied in the models, which correspond to point (l) (Figure 3.30).

From point (l) to point (m), the deviatoric stress (q) reduces, reaching ~2 MPa on the carbonate path and ~1.4 MPa on the shale path. This is the result of sedimentation and tectonic compaction, where the horizontal stress (x) started increasing while the vertical stress (y) started reducing due to the tectonic-induced overpressure (Figures 3.30a and 3.30c).

From point (m) to point (n), sedimentation and tectonic compression continue, and the mean effective stress (p') slightly increases in the carbonate lithology and slightly decreases in the shale lithology. This is because the shale lithologies have more plastic volume strain than the carbonate lithologies. Sedimentation stopped at point (n) and the last erosive event (Erosion6, Table 3.14) occurred.

From point (n) to point (o), during Erosion6, a thickness of 854 m was removed. Tectonic compression continued, resulting in an increase in the deviatoric stress (q). In the carbonate lithology, the deviatoric stress (q) reached ~14 MPa, while in the shale interval, it only reached ~7 MPa (Figures 3.30a and 3.30c). This difference is due to the sediment's properties (e.g., shale lithology has more plastic behaviour), and it takes more time to recover its status. This behaviour is observed in Figure 3.30b, where the horizontal stress continues increasing to the last point (o) in the carbonate lithology. In the shale lithology, the horizontal stress slightly increases while the vertical stress decreases when tectonic compression is applied. However, the horizontal stress starts reducing towards the last point

(o) when the last erosion occurs. This occurs because the rate of overpressure generation due to the tectonic event is greater than the rate of total stress increase.

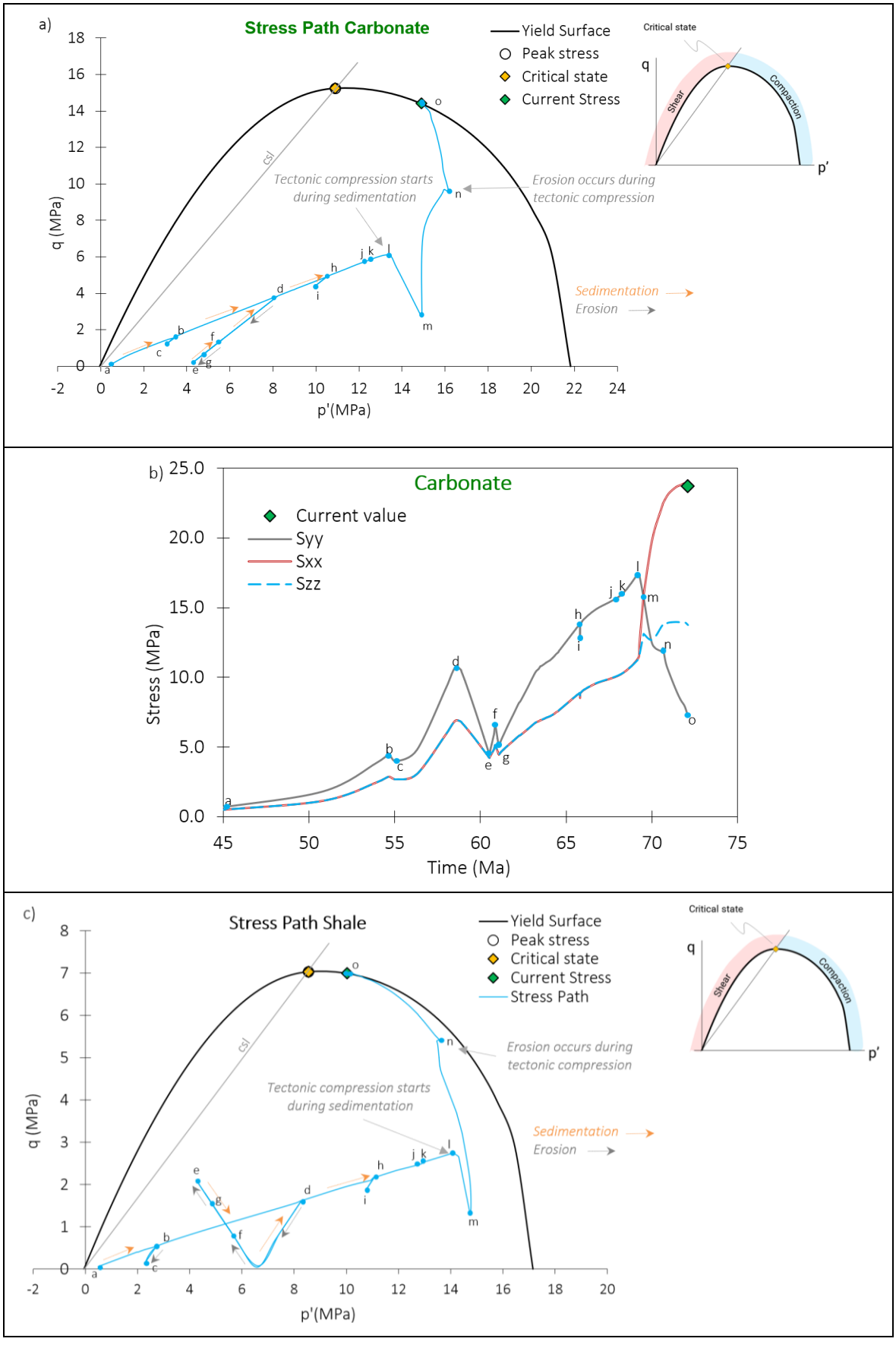

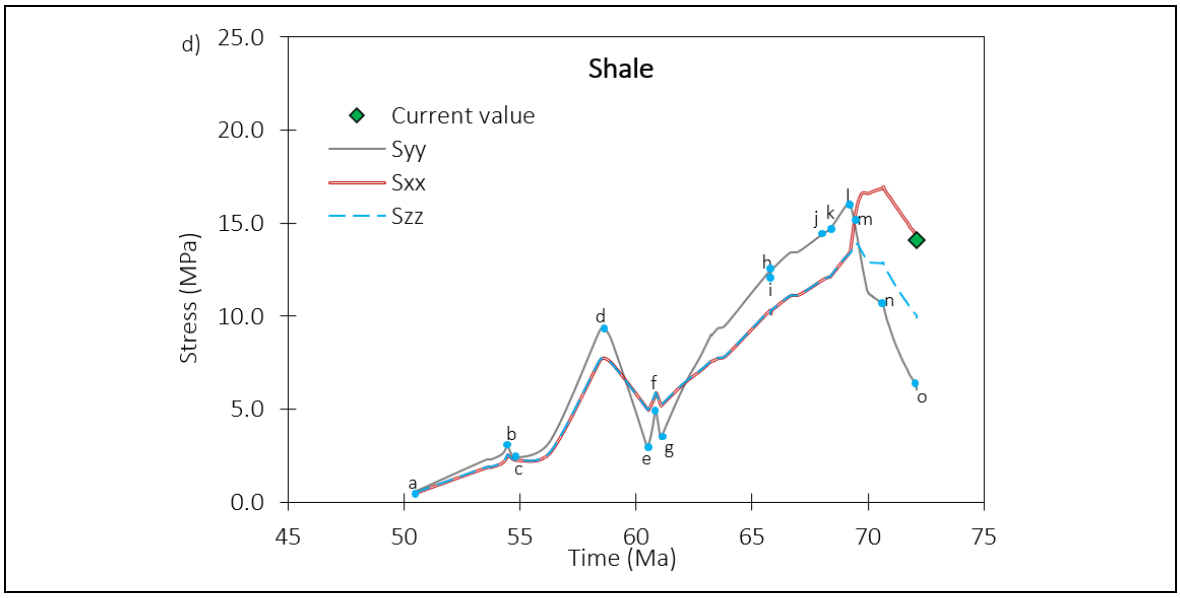

Figure 3.30 a) Disequilibrium compaction and tectonic compression results (Awatere-1_M-2model). a) Carbonate and c) shale stress paths. b) Carbonate and d) shale cross-plots of the evolution of the stresses through time (x, y, and z). The sedimentation and erosion events have been highlighted with letters. Erosive events (total of six events).

3.7 Discussion

3.7.1 Implication of Overpressure in Active Tectonic Basins

The results of this study suggest that tectonic compression is the mechanism that contributes significantly to overpressure generation in the ECB. As suggested by Palciauskas and Domenico (1989), tectonic compression is more evident in compressional systems such as subduction systems, where the tectonic and loading forces compress the pore fluid. High pore pressure values have been recorded in active basins due to the compression exerted by the tectonic plates (Yassir and Addis, 2002; Darby and Funnell, 2001; Barnes et al., 2010). Obradors-Prats et al. (2017a) have also underlined that greater overpressures generated by tectonic compression would be found in basins where sediments have low porosity and permeability values.

Tectonic compression has previously been suggested to have played a significant role in the overpressure encountered in the ECB. Darby and Funnell (2001) used pore pressure data to understand the distribution of the overpressure and its relationship to subduction processes and concluded that tectonic compression generated the high overpressure values in the ECB due to the subduction of the Pacific Plate under the Atlantic Plate. However, quantifying the amount of overpressure generated in compressional systems is not straightforward. While the low porosities found in these systems are caused by the stress and strain of sediments and generally result in high overpressures (Swarbrick et al., 2002), more simplistic overpressure interpretation methods, such as log-based interpretation, based on these low values would likely result in inaccurate estimations of overpressure. As identified by Couzens-Schultz and Azbel (2014) in the fold-thrust belt systems of the deepwater fold-belt of the northwest Sabah region, low porosity values must be corrected before

more accurate overpressure estimations can be produced. Ge and Garven (1992) and Bour et al. (1995) have also highlighted that pressure transfer, through faults during thrusting, can act in compressional systems and contribute to the occurrence of overpressure.

To calculate the tectonic compression acting on the ECB, it is necessary to account for the shortening rate and the period over which this shortening occurs. As this mechanism has not been investigated as thoroughly as others, the shortening compaction of the ECB has not been fully established, and therefore shortening percentages from other studies were taken into consideration. For instance, in the Pegasus Basin, New Zealand, Barnes (1997) determined that approximately 7,000 m of horizontal shortening in 30 km has occurred in the last ~0.5 Ma (for reference of the Pegasus Basin location, see Figure 3.1a). However, that study obtained horizontal shortenings from seismic section restorations without accounting for tectonic compaction; therefore, these values were not considered. Due to the lack of well-constrained tectonic strain estimates for the ECB, horizontal shortening values between 5 and 12.5% were adopted and used to investigate its effect on pore pressure, porosity, and effective stresses. These values were determined by Butler and Paton (2010) and Dalton et al. (2015) in the compressional region of the deep-water sediments of the thrust belt systems in the Orange Basin, offshore Namibia.

The maximum tectonic shortening value of 12.5% was used in the parametric modelling in this study, which caused a displacement of 2.5 m in 20 m or 3,750 m in 30,000 m and generated high overpressures on the low-permeability intervals (e.g., >1,000 m depth an overpressure of 2 MPa, >2,000 m depth an overpressure of 14 MPa, >3,000 m depth an overpressure of 26 MPa; Figure 3.17b). For the ECB models, a shortening of 8% during the last events (around Pliocene to present-day 3 to 5.7 Ma) was used, as this tectonic shortening better matched the registered data. This tectonic shortening causes a displacement of 1.6 m in 20 m or 2,400 m in 30,000 m and generates high overpressures on the low-permeability intervals (e.g., thin limestones, smectite content shales, and thick shale intervals).

Tectonic compression in active basins seems to be the main overpressure mechanism when this mechanism acts during recent geological times. For instance, Wang et al. (2022) determined that the overpressure encountered in the sediments of the Mesozoic-Cenozoic foreland basin of the Tarim Basin (northwestern China) was generated due to tectonic compression during the last 2.4 Ma with a tectonic shortening of 12.5%. Obradors-Prats et al. (20017a) also determined that tectonic compression results in overpressure generation and porosity reduction. This was based on conceptual fully coupled geomechanical models where up to 10% horizontal shortening was applied. Within the ECB, Darby and Ellis (2001 and 2003) also identified tectonic compression as the main overpressure mechanism. This conclusion was based on 2D section models using the finite-element software Abaqus, which investigated disequilibrium compaction, erosion, and later tectonic compression with a shortening of 1%/Ma throughout 10 Ma.

This study also suggests that tectonic compression is the main overpressure-generating mechanism, but with shortening values of 1.4 and 2.7%/Ma applied in recent geological times (e.g., from 3 to 5.7 Ma). This period was selected as tectonic compression increased during the Pliocene to present-day in the ECB (e.g., Field et al., 1997; Barnes, 1997; Erdi et al., 2018; McArthur et al., 2020). For

instance, in all five key wells, it was necessary to apply tectonic compression to generate overpressures similar to the registered data. Even though these studies agree that tectonic compression can cause high overpressures in compressional systems, Burgreen-Chan et al. (2016) determined via 2D basin and poroelastic models that the main overpressure mechanism in the ECB was disequilibrium compaction, with less impact from tectonic compression. This different conclusion is interpreted to be related to the geological complexity of the ECB, the lack of data, and the different approaches used in each study.

3.7.2 Role of Disequilibrium Compaction in the ECB Overpressure

This study determined that disequilibrium compaction contributed to some extent to the present-day overpressure of the ECB, due to the fast sedimentation rates (up to 3,000 m/Ma) from the Cretaceous to the Miocene (Field et al., 1997; Darby and Funnell, 2001; Burgreen-Chan et al., 2016) and the low-permeability intervals deposited from the Cretaceous to present-day.

Rapid sedimentation of mud-rich lithologies is recognised to be the main cause of overpressure generation in young basins such as the Gulf of Mexico, the Gulf Coast in the Louisiana Shelf, and the Louisiana Salt Basin (e.g., Bredehoeft and Hanshaw, 1968; Harrison and Summa, 1991; Audet, 1996; Swarbrick et al., 2002; Nunn, 2012). However, overpressure generated by disequilibrium compaction depends on a range of factors, including sedimentation rates, permeability, and time (Skempton, 1970; Luo and Vasseur, 1992; Schneider et al., 1996; Swarbrick and Osborne, 1998; Swarbrick and Hillis, 1999; Swarbrick et al., 2002). This study focused on two of these factors (different sedimentation rates and permeability), as it has been suggested that these variables may have a greater impact on overpressure generation (Swarbrick and Hillis, 1999; Swarbrick et al., 2002). Sedimentation rates equal to and over 2,000 m/Ma of mud-dominated lithologies have been suggested to generate high overpressures, while sedimentation rates of 100 m/Ma of mud-dominated lithologies generate low overpressures (Swarbrick et al., 2002). In the ECB, sedimentation rates vary from 100/Ma (in the lower slope basin) to 3,000 m/Ma (in the upper slope of the basin) (Lewis, 1980). In a study performed around the Hawkey Bay-1 well (see Figure 3.1a) with 2D poroelastic models, Burgreen-Chan et al. (2016) suggested that disequilibrium compaction is the main mechanism in the ECB due to the high sedimentation rates (>1,000 m/Ma) encountered in the Hawkey Bay area. However, Darby and Funnell (2001), with generic 2D section models constructed for analysing overpressure in the ECB, suggested that disequilibrium compaction has an impact on the present-day pore pressure due to the sedimentation rates calculated during the Miocene (300 m/Ma).

During this research and with the results of the 1D hydro-mechanical models, disequilibrium compaction has been determined to have contributed to the compaction of the sediments and with slightly overpressure generation. However, most of this overpressure was constantly dissipated during the erosive events and hiatus periods that occurred from the Cretaceous to the present-day. The sedimentation rates calculated and used in the models of the five key wells throughout the sedimentary column analysed were between ~370 and ~730 m/Ma. For example, if overpressure values are extracted from the results of the five key wells at 2,000 m, disequilibrium compaction contributed up to 3 MPa of the total overpressure registered in these wells.

3.7.3 Effect of Erosion on Pore Pressure

Several important erosive events occurred in the ECB between the Cretaceous and present-day. Field et al. (1997) and Darby and Funnell (2001) found through pore pressure analysis of the ECB data, that high overpressures close to lithostatic values were preserved in uplifted areas where erosion has occurred without giving a clear conclusion of the reason for its preservation. Studies such as Swarbrick and Osborne (1998), Neuzil and Pollock (1983), and Nunn (2012) highlighted that erosion and lateral drainage transfer can result in overpressure dissipation. In the ECB, Burgreen-Chan et al. (2016) also highlighted through the 2D basin and poroelastic modelling around the Hawke Bay-1 well (see Figure 3.1a) that overpressure dissipates when erosion occurs.

The parametric models used during this study show that erosion and hiatus periods result in overpressure dissipation, with the last erosive events having the greatest impact (e.g., Figures 3.13b, 3.14b, and 3.15b). For example, a monitored point located at 270 m from the base of Model 1 that reached a total depth of around 3,312 m (see section 3.4.2 for model settings) have pore pressures of around 43.30 MPa without any erosive event. With the same model settings, but with an erosive event that removed 1,200 m of sediments, the pore pressure reduces to around 25.52 MPa at around 2,112 m depth (Model 40; section 3.4.3). In the ECB, calculating the thicknesses removed in the last erosive events is a challenge due to the complex geological framework of this basin. In this study, analytical equations that were previously used by Funnell et al. (1996) to calculate the last eroded thickness in the ECB were adopted and compared to the results obtained from the 1D models constructed for the five key wells selected in this basin. The analytical equations suggested that the five well locations have experienced similar uplift events, and therefore a constant thickness from ~1,000 to ~1,200 m was eroded across the studied area of the ECB. In contrast, the 1D hydro-mechanical models suggested that the uplift has occurred differently in each well location due to their individual structures, resulting in different eroded thicknesses (from 654 to 1,792 m; Figure 3.1b). The well Opoutama-1, which is located in the eastern part of this research (Figure 3.1b), presents the highest eroded thickness of the five key wells. To match well-log data with the results of the analytical equations, an eroded thickness of 1,200 m was needed in comparison to the 5,025 m used in the 1D geomechanical models. However, well data can also be matched with an eroded thickness of 1,711 m and hiatus periods from the Early Pliocene (Table 3.9; Figure 3.19).

In the ECB, due to the complex geological histories, different intervals have been exposed to the surface. The time when these intervals were exposed is uncertain, but Field et al. (1997), Barnes (1997), and McArthur et al. (2020) suggested that it could have happened just before and during the Pliocene to the present-day (~5.3 Ma) when tectonic compression increased in the ECB due to the convergence of the Pacific Plate towards the Australian Plate.

A possible lateral flow drainage is suggested to have occurred at some intervals of the ECB. This is based on pressure data and the current interpreted structure (from seismic and well data), which show intervals from the Cretaceous to the present-day exposed to the surface. For example, the low-permeability intervals (Tahaenui Limestone, the Pindari, and Tangihau mudstones) interpreted in the Opoho-1 well are interpreted to be exposed to the surface on the structural section (Figure 3.6), and these intervals do not present any overpressures on the pressure data registered. Furthermore, in

wells where these intervals are not exposed to the surface (according to this research interpretation), overpressure is present (e.g., Awatere-1, Kiakia-1, for reference Figures 3.22 and 3.23).

3.7.4 Overpressure Distribution in a Compartmentalised Basin, the ECB

In the studied region, potentially significant compartmentalisation of fluid flow is likely based on seismic data (e.g., faults), well logs (low-permeability intervals), and pressure data, and these suggest that compartmentalisation affects the amount of the present-day overpressure in the ECB. This basin has a complex structural framework and complex sedimentary history as a result of the subduction of the Pacific Plate underneath the Australian Plate, creating diverse fault systems (e.g., compressional, extensional, and strike-slip) and low-permeability layers (e.g., mudstone, carbonate, and smectite content intervals), which have contributed to the compartmentalisation of this basin (e.g., well reports; Moore and Speden, 1979; Lewis, 1980; Field et al., 1997; Darby and Funnell, 2001; Darby and Ellis, 2001; Burgreen-Chan et al., 2016; McArthur et al., 2022, among others). A recent research focused on the Taranaki Basin (New Zealand) identified the key role of stratigraphy and tectonic compression on overpressure compartmentalisation (O'Neill et al., 2023).

Data from the five key wells were used to identify any lateral and/or vertical connection between them. These wells are from ~10 to ~15 km apart (Figure 3.4), and most of the sedimentary intervals are separated by regional faults (Figure 3.1b). Even though the integrity of the faults was not analysed during this study, pressure data from mud weights and pressure tests show that these wells are not connected. The 1D models also confirmed that different overpressure values can be generated in each well, independent of the other well locations. The vertical fluid flow compartmentalisation is interpreted to be due to the low-permeability intervals (e.g., thin carbonates and mudstone intervals of the Miocene and Pliocene) and the horizontal fluid flow compartmentalisation due to faults acting as seals (e.g., the juxtaposition between mudstone lithologies).

3.7.4.1 Thin Low-permeability Carbonate Intervals and Overpressure

Miocene thin (~10 to 85 m) and low-permeability carbonate intervals (e.g., Kauhauroa, Kiakia, Tahaenui, and the carbonate layer of the Tuhara Formation) act as overpressure seals in the ECB. Burgreen-Chan et al. (2016) also mentioned the possibility of these thin intervals acting as seals but highlighted that the seal integrity could fail due to the thinness of these intervals and the high overpressure encountered in the ECB.

These intervals were first identified on sonic and density well logs and investigated with the 1D geomechanical models. The porosity-permeability relationship used in the 1D models for these intervals was created from the classical Kozeny-Carmen relationships. This relationship is 10 times lower than the porosity-permeability relationship used for the shale lithology (Figure 3.18a).

These low-permeability intervals are located at different depths in each well. For instance, in the Opoho-1 and Tuhara-1 wells, these low-permeability intervals are located above ~740 m depth, while

in the Opoutama-1 well, these intervals were eroded or not deposited. In the wells Awatere-1 and Kiakia-1, these intervals are located between ~2,000 and ~2,300 m depth.

High pore pressure data were registered below these low-permeability intervals in the Awatere-1 and Kiakia-1 wells. Equivalent results were obtained with the 1D hydro-mechanical models of these two wells (Figure 3.22b and Figure 3.23b). Although in the Awatere-1 well, the pore pressure generated through the geomechanical models and the data registered almost reaches lithostatic values to cause the seals to fail by pore pressure reaching the minimum stress, the high pore fluid pressures registered show that these thin intervals located up to ~2,300 m depth can act as overpressure seals.

3.7.4.2 Mudstone Intervals and Overpressure

In the ECB, packages of mudstones deposited during the Miocene have been identified to be hydrocarbon seals due to their low-permeability properties (Field et al., 1997; Davies et al., 2000). In the analysed wells, the thicknesses of these Miocene mudstones are variable (e.g., Pindari Mdst. from ~990 to ~230 m, Waingaromia Mdst. from 0 to ~485 m, and Tangihau Mdst. from 0 to ~125 m), and while there is no clear relationship between these intervals and the exact point where overpressure begins, a slight influence on overpressure preservation is observed through the 1D models that investigated disequilibrium compaction (Figure 3.19b, 3.20b, 3.21b, 3.22b, and 3.23b).

The integrity of these intervals has been investigated by Darby (2002), concluding that the Miocene mudstone seals could be compromised when pore pressure reached lithostatic values at the highest point of geological structures. This study did not directly investigate seal integrity, but the stress paths obtained from the geomechanical models of two lithologies were used to conclude that the Wheao Formation (shale lithology) and Weber Formation (smectite-rich interval) did not reach the yield surface on the dilatation shear side (left side of the critical state) (for reference Figures 3.28, 3.29, and 3.30). These results are based on the assumption that there are no diagenetic processes but a tectonic shortening of 8%. However, if a higher horizontal shortening were applied (e.g., 12%) for a long period, these two formations could experience more compaction, reaching the yield surface on the dilatation share side of the critical state line, which would degrade seal integrity.

3.7.5 Content of Smectite and Overpressure in the ECB

Smectite clay diagenesis was identified to not have any contribution to the present-day overpressure in the ECB, although this overpressure mechanism has been identified to contribute to overpressure generation in other basins (e.g., Powers, 1967; Bruce, 1984; Dutta, 1987; Audet, 1996; Osborne and Swarbrick, 1997; Lahann, 2002). In the ECB, the Wanstead and Weber Formations have been identified to be great seals due to the content of smectite clays (low petrophysical properties) (Mondol et al., 2008; Beloborodov et al., 2019) and not due to the smectite clay diagenesis (Field et al., 1997).

The temperature when this process starts has been determined to be above ~70 °C (Dutta, 1987; Lahann and Swarbrick, 2011). However, the depth at which this process begins depends on the geothermal gradient. The ECB is a cold basin with a geothermal gradient of ~23 °C/km (Funnell et al., 1999), similar to the Pegasus Basin due to the subduction of a cold crust and high sedimentation

rates (Kroeger et al., 2015). Based on the 23 °C/km geothermal gradient, the depth at which smectite transformation could begin in the ECB is at ~2,800 m depth. In the study area, only two wells reach the formations with smectite content: the Opoutama-1 and Opoho-1 wells. In the Opoutama-1 well, the sedimentation thickness calculated for the Wanstead and Weber Formations was 639 and 328 m respectively, with the formations deposited during the Eocene and Oligocene. A thickness of 2,780 m was calculated to have been deposited above these formations over 16.37 Ma (Early Miocene to Late Miocene) and from that thickness, 1,710 m was eroded during the Early Pliocene to the present-day. The Opoho-1 well only reached the Weber Formation, and the sedimentation thickness calculated was 354 m, deposited during the Oligocene. A thickness of 3,570 m was calculated to be deposited above this formation over 18.7 Ma (Early Miocene to Middle Pliocene), and from that thickness, 640 m were eroded during the Pleistocene.

According to the depths calculated, the Weber and Wanstead Formations in these two wells did not reach the depth or temperature required to begin the smectite to illite transformation. Similar conclusions were suggested in the well reports of these wells and other studies (e.g., Darby and Funnell, 2001; Burgreen-Chan et al., 2016).

3.8 Summary and Conclusions

In the ECB and similar basins with complex geological histories, simple approaches such as log-based analysis or measured pressure interpretation are insufficient to identify when and for how long overpressure mechanisms have acted and the parameters needed to maintain this overpressure through time.

2D and 3D hydro-geomechanical models are required to fully evaluate assessments of porosity and pore pressure histories in geologically complex regions. However, as there is a large amount of uncertainty in the geological history, structural development, and material property evolution, the calibration of these models is a challenging task, making this approach impractical. Nonetheless, in the present work, it has been demonstrated that adopting some necessary simplifications in modelling can provide valuable insights into pore pressure development and overpressure dissipation that are not available otherwise.

This study shows that 1D models are an effective tool for testing pore pressure generation hypotheses and gaining a better understanding of the influence of geological histories on pore pressure evolution. Such models capture the importance of individual pore pressure generation mechanisms with a manageable array of input parameters and a practical computational timeframe. In contrast, these simplifications could also result in slight mismatches between the model results and the observed data.

Significant findings from this study include the way in which erosion reduces pore fluid pressure due to the mechanical unloading of the overburden, leading to an increase in elastic porosity, and the flow-driven dissipation of overpressure during a period of erosion. Whilst erosive events are important in terms of understanding the evolution of the basin, only the latest events (e.g., from

Pliocene to Holocene in the ECB or erosive events within 5 Ma) have an effect on present-day pore pressure and porosity.

This research also shows the importance of tectonic compression on pore pressure, demonstrating that the higher the horizontal shortening (12.5%), the higher the pore pressure generated. In addition, results from the 1D hydro-mechanical models also suggested that recent tectonic compression (e.g., ~5.6 Ma in the ECB wells) has a greater impact on porosity reduction and overpressure generation.

The present-day overpressure in the ECB can be mainly attributed to Pliocene to Pleistocene tectonic compression. In addition, disequilibrium compaction played a role in the overpressure generation in this basin; it generated relatively minor overpressures during sedimentation (<3 MPa at 2,000 m depth), which were constantly dissipating during erosive events and hiatus periods (~ 6 erosive events during the Early Miocene to present-day and at least two hiatus periods during the Pliocene to present-day). When porosity was reduced due to mechanical loading, these low values resulted in high overpressures when tectonic compression began once more.

Compartmentalisation is a key factor in the ECB overpressure distribution, as different overpressure values can be generated along the sedimentary column at each well location. The spatial overpressure distribution in the ECB is controlled by regional and local faults, low-permeability intervals, and lateral pressure drainage.

The high pore pressure values encountered from shallow depths (>300 m) in the ECB are not related to any formation, lithology, time, or specific depth. However, overpressure is present below mudstone (e.g., Pindari, Tangihau, and Waingaromia Mdst.), smectite-rich (e.g., Wanstead and Weber Formations), and thin low-permeability intervals (Tahaenui, Kiakia, Kauhauroa, and Tuhara Lm.) that have not experienced lateral flow drainage due to exposure to the surface.

Results from the 1D hydro-mechanical models constructed for the ECB key wells show that different overpressure values can be generated along the sedimentary column of each well location. Therefore, a sole percentage value per pore pressure-generating mechanism is simplistic. In summary, using values taken from each well location at 2,000 m depth, tectonic compression is found to have contributed to overpressure generation by 8 to 16 MPa, while disequilibrium compaction contributed by adding 1 to 3 MPa.

The present-day overpressures of the ECB can also be influenced by other mechanisms that were not investigated in this research (e.g., clay diagenesis of deeper layers, lateral transfer from deep intervals, and gas generation), and those should be considered in further research, especially in complex tectonically active basins.

3.9 Appendix

3.9.1 Formations Description

The description of each formation was obtained from well reports and other studies performed in the area (e.g., NZ Aquitaine Petroleum Ltd., 1967; Field et al., 1997; Brown, 1998 and 1999; well reports).

The names of the formations used in this research are the most common names registered in the wells located in the studied area (Figure 3.2).

The Wairoa Formation consists of thin intercalations of siltstone and very fine sandstone lithologies. The grains are well sorted, from subangular to subrounded. There are shell fragments and carbonaceous material in some intervals.

The Tahaenui Limestone has been described as barnacle coquina limestone deposited on a regional angular unconformity at approximately 40 m depth (Turner, 1989). From well samples, this formation has been described as bryozoan limestone with calcite cement, recrystalised fragments of bivalve, and sand grains. In some wells, traces of glauconite are present. This formation has poor petrophysical properties (e.g., low porosity and permeability).

The Opoti Formation contains a high percentage of siltstone lithologies; the base has more intercalations of claystone with a higher percentage of calcareous material, while the top has more intercalations of sandstone and claystone lithologies with well-sorted sand grains and few shell fragments. Poor visible porosity has been observed on well samples of this formation.

The Tuhara Formation starts with a high content of claystone and siltstone layers and a few shell fragments with scarce calcite cement at the base, followed by sandy limestone. On top of this sequence, an increase in limestone content is observed in all the well samples. The porosity is variable throughout this formation, with good values at the base and poor values at the top.

The Poha Formation consists of a yellow-green siltstone succession with intercalations of claystone and sandstone lithologies. The sandstone grains are well sorted, with angular to subrounded shapes. This formation has calcite cement, traces of glauconite, and shell fragments in the whole interval. Few intercalations of coal are observed in the sandstone lithologies.

The Pindari Mudstone is an interbedded sequence of moderately calcareous silty claystone with few intercalations of very fine sandstone. Traces of glauconite and very hard black cherts have been described in this formation.

The Makareao Sandstone consists of fine to very fine intercalations of sandstone and siltstone lithologies, well sorted, and with sub-angular to subrounded grains. Good porosity values have been determined in some core samples (e.g., 18.9 to 28%).

The Kiakia Limestone is composed of a strongly cemented bryozoan grainstone with recrystallised bivalve and scarce stylolites. There is no visible porosity; however, there are some fractures that have been interpreted to have secondary porosity. This formation was deposited over a regional unconformity. These carbonates were deposited nearshore at approximately 40 m depth (Turner, 1989).

The Tangihau Mudstone has a dark green colour and consists of silty claystone lithologies with thin intercalations of sandy siltstone lithologies and scarce calcite cement. The grains are well sorted from subangular to round shapes. Although this formation does not present visible porosity, loose sand is suggested to have high porosity.

The Tunanui Sandstone consists of intercalations of sandstone, siltstone, and claystone lithologies. The thickness of this formation is variable in the ECB (e.g., 0 to >1,000 m). The sandstone is frequently light grey, very fine-grained, with rare calcite cement. It is also well sorted, with angular to subangular grains.

The Waingaromia Mudstone has a green colouration with rare planktic foraminifera and some calcareous material. Its characteristics are similar to those of the Tangihau Mudstone, which has been described as being deposited afterwards.

The Rere Sandstone presents intercalations of sandstone and claystone lithologies with a grey colour. The sandstone is fine to very fine-grained, well-sorted, with subangular to subrounded grains and rare calcite cement. The thickness of this formation in the studied area is variable (e.g., 0 to 30 m).

The Kauhauroa Limestone has similar characteristics to the Kiakia and Kauhauroa Limestones. This formation consists of strongly cemented bryozoan with fragments of echinoderms, foraminifers, and mollusks (Turner, 1989). This limestone is bound by unconformities at the top and the base.

The Wheao Formation consists of intercalations of claystone lithologies and thin sand layers. At the top of this formation, layers of tuff lithologies have been described in well samples. The sandy layers contain glauconite.

The Weber Formation varies vertically and horizontally in the ECB. In some areas, this formation is moderately hard and bioturbated with calcareous mudstone lithologies, while in other areas, it has intercalations of sandstone and glauconitic limestones. Smectite content has been identified in this formation in some areas (Hines et al., 2013; McArthur et al., 2020). The thickness of this formation varies along the ECB (e.g., from 30 to 900 m).

The Wanstead Formation has been interpreted to be deposited from the mid-bathyal to the lower bathyal-abyssal in some regions. This formation has a variable thickness (e.g., from 100 to 300 m) in the ECB and consists of fine-grained calcareous sediments with intercalations of mudstone, siltstone, and sandy mudstones. The amount of smectite is variable, with an increase up to ~41% of $CaCO_3$ in certain areas (Lillie, 1953; Haskell, 2005), while in others this formation has more intercalations of bentonite (J. A. R., 1985; Simpson et al., 1993).

The Whangai Formation has intercalations of grey green to dark-grey silty micaceous mudstones, siltstones, and argillites with abundant fine plant remains. This formation has organic matter of up to 1.5% in some intervals.

The Mata-Raukumara Formation is Cretaceous and has been named differently depending on the place of its description. For this study, the name of this formation was taken from the well Opoutama-1, which is the only well that crosses this formation in the studied area. This formation consists of intercalations of mudstone, siltstone, and sandstone lithologies. In core data, ripple lamination, flaser structures, and micro-load cast structures have been identified. There is evidence of plant remains in the fine sandstones and Inoceramus fragments in several intervals along the core. Fractures are described throughout the core, with some calcite cement in some of them.

3.10 References

Ansell, J. H. and Bannister, S. C. (1996). Shallow morphology of the subducted Pacific plate along the Hikurangi margin, New Zealand, *Physics of the Earth and Planetary Interiors*, 93, 3-20.

Audet, S. M. (1996). Compaction and overpressuring in Pleistocene sediments on the Louisiana Shelf, Gulf of Mexico, *Marine and Petroleum Geology*, *13*(5), 467-474.

Athy, L. F. (1930). Density, porosity, and compaction of sedimentary rocks. *AAPG Bulletin*, 14(1), 1-24.

Bailey, W. McArthur, A., McCaffrey, W. (2021). Sealing potential of contourite drifts in deep-water fold and thrust belts: Examples from the Hikurangi Margin, New Zealand, *Marine and Petroleum Geology*, 123, 1-13.

Ballance, P. F. (2017). *New Zealand Geology: an illustrated guide*. *Geoscience Society of New Zealand.* Available at: https://www.geotrips.org.nz/downloads.html#:~:text=New%20Zealand%20geology%3A%20an%20illustrated%20guide%20by%20Peter,by%20GNS%20Science%2C%20as%20stated%20in%20the%20captions (Accessed: 03 April 2021).

Bailleul, J., Robin, C., Chanier, F., Guillocheau, F., Field, B. and Ferrière, J. (2007). Turbidite systems in the inner forearc domain of the Hikurangi convergent margin (New Zealand): New constraints on the development of the trench-slope basins, *Journal of Sedimentary Research*, 77, 263-283.

Bailleul, J., Chanier, F., Ferrière, J., Robin, C., Nicol, A., Mahieux, G., Gorini, C. and Caron, V. (2013). Neogene evolution of lower trench-slope basins and wedge development in the central Hikurangi subduction margin, New Zealand, *Tectonophysics*, 591, 152-174.

Barnes, P. M. (1997). Rates and mechanics of rapid frontal accretion along the very obliquely convergent southern Hikurangi margin, New Zealand, *Journal of Geophysical Research,*102(B11), 24,931-24,952.

Barnes, P. M., et al. (2010). Tectonic and geological framework for gas hydrates and cold seeps on the Hikurangi subduction margin, New Zealand, *Marine Geology,* 272, 26-48.

Beloborodov, R., Pervukhina, M., Lebedev, M. and Hauser, J. (2019). Assessing mineral composition and permeability of a shale seal, *ASEG Extended Abstracts*,1, 1-5.

Bour, O., Lerche, I. and Grauls, D. (1995). Quantitative models of very high fluid pressure: the possible role of lateral stresses, *Terra Research*, 68-79.

Burgreen, B. and Graham, S. (2014). Evolution of a deep-water lobe system in the Neogene trench-slope setting of the East Coast Basin, New Zealand: Lobe stratigraphy and architecture in a weakly confined basin configuration, *Marine and Petroleum Geology*, 54, 1-22.

Burgreen-Chan, B., Meisling, K. E. and Graham, S. (2016), Basin and petroleum system modelling of the East Coast Basin, New Zealand: a test of overpressure scenarios in a convergent margin, *Basin Research*, 28, 536-567.

Bredehoeft, J. D. and Hanshaw, B.B. (1968). On the Maintenance of Anomalous Fluid Pressures: Thick Sedimentary Sequences, *Geological Society of America Bulletin*, 79, 1097–1106.

Brown, B. R. (1960). *Mangaone-1.* Unpublished open-file report PR320, Ministry of Economic Development, Wellington, New Zealand.

Brown, I. R. (1998). *Opoho-1 Well Completion Reports, PEP 38329*, Unpublished open-file report PR2414, Ministry of Economic Development, Wellington, New Zealand.

Brown, I. R. (1998). *Kiakia-1/-1A well completion report, PEP 38329*, Unpublished open-file PR2381, Ministry of Economic Development, Wellington, New Zealand.

Brown, I. R. (1998). *Tuhara-1 Well Completion Report, PEP 38329*, Unpublished open-file PR2401, Ministry of Economic Development, Wellington, New Zealand.

Brown, I. R. (1999). *Awatere-1 well completion report*, Unpublished open-file PR2365, Ministry of Economic Development, Wellington, New Zealand.

Brown, I. R. (2002). *The Kehe, Koheru and Hiwihiwi Prospects, PEP38325 and 38326 offshore Hawke Bay, East Coast Basin, New Zealand*, Unpublished open-file PR2939, Ministry of Economic Development, Wellington, New Zealand.

Butler, R. W. H. and Paton, D. A. (2010). Evaluating lateral compaction in deepwater fold and thrust belts: How much are we missing from “nature’s sandbox”?, *GSA TODAY*, *20*(3), 1-10.

Bruce, C. H. (1984). Smectite Dehydration – Its Relation to Structural Development and Hydrocarbon Accumulation in Northern Gulf of Mexico Basin, *AAPG Bulletin,* 68, 673-683.

Campbell, K., Francis, D. A., Collins, M., Gregory, M. R., Nelson, C. S., Grenert, J. and Aharon, P. (2008). Hydrocarbon seep-carbonates of the Miocene forearc (East Coast Basin), Noth Island, New Zealand, *Sedimentary Geology,* 204, 83-105.

Claussmann, B., Bailleul, J., Chanier, F., Caron, V., McArthur, A. D., Mahieux, G., Chaptal, C. and Vendeville, B. C. (2021). Contrasting mixed siliciclastic-carbonate shelf-derived gravity-driven systems in compressional intra-slope basins (southern Hikurangi margin, New Zealand), *Marine and Petroleum Geology*, 134, 1-31.

Couzens-Schultz, B. A. and Azbel, K. (2014). Predicting pore pressure in active fold-thrust systems: An empirical model for the deepwater Sabah foldbelt. *Journal of Structural Geology*, 69, 465-480.

Crook, A. J. L., Obradors-Prats, J., Somer, D., Peric, D., Lovely, P. and Kacewicz, M. (2018). Towards an integrated restoration/forward geomechanical modelling workflow for basin evolution prediction. Oil and Gas Science and Technology - Rev. *IFP Energies Nouvelles*, 73, 1-19.

Dalton, T. J. S. Paton, D. A., Needham, T. and Hodgson, N. (2015). Temporal and spatial evolution of deepwater fold thrust belts: Implications for quantifying strain imbalance Interpretation, G*eoScienceWorld*, 3(4), 59-70.

Darby, D. and Ellis, S. (2001). Evaluating overpressure in Compressional Regimes using Geomechanical Modelling, *Petroleum Exploration Society of Australia*, 613-620.

Darby, D. and Funnell, R. H. (2001). Overpressure associated with a convergent plate margin: East Coast Basin, New Zealand. *Petroleum Geoscience*, 7, 291-299.

Darby, D. (2002). Seal properties, overpressure and stress, in the Taranaki and East Coast Basins, New Zealand, Conference Proceedings, 24-27 February.

Darby, D. And Ellis, S. (2003). Contrasting pressure in sedimentary basins associated with a plate boundary, New Zealand, *Journal of Geochemical Exploration*, 78-79, 149-152.

Davies, E. J., Frederick, J. B., Leask, W. L. and Williams, T. J. (2000). *East Coast drilling results*, in Proceedings of the 2000 New Zealand Petroleum Conference, 19-22 March.

Dutta, N. C. (1987). Shale compaction, burial diagenesis, and geopressures: a dynamic model, solution, and some results, in Burrus, J. (ed.) *Thermal Modeling in Sedimentary Basins.* Paris, 149-172.

Eiby, G. A. (1968) An Annotated List of New Zealand Earthquakes, 1460-1965, *New Zealand Journal of Geology and Geophysics*, 11(3), 630-647.

Erdi, A., Huuse, M. and Bachtiar, A. (2018). Tectonic Evolution and Hydrocarbon Prospectively of East Coast Basin, Offshore Hawke Bay, New Zealand, *Offshore Technology Conference*, 1-18.

Fergusson, L. J. (1985). The mineralogy, geochemistry and origin of lower Tertiary smectite-mudstones, East Coast Deformed Belt, New Zealand. MSc. University of Canterbury.

Field, B. D., Uruski, C. I. and others (1997). Cretaceous-Cenozoic Geology and Petroleum System of the East Coast Region, New Zealand. *Institute of Geological and Nuclear Sciences monograph*, 19, p. 301.

Funnell, R., Chapman D., Allis, R. and Armstrong, P. (1996). Thermal state of the Taranaki Basin, New Zealand, *Journal of Geophysical Research*, 101,197-215.

Funnell, R., H, R., Wood, R. A., Stagpoole, V. M, Uruski, C., Scadden, P., Killops, S. d., Cutress, G., Field, B. D. and Nicol, A. (1999). *Thermal and hydrocarbon generation modelling of Hawke Bay area (PEP38325, 38326, 38329)*, Unpublished open-file PR4311, Ministry of Economic Development, Wellington, New Zealand.

Funnell, R. and Benchilla, L. (2005). *1D Basin Models in the East Coast Basin*, *New Zealand*, Unpublished open-file PR3183, Ministry of Economic Development, Wellington, New Zealand.

Ge, S. and Garven, G. (1992) Hydromechanical Modeling of Tectonically Driven Groundwater Flow with Application to the Arkona Foreland Basin, *Journal of Geophysical Research,* 97(B6), 9119-9144.

GEBCO Gridded Bathymetry Data. (Available at: https://www.gebco.net/data_and_products/gridded_bathymetry_data/ .(Accessed; 05 May 2021).

Gisborne Oil Co. (1910). *Waitangi-1*, Unpublished open-file PR215, Ministry of Economic Development, Wellington, New Zealand.

GNS New Zealand Crown Research Institute. Available at: Home - GNS Science . (Accessed; 20 November 2020).

Hansen, S. (1996). A compaction trend for Cretaceous and Tertiary shales on the Norwegian Shelf based on sonic transit times. *Petroleum Geoscience*, 2, 159-166.

Hantschel, T. and Kauerauf, A. I. (2009). *Fundamentals of basin and petroleum systems modeling.* Aachen, Germany: Springer.

Hart, B. S., Flemings, P. B. and Desphpande, A. (1995). Porosity and pressure: Role of compaction disequilibrium in the development of geopressures in a Gulf Coast Pleistocene basin. *AAPG Bulletin*, 23, 45-48.

Harrison, W. J. and Summa, L. L. (1991). Paleohydrology of the Gulf of Mexico Basin, *American Journal of Science*, 291, 109-176.

Haskell, T. R. (2005). *Development of Definition of Petroleum System used in Exploration Work in the East Coast Basin, New Zealand*, Unpublished open-file PR3178, Ministry of Economic Development, Wellington, New Zealand.

Hines, B. R., Kulhanek, D. K., Hollis, C. J., Atkins, C. B. and Morgans, H. E. G. (2013). Paleocene- Eocene stratigraphy and paleoenvironment Tora, Southeast Wairarapa, New Zealand, *Journal of Geology and Geophysics*, 56(4), 243-262.

Issler, D. R. (1992). A new approach to shale compaction and the stratigraphic restoration, Beaufort-Mackenzie Basin and Mackenzie Corridor, Northern Canada. *AAPG Bulletin*, 76(8), 1170-1189.

J. A. R. (1985). *East Coast Oil Exploration Ltd. NZ, New Zealand*, Unpublished open-file PR1086, Ministry of Economic Development, Wellington, New Zealand.

Jiao, R., Herman, F. and Seward, D. (2017). Late Cenozoic exhumation model of the New Zealand: Impacts from tectonics and climate, *Earth-Science Reviews*, 166, 286-298.

Kroeger, K. F., Plaza-Faverola, A., Barnes, P. M. and Pecher, I. A. (2015). Thermal evolution of the New Zealand Hikurangi subduction margin: Impact on natural gas generation and methane hydrate formation - A model study, *Marine and Petroleum Geology*, 63, 97-114.

Killops, S.D., Woolhouse, A.D., Weston, R.J. and Cook, R.A., (1994). A geochemical appraisal of oil generation in the Taranaki Basin, New Zealand. *AAPG Bulletin*, 78, 1560-1585.

Lahann, R. W. (2002). Impact of Smectite Diagenesis on Compaction Modeling and Compaction Equilibrium, in Huffman, A. R. and Bowers, G. L. (eds.), *Pressure regimes in sedimentary basins and their prediction*: AAPG Memoir, 76, 61–72.

Lahann, R. W. and Swarbrick, R. E. (2011). Overpressure generation by load transfer following shale framework weakening due to smectite diagenesis. *Geofluids*, 11, 362-375.

Lewis, K. B. and Kohn, B. P. (1973). Ashes, turbidites, and rates of sedimentation on the continental slope off Hawes Bay, *New Zealand Journal of Geology and Geophysics*, 16(3), 439-454.

Lewis, K. B. (1980). Quaternary sedimentation on the Hikurangi oblique-subduction and transform margin, New Zealand, in Balance, P. F. and Reading, H. G. (eds.) *Sedimentation in Oblique-Slip Mobile Zones,* Special Publication, 171-189.

Lewis, K. B., Collot, J. and Lallemand, S. E. (1998). The dammed Hikurangi Trough: a channel-fed trench blocked by subducting seamounts and their wake avalanches (New Zealand-France GeodyNZ Project), *Basin Research*, 441-468.

Lillie, A. R. (1953). The Geology of the Dannevirke Subdivision, *New Zealand Geological Survey*, 46, 1-153.

Longman, M. W. (1998). Petrographic Study of the Upper Miocene Limestone and Associated Siliciclastic rocks, Hawkes Bay Area, New Zealand, Unpublished open-file PR2365, Ministry of Economic Development, Wellington, New Zealand.

Luo, X. and Vasseur, G. (1992). Contributions of Compaction and aquathermal Pressuring to Geopressure and the Influence of Environmental Conditions, *AAPG Bulletin*, 76, 1550-1559.

Martin, K. R. (1995). Petrology of reservoir formations in PPL 38316 and PPP 38324, Western and Northern Hawkes Bay, East Coast Basin, New Zealand, Unpublished open-file PR2556, Ministry of Economic Development, Wellington, New Zealand.

McArthur, A. D., Claussmann, B., Bailleul, J., Clare, A. and McCaffrey, W. D. (2020). Variation in syn-subduction sedimentation patterns from inner to outer portions of deep-water fold and thrust belts: examples from the Hikurangi subduction margin of New Zealand, in Hammerstein, J. A., DiCuia, R., Cottam, M. A., Zamora, G. and Butler, R. W. H. (eds.) *Fold and Thrust Belts: Structural Style, Evolution and Exploration.* London: Special Publication, 285-310.

Mondol, N. H., Bjørlykke, K., Jahren, J. and Høeg, K. (2008). Experimental mechanical compaction of clay mineral aggregates-Changes in physical properties of mudstones during burial, *Marine and Petroleum Geology*, 24, 289-311.

Moore, P. R. and Speden, I. (1979). Stratigraphy, structure, and inferred environments of deposition of the Early Cretaceous sequence, eastern Wairarapa, New Zealand, *New Zealand Journal of Geology and Geophysics*, 22(4), 417-433.

Mortimer, N. (2004). New Zealand's Geological Foundations, *Gondwana Research*, 7(1), 261-272.

Neef, G. (1992). Turbidite deposition in five Miocene bathyal formations along an active plate margin, North Island, New Zealand: with notes on styles of deposition at the margins of the east coast bathyal basins, *Sedimentary Geology*, 78, 111-136.

Neuzil, C.E. and Pollock, D.W. (1983). Erosional unloading and fluid pressures in hydraulically tight rocks, *Journal of Geology*, 91, 179-193.

Newman, J. and Moore, N. (2000). *Vitrinite-Inertite Reflectance and Florescence Analysis of Samples from Opoutama-1*, Unpublished open-file PR2582, Ministry of Economic Development, Wellington, New Zealand.

Nicol, A., VanDissen, R., Vella, P., Alloway, B. and Melhuish, A. (2002). Growth of contractional structures during the last 10 m.y. at the southern end of the emergent Hikurangi forearc basin, New Zealand, *New Zealand Journal of Geology and Geophysics*, 45(3), 365-385.

Nunn, J. A. (2012). Burial and Thermal History of the Haynesville Shale: Implications for Overpressure, Gas Generation, and Natural Hydrofracture, *Gulf Coast Association of Geological Societies*, 1, 81-96.

NZ Aquitaine Petroleum Ltd. (1967). *Opoutama-1 well report*, Unpublished open-file PR504, Ministry of Economic Development, Wellington, New Zealand.

NZPAM New Zealand Petroleum and Mine Online Exploration Database. Available at: https://data.nzpam.govt.nz/GOLD/system/mainframe.asp . (Accessed; 05 October 2020).

Obradors-Prats, J., Rouainia, M., Aplin, A. C. and Crook, A. J. L. (2017a). Assessing the implications of tectonic compaction on pore pressure using a coupled geomechanical approach. *Marine and Petroleum Geology*, 79, 31-43.

Obradors-Prats, J., Rouainia, M., Aplin, A. C. and Crook, A. J. L. (2017b). Hydromechanical modeling of stress, pore pressure, and porosity evolution in fold-and-thrust belt systems. *Journal of Geophysical Research: Solid Earth*, 122(11), 9383-9403.

Osborne, M. J. and Swarbrick, R. E. (1997). Mechanisms for Generating Overpressure in Sedimentary Basins: A Reevaluation, *AAPG Bulletin*, 81, 1023-1041.

Palciauskas, V. V. and Domenico, P. A. (1989). Fluid Pressures in Deforming Porous Rocks, *Water Resources Research*, 25(2), 203-213.

ParaGeo. Available at: www.parageo.co.uk

Pedley, K. L., Barnes, P. M., Pettinga, J. R. and Lewis, K. B. (2010). Seafloor structural geomorphic evolution of the accretionary frontal wedge in response to seamount subduction, Poverty Indentation, New Zealand, *Marine Geology*, 270, 119-138.

Petrel. Available at: www.software.slb.com/products/petrel

Phillips Petroleum New Zealand (1976). *Philip's geomechanical reports, New Zealand*, Unpublished open-file PR737, Ministry of Economic Development, Wellington, New Zealand.

Plaza-Faverola, A., Klaeschen, D., Barnes, P., Pecher, I., Henrys, S. and Mountjoy, J. (2012). Evolution of fluid expulsion and concentrated hydrate zones across the southern Hikurangi subduction margin, New Zealand: An analysis from depth migrated seismic data, *Geochemistry, Geophysics, Geosystems*, 13, 1-21.

Powers, M. C. (1967). Fluid-Release Mechanisms in Compacting Marine Mudrocks and their Importance in oil Exploration, *AAPG Bulletin*, 51(7), 1240-1254.

Raine, J. I., Beu, A. G., Boyes, A. F., Campbell, H. J., Cooper, R. A., Crampton, J. S., Crundwell, M. P., Hollis, C. J., Morgan, H. E. G. and Mortimer, N. (2015). New Zealand Geological Timescale NZGT, New Zealand *Journal of Geology and Geophysics*, 58(4), 398-403.

Reyners, M. (2013). The central role of the Hikurangi Plateau in the Cenozoic tectonics of the New Zealand and the Southwest Pacific, *Earth and Planetary Science Letters*, 361, 460-468.

Ridd, M. F. (1970). Mud Volcanoes in New Zealand, *The American Association of Petroleum Geologist Bulletin*, 54, 601-616.

Rogers, K. M., Collen, J. D., Johnston, J. H. and Elgar, N. E. (1999). A geochemical appraisal of oil seeps from the East Coast Basin, New Zealand, *Organic Geochemistry*, 30, 593-605.

Rogers, K. M., Morgans, H. E. G. and Wilson, G. S. (2001). Identification of a Waipawa Formation equivalent in the upper Te Uri Member of the Whangai Formation - implications for depositional history and age, *New Zealand Journal of Geology and Geophysics*, 44(2), 347-354.

Schneider, F. Potdevin, J. L., Wolf, S. and Faille, I. (1996). Mechanical and chemical compaction models for sedimentary basin simulators, *Tectonophysics*, 263, 307-317.

Skempton, A. W. (1970). The consolidation of clays by gravitational compaction, *Quarterly journal of the Geological Society*, 125, 373-411.

Sibson, R. H. and Rowland, J. V. (2003). Stress, fluid and structural permeability in seismogenic crust, North Island, New Zealand, *Geophysics*, 154, 584-594.

Simpson, Jeremy and Jarvis, J. (1993). *Technical review of the East Coast Basin, New Zealand*, Unpublished open-file PR1972, Ministry of Economic Development, Wellington, New Zealand.

Sloss, C. R., Tillquist, S., McGill, S., Penny, Y., Ballington, C., Nothdurft, L. Trofimovs, J., Lawrence, M. J. and Schrank, C. E. (2021). Sedimentology and stratigraphy of syn-subduction Miocene fine-grained turbidites deposited in first stages of trench-slope basin development: Whakataki Formation, North Island, New Zealand, *Sedimentary Geology*, 414, 1-13.

Swarbrick, R. E. and Osborne, M. J. (1998). Mechanisms that Generate Abnormal Pressures: An Overview, in Law, B. E., Ulmishek G. F. and Slavin, V. I. (eds.) *Abnormal pressures in hydrocarbons environments.* AAPG Memoir 70, 13-34.

Swarbrick, R. E. and Hillis, R. R. (1999). The Origin and Influence of Overpressure with Reference to the North West Shelf, Australia, *The APPEA Journal*, 39, 64-72.

Swarbrick, R. E., Osborne, M. O. and Yardley, G. S. (2002). Comparison of Overpressure Magnitude Resulting from the Main Generating Mechanisms, in Huffman, A. R. and Bowers, G. L. (eds.) *Pressure regimes in sedimentary basins and their prediction.* AAPG Memoir 76, 1-12.

Tingay, M. R. P., Hillis, R. R., Swarbrick, R. E., Morley, C. K. and Damit, A. R. (2009). Origin of overpressure and pore-pressure prediction in the Baram province, Brunei. *AAPG Bulletin*, 93, 51-74.

Turner, N. L. (1989) *Petrology/Petrography of the Aute Group, North Island, New Zealand*, Unpublished open-file PR1517, Ministry of Economic Development, Wellington, New Zealand.

Uruski, C and Bland, K. (2011). *Pegasus Basin and the Prospect for Oil and Gas,* Unpublished open-file PR4326, Ministry of Economic Development, Wellington, New Zealand.

Walcott, R. I. (1987). Geodetic strain and the deformational history of the North Island of New Zealand during the late Cainozoic, *Phil. Trans. R. Soc.* London, 163-181.

Wallace, L. M., Beavan, J., McCaffrey, R. and Darby, D. (2004). Subduction zone coupling and tectonic block rotations in the North Island, New Zealand, *Geophysics Research*, 109, 1-21.

Wallace, L. M., et al. (2009). Characterizing the seismogenic zone of a major plate boundary subduction thrust: Hikurangi Margin, New Zealand, *Geochemistry, Geophysics, Geosystems*, 10, 1-32.

Wang, B., Qiu, N., Amberg, S., Duan, Y. and Littke, R. (2022). Modelling of pore pressure evolution in a compressional tectonic setting The Kuqa Depression, Tarim Basin, northwestern China, *Marine and Petroleum Geology,* 146, 1-21.

Watters, W. A. (1990). Petrography and Diagenesis of Rocks from Coastal Wairarapa, adjacent to PPL38318 and 38323 East Coast Belt, New Zealand, Unpublished open-file PR1585, Ministry of Economic Development, Wellington, New Zealand.

Watson, J. F. (1962). *Ruakituri-1*, Unpublished open-file PR324, Ministry of Economic Development, Wellington, New Zealand.

Watson, S. J., Mountjoy, J. J., Barnes, P. M., Crutchley, G. J., Lamarche, G., Higgs, B. Hillman, J., Orpin, A. R., Micallef, A., Neil, H., Mitchell, J., Pallentin, A., Kane, T., Woelz, S., Bowden, D., Rowden, A. A. and Pecher, I. A. (2019). Focused fluid seepage related to variations in accretionary wedge structure, Hikurangi margin, New Zealand, *The Geological Society of America*, 48, 56-61.

Wyllie, M. R. J., Gregory, A. R. and Gardner, L. W. (1956). Elastic wave velocities in heterogeneous and porous media. *Geophysics*, 21, 41-70.

Yang, Y. and Aplin, A. C. (2007). Permeability and petrophysical properties of 30 natural mudstones, *Journal of Geophysical Research*, 112, B03206.

Yang, Y. and Aplin, A. C. (2010). A permeability-porosity relationship for mudstones, *Marine and Petroleum Geology*, 27, 1692-1697.

Yassir, N. and Addis, M. A. (2002). Relationships between Pore Pressure and Stress in Different Tectonic Settings, in Huffman, A. R. and Bowers G. L. (eds.) *Pressure regimes in sedimentary basins and their prediction*: AAPG Memoir 76, 79–88.

Wood, D. M. (1990). *Soil Behaviour and Critical State Soil Mechanics.* Cambridge University Press: Cambridge, UK.

Chapter 4: Controls of High and Variable Pore Pressure in a Salt-Walled Mini-basin: The Magnolia Field, Gulf of Mexico, USA

*Part of this chapter has a published paper titled "**Integrating Petrophysical, Geological and Geomechanical Modelling to Assess Stress States, Overpressure Development and Compartmentalisation Adjacent to a Salt Wall, Gulf of Mexico**" in the journal Marine and Petroleum Geology, doi.org/10.1016/j.marpetgeo.2023.106352*

The contribution made by Erika Calderon Medina (PhD student) to the paper was 40% and formed part of wider scoping research within the GeoPOP4 research consortium.

Abstract

This chapter represents the study performed in the Magnolia Field, located close to a salt wall of the Titan mini-basin in the Garden Banks area of the continental slope of the Gulf of Mexico, where remarkably high overpressures of up to around 35 MPa are commonly encountered. These high pore pressure values are in sand-silt reservoirs of Pliocene-Pleistocene sediments (~3 Ma ago). High-overpressure sediments represent substantial risk and cost during the exploration and development of hydrocarbon extraction and thermal sites, as well as sites that could potentially be used to store CO_2, H_2, and nuclear waste; therefore, an accurate evaluation is vital.

This research integrated data from wells, seismic cubes, and previous studies to create a 3D static model and 1D and 2D geomechanical models. The models were used to analyse the overpressure mechanisms that have affected these sediments and to highlight the main parameters for pore pressure preservation.

This study suggests that the sedimentary environment (deep-water channel systems) and salt movement contributed to the overpressure compartmentalisation encountered in the Magnolia Field. Salt tectonics has two effects on overpressure in this area: first, it changes the quality of the reservoirs close to the salt wall, reducing the petrophysical properties of the sediments (e.g., small-scale faults and soft sedimentary structures), and second, it contributes to the horizontal compaction in areas close to the salt wall. In addition, lateral pressure transfer of high-permeability units transferred pore pressures generated in deep intervals to shallow intervals located close to the salt wall where the reservoirs of the Magnolia Field were located.

Results from the geological analysis and the geomechanical modelling show that disequilibrium compaction is the main overpressure mechanism due to the mud-dominated lithologies deposited in this basin at high sedimentation rates (>1,600 m/Ma), with a contribution of around 74% of the total overpressure registered in the Magnolia Field. However, salt tectonics and lateral pressure transfer from the deep intervals also played a role in the contribution of the high pore pressure values encountered in the wells of the Magnolia Field, with a contribution of 9% and 16%, respectively.

4.1 Introduction

The focus of this project is to investigate the development of overpressure in the Magnolia Field, located on a flank of the salt-bounded Titan mini-basin in the Gulf of Mexico, where variable high overpressures have been registered along the sedimentary column of twenty-five wells.

The Magnolia Field is located in a cold region (geothermal gradient of 15 to 25 C°/km; Garden Banks; Christie and Nagihara, 2016) of the Gulf of Mexico Basin where sediments have been modified by active salt tectonics. Although the Gulf of Mexico Basin has been studied in depth as it is a hydrocarbon basin, few studies were performed in the Magnolia Field with respect to understanding the reason behind its overpressure (e.g., Eaton et al., 2005; Colwart et al., 2007; Sathar and Jones, 2016). In the Gulf of Mexico, different mechanisms have been linked to be the cause of the overpressure encountered in this basin. However, the extent to which each mechanism contributed has not been properly determined. It has been suggested that disequilibrium compaction is the main overpressure mechanism due to the high sedimentation rate (>1,400 m/Ma; Audet, 1996) of mud-dominated lithology deposited between the Pliocene and present-day (Dickinson, 1953; Bredehoeft and Hanshaw, 1968; Ostermeier et al., 2001; Weissenburger and Borbas, 2004). Tectonic compression related to the horizontal stress generated by salt tectonics (Luo et al., 2017; Nikolinakou et al., 2018) has also been identified as a contributing factor. Liaw et al. (2007) and Kane et al. (2012) highlighted how the salt movement has affected the compartmentalisation of the sedimentary column (e.g., faulting, uplifting, slumping, and rotation of the layers). The third mechanism identified is lateral pressure transfer, which is related to the high permeability of well-connected layers from deep intervals to shallow depths (Heidari et al., 2019).

As disequilibrium compaction, tectonic compression due to salt wall growth, and lateral pressure transfer have been suggested as the main overpressure mechanisms acting in the Magnolia Field, this project aims to investigate and quantify the contribution of each mechanism to the registered overpressure. To achieve this goal, a geological assessment that consisted of 3D seismic interpretation, well-correlation, lithofacies interpretation, and 3D static model construction and characterisation was performed to provide a robust geological understanding of the area. A well-log interpretation focused on the identification of the overpressure mechanisms was also conducted, and the results were compared to overpressures predicted using 1D and 2D hydro-mechanical models. The factors that resulted in the overpressure variability of the Magnolia Field are also presented.

4.1.1 Magnolia Field and Gulf of Mexico Geological Background

The Magnolia Field is a decommissioned gas field located in blocks 783 and 784 in the Titan mini-basin of the Garden Banks area of the continental slope of the Gulf of Mexico. The water depth at the location of the field is 1,425 m (~4674 ft) (Stomp et al., 2004; Eaton et al., 2005; Colwart et al., 2009). The Magnolia Field has a sedimentary column of Miocene to Pleistocene sediments that vary across the Titan mini-basin from ~11,582 m (~38,000 ft) at the depocenter (blocks 695 and 696) to between ~2,440 and ~3,660 m (8,000 and 12,000 ft) at the Magnolia Field (Weissenburger and Borbas, 2004) (Figure 4.1). From these sediments, nineteen sand-silt intervals were targeted for

production. Reservoir B-25 was chosen to investigate overpressure development during this study as more data were available (Figure 4.2b).

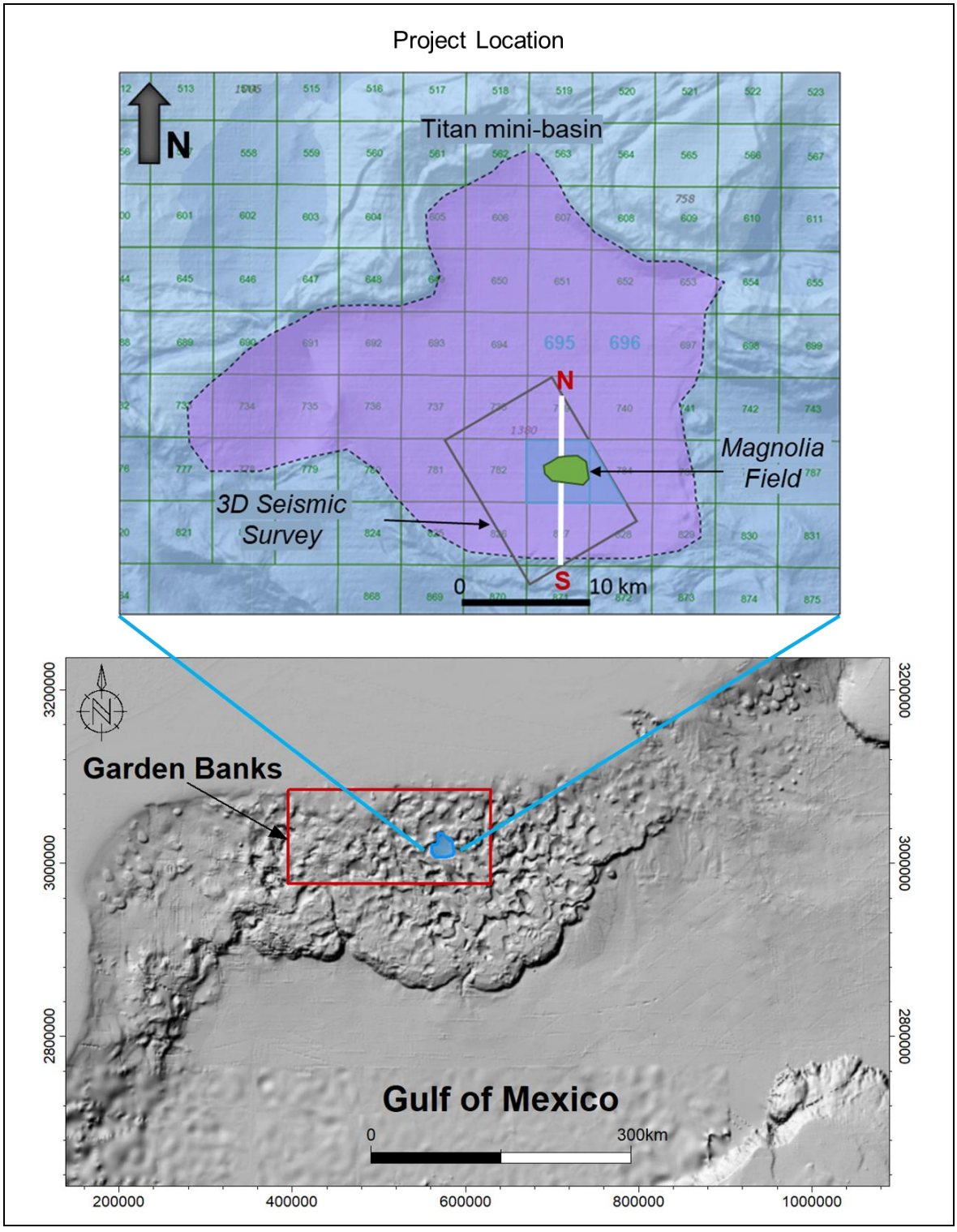

Figure 4.1 Project location, showing a 3D seismic cube, and a cross-section used in Figure 4.4. Map source: BOEM (2021).

The Gulf of Mexico is a passive basin where salt tectonics of the allochthonous salt, which was sourced from the Louann Formation and deposited during the Jurassic, have affected Upper Miocene to Pleistocene sediments (Weissenburger and Borbas, 2004; McGee et al., 2005). The traps in this

region have two components: structural and stratigraphic (Weiner and Pettingill, 2007). Fault systems such as normal, strike-slip, and trust have been identified in this basin (Meng et al., 2020; Galloway, 2008).

Most of the discovered reservoirs in the Gulf of Mexico are mainly very fine, stacked sandstones with intercalations of siltstone and mudstone from the Miocene, Pliocene, and Pleistocene (Figure 4.2b). The supply sources were located in the west, northwest, and north of the Gulf of Mexico Basin (Procyk et al., 2007). These sediments were transported by deltas, turbidites, fluvial channels, and slumps during the Paleocene and Pleistocene (Galloway, 2011). In the Louisiana Shelf, a sedimentation rate of 1,400 m/Ma was determined by Audet (1996) for Pleistocene sediments, while at the location of the Magnolia Field, sedimentation rates of around 1,000 m/Ma were determined by Weissenburger and Borbas (2004).

The Gulf of Mexico Basin is formed by Mesozoic and Cenozoic sediments. The Mesozoic Era is characterised by shelf reefs to deep-water carbonates with intervals of shallow tidal flats and sabkhas sediments (Snedden and Galloway, 2019). The Cenozoic Era is characterised by siliciclastic fluvial-dominated delta systems with the minor influence of tidal currents (Galloway and Hobday, 1996; Snedden and Galloway, 2019). The tectono-stratigraphic evolution of the Gulf of Mexico Basin started during the Triassic to Mid-Jurassic with a rifting event where grabens and horsts were created with subaerial volcanism (Pindell, 1985; Galloway et al., 2008). During the Callovian, the Louann Salt was deposited, a section of salt with a thickness of ~3 to 4 km (Hudec et al., 2013; Pindell, 1985; Galloway, 2008). During the Early Cretaceous to the Miocene, a passive continental margin started to form, which represents the last important stage of the evolution of the Gulf of Mexico (Zhang et al., 2019). However, Galloway et al. (1989) identified extensional and compressional zones as evidence of thermal subsidence periods. As a result of these events, a thick section (up to 12 km) of sediments has been deposited between the Paleocene and Pleistocene, causing flexural loading and salt mobility. Accumulations of clastic and carbonate sediments were deposited at different supply rates during the Late Jurassic to Late Cretaceous, with low sediment supply in the late Cretaceous due to the worldwide transgressive period (Galloway et al., 2011). After this period, the depositional systems were replaced by episodes of progradation of fluvial-deltaic systems, periods of transgression, and periods of volcanic activity (Galloway et al., 2011).

Different source rocks have been identified in the Gulf of Mexico, with some of them occupying larger areas than others (Hood et al., 2002; Zhang et al., 2019). Most of the hydrocarbons produced in this region are from source rocks of the Late Jurassic (Tithonian), Late Cretaceous (Turonian), and Early Tertiary (Eocene). A lacustrine formation from the Triassic and a carbonate from the Early Cretaceous have also been identified as source rocks. The hydrocarbons produced in the Magnolia Field have been interpreted to be from the Late Jurassic (Tithonian) (Hood et al., 2002; Weissenburger and Borbas, 2004). Hydrocarbon fluids in this field have been identified as highly heterogeneous due to the different maturities and expulsions of the source rocks, rapid changes in temperature and pressure, and proximity to a biogenetic methane source (Weissenburger and Borbas 2004) (Figure 4.2a).

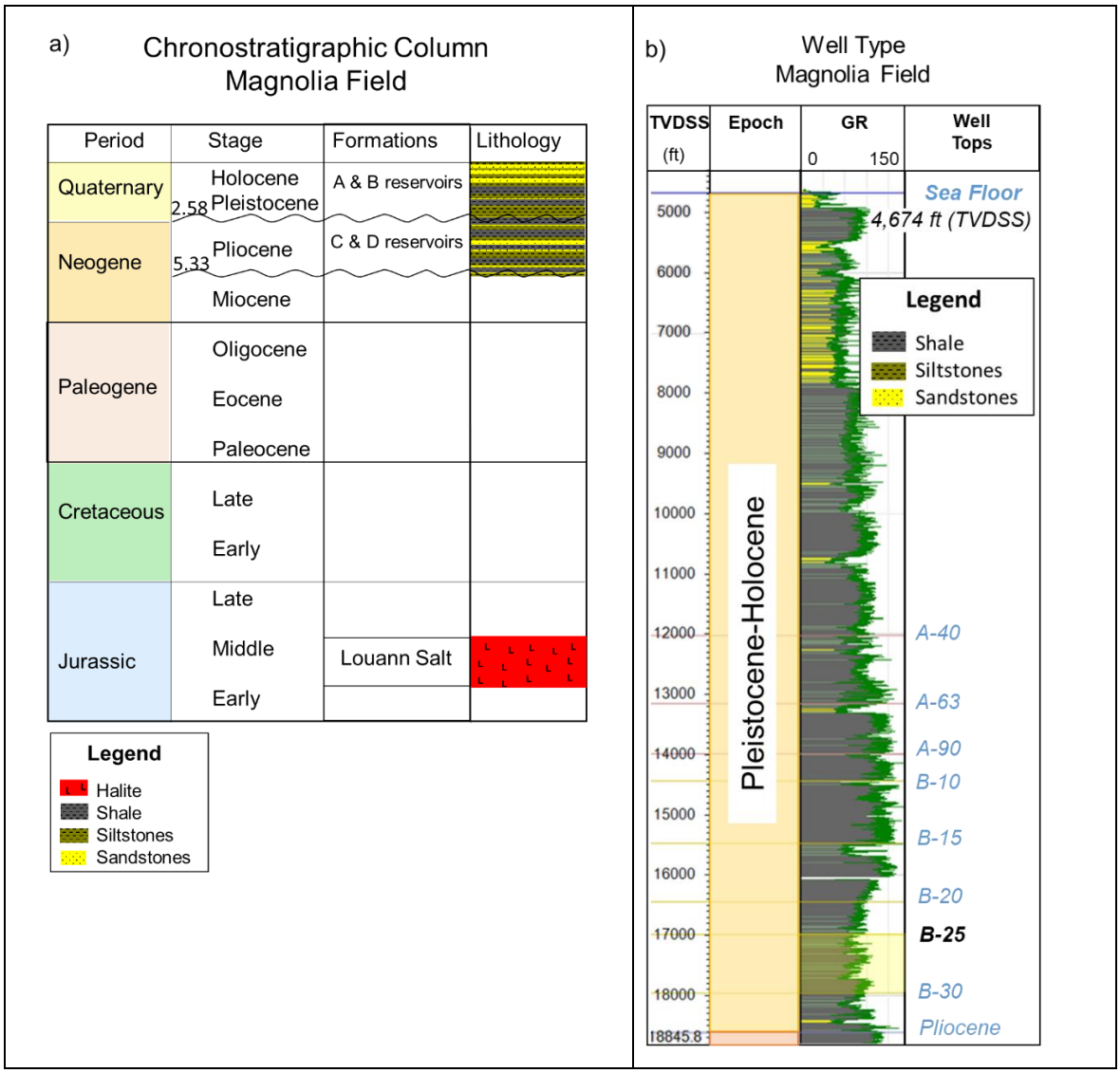

Figure 4.2.- a) Chronostratigraphic chart with the main lithologies encountered in the Magnolia Field. b) Well type with the GR log, the interpreted lithologies with eight of the nineteen productive reservoirs of this field.

4.2 Data and Methods

For this study, a set of well logs, 3D seismic cubes in time and depth, check shots, pressure tests, and core and drilling reports were used (Table 4.1). Well-correlation, seismic and lithofacies interpretation, pressure analysis, and static model construction were performed with Petrel software (version 2022). The software ParaGeo (version 2018) was used for geomechanical modelling.

Table 4.1.- Summary of the data used in this study.

Data	Number of Wells
Well locations and deviation trajectory	25
Drilling reports	8
Logs GR (2400 m TVDSS - TD), DT (~2850 m TVDSS - TD) and resistivity (~3760 m TVDSS - TD)	2

Data	Number of Wells
Logs GR, DT, resistivity and RHOB and NPHI (reservoirs)	22
Check shots (include data from other fields in the area)	30
3D seismic cubes (time and depth) with an area of 130 km2	1
Pressure data (Reservoirs B-25) + (other reservoirs)	12 + 5
Core data Report	1

All interpretations and analyses were conducted on primary data. The overall procedure for this project is presented in a general workflow that contains the main steps (Figure 4.3).

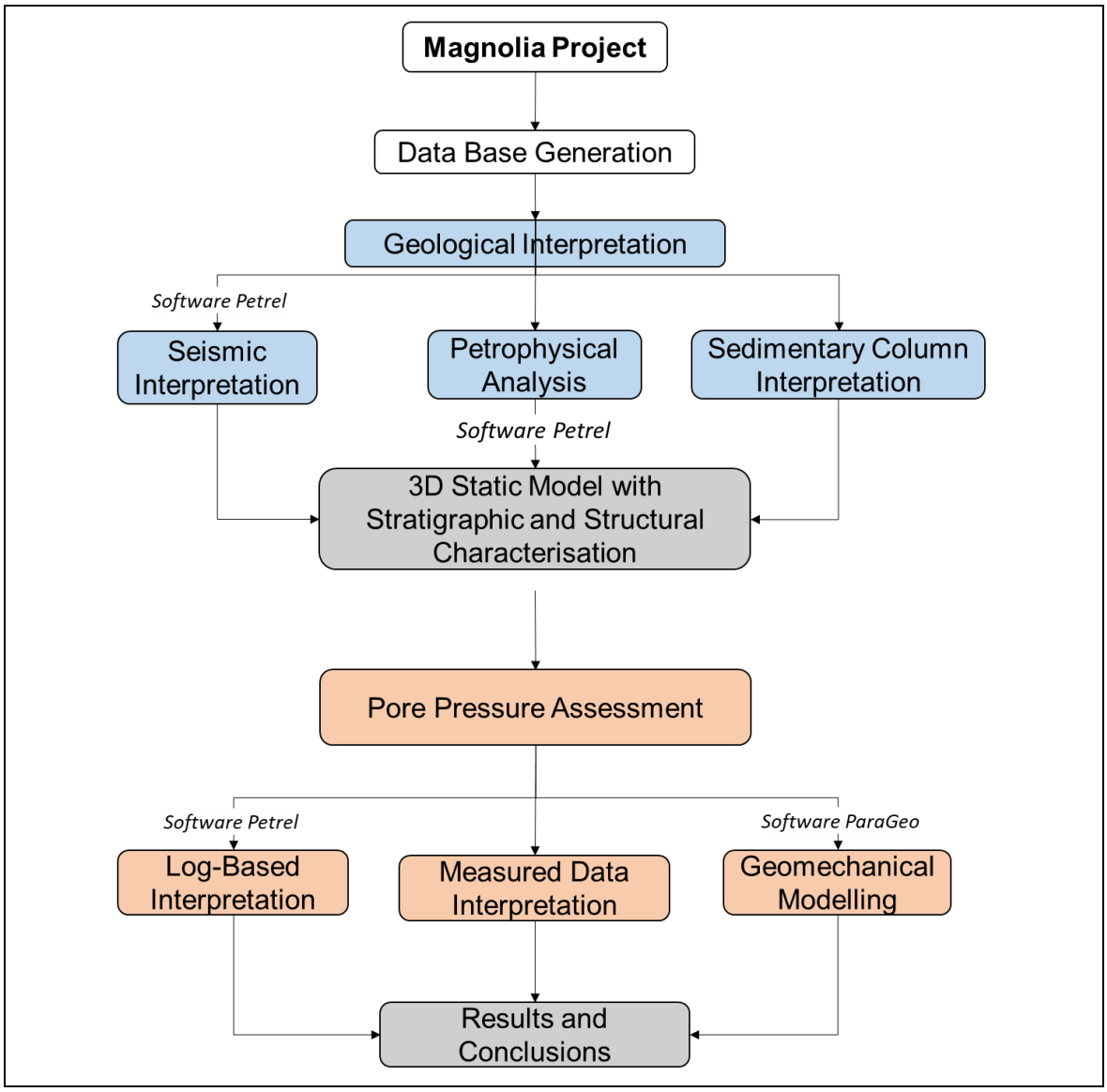

Figure 4.3.- Synthesis of the main processes registered in a workflow.

4.3 Pore Pressure Assessment Using Geological Data

An interpretation of the 3D seismic survey was performed to derive the structural configuration of the area. Seismic attributes such as structural smoothing, variance, chaos, sweetness, and RMS were created to facilitate the interpretation. Due to the quality and chaotic nature of the seismic data, the interpretation close to the salt wall could differ from other interpretations. The salt wall has a variable shape in space. For instance, the calculated angle at which wells GB783-1 and GB783-1ST1BP1 reached the salt top is between ~35 and 41 °. The GB783-A4 well is located in an area where the salt wall is almost vertical (Figure 4.5a).

An indication of active salt tectonics during the deposition of Pliocene and Pleistocene sediments is observed in the thickness variation, the pinch-out reflectors towards the salt wall, and the angle of the reflectors. Near the salt wall, seismic reflectors are almost vertical, and the thickness is reduced in comparison to the sediments towards the centre of the Titan mini-basin, where the reflectors are horizontal with greater thickness. At the Magnolia Field, the Pleistocene thickness is ~3,200 m, while the Pliocene is ~160 m (Figure 4.4b). Hydrocarbon indicators such as flat spots were not identified in any of the reservoirs, but pressure data show different oil and gas water contacts (Figure 4.10). Bright reflectors are present at different depths, including at the B-25 reservoir, although they are not continuous in this reservoir. Blurry reflectors represent mud-dominated sediments. Structural features such as down and top laps were identified in Pliocene and Pleistocene sediments and are interpreted to be the advance of channels/turbidites packages (Figure 4.4b).

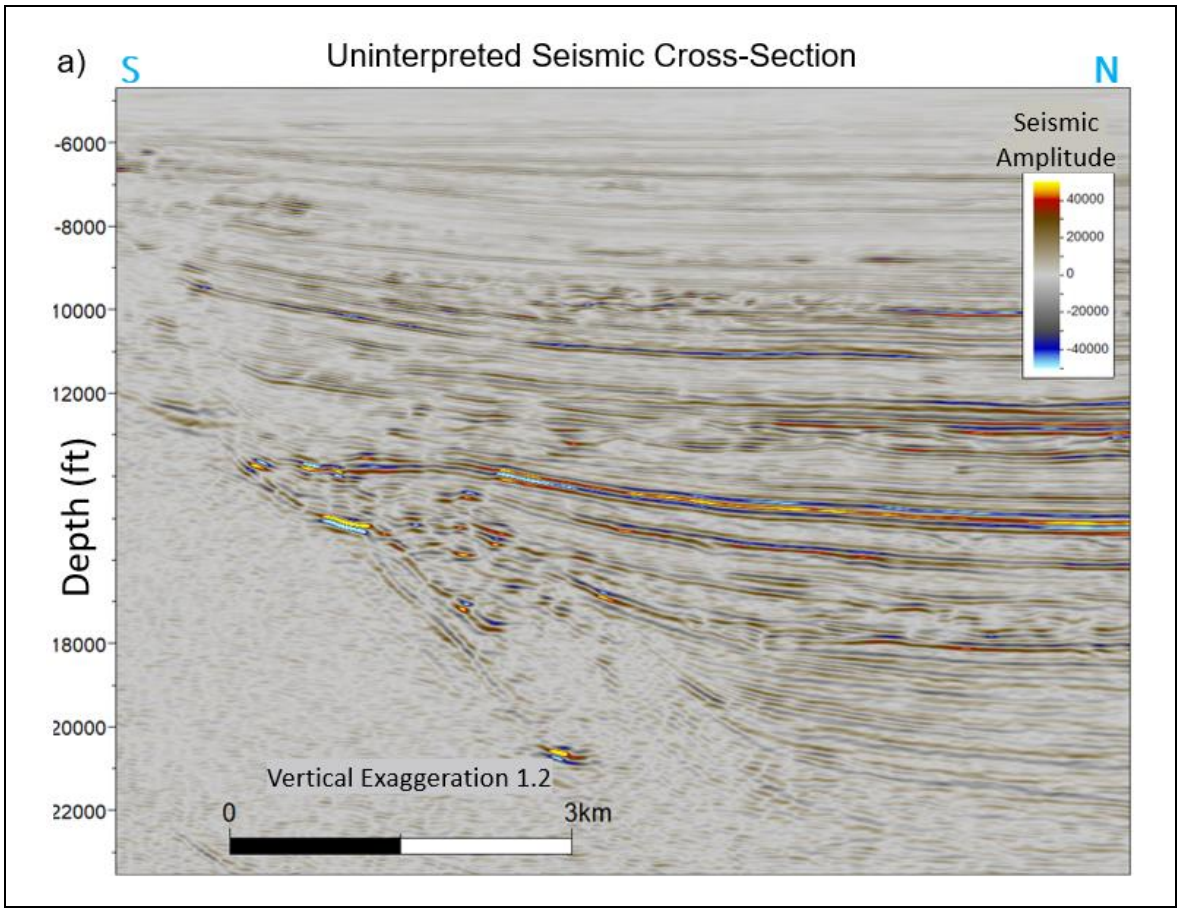

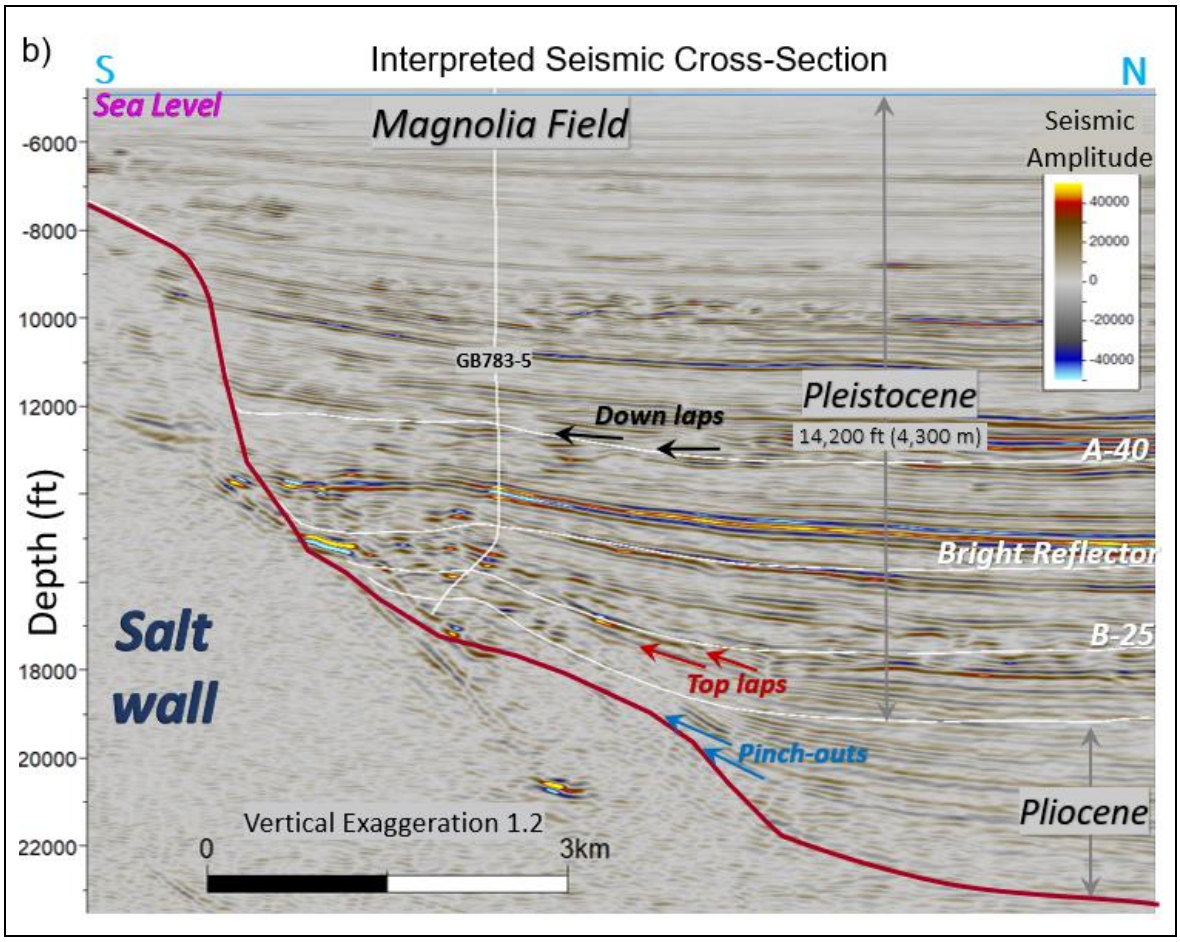

Figure 4.4.- a) Uninterpreted S-N seismic cross-section (for reference location see Figure 4.1). b) Interpreted S-N seismic cross-section used in the geomechanical models showing the GB873-A5 well, the top A-40, a bright reflector, the top Pliocene, and the top of the reservoir B-25, a sand-rich reservoir, which is the main focus of this study.

Sands at the B-25 reservoir level were identified to be hydraulically connected in six wells (GB783-3, GB783-A9, GB783-A7, GB783-A8, GB783-1, GB783-A6) (Figure 4.5a). A structural well-correlation constructed from the sea floor shows the variation in depth and thickness of the B-25 reservoir, which goes from 67 to 265 m (220 and 870 ft), with net to gross (NTG) ratios ranging from 0.13 to 0.92 (fraction).

The distance between the six wells is variable and depends on each well's location. For instance, a distance of ~1,825m (5,987 ft) separates wells GB783-A9 from GB783-A7, while a distance of ~353 m (1,158 ft) separates wells GB783-3 from GB783-A9 (Figure 4.5c). The B-25 reservoir was interpreted based on seismic data as having isolated reflectors with bright and blurry reflectors. The continuity of these reflectors could not be fully established due to the seismic resolution, which is ~20 m at the B-25 reservoir (~65 ft, equivalent to 16 ms) (Figure 4.5b).

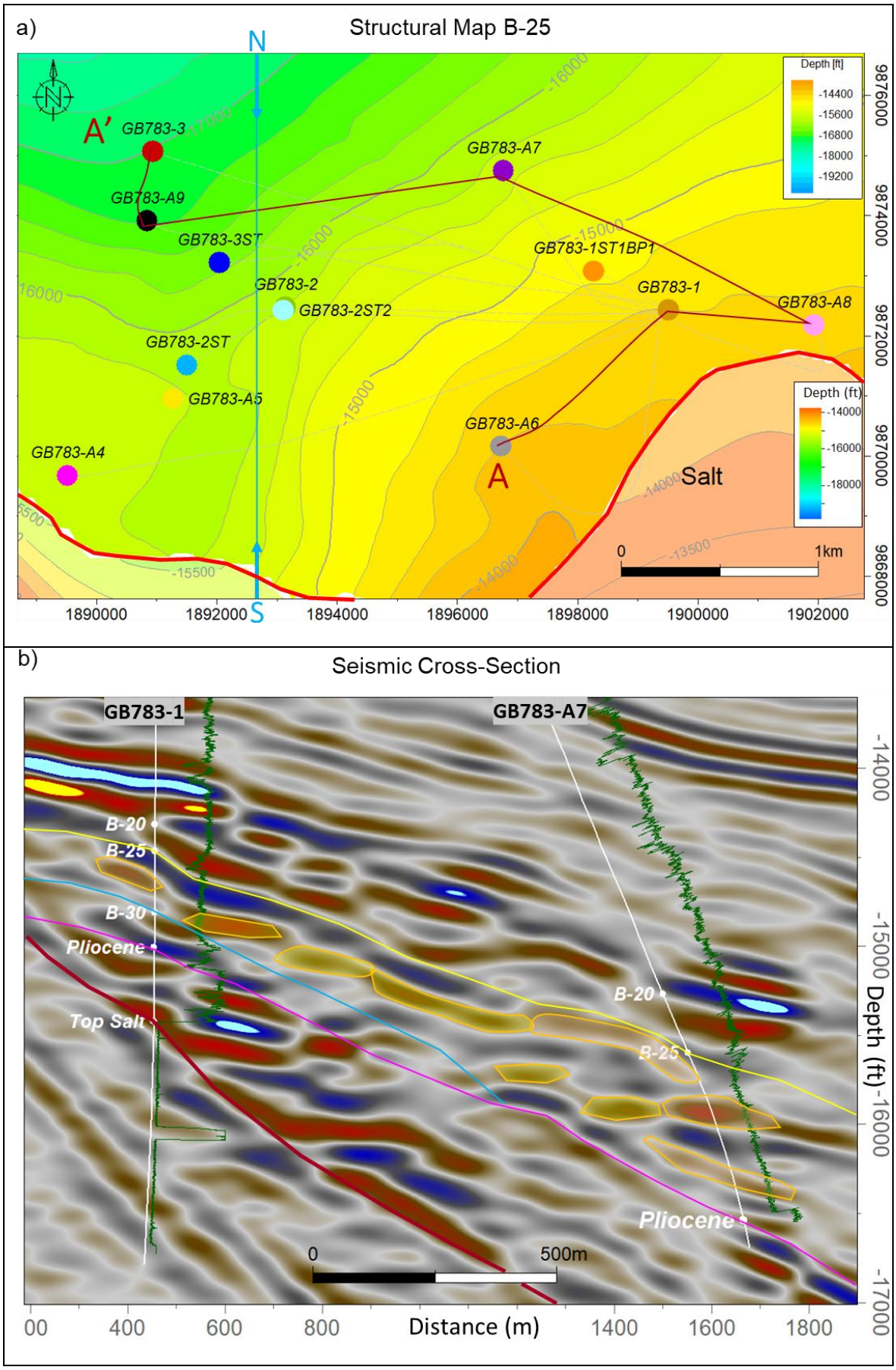
a)
Structural Map B-25
N
S
A
A'
GB783-3
GB783-A9
GB783-3ST
GB783-2
GB783-2ST2
GB783-2ST
GB783-A5
GB783-A4
GB783-A7
GB783-1ST1BP1
GB783-1
GB783-A8
GB783-A6
Salt
Depth [ft]
-14400
-15600
-16800
-18000
-19200
Depth (ft)
-14000
-16000
-18000
0
1km
1890000
1892000
1894000
1896000
1898000
1900000
1902000
9876000
9874000
9872000
9870000
9868000
b)
Seismic Cross-Section
GB783-1
GB783-A7
B-20
B-25
B-30
Pliocene
Top Salt
0
500m
Distance (m)
00
400
600
800
1400
1600
1800
-14000
-15000
-16000
-17000
Depth (ft)

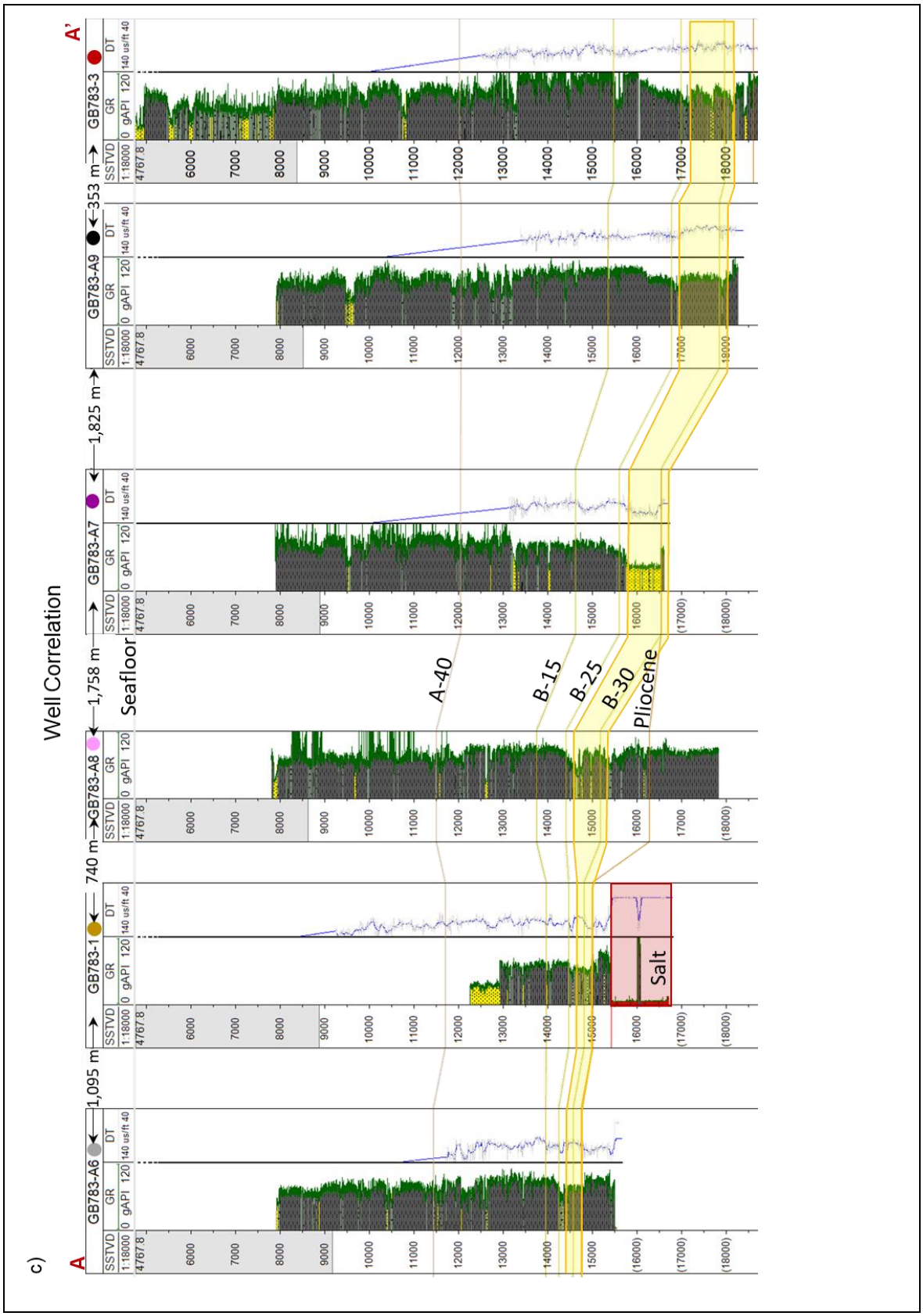

Figure 4.5.- a) Structural map at the top of the B-25 reservoir and structural map of the salt, location of thirteen wells that have measured pressure, showing the well-correlation A-A' and the S-N cross-section used for the geomechanical models (reference Figure 4.4a). b) Seismic cross-section between GB783-1 and GB783-A7 showing the B-25 reservoir. c) Well-correlation showing GR and DT logs with tops of the reservoirs A-40, B-15, B-25, B-30, and Pliocene.

A reservoir-scale analysis performed in ~74 m (242.85 ft) of core images from well GB783-2ST2 (CoreLab, 2003), located approximately 1,433 m (4,700 ft) north of the main salt wall (Figure 4.5a), showed potential vertical and horizontal barriers to fluid flow. These include and are associated with high-angle crossbedding, fractures, small-scale faults, and lithological heterogeneity (Figure 4.6a). These small-scale features are interpreted to be associated with the salt wall formation as interpreted in other areas (e.g., Rowan et al., 2020; Wilkins et al., 2022).

Porosity values between 0.04 and 0.37 (fraction) and permeabilities between 0.001 and 487 mD have been described along the core (Figure 4.6b). No features indicative of clay mineral or quartz diagenesis were identified on photos or thin sections of the B-25 and B-20 reservoirs.

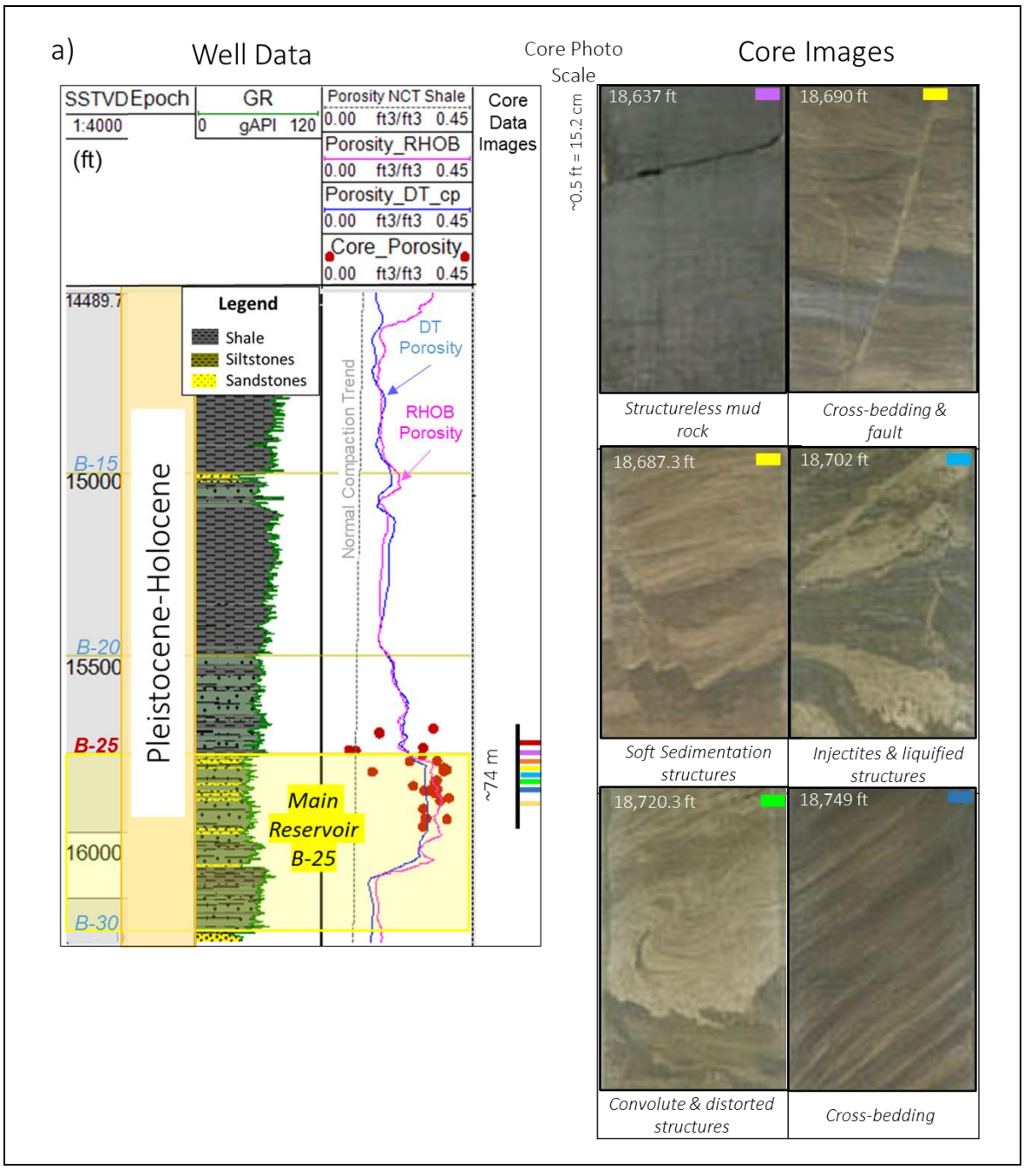

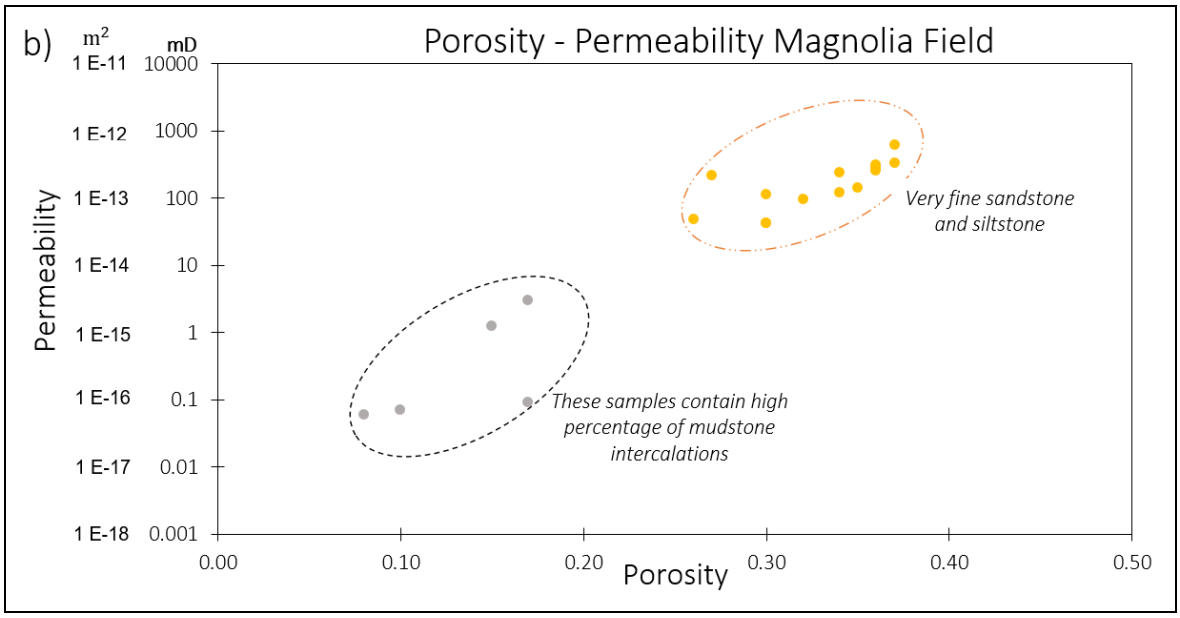

Figure 4.6.- a) From left to right, depths, periods, GR with interpreted lithologies, sonic and density porosity and core data with the location of the depths of the internal structures interpreted on the well GB783-2ST2. b) Cross-plot of the porosity Vs. permeability core data of the GB783-2ST2 well.

During this research, a 3D static model was constructed in depth, from the seabed to the top of the salt. Lithologies, porosities, and registered pore pressure were populated in this model to understand the relationship between them. Pore pressure distribution shows that it increases with depth, and there are areas with higher pressure values than others. This property was distributed with the sequential Gaussian simulation method (stochastic method based on Kriging) using the data from each well.

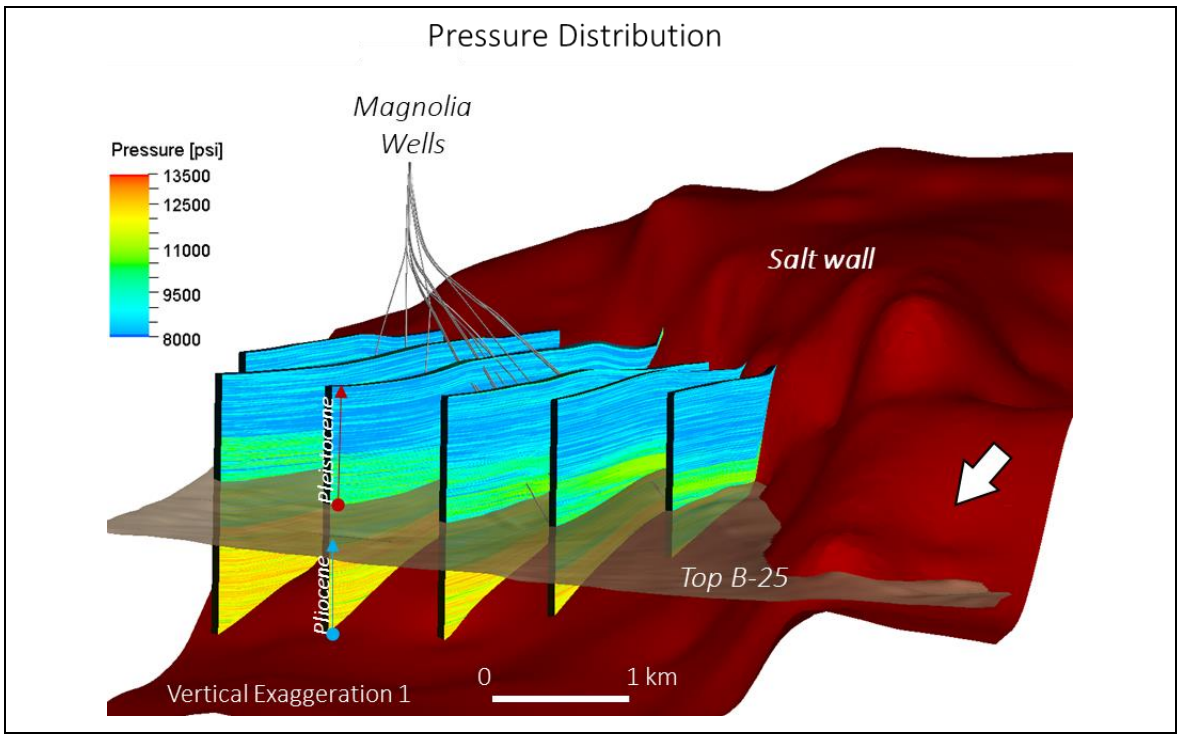

Figure 4.7- Pore pressure distribution is shown in a 3D window with the top of the reservoir B-25, the Pliocene and Pleistocene sediments, and the well locations. Calid colours represent high pore pressures.

4.3.1 Pore Pressure: Log-Based Interpretation

To determine a relationship between porosity and effective stress was not straightforward in this study. There are neither porosity nor porosity-related log data (transit time; density) available from the seafloor to ~2,745 m (9,000 ft) of the sedimentary column, and drilling data suggest that overpressure occurs at depths greater than ~300 m (972 ft) (Figure 4.8).

The lithologies of the overburden were determined with the GR of well GB783-3, which has GR data from the seafloor (~1,425 m or ~4,674 ft) to the total depth (TD), and wells GB783-A-8, GB783-A7, BG783-A9, and GB783A-6, which have GR data from ~2,439 m (8,000 ft) TVDSS (Figure 4.5).

Prior to interpretation, density, sonic, resistivity and GR well logs were edited. In cases where the data were insufficient, the well was not used. The Pliocene and Pleistocene shale intervals do not have any organic matter content as indicated in well reports; therefore, a correction for total organic carbon was not necessary.

Normal (hydrostatic) compaction trends were calculated for sonic, density, resistivity, and porosity using analytical equations. The equations 4.1, 4.2, and 4.4 were developed by Wyllie (1956) and Athy (1930) and were later modified by Tingay et al. (2009) for mechanically compacted sediments from the Gulf of Mexico. The normal compaction trend for resistivity was calculated with equation 4.3 (Zhang 2011).

$$\Delta t_{NC} = \Delta t_{ma} + (\Delta t_{ml} - \Delta t_{ma}) * e^{-c*Z} \quad 4.1$$

$$\rho_{NC} = \rho_{ma} + (\rho_{ml} - \rho_{ma}) * e^{-c*Z} \quad 4.2$$

$$R_{NC} = R_o * e^{b*Z} \quad 4.3$$

$$\emptyset_{NC} = \emptyset_o * e^{-c*Z} \quad 4.4$$

Where Δt_{NC} is the transit time of the normal compaction, Δt_{ma} is the matrix transit time (67 us/ft), Δt_{ml} is the mudline transit time (seabed) (188 us/ft), z is the depth below sea level (m), c is the compaction coefficient (0.0005 m^{-1}) after Hansen (1996) and Tingay et al. (2009), ρ_{NC} is the density of the normal compaction, ρ_{ma} is the matrix density (2.67 gr/cm^3) and ρ_{ml} is the density at the mudline (1.73 gr/cm^3), R_{NC} resistivity normal compaction, R_o shale resistivity at mudline (1.28), b constant (0.000034), $\emptyset_{NC}$ is the normal compaction of shale, and $\emptyset_o$ is the porosity at mudline (fraction) in this case 0.54 was used.

To obtain porosity values, density and sonic logs were used with equations 4.5 and 4.6.

$$\emptyset_{DTcp} = \frac{\frac{\Delta t - \Delta t_{ma}}{\Delta t_f - \Delta t_{ma}}}{C_p} \quad 4.5$$

$$\emptyset_{density} = \frac{\rho_{ma} - \rho_b}{\rho_{ma} - \rho_f} \quad 4.6$$

Where $\emptyset_{DTcp}$ is the corrected porosity from the sonic log, C_p is the correction factor considered to be 1.8 after Raymer et al. (1980), Issler (1992), Hart (1995), Schlumberger (1989), and Tingay et al. (2009), Δt_{ma} is the matrix transit time (67us/ft), Δt is the measured transit time (us/ft), Δt_f is the fluid transit time (188 us/ft), $\emptyset_{density}$ is the porosity from density log, ρ_{ma} is the matrix density (2.67gr/cm^3), ρ_b is the bulk density measured (g/cm^3) and ρ_f is the fluid density (1.03g/cm^3).

Pore fluid pressure values were estimated from sonic logs using relationships developed for mechanically compacted sediments in the Gulf of Mexico. Eaton's (1975) equation was used with exponent 3, which was determined to estimate pore pressure related to mechanical compaction (disequilibrium compaction). Bowers' (1995) equation was applied and compared with pore pressure data (equations 4.7 and 4.8).

$$4.7 \quad P_f = \sigma_L - (\sigma_L - \sigma_{Hy}) \left(\frac{\Delta t_{NC}}{\Delta t}\right)^x$$

$$4.8 \quad P_f = \sigma_L - \left(10^6 * \frac{\frac{1}{\Delta t} - \frac{1}{\Delta t_{ml}}}{a}\right)^{\frac{1}{b}}$$

Where P_f is the pore pressure fluid, σ_{Hy} is the hydrostatic pore pressure, σ_L is equal to the lithostatic stress/overburden, Δt_{NC} is the normal compaction transit time for hydrostatically pressured sediment (us/ft), Δt is the transit time from sonic log (us/ft), Δt_{ma} is the matrix transit time (67 us/ft), Δt_{ml} is the transit time at sea floor (188 us/ft), and x is the exponent 3 (Eaton, 1975).

Results from the well-log analysis are presented in Figure 4.8. The lack of log data precludes any analysis shallower than 2,777 m TVDSS (~9,000 ft), but the log data at greater depths are consistent with increasing overpressure with increasing depth.

There is a fairly constant density and a slight increase in transit time at depths greater than 3,962 m (13,000 ft) TVDSS (interval two; Figure 4.8). A constant density or transit time with increasing depth indicates a constant effective stress, which occurs when the rate of additional pore pressure is due to sedimentation-related loading being much faster than the rate at which pore pressure can decrease due to fluid flow. This occurs at the so-called "fluid retention depth" (Swarbrick, 2002).

An increase in transit time and decrease in density (interval 3; Figure 4.8) with depth below 4,127 m TVDSS (13,543 ft), which correlates to one of the bright reflectors observed on the seismic data, suggests that in well GB783-1, this section reached the fluid retention depth at a slightly shallower depth than in the section immediately above (Figure 4.8).

Pore pressures measured in the upper parts of the more sand-rich reservoir section are similar to those inferred from the Bowers (1995) log analysis of the overlying mud-dominated section. This implies that the pore pressures can be explained as being generated by disequilibrium compaction, which is expected in a sedimentary system dominated by the rapid deposition of low-permeability mudstones, and which has not been subjected to chemical diagenesis. The fit is not as good at the base of the sand-rich section (reservoir B-25) below a very sharp ramp of pore pressure at 4,572 m (15,000 ft) TVDSS (interval 4; Figure 4.8), suggesting that overpressure mechanisms in addition to

disequilibrium compaction may be operating. These could include tectonic stress and lateral transfer (Yardley and Swarbrick, 2000), the analysis of which requires a more sophisticated approach using 2D geomechanical modelling.

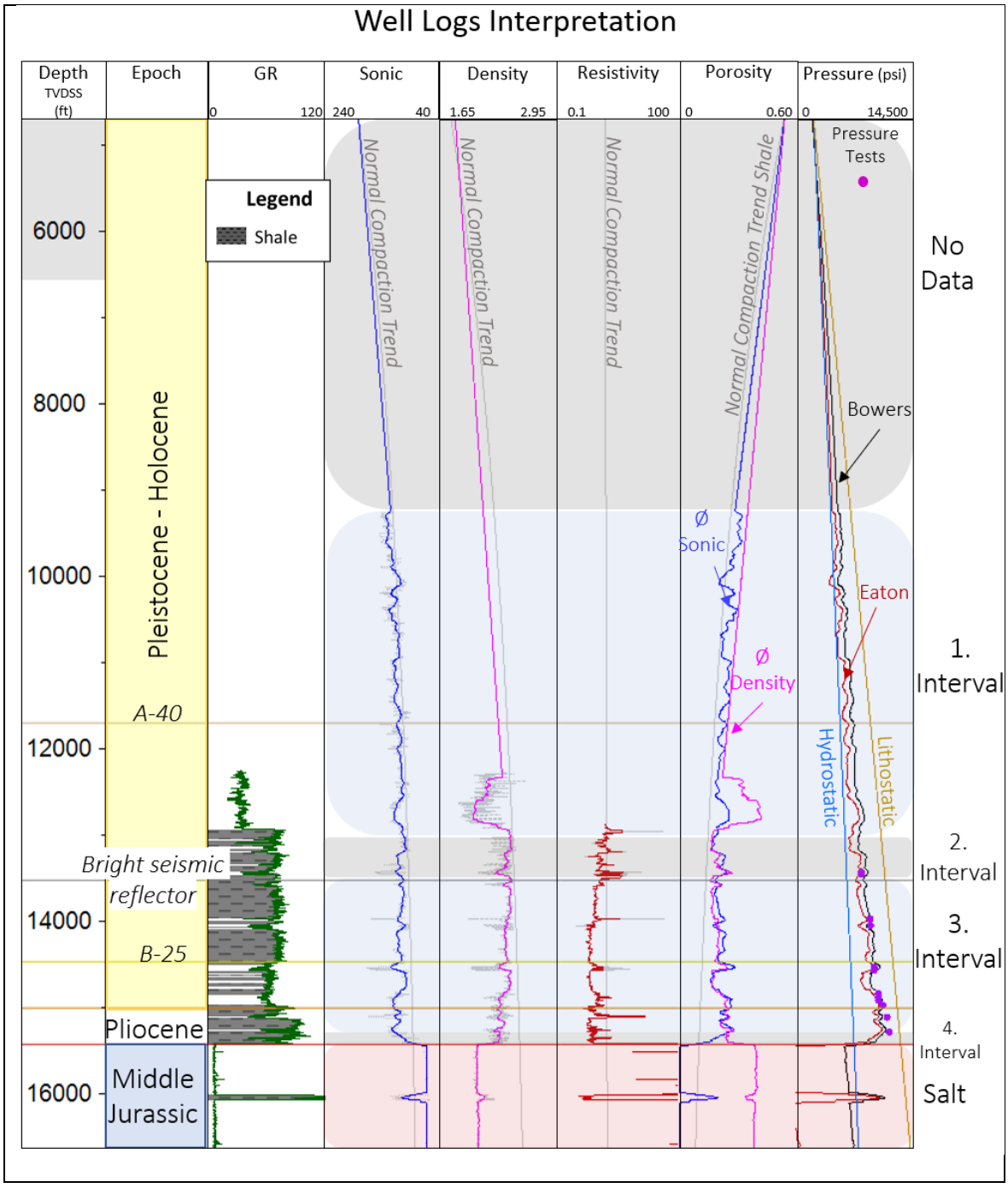

Figure 4.8.- Pore pressure interpretation based on well log data, Well GB783-1. Normal compaction trends for transit time, density, and resistivity (equations 4.1, 4.2, and 4.3). Porosities were calculated with equations 4.5 and 4.6. Pore fluid pressures were calculated with equations 4.7 and 4.8.

Density-velocity cross-plots are particularly useful to identify situations where unloading has occurred because, for a given decrease in effective stress, the relative decrease in velocity is much greater than that of density (Bowers and Katsube, 2002).

Both Bowers (2001) and Gardner (1974) developed density-velocity relationships for mudstones from the Gulf of Mexico and the Gulf Coast, where disequilibrium compaction was identified to be the main overpressure-generating mechanism (equations 4.9 and 4.10).

$$4.9 \quad V = 4790 + 2953 * (\rho - 1.3)^{3.57}$$

$$4.10 \quad V = \left(\frac{\rho}{0.23}\right)^{4}$$

Where V is the velocity (ft/s) and ρ is the registered well log density RHOB (g/cm3), the values 4,790, 2,953, 1.3, 3.57, 0.23, and 4 are constants defined by Bowers and Gardner.

Figure 4.9 shows a velocity-density cross-plot of shale intervals (GR >75) for wells in which such data were available. Although there is scatter as a result of lithological variations and log quality, most of the data fall within the boundaries defined by Bowers (2001) and Gardner (1974), dismissing the possibility of any unloading mechanism.

The values with low density and high velocity that plotted outside of the Bowers-Gardner zone were interpreted as potentially attributable to the presence of salt, which is associated with low density readings within the clastic sediment (e.g., Lopez et al., 2004; Zong et al., 2015).

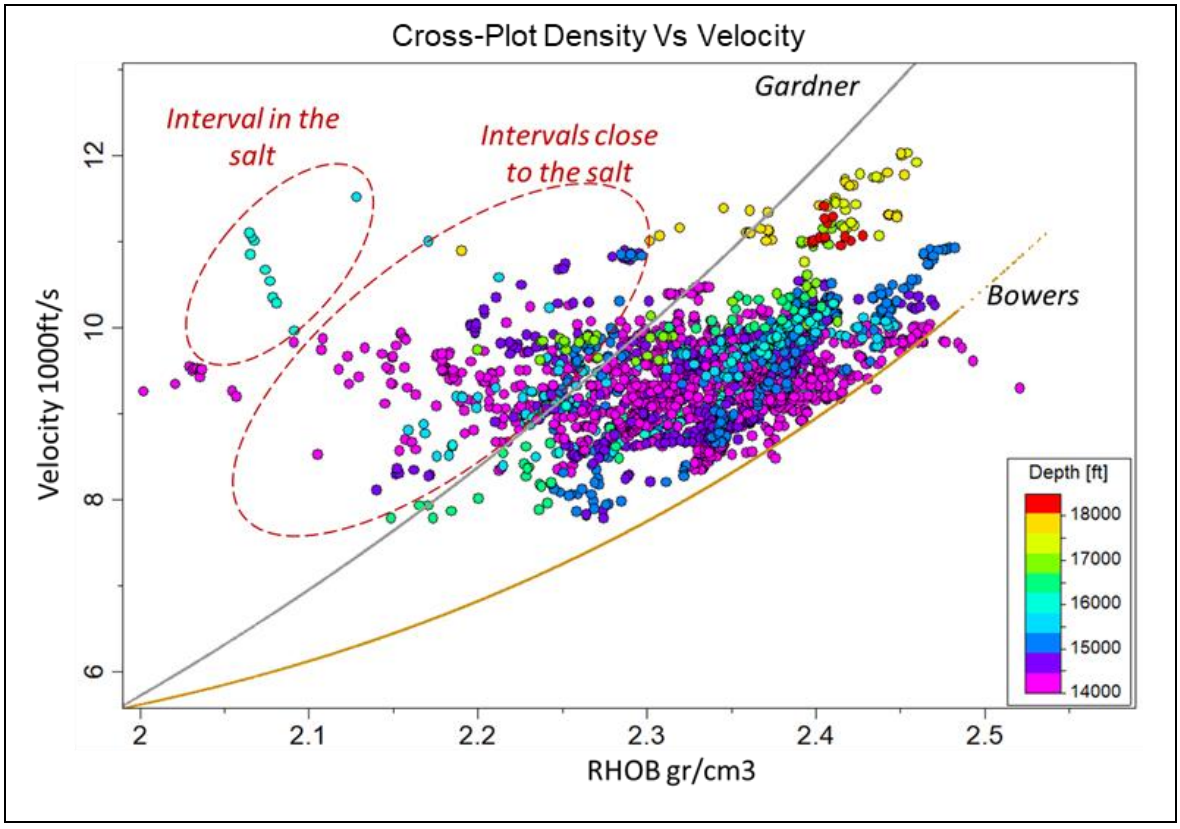

Figure 4.9.- Density-velocity cross-plot of shale intervals >3,700 m (~12,140 ft) depth and with GR >75 of eight wells. Data include shale intervals above and below the B-25 reservoir.

4.3.2 Measured Pore Pressure

The Magnolia Field is located in a region that has been interpreted to be at moderate risk of shallow water flows during drilling. Mud weights of 10.5 to 12.5 ppg were used during the perforation from shallow depths (>300 m) to avoid any flow due to these overpressured sandstones (Eaton et al., 2005).

Pressure tests such as drill stem tests (DST) and modular formation dynamics tester (MDT) were registered in the reservoir intervals of the Magnolia Field. These tests, along with the production data, show high sedimentological heterogeneity with numerous baffles and barriers that affected the development of these reservoirs.

Pore pressure tests in these wells are up to 76 MPa (11,000 psi) at approximately 5,000 m (16,400 ft) TVDSS, at which depth temperatures are between 60 and 70 °C (Sathar and Jones, 2016). Nineteen sand-silt intervals were targeted in this field (A-63, A-80, A-85, A-90, B-10, B-12, B-13, B-15, B-17, B-20, B-25, B-30, C-30, C-40, C-50, C-60, C-70, D-10, and D-Miocene), with letters representing periods (the letters A and B represent Pleistocene, the letter C Pliocene, and the letter D Miocene) and numbers representing the maturity of the reservoir (smaller numbers represent younger reservoirs). B-25 was the main reservoir of this field, with a recovery factor of sixty percent (Procyk et al., 2007).

A pressure-depth plot shows that all nineteen reservoirs in all wells are overpressured, with measurements indicating a high degree of vertical and horizontal fluid compartmentalisation. In addition, overpressure increases with depth, having the highest overpressures in the deepest intervals. For instance, the GB783-1ST1BP1 well has overpressure values of 35 MPa (~5,130 psi) in a Miocene reservoir (D-10) (Figure 4.10a).

Within the B-25 reservoir, both hydraulic connectivity and compartmentalisation are observed. Wells GB784-A6, GB784-A8, GB783-1ST1BP1, GB783-1, GB784-A7, GB783-A9, and GB783-3 present hydraulic connectivity while wells GB783-A4, GB783-A5, GB783-2ST, GB783-2, and GB783-3ST are compartmentalised. The wells which reservoirs are compartmentalised have larger overpressure values than the wells which reservoirs have a hydraulic connection.

The highest pore pressure values for the B-25 reservoir are for wells located close to the salt wall. For example, well GB783-A4 has the highest pore pressure with ~79 MPa (11,500 psi) at 4,750 m (15,600 ft), approximately 28 MPa (4,000 psi) above the hydrostatic pore pressure. This well is located at the steepest side of the salt wall, and it is the closest well to the salt wall in comparison to the rest of the wells at the B-25 reservoir (Figure 4.5a; Figure 4.10b).

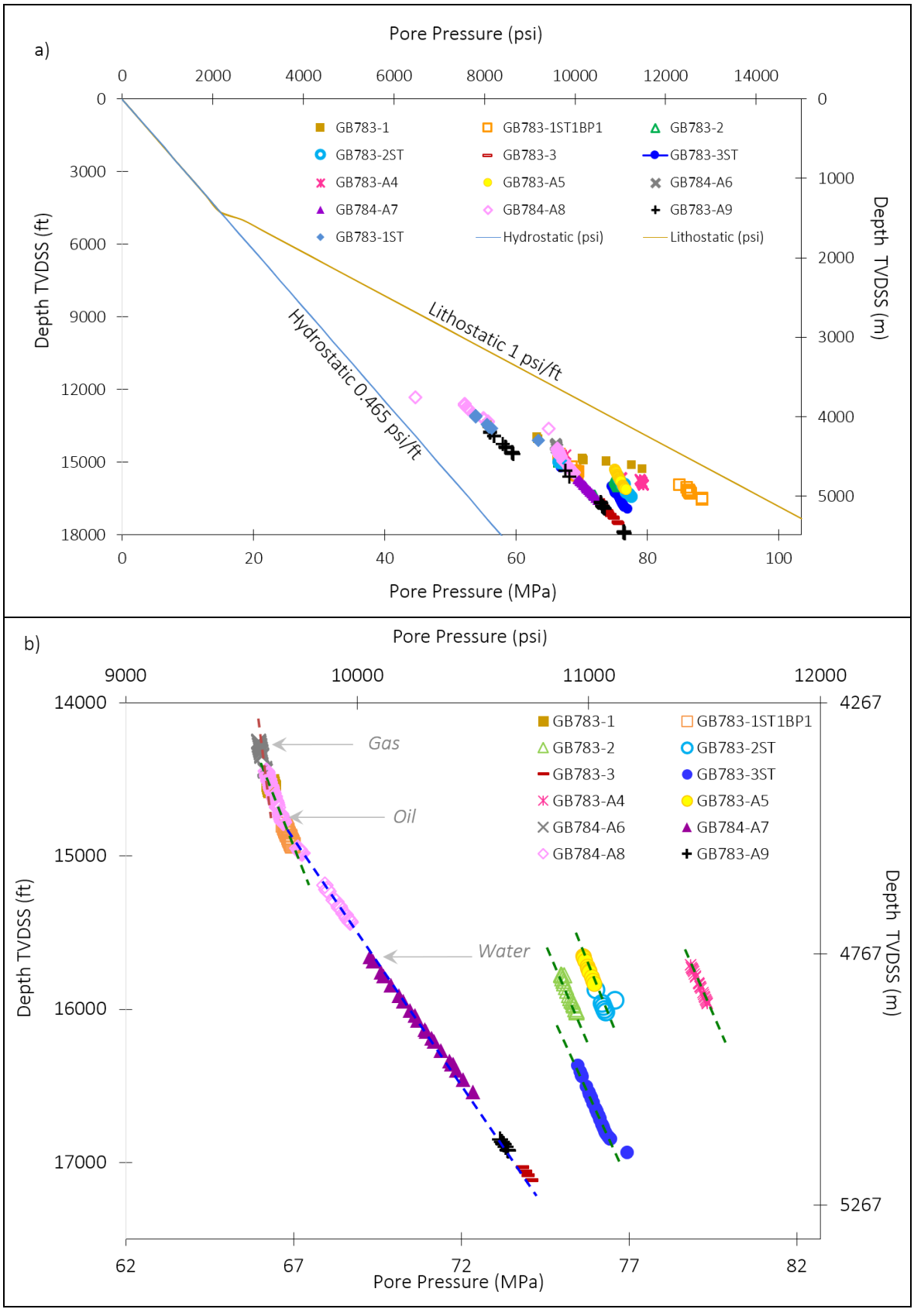

Figure 4.10.- a) Magnolia Field pore pressure test data for seventeen reservoirs (thirteen wells). Reference values of 0.0105 MPa/m (0.465 psi/ft) to represent a hydrostatic gradient and 0.0226 MPa/m (1 psi/ft) to represent a lithostatic gradient were used. b) Pressure test data registered at the B-25 reservoir with an interpretation of gas, oil, and water gradients.

4.4 Pore Pressure Hydro-mechanical Modelling

1D and 2D geomechanical models were used for the analysis of overpressure evolution in the Magnolia Field. The software used was ParaGeo, which works with finite geological elements that capture stresses, strain tensors, pore pressures, and temperatures among other parameters to predict the physical and mechanical evolution of the sediments (Crook et al., 2018; Obradors-Prats et al., 2016, 2017a, 2017b, and 2019).

This software uses the critical state poro-elasto-plastic Soft Rock 4 model, which can capture hardening or softening plastic strain depending on the stress path yielding location (e.g., hardening on the compression side of yield and softening on the tensile side of yield surface). The equations for mechanical and fluid flow fields are the linear momentum for a saturated medium with a single fluid phase, which in these models was water.

The 1D column models were used to investigate disequilibrium compaction without the effect of wall salt growth. These models used three lithologies: sandstone, siltstone, and shale. The 2D models were used to investigate the effects of salt tectonics, disequilibrium compaction, and lateral pressure transfer from deep intervals together. The 2D models used three lithologies: sandstone, shale, and salt. Salt was modelled using Herschel and Bulkley's (1926) stress-dependent viscoplastic model, while the clastic lithologies used the poro-elasto-plastic Soft Rock 4 model.

Porosity-permeability for shale was modelled using the classical Kozeny-Carman relationships. Other relationships depend on several factors, such as the connected mature of the porous medium and clay content (e.g., Yang and Aplin, 2007 and 2010), but these data were not available. For the sandstone lithology, the Kozeny-Carmen relationship was adjusted with the core data of well GB783-2ST2 (Figure 4.11a). For the shale lithology, a relationship that is 40.5 times higher than the porosity-permeability relationship K-C Shale was created. All the relationships were set to a minimum permeability value of 1.E-22 m^2 to avoid convergency problems during the modelling (Figure 4.11a).

Normal compaction trends (hydrostatic porosity-depth trends) were created using Schneider's equations (1996) for each lithology. These equations allow for greater control over the shape of the trends. Shale lithologies were represented by the Schn Porosity Shale compaction trend (Figure 4.11b). Athy's (1930) normal compaction trend is shown for reference.

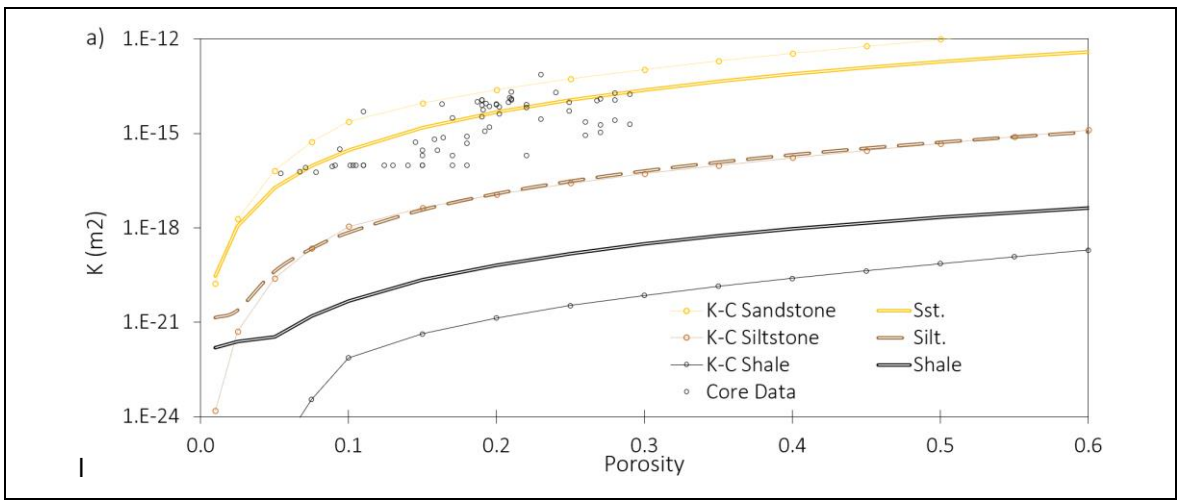

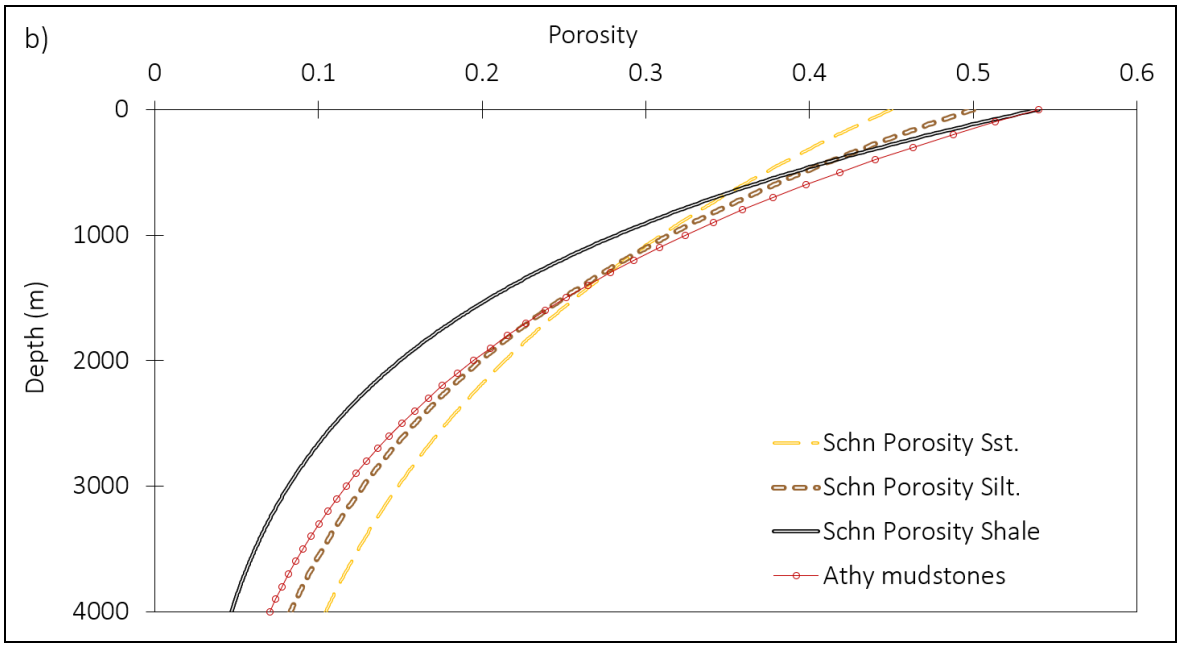

Figure 4.11.- a) Cross-plot of the porosity-permeability relationships used in the 1D and 2D models. b) Cross-plot porosity vs. depth of the compaction trends (hydrostatic trend) used in the geomechanical models.

4.4.1 1D Column Geomechanical Models Approach

These models have isotropic permeability (the vertical and horizontal permeabilities are equal), which depends on the porosity-permeability relationship defined for each lithology in the material datafile. The fluid used in all the models was water, with a density of 1000 kg/m^3.

To calculate the thickness of the initial sedimentation, an average of both the current porosity and the current thickness was obtained to perform decompaction. The 1D column models are based on the vertical well GB783-1, which has a thickness of 3,277 m (10,751 ft) of Pliocene and Pleistocene sediments (from the salt top to the seabed). These sediments were deposited over 2.708 Ma. Table 4.2 shows the initial input for these models.

Table 4.2.- Summary of the variables used in the 1D model per layer. Reference GB783-1 well (Figure 4.5a)

Period	Time	Lithology	Current Thickness (m)
Pleistocene	2.580	Sand-Siltstone-Shale	3,149
Late Pliocene	0.128	Sand-Siltstone-Shale	128

As the thickness of sand, siltstone and shale varies significantly in this area (e.g., the thickness of sand lithologies ranges from 3 to ~200 m) one coarse and one detailed model were constructed to investigate the impact of layer thickness (Table 4.3).

Table 4.3.- Summary of the settings of the coarse and detailed models.

Model	Disequilibrium Compaction	Total Number of Layers Deposited
Model-C (coarse model)	Yes, all the shale layers (Schn Porosity Shale and Shale)	12
Model-D (detailed model)	Yes, all the shale layers (Schn Porosity Shale and Shale)	109

Both the coarse and detailed models generated overpressure. Results also show that due to the variation of thin layers present in this basin, detailed models more accurately capture the small variations in porosity and pore pressure (Figures 4.12a and 4.12b). Porosity values are better matched with the detailed model than the coarse model, and although the pore pressures generated with the detailed model (Model-D) are slightly higher than the coarse model (Model-C), they are still low in comparison to the registered pore pressure in this well.

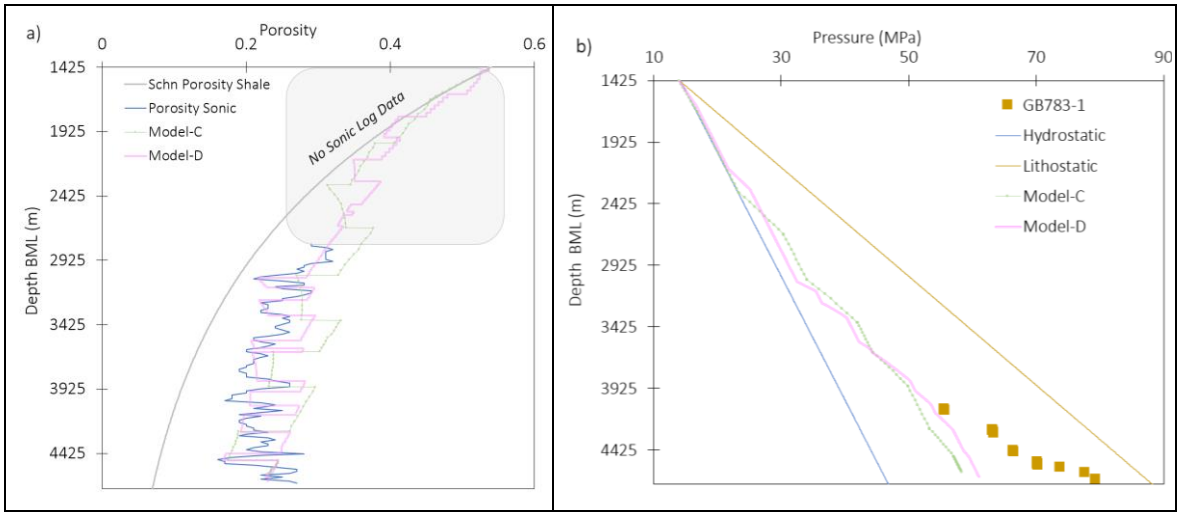

Figure 4.12.- Results of the 1D coarse and detailed models. a) Porosity vs. depth plot with the porosity calculated from the sonic log (blue) and the results of the two models. b) Pore pressure vs. depth plot with the pore pressure registered in the GB783-1 well (brown) and the results of the two models. For reference, values of 0.0105 MPa/m (0.465 psi/ft) were used to represent a hydrostatic gradient and values of 0.0226 MPa/m (1 psi/ft) to represent a lithostatic gradient.

To generate more overpressure similar to the encountered in the GB783-1 well, two additional detailed models, which accounted for a reduction in permeability, were constructed (Model-D-1 and Model-D-2). These two models have the same settings as Model-D (Figure 4.12); the only difference is the use of a low-permeability relationship in one of the shale layers (54 m; layer 17 from the base). The layer where the low-permeability relationship was applied is based on the increase in pore pressures in this well, which are around 4,100 m BML (Figure 4.12b; Table 4.4).

Model-D-1 used the porosity-permeability K-C Shale Ed., which is 40.5 times lower than the porosity-permeability relationship Shale, while Model-D-2 used the porosity-permeability relationship Shale L, which is 5 times lower than the porosity-permeability relationship Shale (Figure 4.13a; Table 4.4).

Table 4.4.- Model-D-1 and Model-D-2 investigated disequilibrium compaction with different porosity-permeability relationships to generate more overpressure similar to the registered in the GB783-1 well.

Model	Disequilibrium Compaction	Total Number of Layers Deposited
Model-D-1	Yes + all the shale layers (Schn Porosity Shale and Shale) except one layer (54 m), which used the porosity-permeability relationship **K-C Shale Ed**.	109
Model-D-2	Yes + all the shale layers (Schn Porosity Shale and Shale) except one layer (54 m), which used the porosity-permeability relationship **Shale L**.	109

The Model-D-1 predicted higher pore pressures, which matched a few values of the registered data; this also resulted in the preservation of high porosities, which are not seen within the registered data (Figures 4.13b and 4.13c). The Model-D-2 preserved slightly high porosity values in comparison to the porosity sonic, but the pore pressure values generated were still low in comparison to the registered data (Figures 4.13a and 4.13b). These results confirm the influence of another overpressure mechanism, which could reduce porosity and allow for the recreation of the high pore pressure values registered in this field.

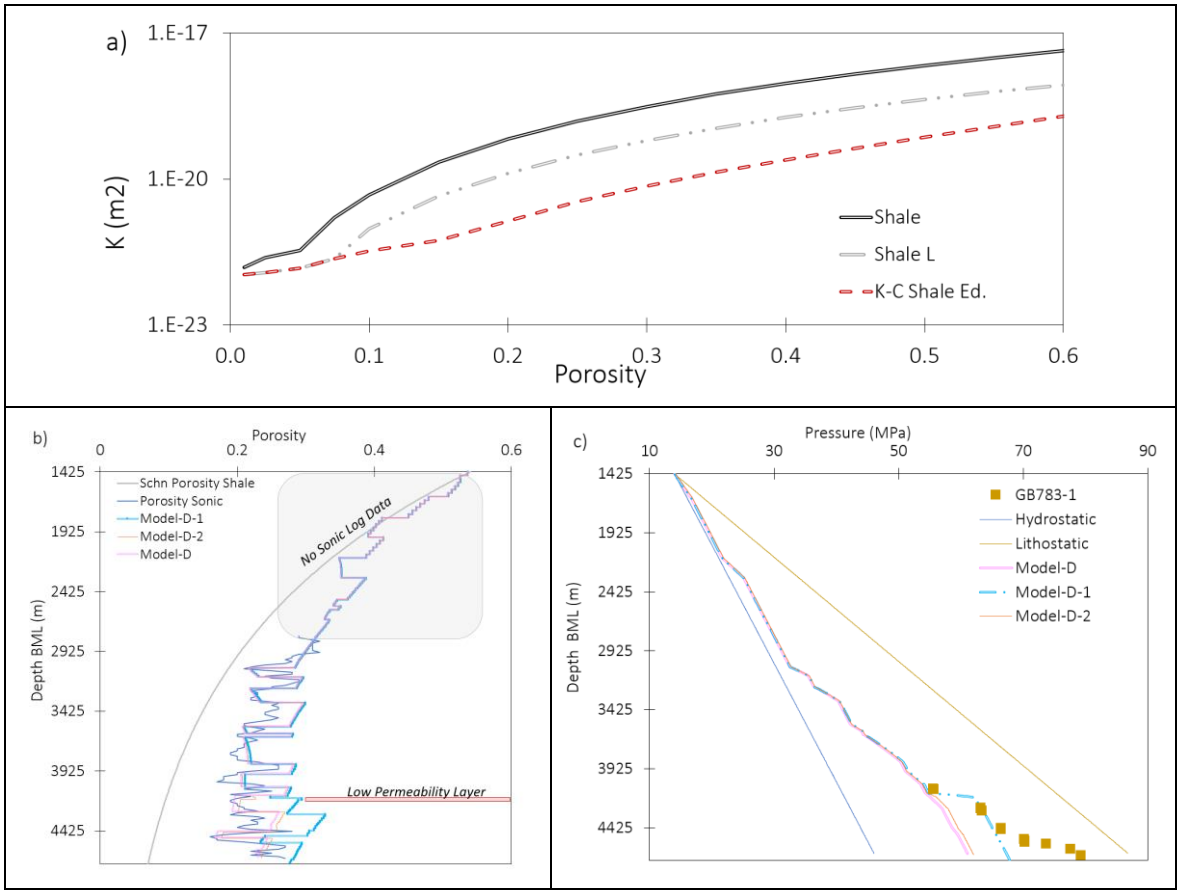

Figure 4.13.- a) Porosity-permeability relationships used in one shale layer. Model-D used the relationship shale in all the layers. The Model-D-1 used the relationship K-C Shale Ed. in one layer. The Model-D-2 used the relationship Shale L in one layer. b) Porosity vs. depth and c) pore pressure vs. depth plot showing the results of the three models.

4.4.2 2D Hydro-Mechanical Models Approach

To investigate the effects of disequilibrium compaction with salt tectonics and lateral pressure transfer on pore pressure, porosity, and stresses, as well as to predict the structural-stratigraphic evolution of the Titan mini-basin, a 2D section was constructed. The configuration of these models was based on the seismic cross-section of the current structure interpreted during this study (Figure 4.4). This section has a length of 13.2 km, which in the 2D models was extended to 20 km to represent the slope of the layers. This allowed the investigation of the influence of a high relief of the salt wall on pore pressure values.

The first step was to obtain the depositional thickness, which was achieved with a restoration model that used twenty layers to represent sediments from the Pliocene to the Pleistocene deposited over 3.6 Ma (Figure 4.14a). From this restoration model, the sedimentation thickness and location of the layers were obtained. However, to minimise machine-time consumption, speed up the calibration process, and reduce convergent problems during simulation, the shape of each layer was simplified. The total thickness (height of the sedimentary column) used in the 2D models was reduced to ~6 km with a length of 20 km (Figure 4.14b).

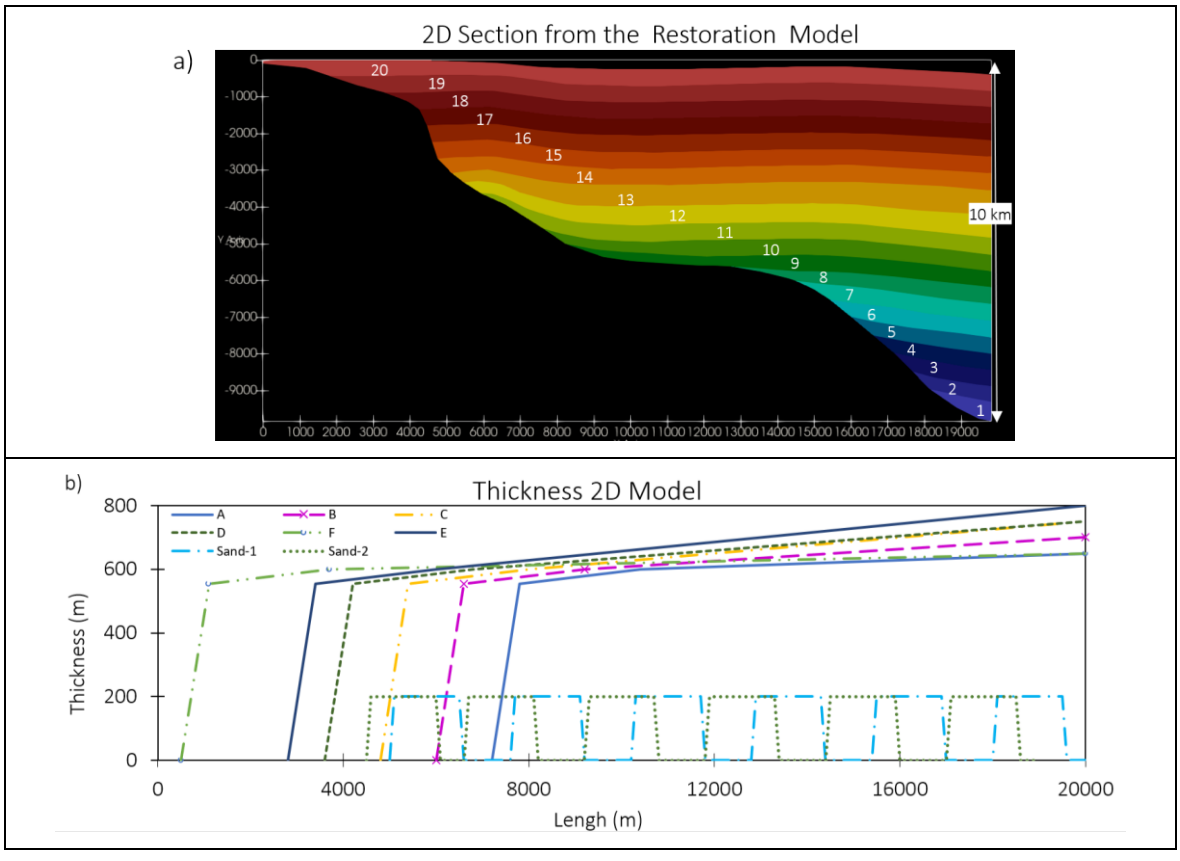

Figure 4.14.- a) Initial restoration model and b) simplified thicknesses used in the forward 2D model. The isolated sand-channels were represented with thicknesses sand-1 and sand-2. The thicknesses A, B, C, D, F and E were used more than once to reach the required thickness.

The 2D forward models were constrained at the base and sides to prevent perpendicular displacements, but this allowed for tangential displacement to the boundaries. The initial dimensions of the salt (first layer) were 20 km width and 6 km height, with deposition over 1 Ma. The two 2D

forward models were constructed and both have the same configuration, except for the second layer from the base. In Model-1, this layer was represented by sand lithologies, while in Model-2, this layer had shale lithologies.

The layers in these two 2D models were deposited from right to left to represent a progradation scenario. The models began with the sedimentation of the salt, followed by the sedimentation of the clastic sediments (thirteen layers of shale lithologies except for the second layer in Model-1, which has sand lithologies) over 3.6 Ma (2.58 Ma for Pleistocene and 1.02 Ma for Pliocene). Additionally, the effect of deep-water systems on pore pressure, which was represented by isolated sand-bodies (twelve), was investigated. To achieve this, two layers (four and six) containing these isolated bodies (sand channels) were added in both forward models. Table 4.5 summarises the configuration of these two 2D forward models.

Table 4.5.- Summary of the configuration of the two 2D forward models with the lithologies selected to represent each layer, sedimentation time, and initial porosity. Model-1 has a sand layer (second layer from the base) highlighted in grey, while Model-2 has a shale layer.

2D Models				
Period of Time	Clastic Layers	Time duration	Lithology	Initial Porosity
Pleistocene	15	0.2150	Shale	0.54
	14	0.2150	Shale	0.54
	13	0.2150	Shale	0.54
	12	0.2150	Shale	0.54
	11	0.2150	Shale	0.54
	10	0.2150	Shale	0.54
	9	0.2150	Shale	0.54
	8	0.2150	Shale	0.54
	7	0.2150	Shale	0.54
	6	0.2150	Sand Channel	0.45
	5	0.2150	Shale	0.54
	4	0.2150	Sand Channel	0.45
Pliocene	3	0.3400	Shale	0.54
	2	0.3400	Sand or Shale	0.45 or 0.54
	1	0.3400	Shale	0.54
		1	Salt	

During sedimentation, the weight of each layer displaced the salt which then started growing on the left side of the model (S), creating a salt wall. This then caused the sediment layers to dip increasingly, from horizontal to almost vertical near the growing salt wall as the basin started to sink. The layer's slope reached an angle of ~14 ° with the deepest side at the right side of the model (N).

High overpressure values were generated in the syncline formed due to the mobilised salt; its distribution was different in models 1 and 2. In Model-2 (shale second layer from the base; Figure 4.15a), the distribution of high overpressure values is wider along the layers than the distribution of the overpressures in Model-1 (sand second layer from the base; Figure 4.15b), where they are only located in a small area above the sand-layer on the right side of the model (N). In this model (Model-1), the overpressure generated in the syncline was transferred through the sand layer (high permeability), bringing high overpressure values to the intersection between the highest point of this layer and the salt wall (Figure 4.15b).

The shape of the salt wall is also different in each model. Model-2 (shale layer) created a relief of around 5,600 m at the deepest side, while Model-1 (sand layer) was 6,330 m. Additionally, Model-2 created a steeper salt wall than Model-1 (Figures 4.15a and 4.15b).

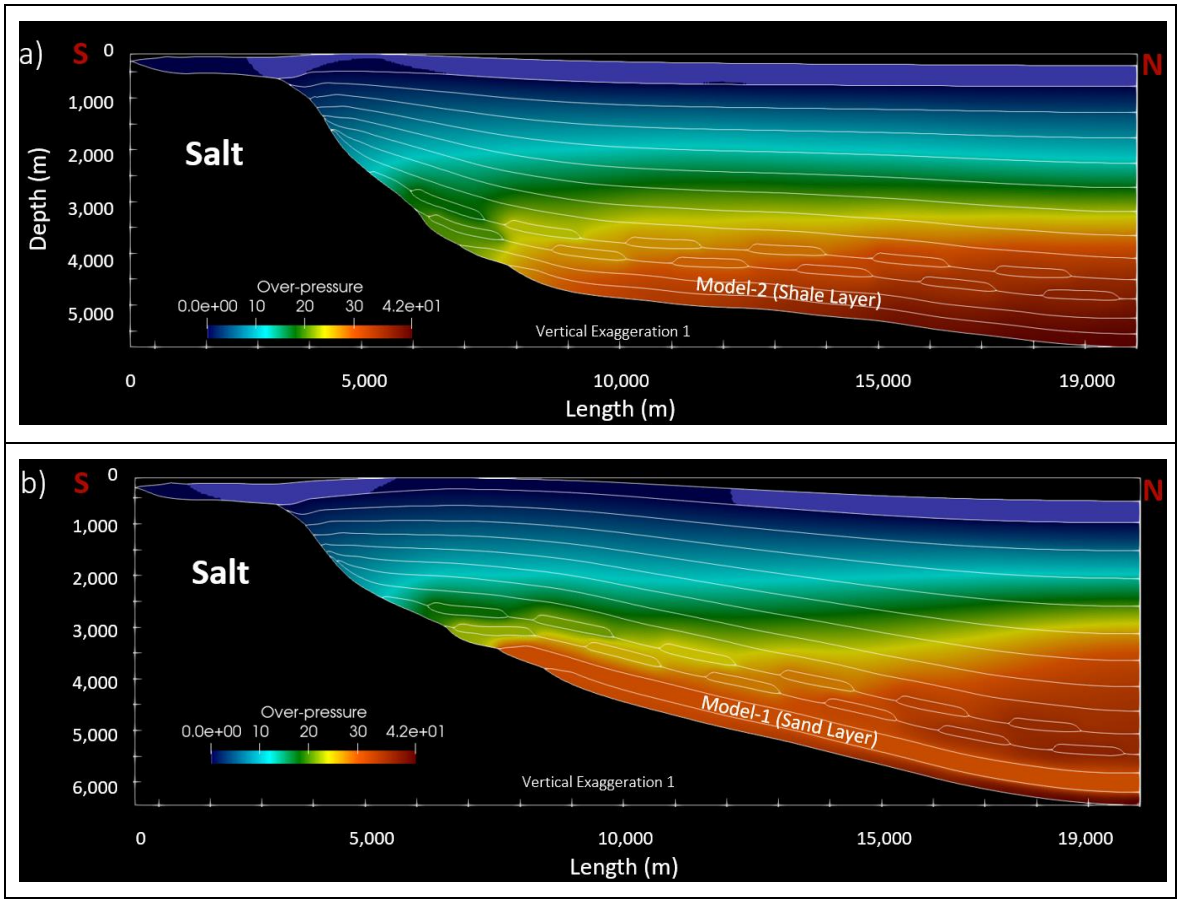

Figure 4.15.- a) Overpressure distribution of Model-2 (shale second layer from the base). b) Overpressure distribution of Model-1 (sand second layer from the base). An increase in overpressure with depth is observed in both models. Thirteen layers are represented by shale lithologies and two layers by isolated sand-channels. Model-1 has an extra sand layer.

Results from the horizontal to vertical effective stress ratio show a horizontal compression in most of the sediments of this basin (calid colours) (Figure 4.16). Salt tectonics have an influence on the sediments located close to the salt wall, but this was minimal in both models (Figure 4.16). The effective stress ratio is lithology-dependent in the absence of tectonic compression and has different values for each lithology (e.g., bulk modulus at deposition conditions (K_0) of sandstones is 0.73 and K_0 of shale is 0.83). Values of the horizontal to vertical effective stress ratio higher than 1 show that the horizontal effective stress is larger than the vertical stress (Figure 4.16).

Model-1 (sand layer; Figure 4.16b) shows two areas where the horizontal to vertical effective stress ratio values are higher than 1, around the lengths 19,000 and 8,000 m (depth >2,200 m around the sand layer). This was caused by the weight of the sediments (greater overburden of around 19,000 m) and the salt deformation (around 8,000 m) (red colours). There are also two areas where the horizontal to vertical effective stress ratio is lower than 1, above the salt wall length of 0 to 4,000 m and between the lengths 5,000 and 10,000 m (depth < 2,000 m). These low values are interpreted to be local horizontal extensions due to the salt growth resulting in an arching-related stretch of the sediments (blue colours). Model-2 shows a more constant horizontal compression along the basin with a small area above the salt wall where the horizontal to vertical effective stress ratio is lower than 1, similar to Model-1.

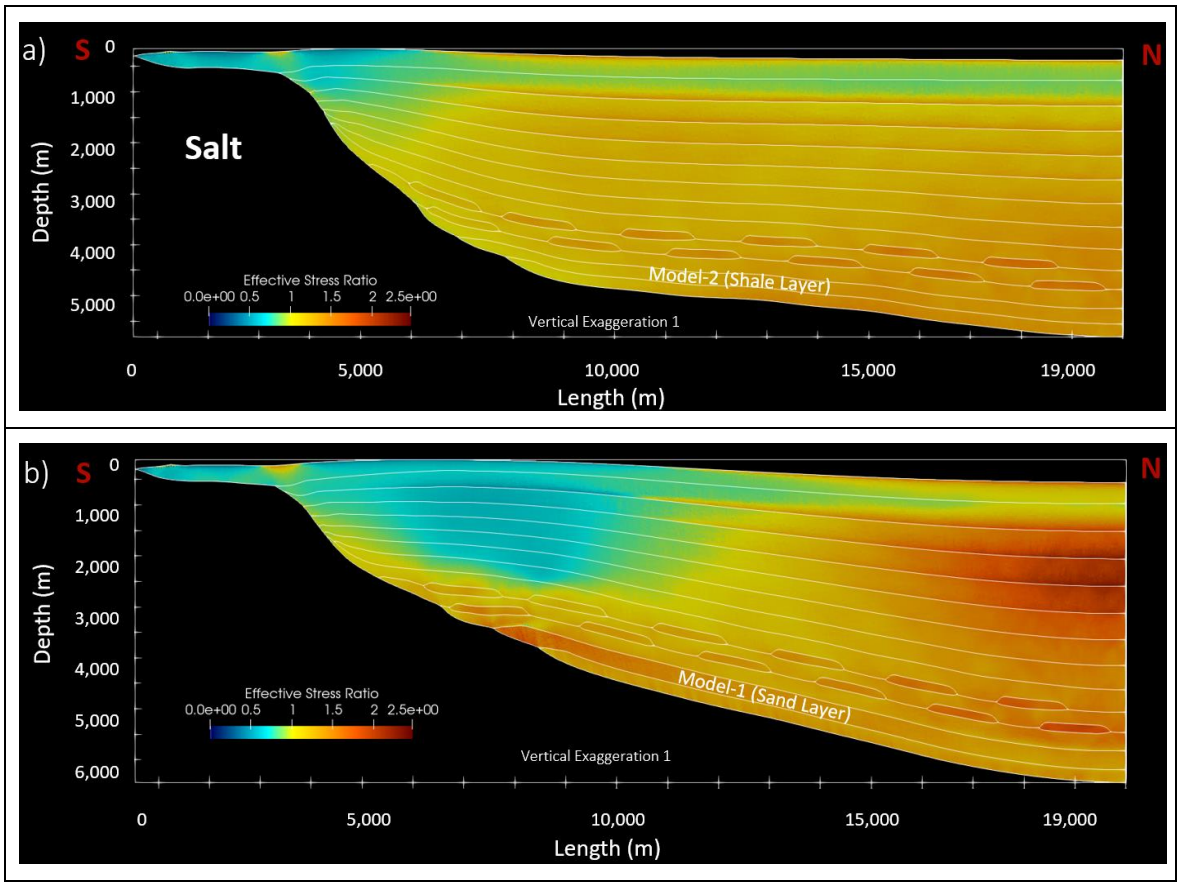

Figure 4.16.- a) Effective stress ratio (horizontal/vertical stress) distribution of Model-2 (shale layer). b) Effective stress ratio (horizontal/vertical stress) distribution of Model-1 (sand layer). Thirteen layers are represented by shale lithologies and two layers by isolated sand-channels. Model-1 has an extra sand layer. An effective stress ratio higher than 1 represents horizontal compression (calid colours).

4.4.3 Pore Pressures Along the Salt Wall

Similar to overpressure, pore pressure increased with depth in both models. Model-2 (shale layer; Figure 4.17b) and Model-1 (sand layer; Figure 4.17a) had the highest values at the thickest part of the model (right side of the models; N), with a value of ~110 MPa.

To see the differences in pore pressure along the salt wall, two locations (A and B) were selected. Position A is located at x = 11,000 m (Figures 4.17a and 4.17b), where the sedimentary column is 4,448 m (Model-1) and 4,649 m (Model-2) of Pliocene and Pleistocene sediments, respectively. Position B is located at x = 19,000 m at the deepest part of the model (the right side of the model) (Figures 4.17a and 4.17b), where the sedimentary column is 5,848 m (Model-1) and 5,396 m (Model-2) of Pliocene and Pleistocene sediments. The different thicknesses at the same locations are related to the overpressure generated in each model, which resulted in porosity preservation and less compaction and the shape of the salt wall.

To see the pore pressure differences, values taken at the second layer in both models are compared. The Model-1 (sand layer; Figure 4.17b) generated pore pressures of ~89 MPa at location B and ~76 MPa at location A, while the Model-2 (shale layer; Figure 4.17a) generated pore pressures of ~96 MPa at location B and ~80 MPa at location A. The pore pressure reduction in Model-1, which has a high permeability layer (sand layer; Figure 4.17b), is due to lateral pressure transfer from the deepest side of the model (N) to shallow depths (S) (Figure 4.18d).

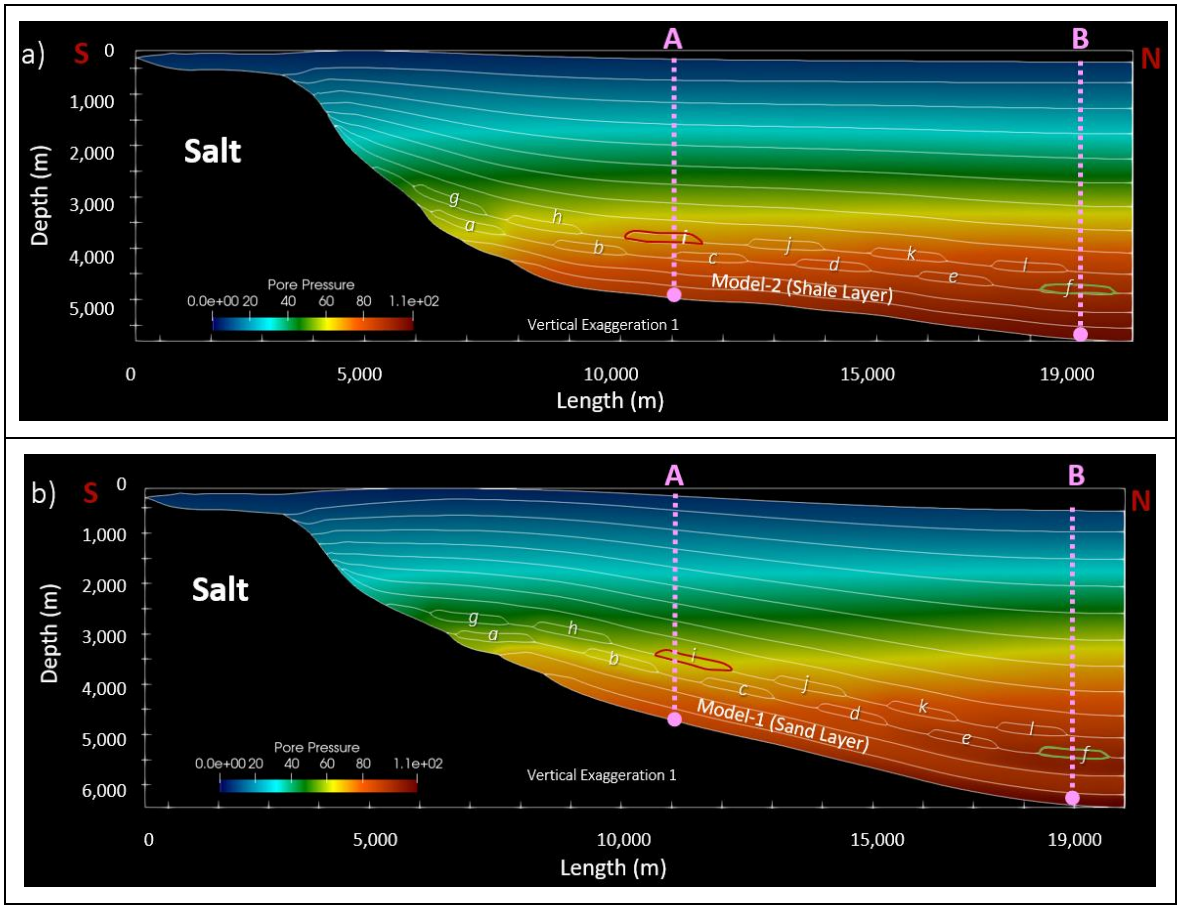

Figure 4.17.- a) Pore pressure distribution of Model-2 (shale layer). b) Pore pressure distribution of Model-1 (high permeability; sand layer).

Location A crossed one isolated sand-channel (i) at ~3,110 m depth in the Model-1 and at ~3,550 m depth in the Model-2 (Figure 4.18a). Location B crossed one isolated sand-channel (f) at ~4,875 m depth in Model-1 and at ~4,410 m depth in Model-2 (Figure 4.18b).

At position A, Model-1 had slightly fewer pore pressures in comparison to Model-2, which resulted in a slightly higher porosity preservation (Figures 4.18a and 4.18c). The opposite effect is observed at location B from around 1,000 m depth, where Model-2 had slightly lower pore pressures, resulting in less porosity preservation in comparison to Model-1 (Figures 4.18b and 4.18d).

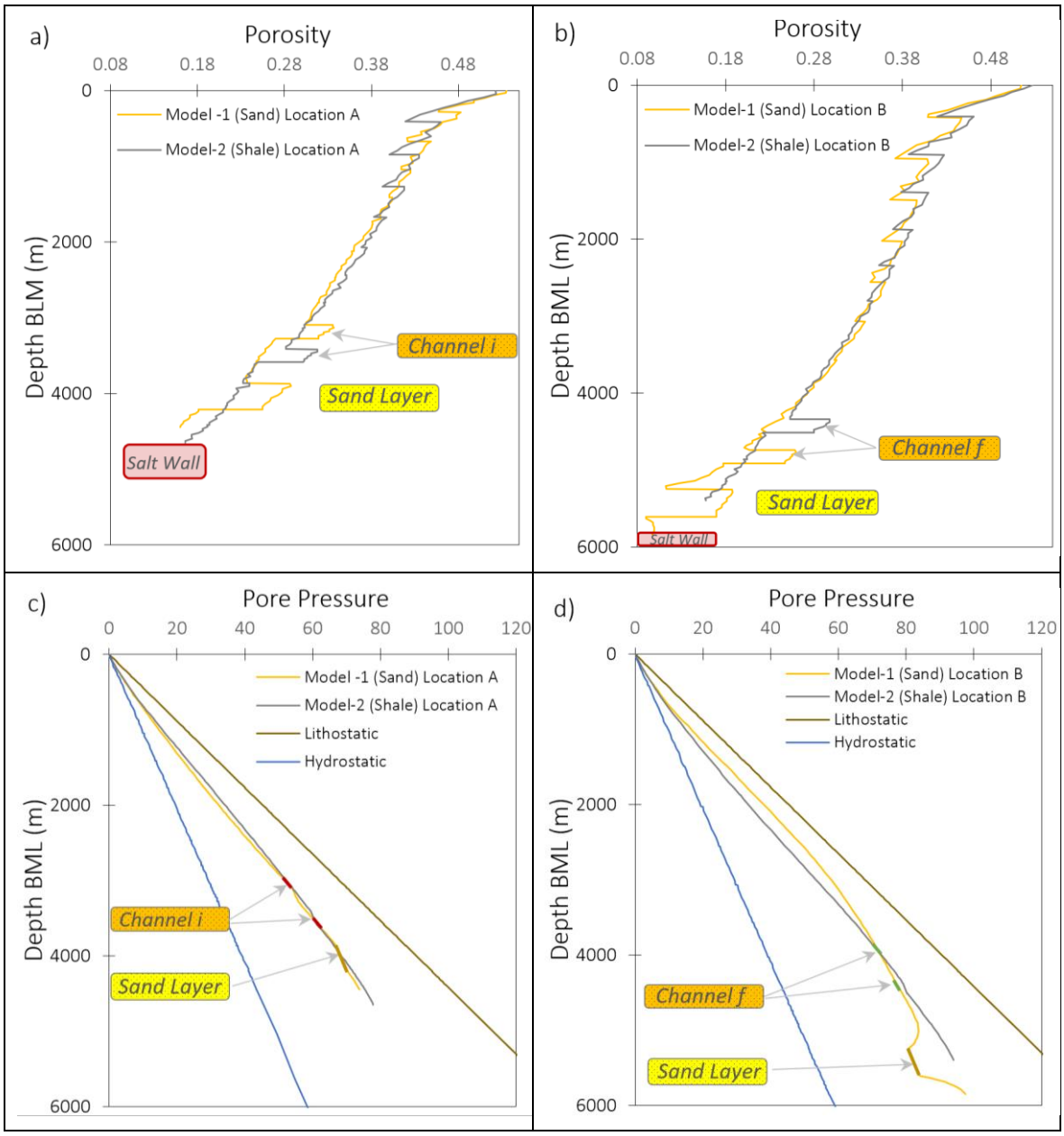

Figure 4.18.- a) Porosity results at the location A of Models 1 (sand layer) and 2 (shale layer). b) Porosity results at location B of Models 1 (sand layer) and 2 (shale layer). c) Pore pressure results at the location A of Models 1 (sand layer) and 2 (shale layer). d) Pore pressure results at location B of Models 1 (sand layer) and 2 (shale layer). Location A is close to the salt wall, while location B is on the deepest side of the models. For reference, values of 0.00995 MPa/m (0.4445 psi/ft) were used to represent a hydrostatic gradient and values of 0.0226 MPa/m (1 psi/ft) to represent a lithostatic gradient.

4.4.4 Sedimentary Environment and Overpressure Distribution

The sedimentary environment was investigated with the 2D models (Model-1 and Model-2). The deep-water system channels were represented by isolated sand-channels (twelve isolated sand-bodies) deposited in two layers. From these twelve sand-channels around four sand-channels represent the B-25 reservoir in the Magnolia Field. Each sand-channel has the same overpressure value throughout the whole section as they have high permeability, which allows a rapid distribution of the overpressure (Figure 4.19).

Overpressure increases with depth in both models. However, the influence of the continuous high permeability layer in Model-1 increased the overpressure of the sand-channels close to it (e.g., sand-channels g and a). The difference in overpressure registered in the B-25 reservoir is around 13 MPa (Figure 4.10b). The models generated around 8 MPa between the isolated sand-channels which represent the same reservoir in the Magnolia Field, and around 19 MPa between all the sand-channels modelled.

Although high compartmentalisation and high overpressure, similar to the registered data in the Magnolia Field, could be reproduced with these models, the uncertainty regarding overpressure distribution is high in this basin.

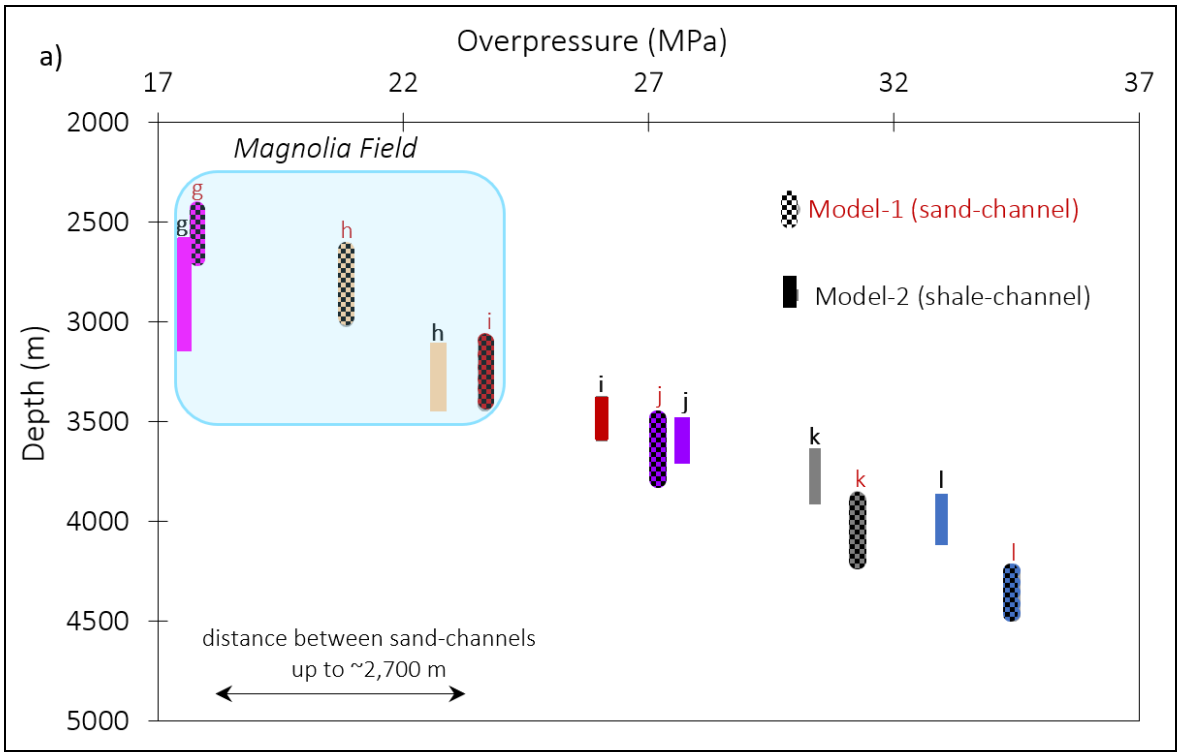

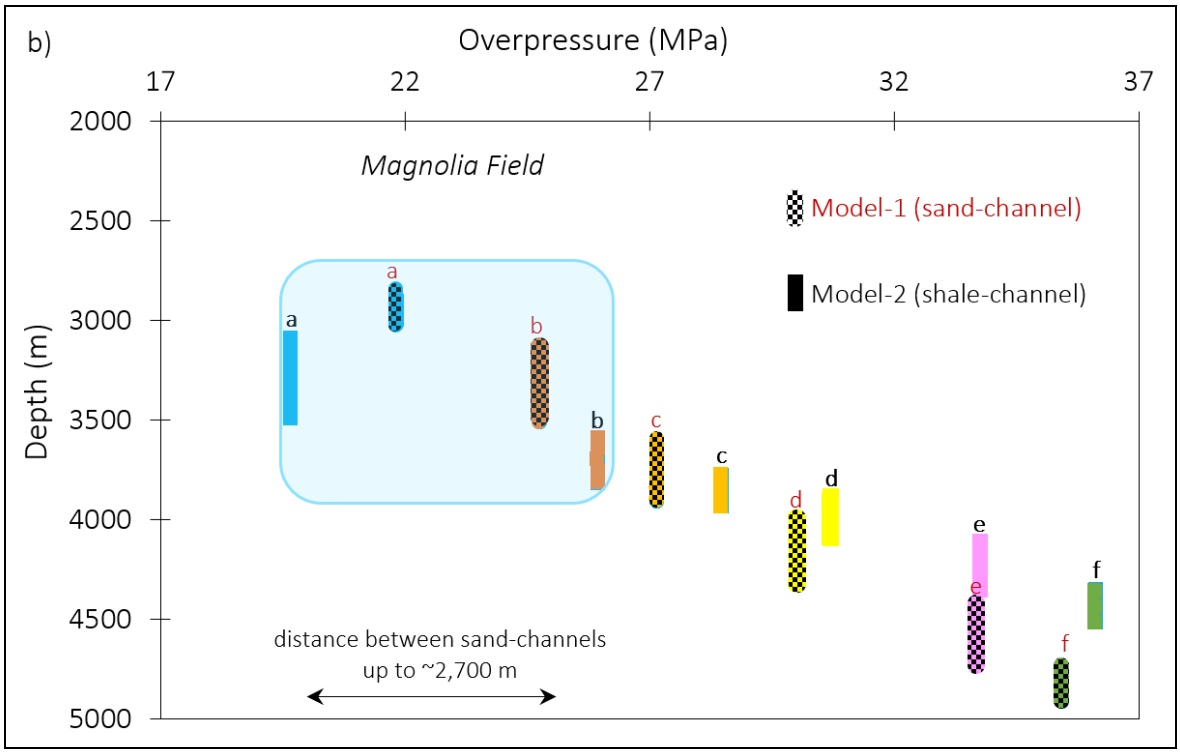

Figure 4.19.- Overpressure vs. depth plot of models 1 and 2. The a and g isolated channels are located close to the salt growth, which represent reservoirs interpreted in the GB783-1 well (reference Figure 4.20).

4.4.5 Quantification of Overpressure in the Magnolia Field

To quantify the contribution of each overpressure mechanism investigated during this research, the 2D and 1D hydro-mechanical models were used. The 1D model investigated disequilibrium compaction. The 2D Model-2 investigated disequilibrium compaction and tectonic compression (due to the salt movement), and the 2D Model-1 investigated, in addition, lateral pressure transfer from deep intervals through a high permeability layer (sand layer).

A line named Well, located at x = 7,050 m in the Model-2 (shale layer) and at x = 7,610 m in the Model-1 (sand layer) was used in the 2D models for this analysis. This location crossed two of the isolated sand-channels named T and U (Figures 4.20a and 4.20b). These results were compared with the 1D model, which has similar model settings.

Results showed that when disequilibrium compaction, salt growth, and lateral pressure transfer act together, high pore pressures similar to those measured in well GB783-1 can be generated (Figure 4.20). From the plotted data, it is observed that disequilibrium compaction is the main overpressure mechanism, accounting for an estimated 74% of the total overpressure, followed by lateral pressure transfer with 16% and salt tectonics with 9% (Figure 4.20).

These percentages were calculated at 3,000 m depth BML (Figure 4.20). It is important to highlight that the results from these models may also be influenced by the high salt relief, the stretching-arch shape generated by the salt growth (Model-1), and the high angle of the layers (14 °). However, the extent of these factors could not be fully accounted for.

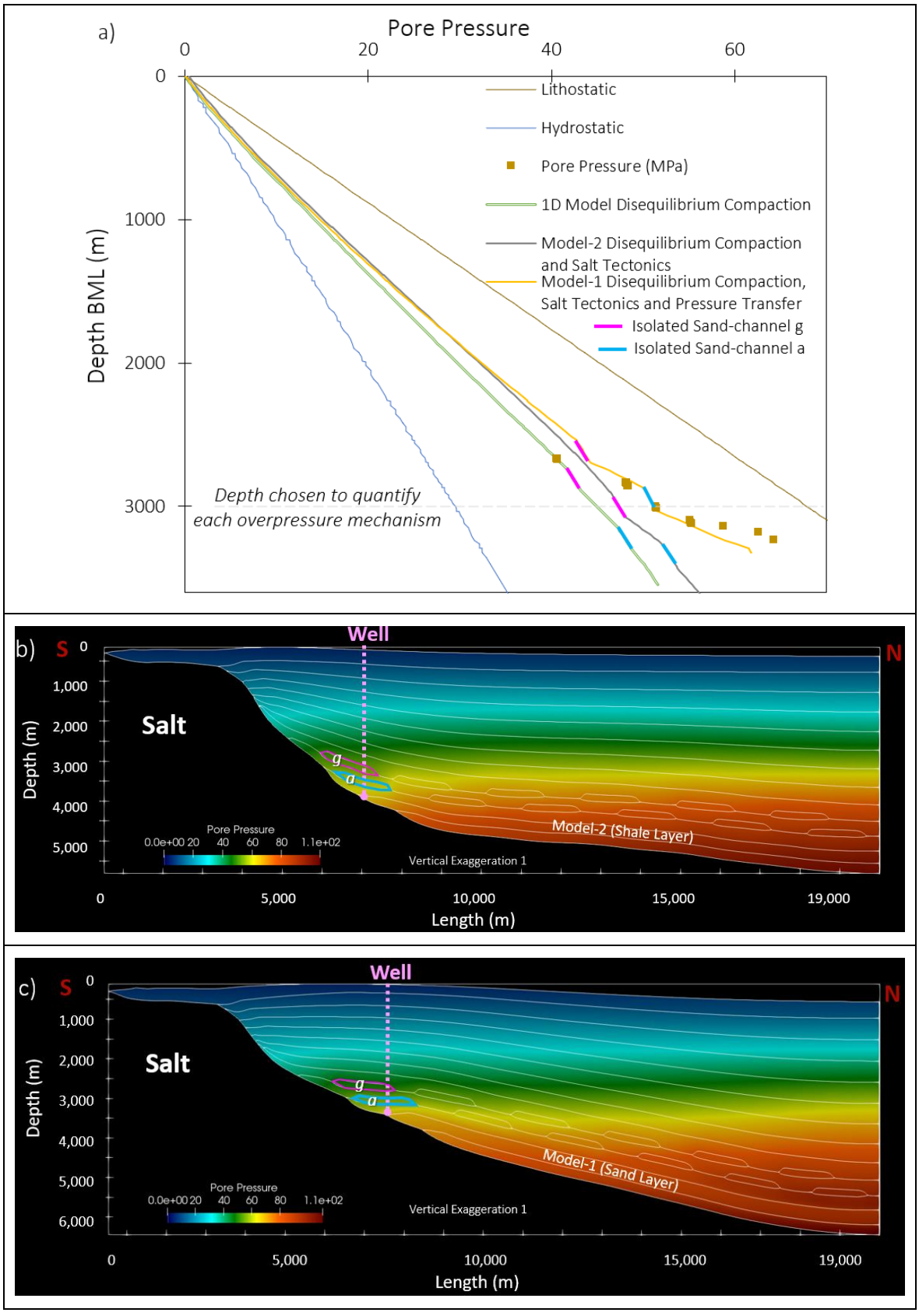

Figure 4.20.- a) Pore pressure vs. depth plot with results from model 1D, which accounted for disequilibrium compaction, Model-2, which accounted for disequilibrium compaction and salt tectonics and Model-1 which accounted for disequilibrium compaction, salt tectonics, and lateral pressure transfer. b) Pore pressure distribution of the results of Model-2. c) Pore pressure distribution of the results of the Model-1. The isolated sand-channels a and g are highlighted for reference.

4.5 Discussion

4.5.1 Effect of High Sedimentation Rates of Mud-dominated Lithologies on Overpressure

As previously highlighted (e.g., Dickinson, 1953; Mello and Karner, 1996; Katahara, 2003; Ostermeier et al., 2001), the main overpressure mechanism in the Gulf of Mexico Basin was identified as disequilibrium compaction due to the high sedimentation rate of mud-dominated lithologies. This mechanism is also called under compaction, and it is caused when the vertical stress increases during loading and the sediments cannot release the fluid at the same rate (Osborne and Swarbrick, 1997). During this research, disequilibrium compaction was also determined to be the main overpressure-generating mechanism in the Magnolia Field. This was concluded through a log-based interpretation and geomechanical modelling.

The high sedimentation rates (~1,650 m/Ma) of mud-dominated lithologies deposited over the Miocene to present-day, preserved high porosities up to an average of 0.27 (core data of well GB783-2ST2) in the reservoirs of the Magnolia Field. The analysis of the sonic log response with a standard Eaton exponent of 3, which was developed to predict pore pressure due to mechanical compaction loading (Eaton, 1975), gives reasonable agreement with the observed pore pressure data (Figure 4.8), indicating that disequilibrium compaction could be identified by log data in this basin. However, this simple approach cannot be used to distinguish between different mechanisms acting at the same time and nor their individual contributions.

1D hydro-mechanical models were constructed to investigate this overpressure mechanism during this research. Results show that disequilibrium compaction can generate overpressure due to the high sedimentation rates. However, the amount of overpressure generated also depends on the permeability relationships used in the models.

In the Magnolia Field, there were available permeability data for the B-25 reservoir (sandstone and siltstone lithologies); therefore, the classical Kozeny-Carman relationships for shale, siltstone, and sandstone lithologies were adopted and used in the models. The porosity-permeability relationship Shale, which is 40.5 higher than the shale Kozeny-Carmen relationship, was initially used in the 1D models. The overpressure generated when this relationship was used was low (58 MPa) in comparison to the registered data (63 MPa). The values were taken at 4,300 m BML (Figure 4.12b).

To generate more overpressure, low-permeability relationships were investigated. Results show that low porosity-permeability relationships can generate high overpressure, almost similar to the registered in the Magnolia Field. However, if a low-permeability relationship were used, high porosities up to 0.37 would be preserved, which does not agree with the data of this field.

4.5.2 Overpressure Compartmentalisation in the Magnolia Field.

Pore pressure data show that the Magnolia Field has vertical and horizontal compartmentalisation at both reservoir and field scales. Previous studies (e.g., Weissenburger and Borbas, 2004; Stomp et al., 2004; Procyk et al., 2007; Zane et al., 2012; Heidari et al., 2019) have attributed this compartmentalisation to lithological heterogeneity due to the sedimentary environment and the syn

and post effect, of salt tectonics on the sediments. McCarthy et al. (2006) determined through geostatistical inversion of rock properties that the Magnolia Field has two areas: one named the eastern province (the steepest side of the salt wall), which has more compartmentalised sand intervals with gas-rich fluids, and a second named the western province, where the sand intervals are thicker and more connected with oil-rich fluids. Jackson and Hudec (2017) interpreted at least four different processes in the sediments close to salt walls that could increase barriers in the sedimentary column (e.g., bedding rotation, shale sheath, large strains, and shear zones). Kane et al. (2012), during the analysis of core and seismic data from the Magnolia Field, also suggested that salt tectonics has affected the sediment distribution and their characteristics.

To identify if the salt wall has any effect on the sedimentary column, the distance from the salt wall to the wells at the B-25 reservoir was reviewed. This analysis revealed that the wells (e.g., GB783A4, GB783-A5, GB783-2ST, GB783-2, and GB783-3ST) exposed to an almost vertical salt wall have the highest overpressures at this reservoir (Figures 4.5a and 4.10b). Although the extension of which of these two processes (sedimentary environment and salt movement) has the greatest effect on the sediment heterogeneity could not be identified during this study, the high overpressure compartmentalisation in the Magnolia Field is interpreted to be related to a combination of both. Salt tectonics changed the shape of the sedimentary layers from horizontal to almost vertical (e.g., seismic reflectors close to the salt wall) and increased the soft-sediment deformation already caused by the sedimentary environment (e.g., convolute, distorted, slump structures).

Salt tectonics have certainly contributed to the high compartmentalisation of the Magnolia Field, but the effect on pore pressure is difficult to quantify due to the high sedimentation rate of the mud-dominated lithologies deposited during the Pliocene to present-day which masks the overpressures generated. Therefore, 1D and 2D models were used with different settings (e.g., disequilibrium compaction alone, disequilibrium compaction and tectonic compression, and disequilibrium compaction, tectonic compression, and lateral pressure transfer) to investigate the contribution of each overpressure mechanism.

4.5.3 Impact of Salt Walls on Overpressure

The influence of a growth salt wall has been explored in previous studies (e.g., Luo et al., 2012 and 2015; Nikolinakou et al., 2018), suggesting that high overpressure values can be generated during the growth of salt. Results from the 2D model (Model-2), which accounted for tectonic compression due to salt tectonics and disequilibrium compaction, show that overpressure increased due to the growing salt wall. However, the values obtained were not as high as suggested by previous studies. This difference is attributed to the configuration of the models. As highlighted by Obradors-Prat et al. (2023), the configuration of the models can play a key role in the exact places where pore fluid pressure increases due to the movement of the salt. Furthermore, as described by Jackson and Hudec (2017), salt behaviour is unpredictable, and any change in the density of the sediments, temperature, thicknesses, or connectivity can result in different overpressure values.

The results from the geomechanical modelling suggested that 9% of the total overpressure encountered in the Magnolia Field was due to the growing salt wall.

4.5.4 Lateral Pore Pressure Transfer from Deep Intervals

Overpressure increases with depth in the Magnolia Field, but there are shallow intervals with higher overpressure values than deep intervals. These intervals were mapped during this research and are located close to the salt wall. For instance, the B-25 reservoir of the well GB783-A4 has the highest overpressure in this reservoir (~28 MPa) (Figure 4.10b). The high overpressure values could not be matched with disequilibrium compaction nor tectonic compression caused by the salt growth; therefore, lateral pore pressure transfer was investigated.

To investigate this mechanism, a continuous high-permeability layer was used in Model-1, which represents the connectivity between stacked isolated sand-channels. The 2D models suggested that overpressures generated in deep units (the deepest part of the syncline; Figure 4.15b) were brought to shallow depths through the high permeability continuous layer. In addition, the high-permeability layer has an influence on the salt wall geometry at the deepest and shallowest sides of the models. Model-1 (sand layer) created a high-slope salt wall with layers dipping around ~14 ° at the deepest side of the model, in contrast to the slope of the layers in Model-2 (shale layer), which created only ~2.8 °. Model-2 generated a stepper salt wall around the Magnolia Field than Model-1.

This mechanism was previously investigated by Heidari et al. (2019) with 2D forward finite-element models, suggesting that the high overpressure values observed at the top of the high permeability layer close to the salt wall in the 2D forward finite-element models were transferred along the high permeability layer from deep intervals and that the high permeability continuous layer increased the salt wall rise, creating a steeper salt wall. The second conclusion is different from the results obtained during this research, where the slope of the salt increased at the deepest side of the model but did not generate a steeper salt wall. This difference between these two studies is interpreted to be related to the model settings. Heidari et al. (2019) deposited the layers over 40 Ma, reaching a thickness of 11 km, while the models of this research represent the time and thicknesses interpreted around the Magnolia Field (~6 km deposited in 2.708 Ma).

4.6 Conclusions

Results from the hydro-mechanical models and log-based interpretation suggested that the present-day overpressures encountered in the Magnolia Field were generated mainly by disequilibrium compaction due to the high sedimentation rate of mud-dominated lithologies (>1,600 m/Ma) deposited over 3 Ma. This overpressure-generating mechanism was determined to have contributed to around 74% of the total overpressure encountered in data of this field.

The high compartmentalisation of the reservoirs of the Magnolia Field is interpreted to be a combination between the sedimentary environment and the salt tectonic processes that created barriers and baffles (e.g., more soft sedimentary structures, reservoir scale faults, and high-angle bedding), increasing low-permeability intervals.

The 2D hydro-mechanical modelling, which allowed the analysis of overpressure evolution related to fluid flow, suggested that 9% of the total overpressure encountered in the reservoirs of the Magnolia Field is due to tectonic compaction caused by salt wall growth.

Lateral pore pressure transfer through high permeability connected layers is interpreted to have played a significant role in the present-day overpressure of the Magnolia Field. Results from the 2D models suggested that this mechanism contributed to 16% of the total overpressure registered in this field. This percentage was obtained from the 2D hydro-mechanical model (Model-1), which accounted for a high permeability layer represented by sand lithologies. This layer connected the overpressure generated at the deepest units to shallow depths.

The uncertainty related to overpressure distribution in basins similar to the Titan min-basin could be mitigated with hydro-mechanical modelling, but it would remain high due to the complex sedimentary environment and the unpredictable shape of the salt wall.

4.7 References

Athy, L. F. (1930). Density, porosity, and compaction of sedimentary rocks. AAPG Bulletin, 14(1), 1-24.

Audet, M. D. (1996). Compaction and overpressuring in Pleistocene sediments on the Louisiana Shelf, Gulf of Mexico, *Marine and Petroleum Geology*, 467-474.

Beers, R. F. (1945). Radioactivity and organic content of some Palaeozoic shales, *AAPG Bulletin,* 29*,* 1-22.

BOEM Bureau of Ocean Energy Management (2021). Available at https://bobson.maps.arcgis.com/apps/webappviewer/index.html?id=a4b1e09480d244188f531dfe0162cff8, (Accessed on November-2021).

BOEM Bureau of Ocean Energy Management (2020). *HPHT Production in the Gulf of Mexico (042).*

Bowers, G. L. (1995). Pore pressure estimation from velocity data: accounting for overpressure mechanisms besides undercompaction, *SPE Drilling and Completion*, 89-95.

Bowers, G. L. (2001). Determining an appropriate pore-pressure estimation strategy, Offshore Technology Conference, Houston, Texas. April 2001. *OnePetro*, 1-14.

Bowers, G. L. and Katsube, T. J. (2002). The role of shale pore structure on the sensitivity of wire-line logs to overpressure, in Huffman, A. R. and Bowers, G. L. (eds.) *Pressure regimes in sedimentary basins and their prediction*. AAPG, 43-60.

Bredehoeft, J. D. and Hanshaw, B.B. (1968). On the Maintenance of Anomalous Fluid Pressures: Thick Sedimentary Sequences, *Geological Society of America Bulletin*, 79, 1097–1106.

CoreLab (2003). Petrographic Analysis of Conventional Core Samples from: ConocoPhillips OCS-G 11573, #2 ST-2, Garden Banks 783, Offshore Louisiana.

Colwart, G., Burton, R. C., Eaton, L. F., Hodge, r. M and Blake, K. (2007). Lessons Learned on Sand-Control Failure and Subsequent Workover at Magnolia Deepwater Development, *SPE*, 1-17.

Colwart, G., Burton, R. C., Eaton, L. F., Hodge, R. M. and Blake, K. (2009). Lessons Learned on Sand-Control Failure and Subsequent Workover at Magnolia Deepwater Development, *SPE*, 144-156.

Christie, C. H. and Nagihara, S. (2016). Geothermal gradients of the northern continental shelf of the Gulf of Mexico, *The Geological Society of America*, 12(1), 26-34.

Crook, A. J. L., Obradors-Prats, J., Somer, D., Peric, D., Lovely, P. and Kacewicz, M. (2018). Towards an integrated restoration/forward geomechanical modelling workflow for basin evolution prediction. Oil and Gas Science and Technology - Rev. *IFP Energies Nouvelles*, 73, 1-19.

Dickinson, G. (1953). Geological Aspects of Abnormal Reservoir Pressures in Gulf Coast Louisiana, *The American Association of Petroleum Geologist*, 37, 410-432.

Eaton, B., A. (1975). The Equation for Geopressure Prediction from Well Logs, *SPE*, 1-11.

Eaton, L. F., Actis, s. C. and Williamson, R. N. (2005). Deepwater Batchset Operations Through the Magnolia Shallow Water Flow Sand, *SPE*, 1-20.

Hart, B. S., Flemings, P. B. and Desphpande, A. (1995). Porosity and pressure: Role of compaction disequilibrium in the development of geopressures in a Gulf Coast Pleistocene basin. *AAPG Bulletin*, 23, 45-48.

Heidari, M., Nikolinakou, M. A, Hudec, M. R. and Flemings, P. B. (2019). Influence of a reservoir bed on diapirism and drilling hazards near a salt diapir: a geomechanical approach, *Petroleum Geoscience*, 282-297.

Herschel, W. H. and Bulkley, R. (1926) Konsistenzmessungen von Gummi-Benzollösungen. *Kolloid-Zeitschrift* 39, 291-300. doi.org/10.1007/BF01432034

Gardner, G. H. F., Gardner, L. W. and Gregory, A. R. (1974). Formation velocity and density - the diagnostic basics for stratigraphic traps. *Geophysics*, 39(6), 770-780.

Green, S. and Vernik, L. (2020). Correcting density/sonic logs for total organic carbon to reduce uncertainty in pore pressure prediction, *Geophysical Prospecting*, 69, 586-597.

Hansen, S. (1996). A compaction trend for Cretaceous and Tertiary shales on the Norwegian Shelf based on sonic transit times. *Petroleum Geoscience*, 2, 159-166.

Hood, K. C., Wenger, L. M., Gross, O. P. and Harrison, S. C. (2002). Hydrocarbon systems analysis of the northern Gulf of Mexico: Delineation of hydrocarbon migration pathways using seeps and seismic imaging, in Schumacher, D. and LeSchack, L. A. (eds.) *Surface exploration case histories: Applications of geochemistry, magnetics, and remote sensing*, AAPG Studies in Geology No. 48 and SEG Geophysical References Series No. 11, 25-40.

Hottmann, C. E. and Johnson, R. E. (1965). Estimation of Formation Pressures from Lo-Derived Shale Properties, *Journal of Petroleum Technology*, 17, 717-722.

Hudec, M. R., Norton, I. O., Jackson, M. P. A. and Peel, F. J. (2013). Jurassic evolution of the Gulf of Mexico salt basin, *The American Association of Petroleum Geologist*, 97(10), 1683-1710.

Issler, D. R. (1992). A new approach to shale compaction and the stratigraphic restoration, Beaufort-Mackenzie Basin and Mackenzie Corridor, Northern Canada. *AAPG Bulletin,* 76(8), 1170-1189.

Jackson, M. P A. and Hudec, M. (2017). Salt Welds, in *Salt Tectonics: Principles and Practice*. Cambridge: Cambridge University Press, 229-254. doi:10.1017/9781139003988.012

Katahara, K. (2003). Analysis of overpressure on the Gulf of Mexico Shelf, *SPE*, 1-10.

Katahara, K. (2006), Overpressure and shale properties: Stress unloading or smectite-illite transformation?, *SEG*, 1520-1524.

Kane, I. A., McGee, D. T. and Jobe, Z. R. (2012). Halokinetic effects on submarine channel equilibrium profiles and implications for facies architecture: conceptual model illustrated with a case study from Magnolia Field, in Alsop, G. I., Archer, S. G., Hartley, A. J., Grant, N. T and Hodkinson, R. (eds.) *Salt Tectonics, Sediments and Prospectively*. London, 289-302.

Galloway, W. E. (1989). Genetic Stratigraphic Sequences in Basin Analysis II: Application to Northwest Gulf of Mexico Cenozoic Basin. *The American Association of Petroleum Geologist*, 73(2), 143-154.

Galloway, W.E. and Hobday, D. K. (1996). Terrigenous Clastic Depositional Systems: Applications to Fossil Fuel and Groundwater Resources in Fleischhacker, W. W. and Brooks, D. J. (eds.) *Addiction. Mechanisms, Phenomenology and Treatment*, Springer Berlin / Heidelberg Berlin. Available from: ProQuest Ebook Central. [8 December 2021].

Galloway, W. E. (2008). Depositional Evolution of the Gulf of Mexico Sedimentary Basin, in Hsü, K. J. (ed.) *Sedimentary Basins of the World, Vol 5, The Sedimentary Basins of the United States and Canada, Andrew D. Miall*, The Netherlands, Elsevier, 505–549.

Galloway, W. E., Whiteaker, T. L. and Ganey-Curry, P. (2011). History of Cenozoic North American drainage basin evolution, sediment yield, and accumulation in the Gulf of Mexico basin. *The Geological Society of America*, 7(4), 938-973.

Lahann, R. W. and Swarbrick, R. E. (2011). Overpressure generation by load transfer following shale framework weakening due to smectite diagenesis, *Geofluids*, 11, 362-75.

Liaw, A., Kan, T. K., Kennedy, N., Belk, K. and Gallice, F. L. (2007). Integrated Pore Pressure Prediction in Gunnison Field, *SEG*, 388-392.

Lopez, J. L., Rappold, P. M., Ugueto, G. A., Wieseneck, J. B. and Vu, C. K. (2004). Integrated shared earth model: 3D pore-pressure prediction and uncertainty analysis, *The Leading Edge*, 52-59.

Luo, G., Nikolinakou, M. A., Flemings, P. B. and Hudec, M. R. (2012). Geomechanical modelling of stresses adjacent to salt bodies: Part 1- Uncoupled models, *AAPG*, 96(1), 43-64.

Luo, G., Flemings, P. B., Hudec, M. R. and Nikolinakou, M. A. (2015). The role of pore fluid overpressure in the substrates of advancing salt sheets, ice glaciers, and critical-state wedges, *Journal of Geophysical Research: Solid Earth*, 120, 87-105.

Luo, G., Hudec, M. R., Flemings, P. B. and Nikolinakou, M. A. (2017). Deformation, stress, and pore pressure in an evolving suprasalt basin, *Journal of Geophysical Research: Solid Earth*, 122, 5663-5690.

Meng, J., Pashin, J., Chandra, A. Xue, L., Sholanke, S. and Spears, J. (2020). Structural framework and fault analysis in the east-central Gulf of Mexico shelf: Implications for offshore CO_2 storage, *Journal of Structural Geology*, 134,1-16.

McGee, D. T., Fitzsimmons, R. F. and Haddad, G. A. (2005). From Fill to Spill: Partially Confined Depositional Systems, Magnolia Field, Garden Banks, Gulf of Mexico, *Proceedings of the SEG Annual Meeting*, Houston. U. S. A. 6th -11th November 2005. Society of Exploration Geophysicists. 2297-2299.

Mello, U. T. and Karner, G. D. (1996). Development of Sediment Overpressure and Its Effect on Thermal Maturation: Application to the Gulf of Mexico Basin, *AAPG Bulletin*, 80(9), 1367-1396.

Meyer, B. L. and Nederlof, M. H. (1984). Identification of Source Rocks on wireline Logs by Density/Resistivity and Sonic Transit Time/ Resistivity Crossplots, *AAPG Bulletin*, 68, 121-129.

Nikolinakou, M. A., Flemings, P. B., Heidari, M. and Hudec, M. R. (2018). Stress and pore pressure in mudrocks bounding salt systems. *Rock Mechanics and Rock Engineering*, 51, 3883-3894.

Ostermeier, R. M., Pelletier, J. H., Winter, C. D., Nicholson, J. W., Rambow, F. H. and Cowan K. M. (2000). Dealing with Shallow-Water Flow in the Deepwater Gulf of Mexico, *SPE*, 1-12.

Ostermeier, R. M., Pelletier, J. H., Winter, C. D. and Nicholson, J. W. (2001). Trends in Shallow sediment Poore Pressures- Deepwater Gulf of Mexico, *SPE*, 1-12.

Obradors-Prats, J., Rouainia, M., Aplin, A. C. and Crook, A. J. L. (2016). Stress and pore pressure in complex tectonic settings predicted with coupled, 3D geomechanical-fluid flow models. *Marine and Petroleum Geology*, 76, 464-477.

Obradors-Prats, J., Rouainia, M., Aplin, A. C. and Crook, A. J. L. (2017a). Assessing the implications of tectonic compaction on pore pressure using a coupled geomechanical approach. *Marine and Petroleum Geology*, 79, 31-43.

Obradors-Prats, J., Rouainia, M., Aplin, A. C. and Crook, A. J. L. (2017b). Hydromechanical modeling of stress, pore pressure, and porosity evolution in fold-and-thrust belt systems. *Journal of Geophysical Research: Solid Earth*, 122(11), 9383-9403.

Obradors-Prats, J., Rouainia, M., Aplin, A. C. and Crook, A. J. L. (2019). A diagenesis model for geomechanical simulations: formulation and implications for pore pressure and development of geological structures. *Journal of Geophysical Research: Solid Earth*, 124(5), 4452-4472.

Pindell, J. L. (1985). Alleghenian Reconstruction and Subsequent Evolution of the Gulf of Mexico, Bahamas, and Proto-Caribbean, *Tectonics*, 4, 1-39.

Pinkston, F. W. and Flemings, P. B. (2019). Overpressure at the Macondo Well and its impact on the Deepwater Horizon blowout, *Scientific Reports*, *1-19.*

Procyk, A. D., Jamieson, D. P., Miller, J. A., Burton, R. C., Hodge, R. M. and Morita, N. (2007). Completion Design for a Highly Compacting Deepwater Field, *Proceedings of the SPE Annual Technical Conference and Exhibition*, Anaheim, California, U.S.A., November. 2007. Society of Petroleum Engineers. 1-21.

Raymer, L. L., Hunt, E. R. and Gardner, J. S. (1980). An improved sonic transit time-to-porosity transform, *OnePetro*, 1-13.

Rowan, M. G., Muñoz, J. A., Giles, K. A., Roca, E., Hearon IV, T., E., Fiduk, J. C., Ferrer, O. and Fisher, M. P. (2020). Folding and fracturing of rocks adjacent to salt diapirs, *Journal of Structural Geology*, 141, 1-30.

Sathar, S. and Jones, S. (2016). Fluid overpressure as a control on sandstone reservoir quality in a mechanical compaction dominated setting: Magnolia Field, Gulf of Mexico, *Terra Nova*, 28, 155-162.

Schlumberger. (1989). *Log interpretation principles/applications*. Houston, Texas: Schlumberger Educational Services.

Snedden, J. W. and Galloway, W. E. (2019). The Gulf of Mexico Sedimentary Basin: Depositional Evolution and Petroleum Applications, Cambridge: Cambridge University Press.

Schneider, F., Burrus, J. and Wolf, S. (1993). Modelling overpressures by effective-stress/porosity relationships in low-permeability rocks: Empirical artifice or physical reality, in Doré, A. G. et al., (eds.) *Basin Modelling: Advances and Applications*, 333-341.

Schmoker, J. W. (1981). Determination of Organic-Matter Content of Appalachian Devonian Shales from Gamma-Ray Logs, *AAPG Bulletin*, 63(9), 1504-1509.

Stomp, R. J., Fraser, G. J., Actis, S. C., Eaton, L. F. and Freedman, K. C. (2004). Deepwater DST Planning and Operations from a DP Vessel, *SPE*, 1-19.

Swarbrick, R. E., Osborne, M. O. and Yardley, G. S. (2002). Comparison of Overpressure Magnitude Resulting from the Main Generating Mechanisms, in Huffman, A. R. and Bowers, G. L. (eds.) *Pressure regimes in sedimentary basins and their prediction.* AAPG Memoir 76, 1-12.

Tingay, M. R. P., Hillis, R. R., Swarbrick, R. E., Morley, C. K. and Damit, A. R. (2009). Origin of overpressure and pore-pressure prediction in the Baram province, Brunei. *AAPG Bulletin*, 93, 51-74.

Weissenburger, K. s. and Borbas, T. (2004). Fluid properties, phase and compartmentalization: Magnolia Field case study, Deepwater Gulf of Mexico, USA, *Geological Society*, 237, 231-255.

Weiner, P. and Pettingill, H. S. (2007). Global Overview of Deep-water Exploration and Production, in Gillis, M (ed.) *Atlas of Deep-Water Outcrops*. Tulsa: Geological Society, 7-11.

Wilkins, S. J., Mount, V. S. and Davies, R. K. (2022). Structural geometry, evolution, and subseismic-scale deformation in traps adjacent to salt walls/welds: Observations from Green Canyon, Gulf of Mexico, *Marine and Petroleum Geology,* 135, 1-30.

Yang, Y. and Aplin, A. C. (2007). Permeability and petrophysical properties of 30 natural mudstones, *Journal of Geophysical Research*, 112, B03206.

Yang, Y. and Aplin, A. C. (2010). A permeability-porosity relationship for mudstones, *Marine and Petroleum Geology*, 27, 1692-1697.

Yardley, G. S. and Swarbrick, R. E. (2000). Lateral transfer: a source of additional overpressure?. *Marine and Petroleum Geology*, 17(4), 523–537.

Zhang, G., Qu, H., Chen, G., Zhao, C., Zhang, F., Yang, H., Zhao, Z. and Ma, M. (2019). Giant discoveries of oil and gas fields in global deepwaters in the past 40 years and the prospect of the exploration. *Journal of Natural Gas Geoscience*, 4, 1-28.

Zong, J., Coskun, S., Stewart, R. R., Dyaur, N. and Myers, M. T. (2015). Salt densities and velocities with application to Gulf of Mexico salt domes, *Salt Challenges in Hydrocarbon Exploration SEG Annual Meeting Post-Convention Workshop*, New Orleans, 1-5.

Chapter Five: 1D Thermo-Hydro-Mechanical Models Used to Identify Different Present-day Overpressures in a Passive Margin Basin, West Africa

This chapter contains confidential data; therefore, depths, locations, maps, and names have been removed.

Abstract

This chapter is based on data located in the West African coast, a passive margin basin with high geothermal gradients (>39 °C/km) where unexplained high overpressures (~12 MPa) have been encountered in the Albian-Cenomanian reservoir intervals of one well of three wells (Well A, Well B, and Well C). Wells A and C are located in the same structural trap at deep-water system channels and share similar overpressures (~1 MPa), while Well B is located at the base of the continental slope 44 km apart from wells A and C and has the highest overpressures.

The objective of this project is to investigate different scenarios that allow the identification of the mechanisms that could have contributed to the high overpressure generation in Well B. To achieve this, a geological evaluation focused on pore pressure was conducted, which included seismic interpretation, biostratigraphic well-correlation, lithology interpretation, and log-based pore interpretation, and which was used in the construction of the geomechanical models (hydro-mechanical and thermo-hydro-mechanical models). 1D thermo-hydro-mechanical models were used to investigate the effect of disequilibrium compaction and clay diagenesis on pore pressure and porosity. 2D hydro-mechanical models evaluated the effect of external structures such as canyons and channels.

Geological assessment revealed that both A and B Wells have relatively low sedimentation rates (<350 m/Ma), with several erosive events and hiatus periods during the Late Cretaceous to the Paleocene-Eocene. The reservoir intervals of Well A are compartmentalised, while Well B has one connected reservoir interval. In addition, there is a porosity reduction from the Campanian (below Cam2) to the Albian (Al11) in both wells A and B, which could suggest a change in lithologies or diagenetic processes.

While a log-based interpretation based on sonic and resistivity logs follows normal compaction trends, which suggests hydrostatic pore fluid pressures are present in these wells, a density-velocity cross-plot (shale lithology within the reservoir intervals) suggests unloading, interpreted as chemical compaction and/or clay diagenesis. Through the 2D geomechanical models, it was observed that external structures (e.g., canyons) had negligible impact on overpressure with respect to the Well B location. 1D hydro-mechanical models revealed that, due to the low sedimentation rate, erosive events, and hiatus periods, disequilibrium compaction is also unlikely to be the sole cause of the overpressure registered in Well B. However, 1D thermo-hydro-mechanical models suggest that clay diagenesis (load transfer process) can generate high overpressures, and due to this process, porosity could be reduced, which aligns with recorded well data.

To match the porosity and pore fluid pressure data of wells A and B, chemical compaction (clay diagenesis) and mechanical compaction (sedimentation) are necessary. Clay diagenesis (smectite to illite transformation) was investigated at different temperatures, having a better match with temperatures of 72 °C. With this temperature, clay diagenesis started 83 Ma ago (from the Cretaceous) in Well B while in Well A around 32 Ma ago (Oligocene).

5.1 Introduction

This project focuses on identifying the mechanisms that have generated overpressure at the Cenomanian and Albian reservoir intervals (~2,300 m BML) of three wells located in the Mauritania-Senegal Coastal Basin. The position of the well with high overpressure (~12 MPa; Well B) is 44 km apart from the other two wells (slightly overpressured ~1.26 MPa; wells A and C). While sonic and resistivity logs follow normal compaction trends in most parts of the sedimentary succession of these three wells, suggesting hydrostatic pressures to be present, a density-sonic cross-plot suggests overpressure due to clay diagenesis or chemical compaction.

The Mauritania-Senegal Coastal Basin is a passive margin basin with high geothermal gradients (~40 to 43 °C/km; McGuinness et al., 2021) due to volcanic activity between the Cretaceous and Holocene (Goumbo Lo et al., 1992; Bellion and Crevola, 1991; Crevola, 1995; Davison, 2005). It is a mud-dominated basin with a high content of calcium carbonate, with intervals of sand-silt lithologies and packages of carbonate lithologies deposited over the Palaeozoic to Cenozoic eras (Dean et al., 1978; Brownfield and Charpentier, 2003; Davison, 2005; Brownfield, 2016). This basin also presents several erosive events or hiatus periods, particularly during the Cretaceous (Effimoff et al., 2010; Fairhead et al., 2013; McGuinness et al., 2021; well reports). While there has been relatively little exploration of the contributing overpressure mechanisms in this basin, pore pressure cubes have been created from seismic data suggesting overpressures at different stratigraphic intervals (Banik et al., 2004). McGuinness et al. (2021) indicated that the overpressure encountered in the clastic reservoirs of the Late Cretaceous in Pelican-1, Cormoron-1, and Marsouin-1 wells was due to pore pressure transfer from deep intervals associated with gas migration. Vear (2005) highlighted that the overpressure encountered in the source rocks of the Paleocene intervals of the MTO-1 well was identified to be related to in situ oil generation (Figure 5.1, location of these wells in black dots). Further south in the Niger Delta basin, smectite dehydration has been identified with thermo-hydro-mechanical modelling to be the main cause of around 30% of the present-day overpressure in addition to disequilibrium compaction (Tremosa et al., 2020).

The mechanisms previously proposed have not been tested; therefore, the aim of this study is to use thermo-hydro-geomechanical models to identify and quantify the mechanisms that could have contributed to overpressure generation in Well B. 1D geomechanical models were used to investigate disequilibrium compaction and clay diagenesis (smectite to illite transformation) and 2D geomechanical models to investigate the external structures that could contribute to high pore pressure generation (e.g., canyons and channels). Pressure transfer and hydrocarbon generation were evaluated during the geological analysis, which consisted of 3D seismic interpretation, well-correlation with biostratigraphic data, lithology interpretation, and 1D basin modelling. An interpretation of well-log data through the use of analytical equations focused on the contribution of overpressure was also performed. The results of this integrated study allowed to identify the factors needed for overpressure generation and maintenance through geological time.

5.1.1 Geological Background

The study region is located in the Senegal-Mauritania Basin, which is part of the Mauritania-Senegal-Gambia-Bissau-Conakry (MSGBC) Coastal Basin of the North-Western African coast (Figure 5.1). The MSGBC basin was formed during the Late Permian to Early Cretaceous (Albian age) with the rifting of the Central Atlantic margin (Dean et al., 1978; Reymond and Negroni, 1989; Bellion and Crevola, 1991; Brownfield and Charpentier, 2003).

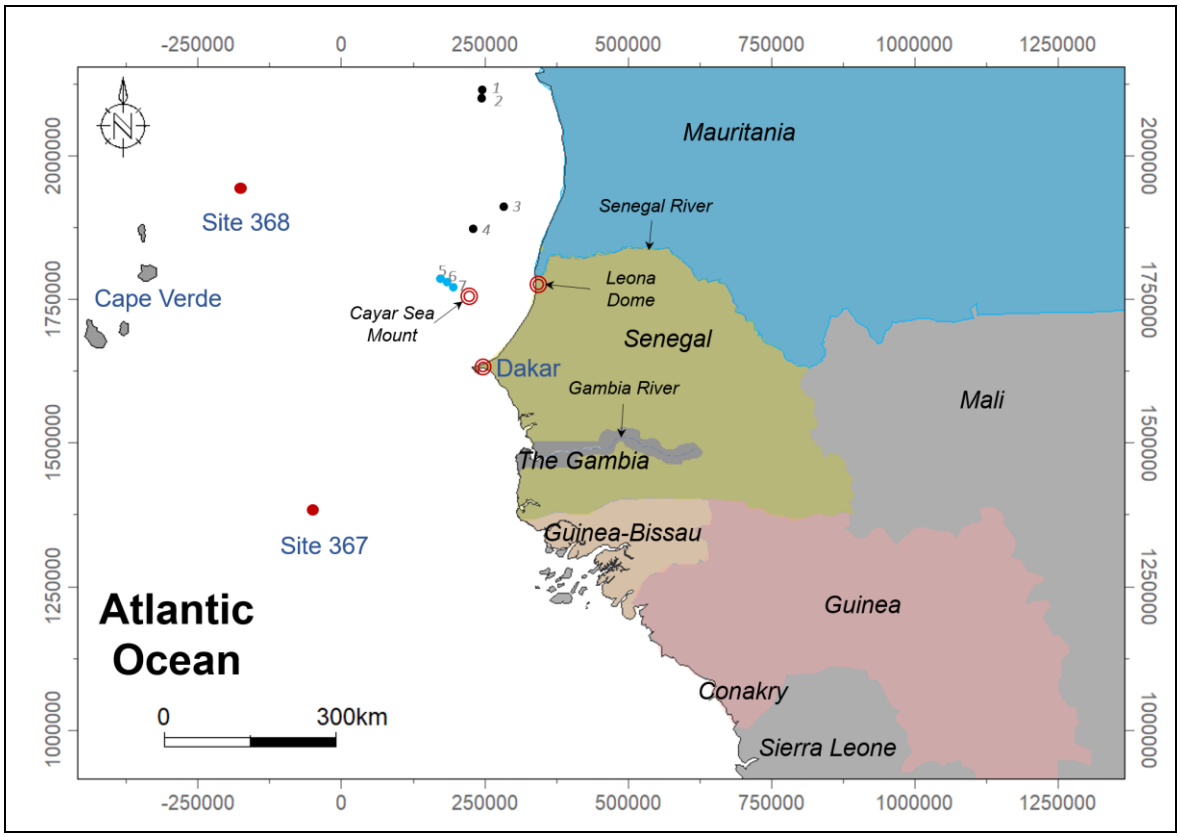

Figure 5.1.- Map of the area studied with the location of the sites 368 and 367. Black dots (1, 2, 3, and 4) represent wells (Cormoron-1, Pelican-1, MTO-1, and Marsouin-1) with overpressure (McGuiness et al., 2021; Vear, 2005). Blue dots (5, 6, and 7) represent wells (Ahmeyim, Tortue, and Guembeul) with fluid from mature source rocks and from cracked oil expulsed during different events (McGuinness et al., 2021).

Onshore and offshore exploration in this basin started in the 1950s and 1990s, respectively, and focused on clastic reservoirs with gas and oil (McGuinness et al., 2021). The most productive reservoirs are the clastic sediments of the Late Cretaceous and Miocene deposited by deep-water channel systems (Davison, 2005; McGuinness et al., 2021). Generally, the hydrocarbon traps in this basin have two components: structural and stratigraphic. The reservoirs are mainly located in anticlines formed by the sliding of a detachment layer interpreted to be Turonian in age. Other structures are the result of salt tectonics and the reactivation of the rifting faults. The main fault system has a N-S direction dipping towards the W, followed by a W-E transform system related to the Central Atlantic rifting (Bellion and Crevola, 1991; Beauchamp et al., 1999).

Sediments are predominantly sourced directly from the West Africa Craton and the Pan-African Mobile Belt (Mauritanides) (Dean et al., 1978; Bonne, 2014). They have been largely transported by

three long-lived rivers (the Nouadibou, Nouakchott, and Senegal) from the Cretaceous to the present (McGuiness et al., 2021), deposited by different sedimentary systems (e.g., deltaic and turbidite), and transported and redeposited by bottom currents (tidal and internal waves) (Mourlot et al., 2018; Casson et al., 2021; McGuiness et al., 2021). Sealing layers have been identified to be Coniacian, Santonian, and Campanian shales (Figure 5.2) identified in well data at ~65 km south of the project location (Martin et al., 2010).

Data from the Ahmeyim, Tortue, and Guembeul wells (blue dots in Figure 5.1) show that the fluid in the Cenomanian reservoirs is from mature source rocks and cracked oil expelled during different events (McGuinness et al., 2021). The source rocks vary between basins and could be mature or immature depending on the conditions of the basin (e.g., depth, temperature, location, pressure, salt tectonics, and volcanism; Davison, 2005). Source rocks in the Mauritania Basin have been identified to be the marine shales of the Cenomanian, Turonian, Albian (Vear, 2005), and Early Jurassic, while in the Senegal Basin are also the Aptian, Lower Cretaceous (Davison, 2005; Brownfield and Charpentier, 2003), and the clastic and lacustrine shales of the Permian and Lower Triassic (Brownfield and Charpentier, 2003). Shales up to 400 m thick from the Silurian have been described to be a regional oil-prone source with an organic content between 1 and 5.5%, while the source rocks from the Late Aptian to Turonian contain organic levels between 5 and 28% (Dean et al., 1978; Reymond and Negroni, 1989). In the Mauritania Basin, oil generation windows are interpreted to have started at different times. For example, Albian source rocks began generating in the Late Eocene, while Cenomanian, Turonian, and Upper Cretaceous source rocks started generating in the Miocene (Brownfield and Charpentier, 2003) (Figure 5.2).

In the Senegal Basin, volcanic activity occurred between the Cretaceous and Pleistocene (Bellion and Crevola, 1991; Davison, 2005). It intensified during the Late Eocene-Oligocene (~35 Ma) to Late Miocene (~8 Ma) around the Cape Verde and Dakar areas (African mainland) (Goumbo Lô et al., 1992; Crevola, 1995; Davison, 2005). Heat flow models showed that the Cape Verde was formed within the last 3 to 12 Ma (Courtney and White, 1986). The Cayar Sea Mount, Leona, and Dakar intrusions have been identified as being Middle Cretaceous (Davison, 2005). However, the Cayar Sea Mount and the Dakar intrusion have also been dated to be Eocene-Pliocene (Bellion and Crevola, 1991) (Figure 5.1).

The tectono-stratigraphic evolution of this area started with the pre-rift section of Precambrian to Devonian rocks, which were affected by different compressional events and have contributed to the formation of different fault systems that have a structural influence on the young sediments (Guiraud et al., 2005). Cambrian and Devonian stratigraphy is dominated by shale and sandstone lithologies. The syn-rift section began during the Early Triassic to Early Jurassic, where clastic rocks followed by a thick layer of 1.5 km of evaporites (gypsum and anhydrite) were deposited in the MSGBC Basin with a sedimentation rate of 1,000 m/Ma (Davison, 2005). Late Triassic to Early Jurassic (~200 Ma) dykes and sills, related to extensional regimes, have been identified in part of the Central Atlantic Magmatic Province (Olsen et al., 2003) (Figure 5.2). The post-rift began from the Early Jurassic to the Early Cretaceous, when extensive carbonate platforms were deposited with variable thicknesses of limestone, dolomite, and anhydrite lithologies with intercalations of shales (Davison, 2005). On

seismic data, these carbonate platforms are characterised by parallel and continuous reflectors with a regional unconformity on the top (Casson et al., 2021). From the Late Cretaceous to the Pleistocene, clastic material has been deposited by deep-water systems (e.g., turbidites, slumps and mass flow transport). These sediments have sculpted the carbonate platform, creating canyons and confined channels (Casson et al., 2021) (Figure 5.2). In the Late Cretaceous and Turonian-Albian, dark black shales with high organic matter were deposited. In the Paleocene to Eocene, thin intercalations of carbonate and sandstone lithologies were deposited, followed by a thick section of foraminiferal limestones deposited in a regressive system during the Oligocene (Davison, 2005) (Figure 5.2). During the Early Miocene to the present-day, intervals of clastic sediments have been deposited by turbidite, deltaic, and fluvial systems (Vear, 2005; Hathon, 2018). Compressional deformation from the Santonian to the Middle Miocene due to a change in the direction of the tectonic plates created a sequence of anticlines that can be identified in the Senegal-Mauritania Basin (McGuinness et al., 2021).

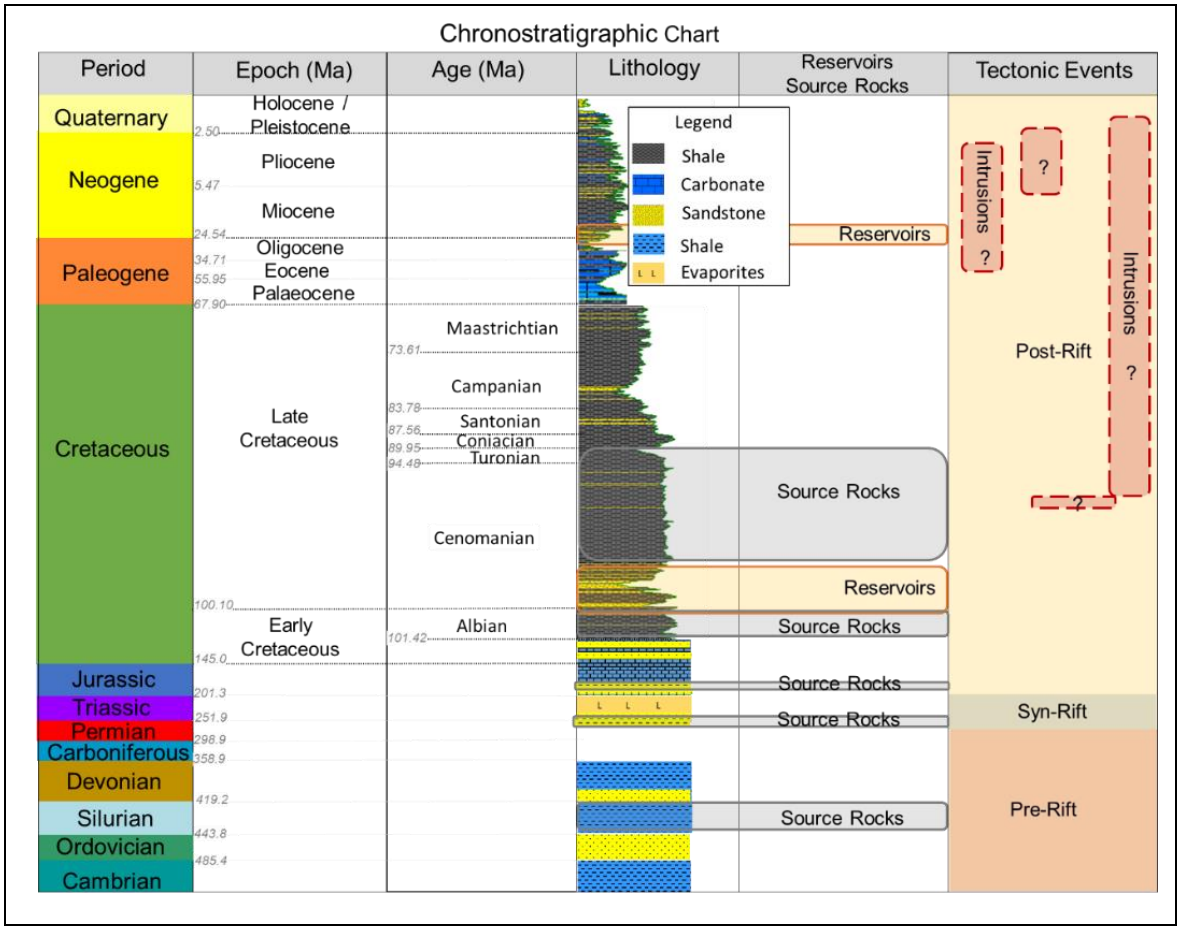

Figure 5.2.- Chronostratigraphic chart based on Gradstein et al. (2012) and Brownfield and Charpentier (2003) with data from wells A, B, and C. It highlights reservoirs, sourced rocks, and tectonic events with the volcanic activity described in previous studies (e.g., Goumbo Lô et al., 1992; Crevola, 1995; Davison, 2005; Bellion and Crevola, 1991).

5.2 Data and Methods

Data were provided by BP and comprised well data and seismic cubes. All data used were uninterpreted primary data aside from the interpretation already contained within the well reports, presentations with general information, and well tops interpreted by BP that were updated during this project with biostratigraphy reports. Table 5.1 summarises the well data, and Table 5.2 presents the seismic cubes used.

Table 5.1.- Summary of the data used during this project.

Well Data	Number of Wells
Coordinates, KB, and mud log (image report)	3
Well logs (density, neutron, and resistivity) only reservoir intervals	3
Well logs (GR, sonic, and resistivity) complete section (wells A and C), and an incomplete section (Well B)	3
Rotary sidewall core (reports of wells A and C)	2
Pressure data MDT and XPT (text file of wells A, B and C)	3
Borehole image for the reservoir section (wells A and C)	2
Mud weight values (excel) complete section (wells A and B)	2
Rock -Eval data for sections above and below the reservoirs (wells A and B)	2

Table 5.2.- Summary of the seismic cubes used during this study.

3D Seismic Survey	Area km2	Sample Rate (HZ)	Filter
Stack Reflectivity	2,556.57	125	yes
Genetic Inversion			
Acoustic Impedance			

Petrel software (version 2022) was used for seismic interpretation, well correlation, 3D static model structural, and sedimentary column characterisation. This software was also used to support the 1D basin models that were simulated with PetroMod (version 2022) and the 1D and 2D geomechanical models performed with the software ParaGeo (version 3.9.3).

The methods used in this project were both qualitative and quantitative. Two workflows that represent the main steps are presented. One summarised the assessment performed on geological data, with the pore pressure evaluation on the well logs using analytical equations and the analysis of measured data (Figure 5.3a). The second workflow has the potential overpressure mechanisms analysed during this project. It was constructed based on well data, the geological characteristics that this

project has in regard to its location, and the possible overpressure mechanisms that could have contributed to its generation and preservation (Figure 5.3b).

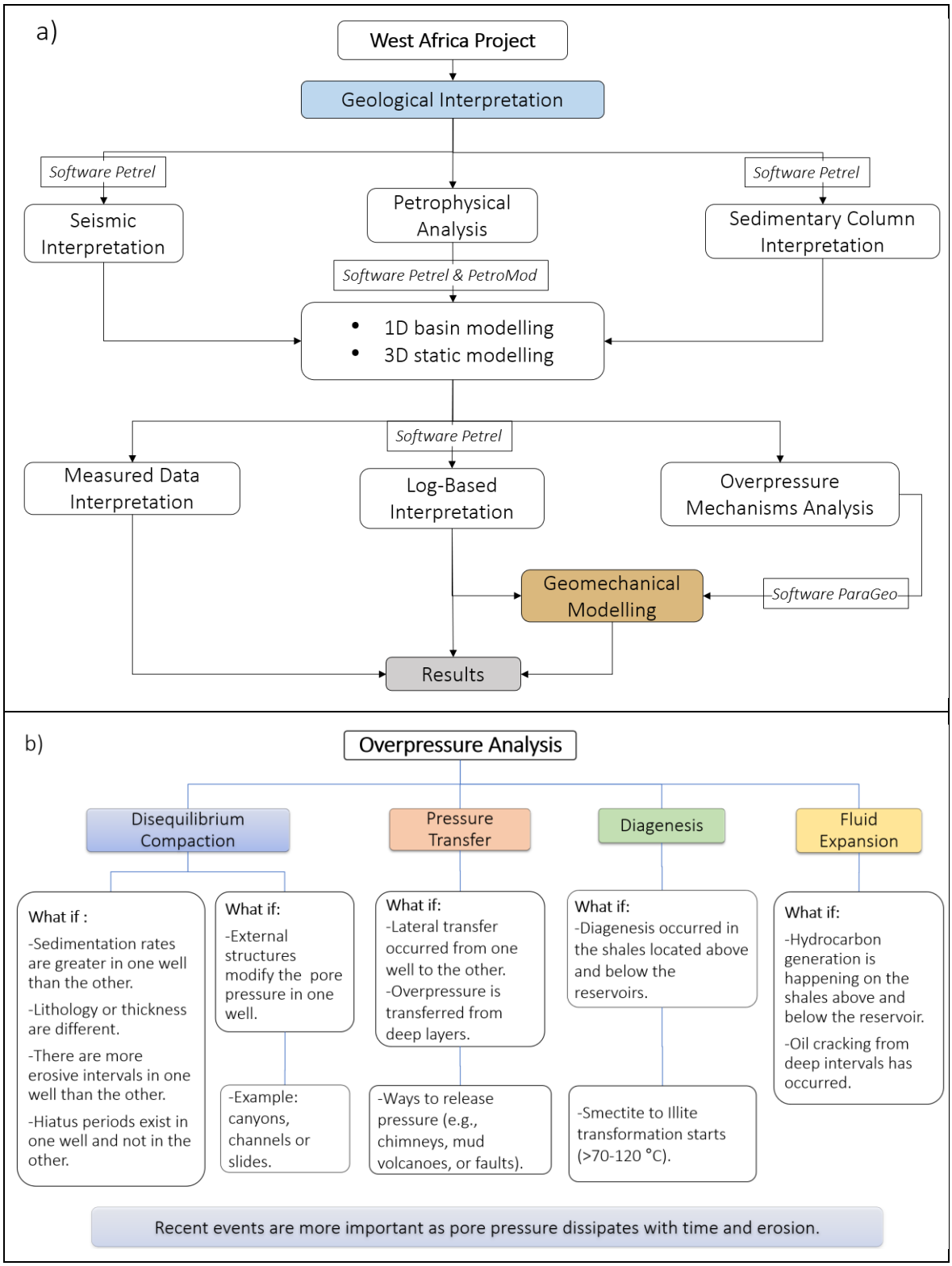

Figure 5.3.- a) Workflow of the main steps taken in the geological assessment. b) Workflow of the overpressure mechanisms analysed in this project, highlighting the possible scenarios.

5.3 Geological Data Interpretation Focused on Overpressure Generation

To understand the overpressure-generating mechanics, geomechanical modelling and a geological assessment using seismic and well data were performed. The analysis started by identifying any characteristic that can be related to overpressure generation, preservation, compartmentalisation, and sealing. Three wells were used in this assessment, named A, B, and C. Wells A and C have been interpreted as belonging to the same hydrocarbon trap, while Well B belongs to a different trap.

The hydrocarbon traps in these three wells have both structural and stratigraphic components. Wells A and C are located ~8.8 km apart from each other and have reservoirs in the Cenomanian Ce3. These two wells are located in deep-water systems. In addition, Well A also has a reservoir in the Albian (Al11), similar to Well B, which is located upslope (at the base of the shelf) approximately 44 km from this well (Figure 5.4).

An interpretation based on the gamma-ray logs (GR) of these three wells shows a different stacking pattern on the overburden section (the sedimentary column above the reservoirs) in Well A with similar successions in wells B and C.

Well C has thicker shale (mudstone) intervals than Well A. For instance, Well C has a thick shale package of ~480 m above the reservoirs from the Cenomanian to the Turonian, while Well A has a section of ~336 of sand-shale intercalations. The reservoir intervals are also different; Well A has thinner finning upward sections than Well C, which has two thick sand packages separated by a shale interval with a thin interval of carbonates (Figure 5.4). Even though the overburden and the reservoirs of wells A and C have different succession intervals, both wells have similar pore pressure values of ~21 MPa (3,024 psi) at around 1,921 m BML (for reference, see Figure 5.8b).

A comparison between the staking patterns of wells B and A shows more shaly and blocky intervals in Well B than in Well A. For example, above the reservoir of Well B, there is a thick package of shale lithologies of ~564 m (from the Cenomanian to the Turonian). The reservoir intervals in Well B have more sand lithologies, with a coarsening upward at the base changing to a fining upward at the top. The pore pressure values in Well B are around 37 MPa (5,295 psi) at 2,295 m BML which are 16 MPa higher than those of wells A and C (for reference, see Figure 5.8b).

The well correlation used for this interpretation was based on biostratigraphic tops created from the reports of wells A, B, and C (Figure 5.4). As wells A and C have similar pore pressure values and belong to the same hydrocarbon trap, Well A has only been compared through most of the data and results with Well B during this study.

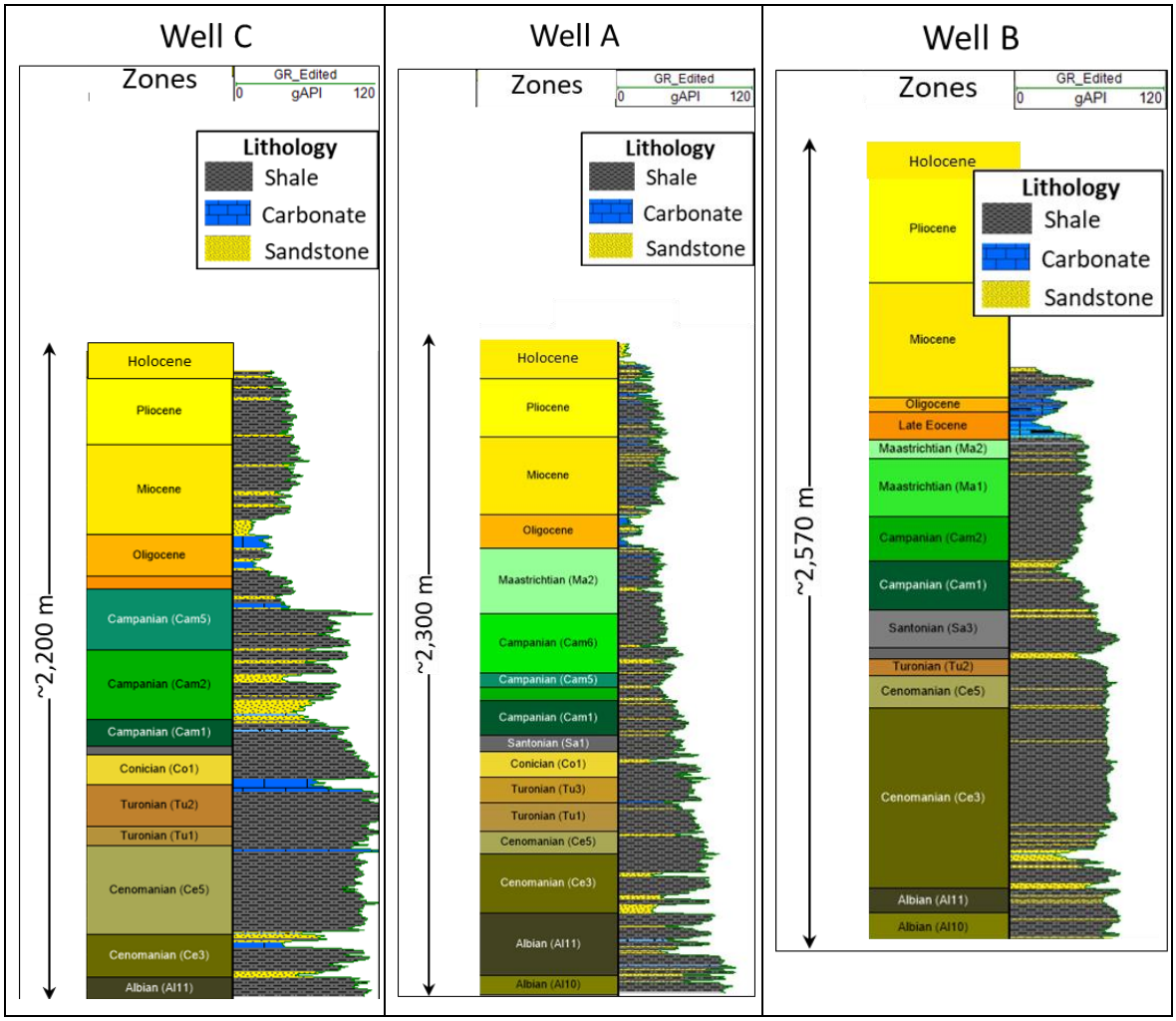

Figure 5.4.- Well correlation with zones based on biostratigraphic reports of wells A, B, and C. The lithology was interpreted with a set of well logs (e.g., GR, density (ROHB), sonic (DT), and resistivity), mud logs, and petrographic studies.

As previously interpreted, the reservoir intervals in this study region correspond to deep-water deposits (Dean et al., 1978; Brownfield and Charpentier, 2003; Davison, 2005; Brownfield, 2016; McGuiness et al., 2021).

The facies described in well reports for Well A correspond to channels, levee deposits, slump and debris flows, and mudstones (shales), which indicate that this well is located in an area where deep-water channels can develop (e.g., Mayall et al., 2006). Seismic data show that Well A is located in a more deep-water area than Well B, which is located close to the edge of the shelf region. Considering the location of the wells A and B with regard to the shelf, the analogy chosen puts Well B between submarine canyons with small development of turbidite deposits, while Well A in the proximal basin floor to medial basin floor (e.g., Rossen and Beaubouef, 2007; Wignall and Best, 2016) (Figure 5.5).

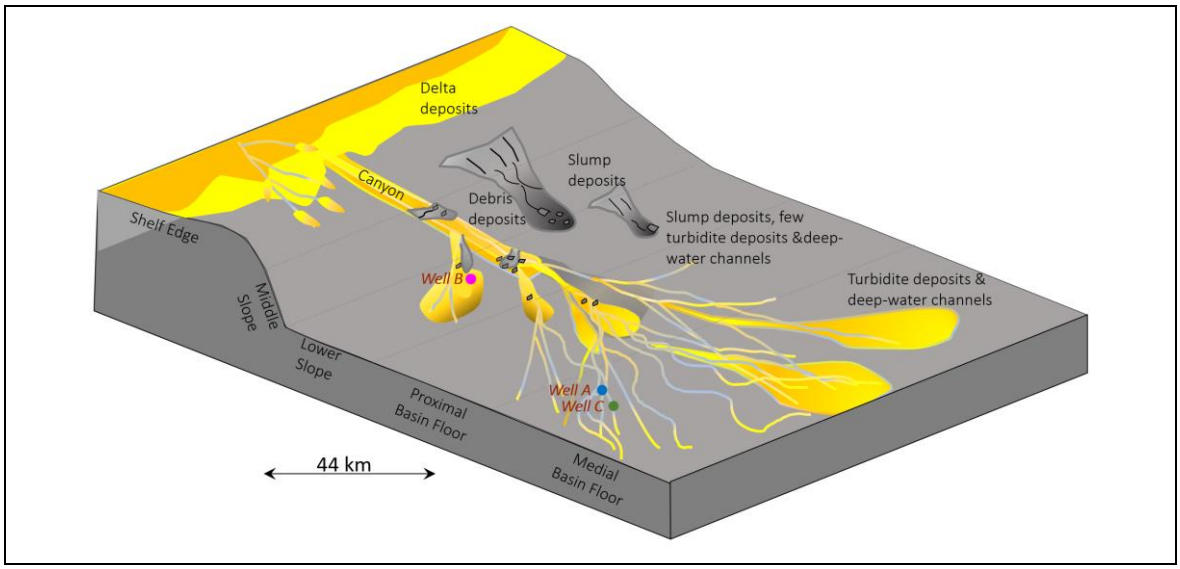

Figure 5.5.- Sketch of the analogy chosen to represent deep-water systems of the Cretaceous period with the location of the three wells A, B, and C. Model based on seismic data and deep-water models (e.g., Stow et al., 2006; Mulder, 2011; Wignall and Best, 2016; Rossen and Beaubouef, 2007; Mayall et al., 2006).

Nine horizons were interpreted using the 3D seismic cubes (sea floor, Oligocene, Maastrichtian, Cenomanian, Albian Al10, Albian Al11, Early Cretaceous, named Jurassic, and lower horizon, which is the oldest; Figure 5.6b). The age of the horizons interpreted below the Albian age was extrapolated from other studies performed in the area (e.g., Mourlot et al., 2018; Casson et al., 2021).

During the interpretation, there was no clear evidence of any displacement in the reflectors that could be mapped as faults. From the seismic cubes, a slope of ~1° was calculated, dipping towards the west. The thicknesses of the reflectors change from high frequency (thin reflectors) in the Pleistocene-Holocene to low frequency (thick reflectors) in the Late Cretaceous. Multiple stacked canyons were observed on the seismic data at different periods (e.g., Cretaceous to Holocene; Figure 5.13).

A thickness variation through time was observed in seismic data. It is observed that during the Miocene to the present-day a thick section was deposited at the location of Well B, but Well A has a thicker section in the Turonian to Maastrichtian epoch. The thickness variation was considered in the geomechanical models, and it is presented in section 5.4.4 (Figure 5.19c).

Features such as unconformities, channelised areas, and distorted, bright, and blurry reflectors were mapped on seismic data and analysed to identify any relationship to overpressure generation and preservation (Figures 5.6 and 5.23b).

An interval with parallel bright reflectors (high amplitudes) of ~160 m thickness, interpreted as Eocene-Oligocene, was observed in the whole seismic cube (Figure 5.6b). This interval has low porosities (from the sonic logs) in Well A and was defined as a low-permeability interval in the geomechanical models. Below this interval, a package of ~800 m thickness with distorted reflectors, interpreted to be Maastrichtian in age, was also mapped through the whole seismic cube. According to the sonic logs of wells A and B, this interval does not have low values (low porosities), but it shows the instability of the area at that time. The next interval, interpreted as Campanian-Turonian, shows

erosive events that increase in number towards the Cenomanian period. At the top of the Cenomanian, a bright reflector was interpreted to be an unconformity (Figure 5.6b). This unconformity does not present any change in the well logs (GR, sonic, and resistivity) values in the A, B, and C wells.

Local erosive events were observed in some parts of the seismic data during the Albian interval. The reflectors below this period are blurry with low amplitudes, making the interpretation difficult (Figure 5.6). Other features, such as vertical blurry reflectors and canyons were mapped in more detail in this study, and the results are presented in the discussion section.

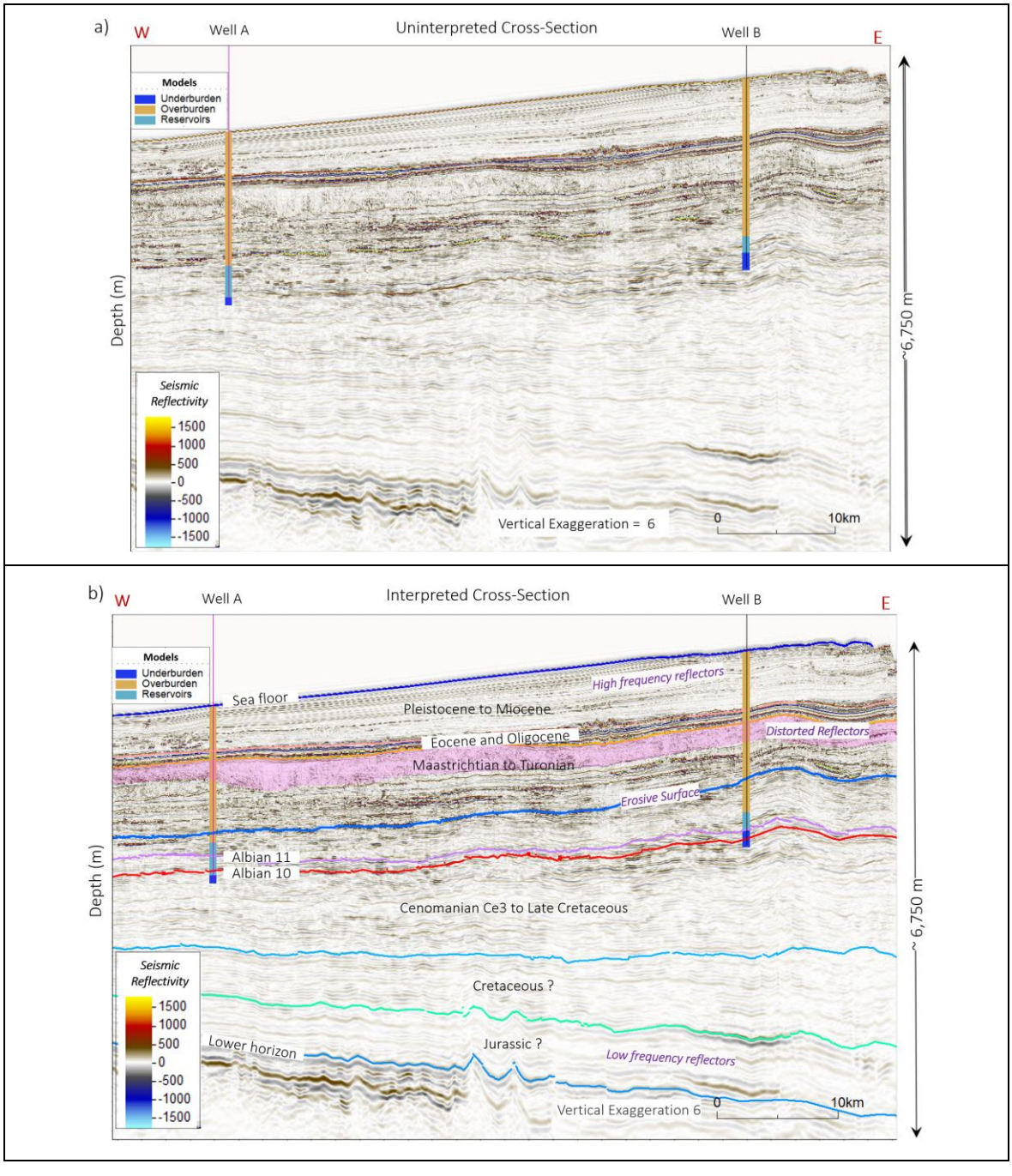

Figure 5.6.- Seismic reflectivity cross-sections with the location of wells A and B. Overburden, reservoirs, and underburden intervals are marked. a) Uninterpreted cross-section and b) interpreted cross-section with the horizons mapped during this study.

Petrographic reports of wells A and C were used in this study. These data refer to the reservoir intervals where the main grain observed was quartz with up to 80%. The size of these grains is from very fine to coarse, poor to well-sorted, and from angular to sub-rounded with a clay matrix, which indicates immature sandstones. There are intervals with around 5% of quartz overgrowth, 3% of calcite cement, and up to 35.3% of ferroan calcite, and intervals with authigenic chlorite, kaolinite, calcite, and ferroan dolomite cement. In these reports (confidential reports), it was highlighted that authigenic cements have an influence on the reservoirs' quality and was determined a porosity reduction of 15% due to mechanical compaction. These reports were not available for Well B. A cross-plot of porosity vs. permeability of core data of wells A and C shows a high variation of porosity and permeability in the Cenomanian and Albian intervals, with the lowest permeabilities in calcite cemented intervals (Figure 5.7).

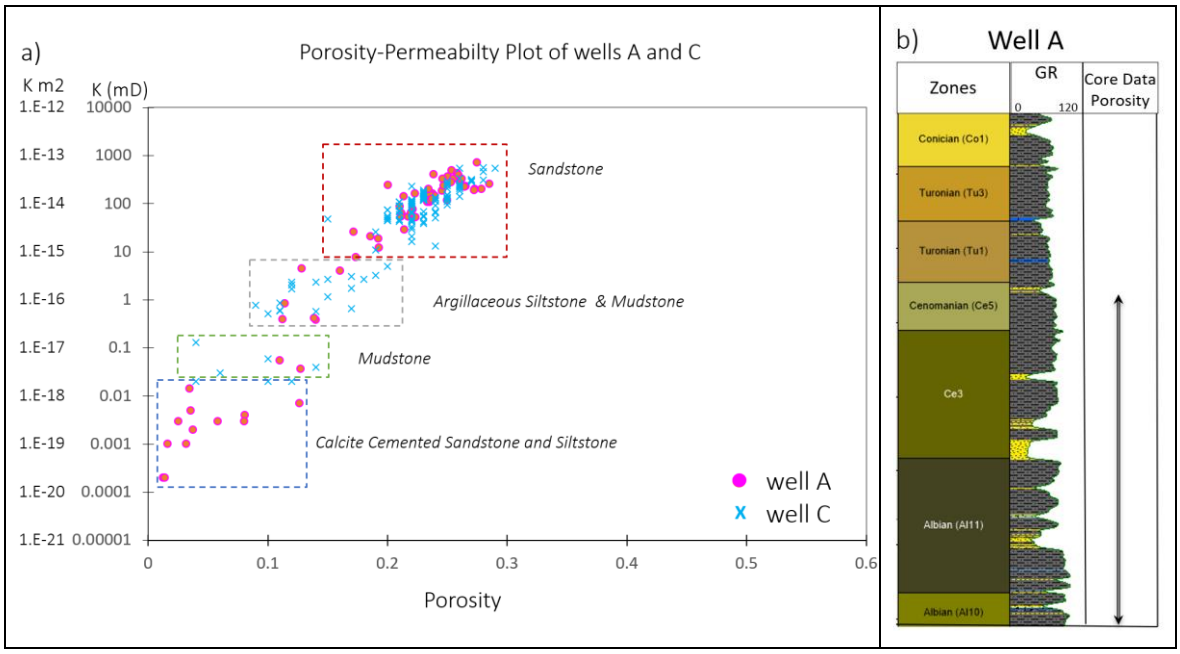

Figure 5.7.- a) Cross-plot of porosity vs. permeability of the core data of wells A and C. Cemented samples, which are present in greater quantities in Well A, have low porosity and permeability values. b) Well A for reference on the depth of the core values.

Well-log image reports have also determined the reservoirs of wells A and B as deep-water systems. In these reports, there are intervals described as deformed/overstep heterolithic mudstones that correspond to mass transport packages (reservoir scale). These soft sedimentary structures have angles from 0 to almost 90 °and were analysed as possible pore pressure barriers (Figures 5.9a and 5.9b).

In Well B, these intervals are located at the base of the main reservoir in two packages separated by a thin sandstone layer. In Well A, these intervals are more common and are located along the whole reservoir interval. There are also other thin intervals in this well. These intervals do not have any great impact on pore pressure and are not different from the other shale intervals where these structures are not present (Figures 5.9a and 5.9b).

5.3.1 Measured Pore Pressure Data

Data from drill stem tests (DST) and pressure xpress tests (XPT) of the three wells (A, B, and C) recorded prior to production were also analysed. These data were taken only in the Albian-Cenomanian reservoirs of these wells. The reservoir intervals of Well B are located deeper than the reservoirs of wells A and C. Data are presented from TVDSS (m) in Figure 5.8a and from the same mudline in Figure 5.8b. It is observed that pore pressure values in wells A and C are almost hydrostatic with overpressures of ~1.26 MPa (182 psi), while data from Well B is ~12 MPa (1,740 psi) higher. An interpretation of the gas and water gradients of both wells is presented in Figure 5.8c. It is observed that the reservoir intervals in Well A are compartmentalised while the reservoir intervals in Well B have only one connected reservoir with one gas-water contact.

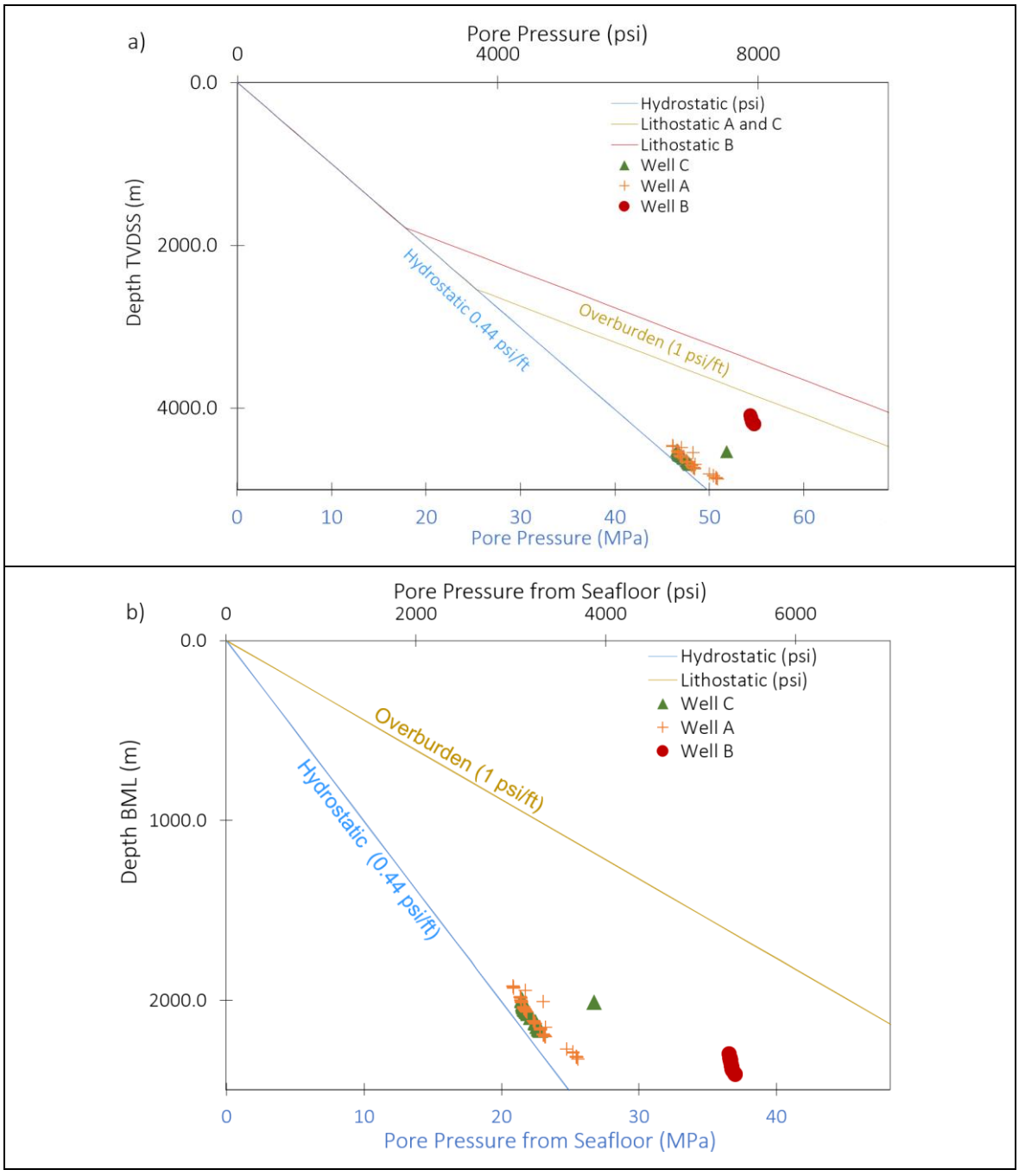

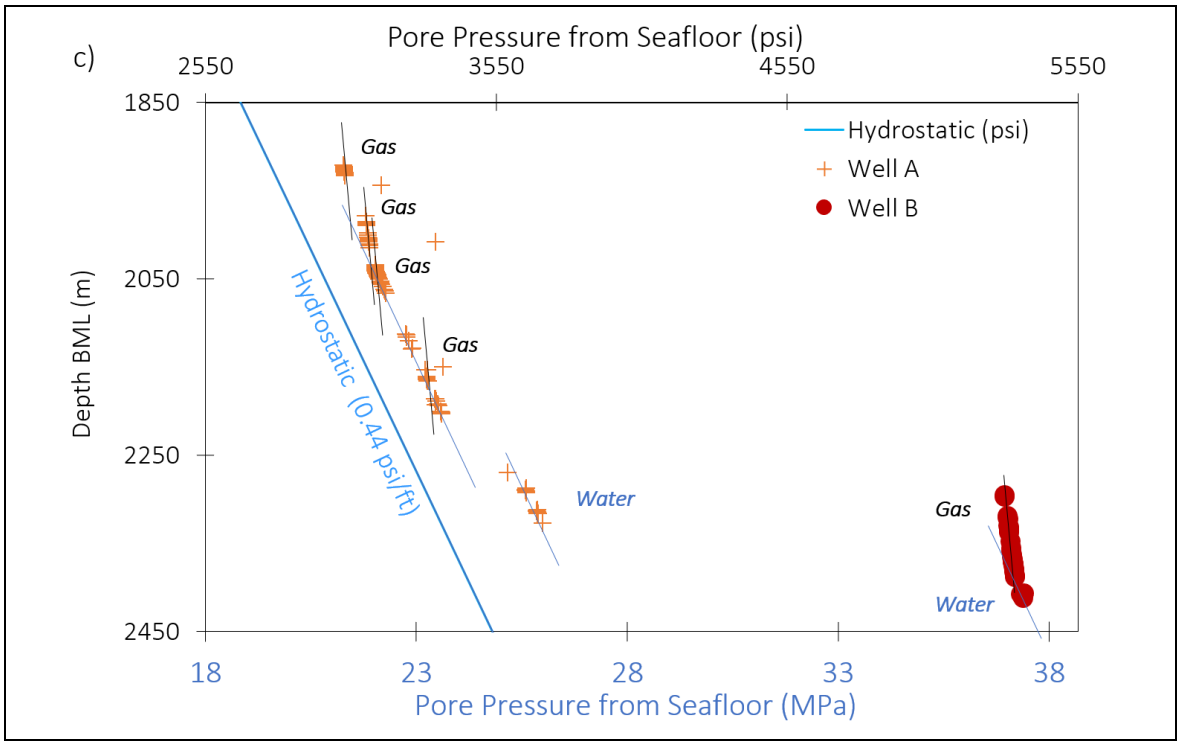

Figure 5.8.- Measured pore pressure data vs. depth of the wells A, B, and C. a) Data from True Vertical Depth Sub-Sea (TVDSS). b) Data below mudline (BML). c) Data from wells A and B with the interpretation of gas and water gradient. Well A data show compartmentalised reservoirs, while Well B data show one connected reservoir.

5.3.2 Log-Based Pore Pressure Interpretation

Well logs of wells A and B were used for this analysis. Density logs (RHOB), temperature, and pressure data were only registered at the reservoir intervals. If a well log was too short to quantify, it was not used in the analysis. For instance, Well B has a digital sonic log (DT) for the deep section (Cam1 to Al11) and a paper copy from the Campanian (Cam2) to part of the Miocene, which were edited together for the analysis. This well also has resistivity and gamma-ray (GR) logs from the Albian (A10) to part of the Miocene. However, data were not available from the Late Miocene to the Holocene (Figure 5.9b). On the other hand, Well A has sonic, GR, and resistivity logs from the shallow section to the total depth of this well (Figure 5.9a).

In Well A, the sonic log presents an atypical behaviour from the seafloor to ~385 m depth with values < 160 to 110 us/ft, causing low porosities (~0.20), which are highly unlikely to be at those depths. A possible interpretation is that the sonic readings have been affected by heavy minerals from the intrusions present in the region (e.g., Davison, 2005; Mounteney et al., 2021) or by calcium carbonate intervals that are common along the sedimentary column (Dean et al., 1978). The data for this interval were not used in the analysis, but it is presented in the figures of this well.

Prior to investigating the response of the well logs to overpressure, the analytical equations 5.1 and 5.2 described by Passey et al. (1990) were applied to both wells (A and B) to identify potential organic matter in shale intervals. The interpretation is based on the separation between scale sonic and scale resistivity logs, which provide the intervals with total organic carbon (TOC). The level of maturity

(LOM) is based on the level of organic maturity of the shales (e.g., 5-7 immature, 10 mature, and 12 overmature). In both wells, shale intervals above (Cenomanian, Turonian, and Coniacian) and below (Albian) the reservoirs were interpreted to have some levels of organic matter. The maturity was not clearly identified with these equations. However, rock-eval data for both wells (A and B) were used, and the results are presented in section 5.4.5.

Normal compaction curves (hydrostatic) described by Athy (1930) and Wyllie (1965), with a later modification performed by Tingay et al. (2009), were used and applied to the sonic, density, and resistivity logs of both wells A and B to identify intervals with a deviation from these trends that could be related to overpressure (equations 5.3, and 5.4). The normal compaction trend for resistivity was calculated with equation 5.5 (Zhang 2011).

5.1 $$\Delta \log R = log_{10}\left({R}/{R_{baseline}}\right) + 0.02 * (\Delta t - \Delta t_{baseline})$$

5.2 $$TOC = (\Delta \log R) * Exp(2.297 - 0.1688 * LOM)$$

5.3 $$\Delta t_{NC} = \Delta t_{ma} + (\Delta t_{ml} - \Delta t_{ma}) * e^{-c*Z}$$

5.4 $$\rho_{NC} = \rho_{ma} + (\rho_{ml} - \rho_{ma}) * e^{-c*Z}$$

5.5 $$R_{NC} = R_o * e^{b*Z}$$

Where $\Delta logR$ is the separation between the resistivity and sonic logs, R is the measured resistivity, $R_{baseline}$ is the value obtained from the interval above or below the shale interval analysed, Δt is the measured transit time (µs/ft), $\Delta t_{baseline}$ is the values obtained from the interval above or below the shale interval analysed (µs/ft), TOC is the total organic matter, and the LOM is the level of organic maturity. LOM between 5-7 are immature shales and, LOM >10 mature shales, Δt_{NC} is the transit time of the normal compaction, Δt_{ma} is the matrix transit time (54 µs/ft) after Tingay et al. (2009), Δt_{ml} is the mudline transit time (seabed) (188 µs/ft) after Schlumberger (1989), z is the depth below sea level (m), c is the compaction coefficient (m^{-1}) the values used for shales was 0.0051 after Hansen (1996), ρ_{NC} is the density of the normal compaction, ρ_{ma} is the matrix density (2.67 gr/cm^3) after Tingay et al. (2009), and ρ_{ml} is the density at the mudline (g/cm^3) which value was modified from 1.8 after Couzens-Schultz and Azbel (2014) to 2.2 to better match the data, R_{NC} resistivity normal compaction, R_o shale resistivity at mudline (1.28), b constant (0.000034) after Zhang (2011) (Figure 5.9).

The normal compaction trend for shale porosities proposed by Athy (1930) (equation 5.6), the pore fluid pressure proposed by Eaton (1975) (equation 5.7), and Bowers (1995) (equation 5.8) were developed to predict normal compaction trends and pore pressure due to mechanical compaction and were used in this study to identify whether the overpressure was caused by disequilibrium compaction in both wells A and B.

5.6 $$\emptyset_{NC} = \emptyset_o * e^{-c*Z}$$

$$5.7 \quad P_f = \sigma_L - (\sigma_L - \sigma_{Hy}) \left(\frac{\Delta t_{NC}}{\Delta t}\right)^x$$

$$5.8 \quad P_f = \sigma_L - \left(10^6 * \frac{\frac{1}{\Delta t} - \frac{1}{\Delta t_{ml}}}{a}\right)^{\frac{1}{b}}$$

Where $\emptyset_{NC}$ is the normal compaction of shale, $\emptyset_o$ is the porosity at mudline (fraction) in this case 0.54 was used, z is the depth in metres below sea level and c is a constant value that represents the compaction (0.00051 m^{-1}), P_f is the pore pressure fluid, σ_{Hy} is the hydrostatic pore pressure, σ_L is equal to the lithostatic stress/overburden, Δt_{NC} is the normal compaction transit time for hydrostatically pressured sediment (us/ft), and x is an exponent which for mechanical compaction has been determined to be 3 (Eaton, 1975), a and b are constants 4.4567 and 0.868 after Bowers (1995).

Porosity curves using sonic well logs of both wells A and B were created with equation 5.9. This equation was proposed by Wyllie (1965) and modified by Raymer et al. (1980).

$$5.9 \quad \emptyset_{DTcp} = \frac{\frac{\Delta t - \Delta t_{ma}}{\Delta t_f - \Delta t_{ma}}}{C_p}$$

Where $\emptyset_{DTcp}$ is the corrected porosity from the sonic log, C_p is the correction factor considered to be 2.05 after Schlumberger (1989) and Tingay et al. (2009).

Sonic, resistivity, and porosity curves follow normal compaction trends in most of the sedimentary column of both wells A and B, indicating hydrostatic pore pressures. There is a slight reversal observed on sonic and resistivity logs below the carbonate interval in both wells (Section 1 in Well A and Section 3 in Well B; Figure 5.9), which could be related to an increase in pore pressure due to the low permeability of the carbonate interval or a change in lithology. A second reversal (Section 2 in Well A and Section 4 in Well B; Figure 5.9) is also observed, but only on the sonic logs above the reservoir in Well A and below the reservoir in Well B. A possible interpretation is that a greater TOC correction must be applied in those intervals.

Pore pressure from mud weights increased from Turonian (Tu2) in Well B and from Maastrichtian (Ma2) in Well A. However, only the pore pressure values registered by pressure tests in Well B are similar to the mud weight values. Therefore, the pore pressures from the mud weights of Well A were not used for the interpretation. Pore pressure curves were calculated with Eaton's equation exponent 3, which was determined for compaction, but did not have a good match in either of the wells A and B. A better match is observed when Bowers' equation was applied (black curve in Figures 5.9a and 5.9b).

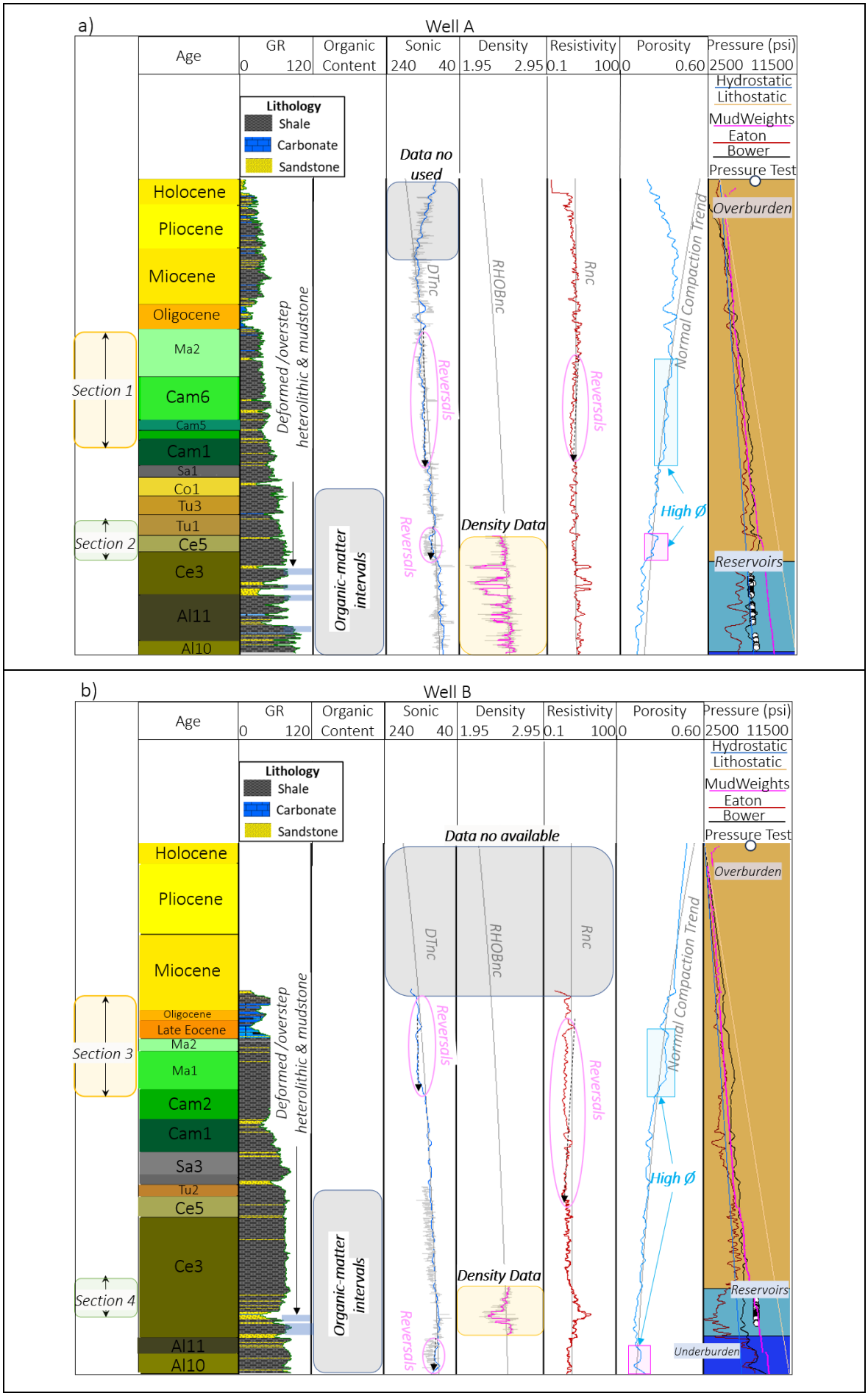
a)
Well A
Age
GR
0 120
Organic Content
Sonic
240 40
Density
1.95 2.95
Resistivity
0.1 100
Porosity
0 0.60
Pressure (psi)
2500 11500
Hydrostatic
Lithostatic
MudWeights
Eaton
Bower
Pressure Test
Lithology
Shale
Carbonate
Sandstone
Data no used
Holocene
Pliocene
Miocene
Oligocene
Ma2
Cam6
Cam5
Cam1
Sa1
Co1
Tu3
Tu1
Ce5
Ce3
Al11
Al10
Section 1
Section 2
Deformed /overstep heterolithic & mudstone
Organic-matter intervals
DTnc
RHOBnc
Rnc
Reversals
Density Data
Normal Compaction Trend
High Ø
Overburden
Reservoirs
b)
Well B
Data no available
Oligocene
Late Eocene
Ma2
Ma1
Cam2
Cam1
Sa3
Tu2
Ce5
Ce3
Al11
Al10
Section 3
Section 4
Underburden

Figure 5.9.- From left to right: age, gamma-ray (GR) with interpreted lithology, sonic log corrected by TOC and normal compaction (DTnc), density log and normal compaction trend (RHOBnc), resistivity log and normal compaction trend (Rnc), porosity curve obtained from sonic logs using equation 5.9 and normal compaction trend for porosity, pore pressure with hydrostatic (0.44 psi/ft) and lithostatic (1 psi/ft) gradients, measured pressure data (white dots), and Eaton and Bowers curves'. a) Well A and b) Well B; both wells show the intervals with high porosity values, the reversals, and the intervals corrected by organic matter content. Thin low-permeability layers (deformed /overstep heterolithic and mudstone) are highlighted on the GR track.

An analysis of a density-velocity cross-plot was performed to identify any unloading processes in wells A and B. Normal compaction boundaries have been defined previously by Bowers (1995 and 2001) and Gardner (1974) (equations 5.10 and 5.11).

$$V = 4790 + 2953 * (\rho - 1.3)^{3.57} \quad 5.10$$

$$V = \left(\frac{\rho}{0.23}\right)^{4} \quad 5.11$$

Where V is the velocity (ft/s) and ρ is the registered well log density RHOB (g/cm3). The values 4790, 2953, 3.57, 0.23, and 1.3 are constants defined by Bowers and Gardner.

Data values within the boundaries, which increase with depth, are interpreted to indicate normal compaction by mechanical compaction as a function of effective stress. In the case of unloading, the effective stress decrease affects velocity values more than density values (Bowers and Katsube, 2002). When clay diagenesis occurs, density values increase more than velocity values (Lahann, 2002).

This interpretation was based on the shales in the reservoir intervals where a density log was registered. Data from Well A show few values inside these boundaries, but the majority outside. In Well B, something similar is observed, with most of the values being outside Bowers and Gardner's boundaries. In both cases, unloading is interpreted, and this could be due to clay diagenesis or chemical compaction. The clay diagenesis described by Lahann (2002) is related to the transformation from smectite to illite, which generally occurs at temperatures higher than 70°C. In the case of chemical compaction (Goulty et al., 2012), this is related to the reduction of porosity due to the rearrangement of the clay grains.

The temperatures of both wells A and B reached higher values than 70°C, and mineralogy data obtained in Well A also show that approximately 30% of all the minerals in the shale intervals (GR> 70) in the reservoir sections are either illite or illite-smectite. Also, both wells show low porosity values in the deep section, which could imply that the shales in these intervals have not only been affected by mechanical compaction (Figure 5.10).

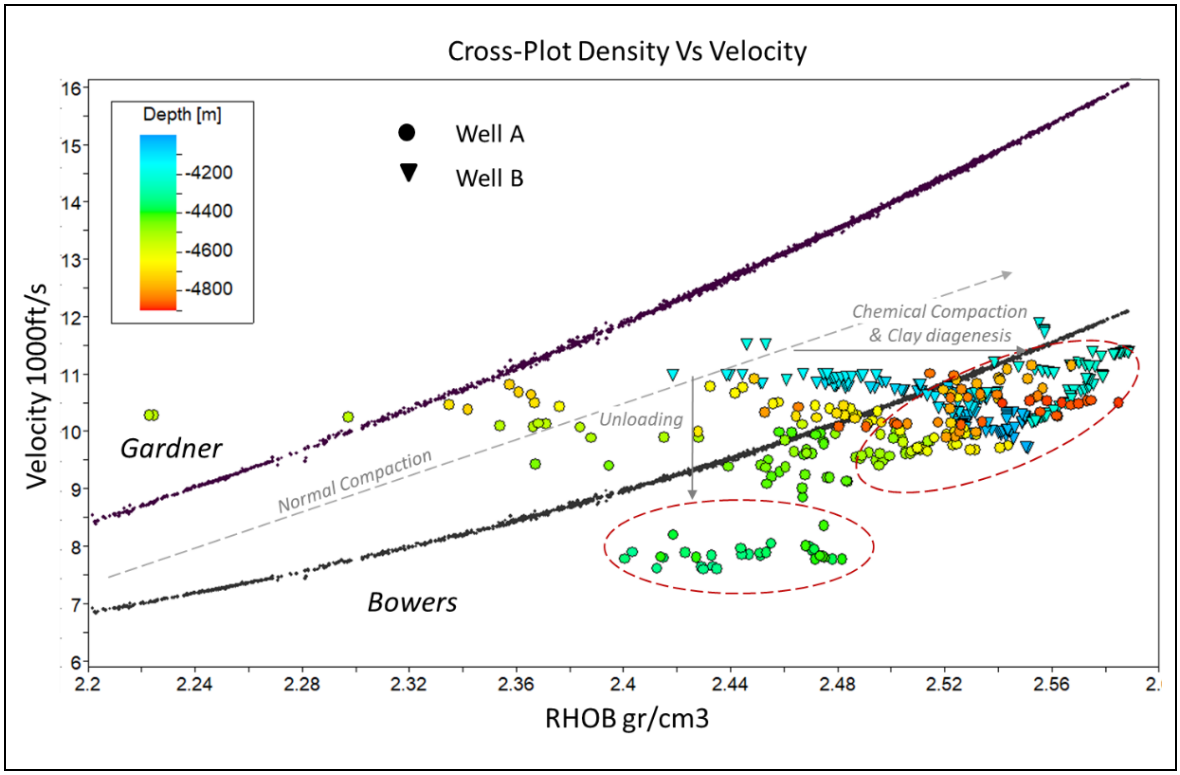

Figure 5.10.- Density-velocity cross-plot for the reservoir intervals and filter of shales interpreted based on the GR of each well A and B. The upper boundary corresponds to Gardner's equation, and the lower boundary to Bowers' equation. The interpretation of the data was based on Bowers and Katsube (2002) and Lahann (2002). The implications of this interpretation were evaluated with 1D geomechanical models in both wells, and the results are presented in section 5.4.3.

5.4 Overpressure Mechanisms Assessment

A review of the mechanisms that could have contributed to the overpressure registered in wells A and B was performed. This included 1D and 2D geomechanical modelling and 1D basin burial history modelling. Table 5.3 shows the comparison performed in both wells A and B.

Table 5.3.- Summary of the main differences found between wells A and B during the geological assessment.

Parameters	Well A	Well B
Water column (m)	2,537	1,784
Overburden (m)	~1,900	~2,239
Distance from 0 water level to wells (km)	~125	~81
Location regarding basin structure	~Transition zone	~Extension zone
Location regarding basin sedimentary environment zones	~Basin floor	~Slope
Cretaceous to Pleistocene	Yes	Yes
Shale-Sandstone intercalations with carbonate sections	Yes	Yes

Parameters	Well A	Well B
Sedimentary Environment	Deep-water systems (medium to low slope)	Deep-water systems (high to medium slope)
Carbonate section (Oligocene and Eocene) (m)	~127	~142
Organic matter (m) (shales)	~160	~400
Average sedimentation rate (m/Ma) of the overburden (Cenomanian Ce5 to present; 95.48 Ma based on Gradstein et al., 2012)	~108	~84
Average sedimentation rate (m/Ma) during Cenomanian Ce3	~127	~357
Average sedimentation rate (m/Ma) during Albian Al11	~234	~86
Erosive events or hiatus periods in the overburden (Ma)	16 events in 49.5 Ma	17 events in 31.5 Ma
Current Cenomanian Ce3 thickness (m)	216	602

5.4.1 Disequilibrium Compaction

This overpressure mechanism was investigated in wells A and B. Geomechanical models were constructed for wells A and B to investigate the influence of disequilibrium compaction on pore pressure and porosity values. The sedimentary column analysed corresponds to the total thickness in each well: 2,295 m for Well A and 2,565 m for Well B (Cretaceous to Holocene sediments). The normal compaction (hydrostatic) and porosity-permeability relationships used in these models are modifications of the curves created by Schneider et al. (1996) and Kozeny-Carmen (see Figure 5.11).

Normal compaction curves that compact fast at shallow depths to match the low porosity intervals observed in both wells were created and used in models A, A1, A2, B, B1, and B2 (Table 5.6). For instance, if the normal compaction trend (Schn Porosity Shale) and the registered data in Well A at ~4,220 m depth are considered, there is a porosity reduction from ~0.24 to ~0.20, with this reduction continuing until the end of the well (>4,800 m depth) from ~0.18 to ~0.10 (Figure 5.12a). A similar behaviour is observed in Well B, at ~3,080 m depth, with a slight porosity reduction from ~0.28 to ~0.26 m depth and from ~0.15 to ~0.12 at the end of the well (>4,400 m depth) (Figure 5.12c). The intervals where porosity reduction is observed are shale lithologies with more sand intercalations at the Campanian (~Cam2).

The low porosity values observed in the Oligocene interval of Well A were evaluated with a low porosity-permeability relationship (Carb. tight) in all the models (A, A1, and A2). In Well B, the carbonate interval used the porosity-permeability relationship (Carb.) as this interval does not present low porosity values (Figure 5.11). To generate more overpressure during sedimentation, a low porosity-permeability relationship (K-C Shale Ed.) was used in some shale intervals (Table 5.6).

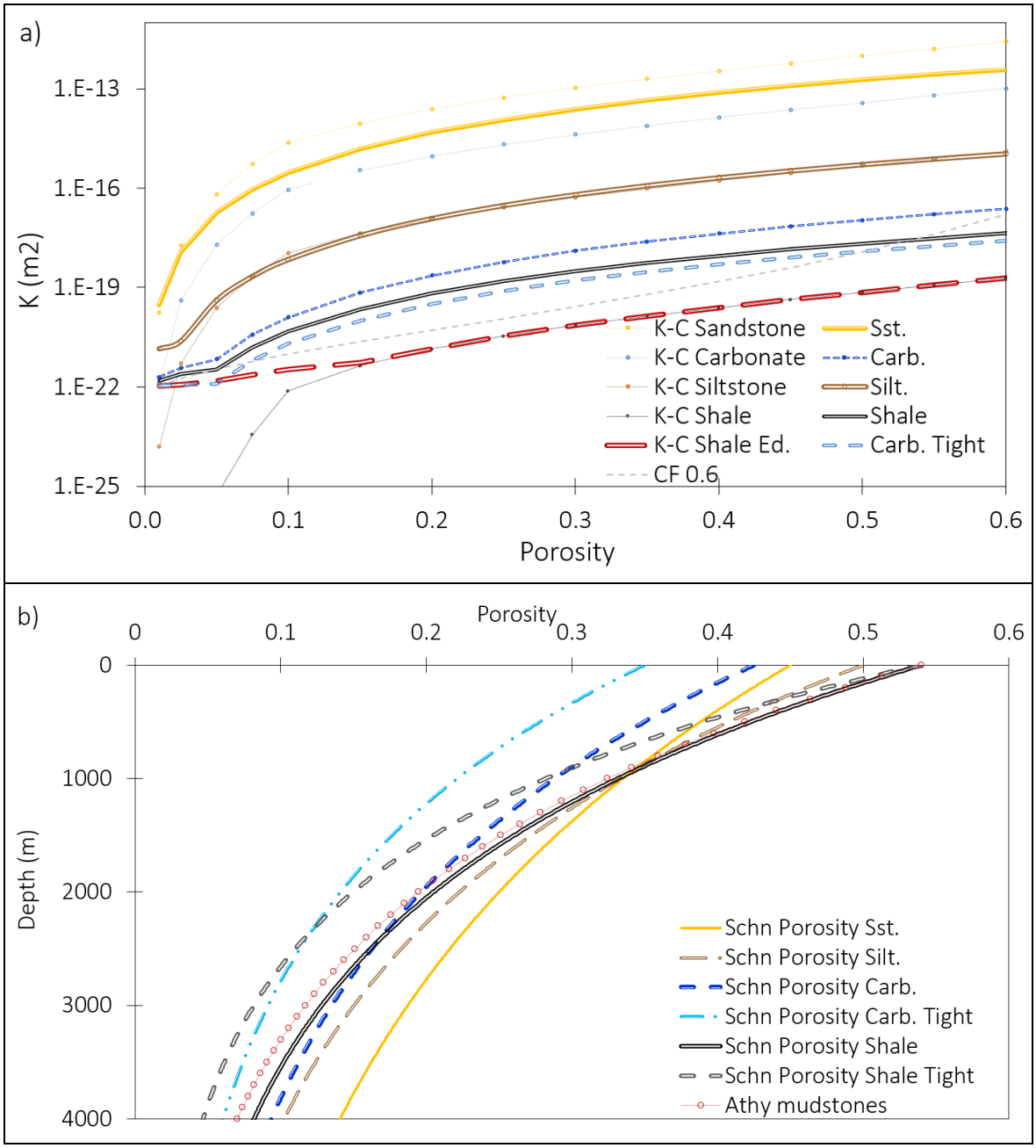

Figure 5.11.- a) Different porosity-permeability relationships were adopted for the lithologies described in this area. The classical Kozeny-Carmen relationships as defined in Hantschel and Kauerauf (2009) and the porosity-permeability relationship CF 0.6 from Yang and Aplin (2010) are provided for reference. A cut-off in permeability of 1.E-22 m^2 was set in all the models. b) Compaction trends created based on Schneider et al. (1996) allow for better modification of the shape of each lithology. Athy's compaction trend is displayed as a reference of the shale compaction.

The models represent sediments from the Cretaceous to the Pleistocene. The initial thickness was calculated using the current porosity and thickness. Each layer was represented by one lithology (e.g., sand, siltstone, carbonate, or shale), which was interpreted in each well with data from well reports and well logs.

Table 5.4 shows the settings for Well A, and Table 5.5 shows the settings for Well B. The periods Al11 and Ce3 were divided into three and four layers in both wells A and B, respectively, to better

represent these intervals. Erosive events at different periods were observed on seismic sections (e.g., Figure 5.6). These events are important for overpressure dissipation and to match porosities (Calderon et al., 2023). In these cases, porosity values present a shift in the compaction curve.

The erosive events identified were not investigated with the 1D geomechanical models using the eroded thickness. Instead, hiatus periods were used to represent both erosive events and hiatus periods. This approach was applied because the calculation of the eroded thickness is difficult to obtain when the data is limited.

The chronostratigraphic time used was based on Gradstein et al. (2012), together with the biostratigraphic reports of both wells A and B and the current thickness of each well. When a period was missing in any of the wells, this layer or section was interpreted as not being deposited (hiatus periods highlighted in grey in Tables 5.4 and 5.5).

Table 5.4.- Summary of the 1D geomechanical models constructed for Well A to investigate disequilibrium compaction. The cells in grey represent either hiatus periods or erosive events. The total period investigated was 101.42 Ma. The chronostratigraphic time was based on Gradstein et al. (2012). One lithology per layer was used to represent each period. Pore pressure data was taken in the Cenomanian interval (highlighted in green).

Well A			
Period of Time	Time duration	Lithology	Current Thickness (m)
Pleistocene	2.50	Siltstone	129
Pliocene	2.97	Siltstone	212
Miocene	19.12	Sand	278
Oligocene	10.12	Carbonate Tight	127
Eocene	21.24		
Paleocene	11.95		
Maastrichtian Ma5	0.49		
Maastrichtian Ma4	0.13		
Maastrichtian Ma3	0.45		
Maastrichtian Ma2	2.78	Sand	237
Maastrichtian Ma1	1.86		
Campanian Cam9	1.73		
Campanian Cam8	1.30		
Campanian Cam7	1.40		
Campanian Cam6	1.87	Shale	216

Period of Time	Time duration	Lithology	Current Thickness (m)
Campanian Cam5	0.46	Shale	52
Period of Time	Time duration	Lithology	Current Thickness (m)
Campanian Cam4	0.46		
Campanian Cam3	0.40		
Campanian Cam2	1.52	Shale	46
Campanian Cam1	1.03	Shale	129
Santonian Sa3	1.15		
Santonian Sa2	0.76		
Santonian Sa1	1.87	Shale	59
Coniacian Co1	2.39	Shale	91
Turonian Tu4	1.12		
Turonian Tu3	0.41	Shale	93
Turonian Tu2	1.47		
Turonian Tu1	1.53	Shale	103
Cenomanian Ce5	1.00	Shale	82
Cenomanian Ce4	0.46		
Cenomanian Ce3	2.28	Ce3-d Shale	216
		Ce3-c Sand	
		Ce3-b Shale	
		Ce3-a Sand	
Cenomanian Ce2	1.29		
Cenomanian Ce1	0.59		
Albian Al11	1.32	Al11-c Shale	226
		Al11-b Sand	
		Al11-a Shale	

Table 5.5.- Summary of the 1D geomechanical models constructed for Well B to investigate disequilibrium compaction. The cells in grey represent either hiatus periods or erosive events. The total period investigated was 101.42 Ma. The chronostratigraphic time was based on Gradstein et al. (2012). One lithology per layer was used to represent that period. Pore pressure data was taken in the Cenomanian interval (highlighted in green).

Well B			
Period of Time	Time duration	Lithology	Current Thickness (m)
Pleistocene	2.50	Siltstone	109
Pliocene	2.97	Siltstone	357
Miocene	19.12	Siltstone	381
Oligocene	10.12	Carbonate	50
Eocene	21.24	Carbonate	92
Paleocene	11.95		
Maastrichtian Ma5	0.49		
Maastrichtian Ma4	0.13		
Maastrichtian Ma3	0.45		
Maastrichtian Ma2	2.78	Sand	62
Maastrichtian Ma1	1.86	Shale	191
Campanian Cam9	1.73		
Campanian Cam8	1.30		
Campanian Cam7	1.40		
Campanian Cam6	1.87		
Campanian Cam5	0.46		
Campanian Cam4	0.46		
Campanian Cam3	0.40		
Campanian Cam2	1.52	Shale	150
Campanian Cam1	1.03	Shale	164
Santonian Sa3	1.15	Shale	124
Santonian Sa2	0.76		
Santonian Sa1	1.87	Shale	37
Coniacian Co1	2.39		

Period of Time	Time duration	Lithology	Current Thickness (m)
Turonian Tu4	1.12		
Turonian Tu3	0.41		
Turonian Tu2	1.47	Shale	58
Turonian Tu1	1.53		
Cenomanian Ce5	1.00	Shale	106
Cenomanian Ce4	0.46		
Cenomanian Ce3	2.28	Ce3-d Shale	602
		Ce3-c Shale	
		Ce3-b Sand	
		Ce3-a Shale	
Period of Time	Time duration	Lithology	Current Thickness (m)
Cenomanian Ce2	1.29		
Cenomanian Ce1	0.59		
Albian Al11	1.32	Al11-c Shale	82
		Al11-b Sand	
		Al11-a Shale	

Six 1D column models, three for Well A and three for Well B, were constructed. Models A and B used the compaction trend named Schn Shale and the porosity-permeability relationship named Shale (Figure 5.11). To reach the low porosity values encountered in both wells, tight compaction curves were used in some of the layers of the models A1, A2, B1, and B2. To represent low-permeability layers, the low porosity-permeability relationship (K-C Shale Ed.) was used in models A2 and B2 (Table 5.6).

Table 5.6.- Summary of the six models constructed to investigate disequilibrium compaction in wells A and B. Models A2 and B2 investigated the effect of low petrophysical properties with a current thickness of 1,155 m for model B2 and 117 m for model A2.

Model	Layers with tight compaction trends (shale lithologies)	Layers with low porosity-permeability relationships(shales)	Compaction and porosity-permeability relationships
A	none	none	Schn Shale and Shale
A1	Al11a, Al11c, Ce3b, Ce3d, Ce5 and Tu1 (544 m)	none	Schn Shale Tight and Shale

Model	Layers with tight compaction trends (shale lithologies)	Layers with low porosity-permeability relationships(shales)	Compaction and porosity-permeability relationships
A2	Al11a, Al11c, Ce3b, Ce3d, Ce5 and Tu1 (416 m)	1 layer (Al11c) (117 m)	Schn Shale Tight and K-C Shale Ed.
B	none	none	Schn Shale and Shale
B1	Al11a, AL11c, Ce3a, Ce3c, Ce3d, Ce5, Tu2, Sa1, Sa3, Cam1, and Cam2 (1,155 m)	none	Schn Shale Tight and Shale
B2	Al11a, AL11c, Ce3a, Ce3c, Ce3d, Ce5, Tu2, Sa1, Sa3, Cam1, and Cam2 (1,155 m)	11 layers (Al11a, AL11c, Ce3a, Ce3c, Ce3d, Ce5, Tu2, Sa1, Sa3,Cam1 and Cam2) (1,155 m)	Schn Shale Tight and K-C Shale Ed.

Models A and B generated slight overpressure in both wells, ~1 MPa in Well A and ~1.8 MPa in Well B. This small amount is almost enough to match the first section of the pressure data for Well A. However, porosity values in both wells are high in comparison to well data. Different porosity trends are observed in the sediments above ~3,960 m depth in Well A and ~3,000 m depth in Well B. The reduction of porosity can be interpreted to be related to diagenetic processes (see Section 5.4.3). Another interpretation can be related to further compaction due to sedimentation and erosive events. In this case, a thick interval has to be eroded (see Figure 3.12a in Chapter 3), causing an apparent porosity reduction. This interpretation is unlikely to have occurred in this basin.

Model A1 (Well A) shows that pore pressure and porosity have a better match with the tight compaction curve in the interval ~4,570 to ~4,750 m depth, but not in the interval ~4,850 to ~4,865 m depth (Figures 5.12a and 5.12b).

Model B1 (Well B) generates ~1 MPa overpressure at ~4,100 m depth, which is below the pore pressure values registered. Porosity values matched better until ~4,780 m; below this depth, registered porosities are lower than the results obtained with this model (Figures 5.12c and 5.12d).

A low porosity-permeability relationship was used in Models A2 and B2 to generate higher pore pressure values as registered in Well B. This low porosity-permeability relationship (K-C Shale Ed.) is ~24 times lower than the porosity-permeability relationship (Shale) used for the rest of the shale intervals.

Model A2 has one layer (Al11c) with a low permeability relationship, with a thickness of 117 m. This model matched better the interval below ~4,740 m depth. However, porosity values are higher than observed values due to the overpressure generated by the low permeability layer.

Model B2 has eleven layers with a low permeability relationship, with a total thickness of 1,155 m. High pore pressure values similar to the registered values were generated due to the low permeability in the eleven layers, but porosities and thicknesses could not be matched. This is because the high pore pressures generated during sedimentation preserve high porosities (Figure 5.12).

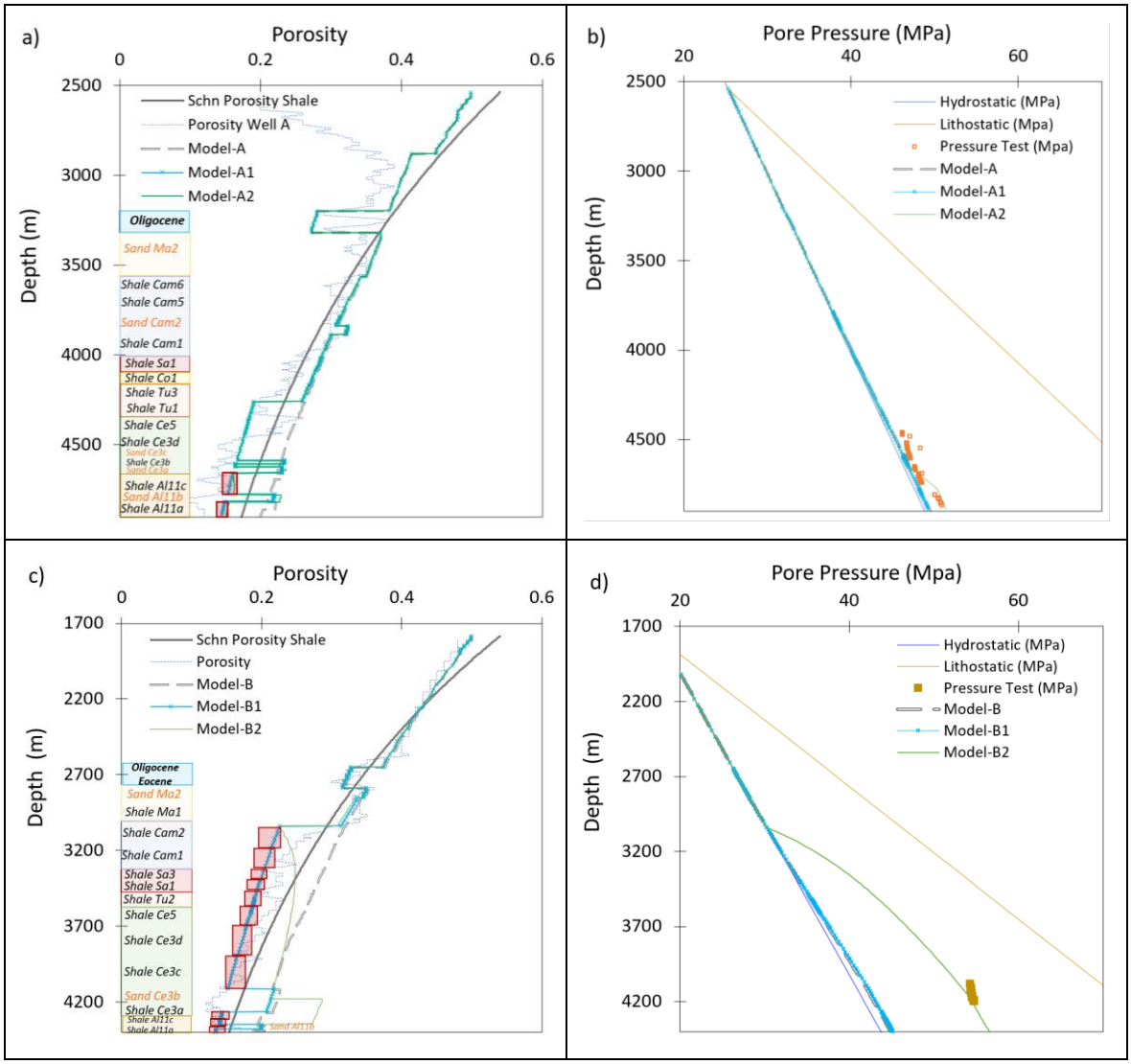

Figure 5.12.- a) Porosity vs. depth plot of Well A with the porosity obtained from the sonic log and results from models A, A1, and A2. b) Pore pressure vs. depth plot of Well A with data from pressure tests and results of models A, A1, and A2. c) Porosity vs. depth plot of models B, B1, and B2 with the porosity obtained from the sonic log. d) Pore pressure vs. depth plot of models B, B1, and B2 with data from pressure tests. The periods and the layers where permeabilities were reduced have been highlighted with red squares in the porosity plots. Schneider et al. (1996) normal compaction trend for shale lithologies (Schn Porosity Shale) is presented as a reference.

5.4.2 Overpressure Generated due to an External Structure

External structures, such as canyons and channels, have also been investigated to see if they could have caused the overpressure encountered in Well B. In the studied area, multiple canyons with different sizes have been identified from the Cretaceous to the Holocene (e.g., Figure 5.13).

The canyon investigated was mapped using seismic data. This canyon crosses from east to west and has eroded sediments from the Holocene to the Oligocene (Figure 5.13). It is observed that it is not connected to a current fluvial system; therefore, it is interpreted to have developed either by bottom currents (e.g., detached canyon as suggested by McArthur et al., 2019 in the East Coast Basin, New Zealand, or type II canyon as suggested by Jobe et al., 2011 in the Rio Muni Basin of

Equatorial Guinea, West Africa) or by an ancient feeder (e.g., Antobreh and Krastel, 2006; study performed in the Cap Timiris Canyon, offshore Mauritania). The closest active river in this region is the Senegal River, which has not changed its current course since the Miocene to the present-day (Dietz et al., 1968). The distance from this canyon to Well B is ~1,500 m and to Well A is ~7,000 m. It has a width of 5,000 m, and a height of 970 m (Figure 5.13).

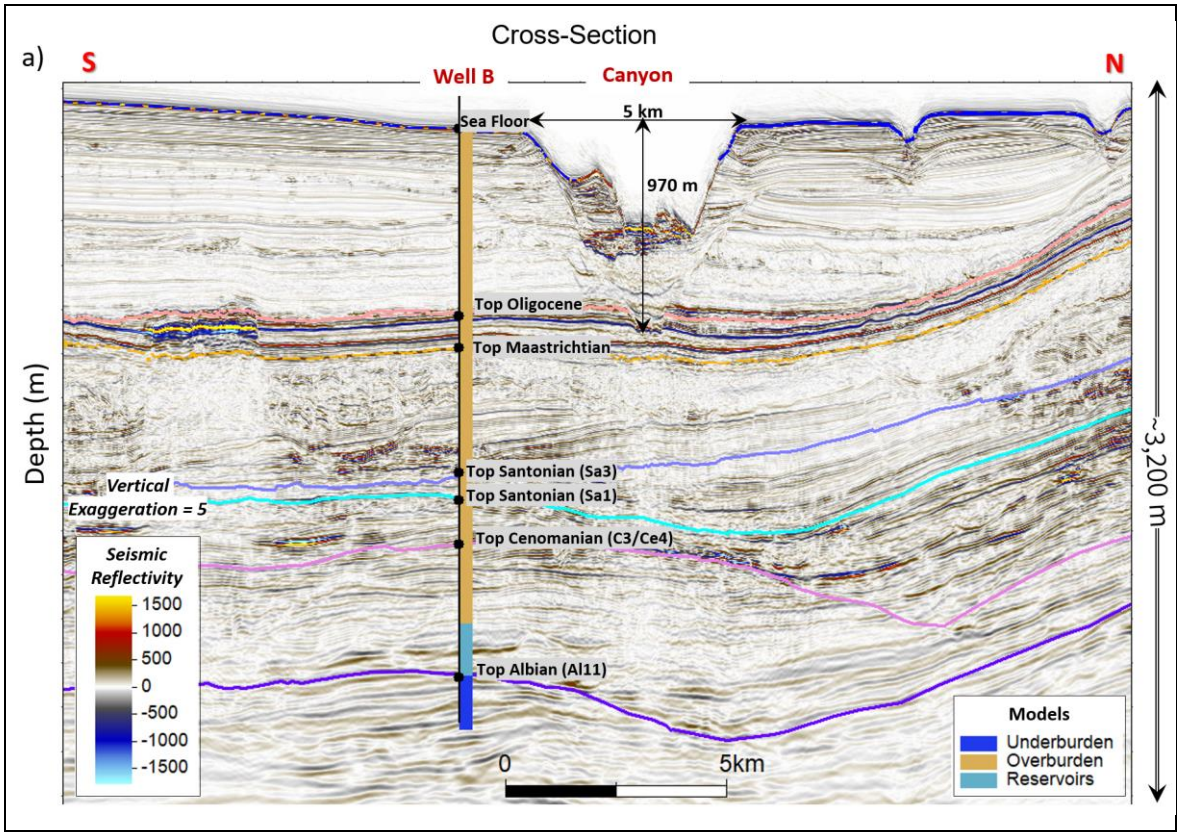

Figure 5.13.- a) Seismic cross-section of the canyon with the main horizons interpreted in this study and the dimensions of the canyon. It has been highlighted in three sections: the overburden, the reservoirs, and the underburden.

Two models were constructed; the first model considered the shape of the canyon at the initial stage, followed by sedimentation that filled the canyon during a period of 0.01 Ma (Figure 5.14). In the second model, the initial stage started with all the sediments in place, followed by the erosion of the canyon during a period of 0.01 Ma (Figure 5.15).

A pseudo-well named X was located in the middle of the canyon to compare the pore pressure values at this location with the B well. The model layers were constructed with three sections: underburden, reservoir, and overburden. A continuous layer is used for the reservoir, which is represented by sand lithologies; the other two sections are shale lithologies. The dimensions of the modelled canyon are ~4,500 m in width and ~950 m in height.

Results from the first model show that when sediments are deposited at a fast sedimentation rate, pore pressure increases at the canyon location, and this pore pressure is transferred to the location of Well B through the reservoir interval. However, the pore pressure contribution from this structure to Well B is negligible.

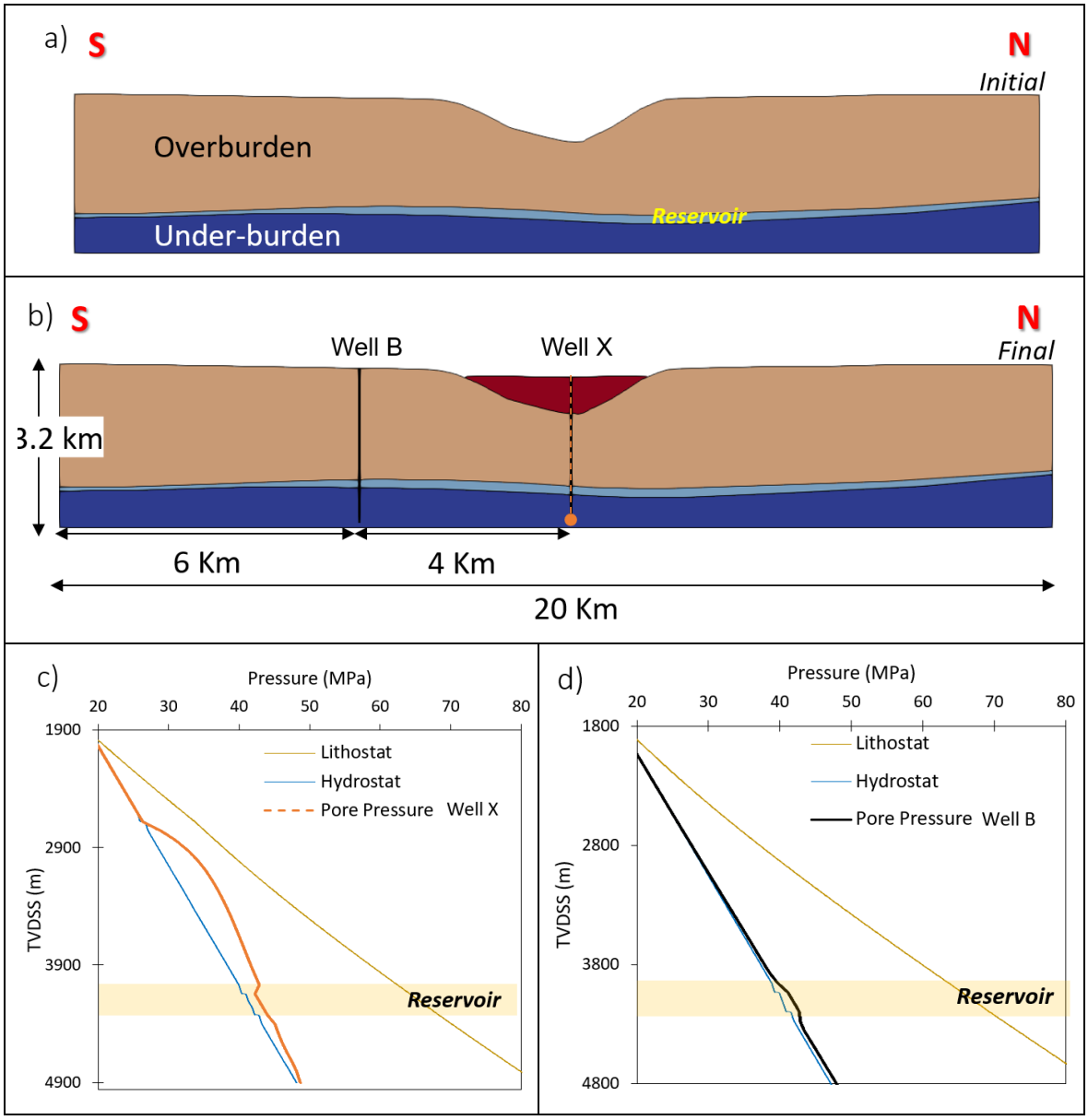

Figure 5.14.- a) Cross-section of the initial stage of the model with the overburden, the reservoir layer, and the underburden with the shape of the canyon. b) Cross-section of the final stage when the canyon was filled. c) Plot of the pressure at the X location, representing the effect of the canyon sedimentation on pore pressure. d) Pressure plot at the location of Well B with the hydrostatic and lithostatic gradients as references.

Results from the second model show that the erosive event resulted in pore pressure reduction, and this reduction was transferred to the location of Well B. The pore pressure at Well B is slightly lower than the hydrostatic gradient. It is important to highlight that in both models, the pore pressure will return to its initial value over time in the absence of any other overpressure-generating mechanism (Figure 5.15).

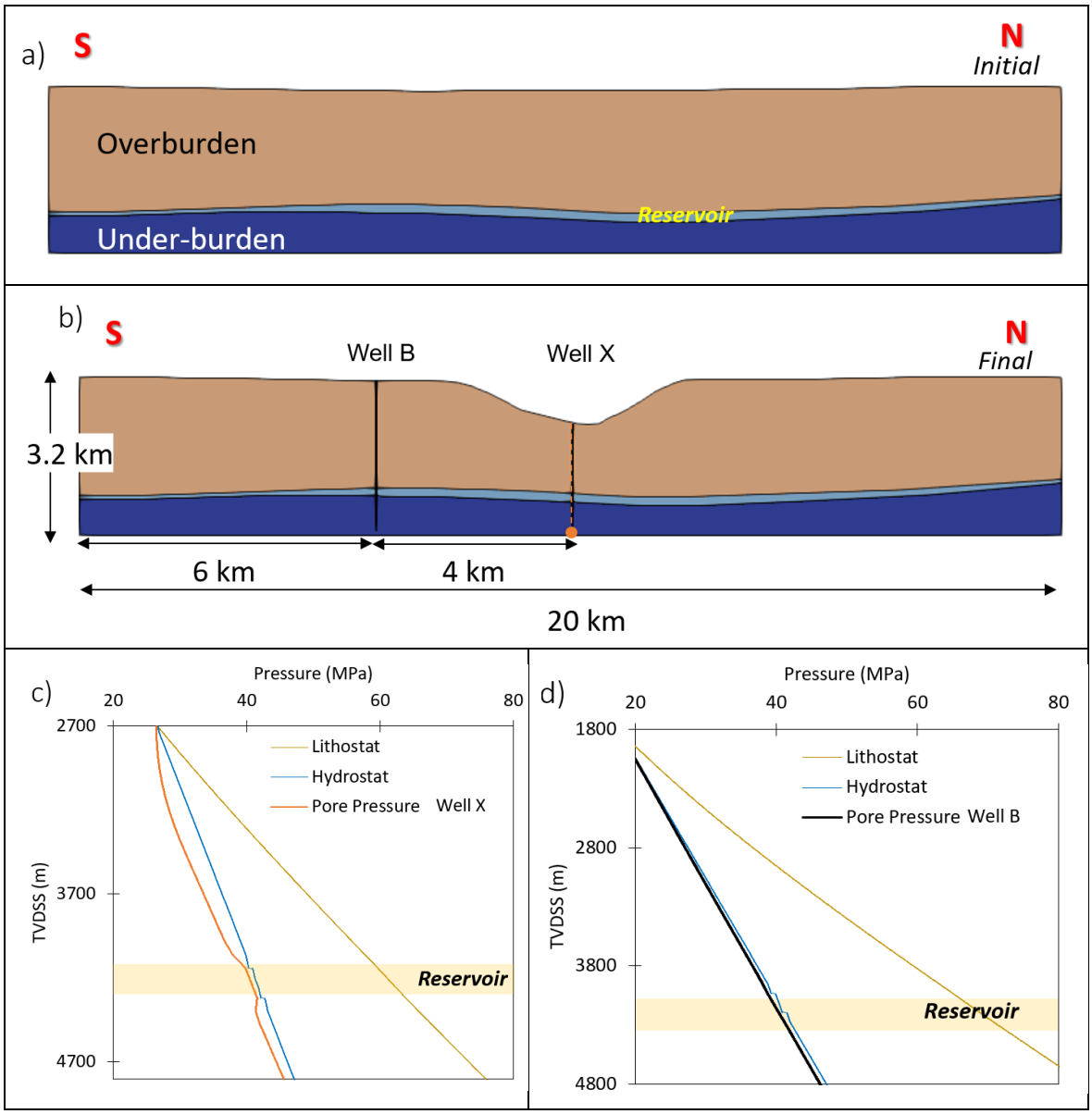

Figure 5.15.- a) Cross-section of the initial stage of the model with the whole overburden, the reservoir layer, and the underburden. b) Cross-section of the final stage when the canyon was eroded. c) Plot of the pressure at the X location, representing the effect of the canyon erosion on pore pressure. d) Pressure plot at Well B location with the hydrostatic and lithostatic gradients as references.

5.4.3 Clay Mineral Diagenesis

This overpressure mechanism depends on several factors, such as geothermal gradient, time, pore water chemistry, smectite compositions, depth, salinity, distribution of the clays, and sealing conditions (Powers, 1967; Bruce, 1984; Tosaya and Nur, 1982; Dutta, 1987). The temperature at which smectite starts the transformation to illite is debatable as it depends on many factors (see Bruce 1984). Dutta (1987) proposed that the main phase of the reaction is produced at temperatures between 70 and 100°C, while Lahann (2002) suggested that this process could start between 50 and 75°C, and O'Connor et al. (2011) suggested temperatures between 100 and 120 °C.

As the smectite to illite transformation occurs, the structure of the clay changes, reducing the flow properties and permeabilities (Lothe et al., 2023). According to Tosaya and Nur (1982), the

distribution of clays seems to have an effect on the response of velocities; when a rock contains clay coatings, compressional velocities are higher than if clays are found in the pore spaces.

Different processes occur during clay diagenesis. One is the release of interstitial water into the system, either partially or completely. The expandable clay smectite dehydrates into the non-expandable illite clay, and this process can contribute up to 1/3 of the overpressure encountered in wells (e.g., Audet, 1995; Tremosa et al., 2020). Another is the change in the arrangement of the clay mineral grains (Powers, 1967; Aplin et al., 2003; Goulty et al., 2012). This arrangement is known as chemical compaction (see Goulty et al., 2012). The porosity lost due to chemical compaction is more or less independent of the effective stress. A third process is related to the whole system; in this case, if it is a closed system, the pressure could increase as the pressure of the grains is passed to the pore fluid, often referred to as load transfer (Lahann and Swarbrick, 2011).

Studies related to any diagenetic process are scarce within the studied area, and this suggests that these processes are poorly understood and should not be discounted. For instance, the only diagenetic processes described in this basin are from samples of sites 367, 368, and 370 (Figure 5.1). Dean et al. (1978) described the formation of siderite, the reprecipitation of carbonates, and the precipitation of silica mainly in Eocene sediments while Baker et al. (1978) identified a short-term thermal metamorphism related to igneous intrusions in this basin. The temperature at the sediment contact has been determined to be ~1,000 °C, which makes the geothermal gradient of these basins to increase, causing heat-induced diagenesis (Baker et al., 1978). The Senegal and Mauritania Basins have geothermal gradients between 40 and 43 °C/km (McGuinness et al., 2021).

As temperature is an important factor that allows clay diagenesis to occur, the cause of the high geothermal gradients registered in both wells A and B was reviewed. The high geothermal gradients in the Senegal Basin have been related to a normal post-rift thermal subsidence (e.g., von Rad and Einsele, 1980; Mourlot et al., 2018). Although, magmatic intrusions (magma temperature ~1,200 °C) between the Cretaceous and Pleistocene (Bellion and Crevola, 1991; Davison, 2005), which intensified during the Late Eocene-Oligocene (~35 Ma) to Late Miocene (~8 Ma), have been described in the Senegal-Mauritania Basins, these magmatic intrusions were not identified on the data of the studied area.

The temperatures registered in wells A and B are higher than 80 °C in the reservoir intervals, reaching temperatures of 118 °C in Well B. The temperature chosen to investigate the smectite clay diagenesis process was 80 °C. Well A only reached this temperature at the top of the reservoir interval in the sand reservoir. Therefore, the shale below this interval was considered the start of the smectite to illite transformation (~Shale Ce3b; Figure 5.18). Well B reached 80 °C from ~600 m above the top of the reservoir interval (~Shale Tu2; Figure 5.18).

Temperature values in both wells do not follow a linear trend and vary depending on the interval. This effect was not investigated, and instead two linear gradients that crossed the top of the first value in each well with a surface temperature of 5 °C were created and used during the analysis (Well A 39°C/km and Well B 44 °C/km) (Figures 5.16a and 5.16b).

The temperature difference in both wells could be due to external factors such as vulcanism. According to Bellion and Crevola (1991), sills and intrusions have been identified around the Dakar area, which is close to Well B. However, these structures could not be identified during the seismic interpretation performed for this project.

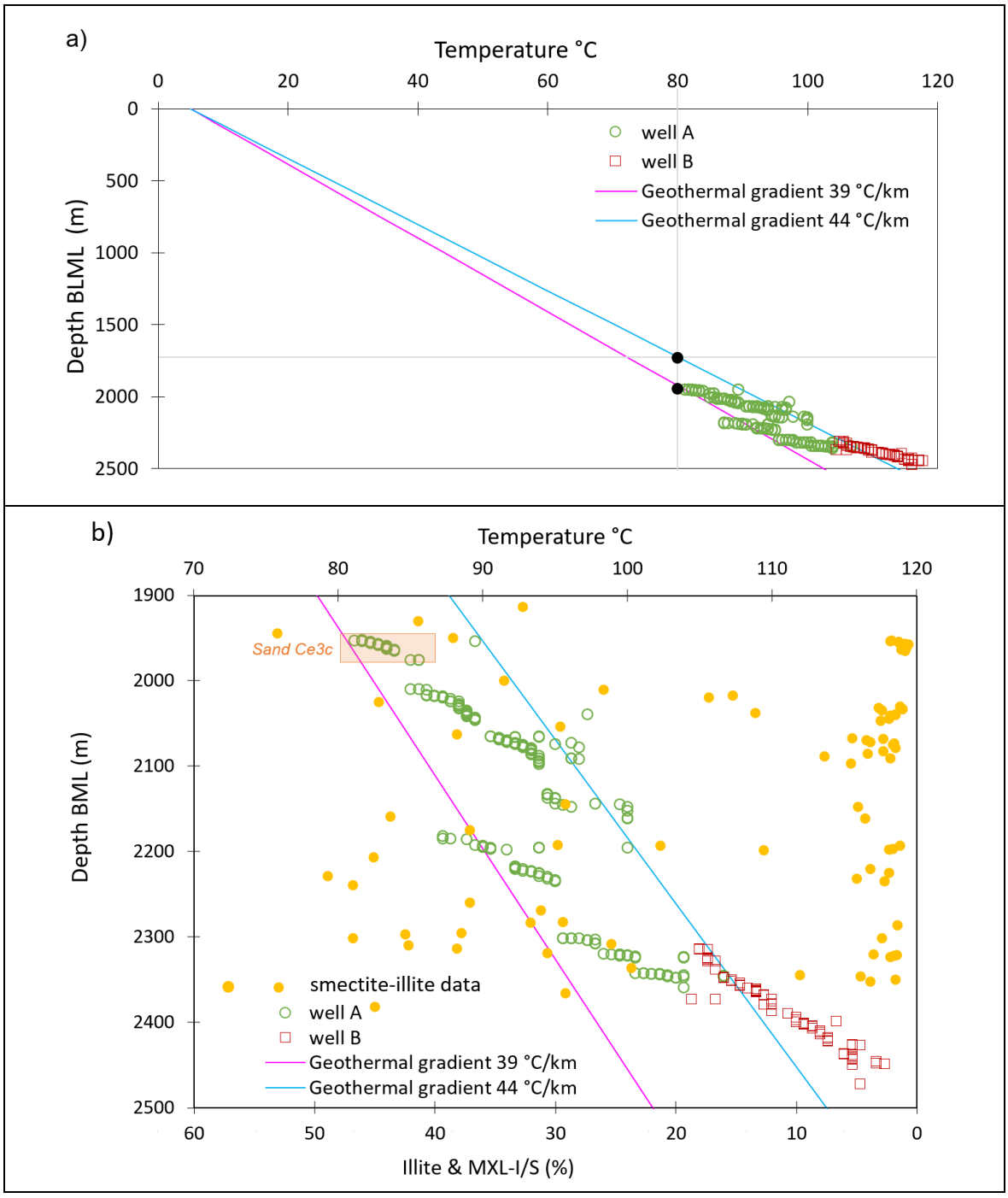

Figure 5.16.- a) Temperature data and geothermal gradients of wells A and B. b) Temperature plots focus on the reservoir intervals of both wells. In Well A, temperature values have multiple trends similar to the multiple reservoirs interpreted on pore pressure data. A similar situation is observed in Well B, where one temperature trend is interpreted, which corresponds to one connected reservoir.

From the petrographic report of Well A, it is observed that illite and smectite/illite are abundant in the shale lithologies of the reservoir intervals. These studies were not available for Well B, but it is

assumed to have similar mineralogy as the sediments deposited in Well A passed through the area where Well B is located. Consequently, smectite to illite transformation could have started first in Well B due to the thick overburden and the high temperatures this well has (e.g., possibly from the Campanian). To investigate this overpressure mechanism, geomechanical models were constructed for Well A and Well B. These models have the same configuration used for the 1D models that investigated disequilibrium compaction (Tables 5.4 and 5.5). Models A and B investigated only disequilibrium compaction and were used in this section for comparison between the results.

The clay diagenesis process investigated was the reduction of porosity due to clay diagenesis, using the ParaGeo software. The reaction model used was a power law (equation 5.12) that describes the rate of loss of porosity due to diagenesis as a function of temperature, starting at a threshold temperature.

$$\frac{d_\emptyset}{dt} = -A\left(\frac{T}{T_{init}} - 1\right)^m \left(\frac{\Delta\emptyset_{max}^{diag} - \Delta\emptyset^{diag}}{\Delta\emptyset_{max}^{diag}}\right)^n \quad 5.12$$

Where $\frac{d_\emptyset}{dt}$ is the rate of porosity change, A is a constant (0.07 Ma^{-1}), T is the current temperature (°C), T_{init} is the temperature when the process will begin (80 °C), $\Delta\emptyset_{max}^{diag}$ is the maximum porosity change for the reaction (12%), $\Delta\emptyset^{diag}$ is the current porosity change for the reaction, m (0.1) and n (0.5) are constants with values ranging from 0 to 1.

Models A-D and A-DT used a geothermal gradient of 39 °C/km, while models B-D and B-DT used 44 °C/km. The maximum porosity reduction to occur during the smectite to illite transformation was set to be 12% (Lahann, 2002) (Figure 5.18).

As permeability reduction has been observed to occur during smectite to illite transformation and this has been related to overpressure generation (Aplin et al., 2003; Lothe et al., 2023), this approach was applied to the layers where low porosity values were identified.

Models A-D and B-D used a low porosity-permeability relationship (K-C Shale Ed.; Figure 5.11a) to represent the reduction of porosity and permeability due to clay diagenesis. This relationship was applied from the beginning of the sedimentation in the selected layers, where temperatures reached 80 °C. This porosity-permeability relationship is 24 times lower than the curve (Shale; Figure 5.11a) used for the rest of the layers (value taken at 0.15 porosity).

In model B-D, three shale layers on top of the reservoir interval, three shale layers in the reservoir interval, and two shale layers below the reservoir interval that reached 80 °C were defined. Model A-D does not have any shale layer on top of the reservoir intervals that reached 80 °C, but it has one shale layer within the reservoir intervals and two shale layers below the reservoir intervals that reached this temperature (Table 5.7).

Models A-DT and B-DT used the porosity-permeability relationship (Shale) for all layers from the beginning of the sedimentation. This curve was then changed to the low porosity-permeability relationship (K-C Shale Ed.; Figure 5.11a) per model B-DT (Well B) and per model A-DT (Well A).

The time when these curves were changed was when these intervals reached 80 °C and the smectite to illite transformation is set to start (Figure 5.17).

Table 5.7.- Summary of the two models created to investigate the overpressure caused by the smectite to illite transformation. Models A and B consider only disequilibrium compaction and are displayed to highlight the differences.

Model	Smectite Transformation Temperature	Layers with low porosity-permeability relationships (shale lithologies)	Compaction trends and porosity-permeability relationships used
A	none	none	Schn Shale and Shale
A-D	When the sediments reach 80 °C perambility reduces further	3 layers (Al11a, Al11c, and Ce3b) (359 m)	From the beginning Schn Shale and K-C Shale Ed.
A-DT	When the sediments reach 80 °C permeability reduces	3 layers (Al11a, Al11c, and Ce3b) (359 m)	From the beginning Schn Shale and Shale when reached 80 °C change to Schn Shale and K-C Shale Ed.
B	none	none	Schn Shale and Shale
B-D	When the sediments reach 80 °C permeability reduces further	8 layers (Al11a, Al11c, Ce3a, Ce3c, Ce3d, Ce5, Tu2 and, Sa1 (717m)	From the beginning Schn Shale and K-C Shale Ed.
B-DT	When the sediments reach 80 °C permeability reduces	8 layers (Al11a, Al11c, Ce3a, Ce3c, Ce3d, Ce5, Tu2 and, Sa1 (717m)	From the beginning Schn Shale and Shale when reached 80 °C change to Schn Shale and K-C Shale Ed.

These two different approaches generated different results, and this difference is more evident in the models of Well B because these sediments reached 80 °C from the beginning of the sedimentation (~82 Ma; Figure 5.17b). When the low porosity-permeability relationship (K-C Shale Ed.) was used from the beginning of the sedimentation in models A-D and B-D, porosity and permeability started reducing, first due to mechanical compaction, and when the sediments reached 80 °C due to mechanical compaction and clay diagenesis (smectite to illite transformation) (Figures 5.17e and 5.17f).

In models A-DT and B-DT, a relatively high porosity-permeability relationship named Shale (for reference, see Figure 5.11a) was used at the beginning of the sedimentation process and then changed to a low porosity-permeability relationship (K-C Shale Ed.) when the sediments reached temperatures of 80 °C. The maximum imposed porosity reduction value in all four models (A-D, B-D, A-DT, and B-DT) was 0.12 (Figures 5.17g and 5.17h).

To better visualise the smectite to illite transformation through time, a location at the base of each model was selected (Point Monitored; Figures 5.17a and 5.17b). It is observed that the smectite to illite transformation begins at the monitored point ~14 Ma ago in Well A and ~82 Ma ago in Well B.

This time difference is due to the geothermal gradients and the overburden thicknesses of each well (Figure 5.17).

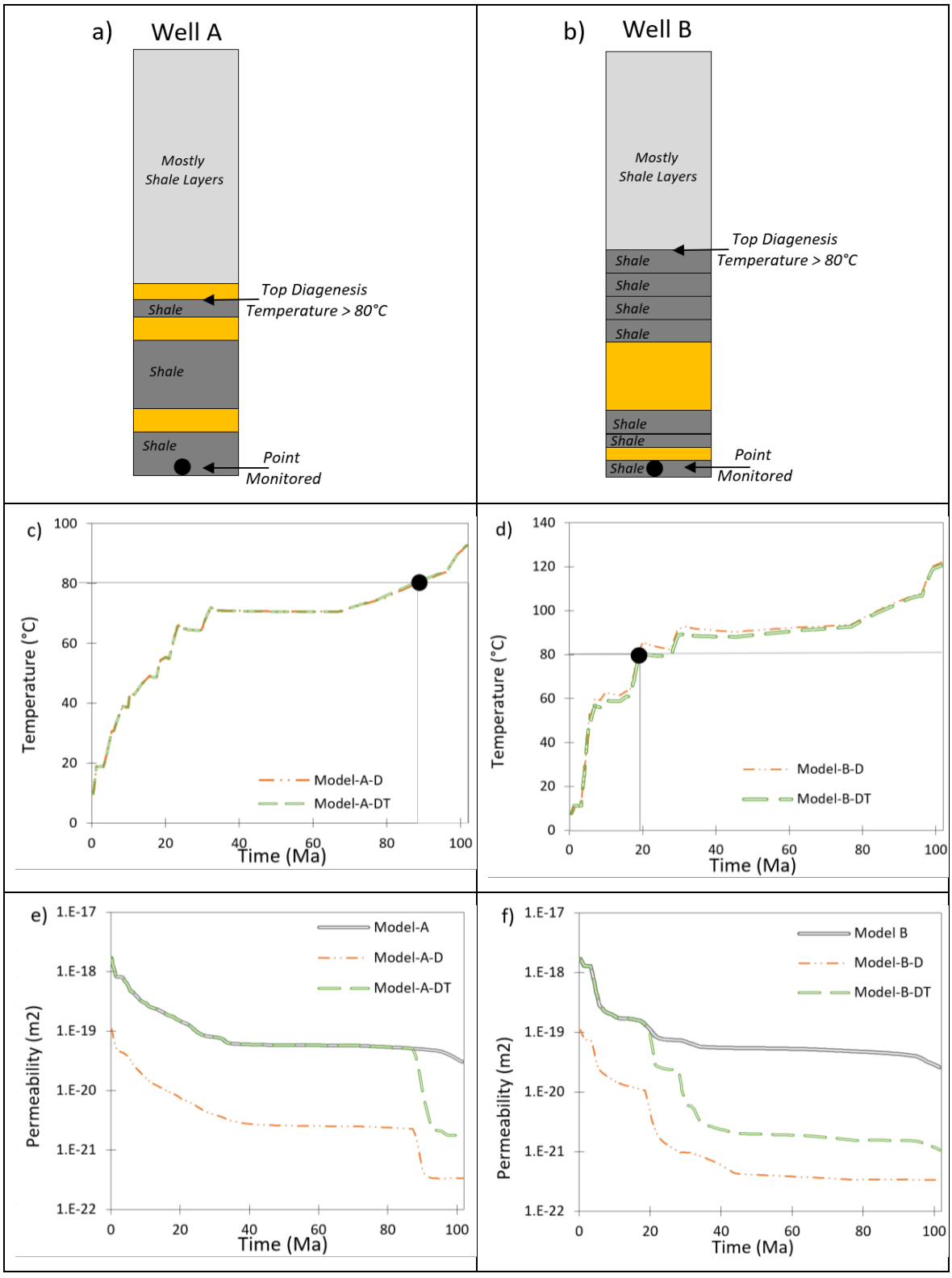

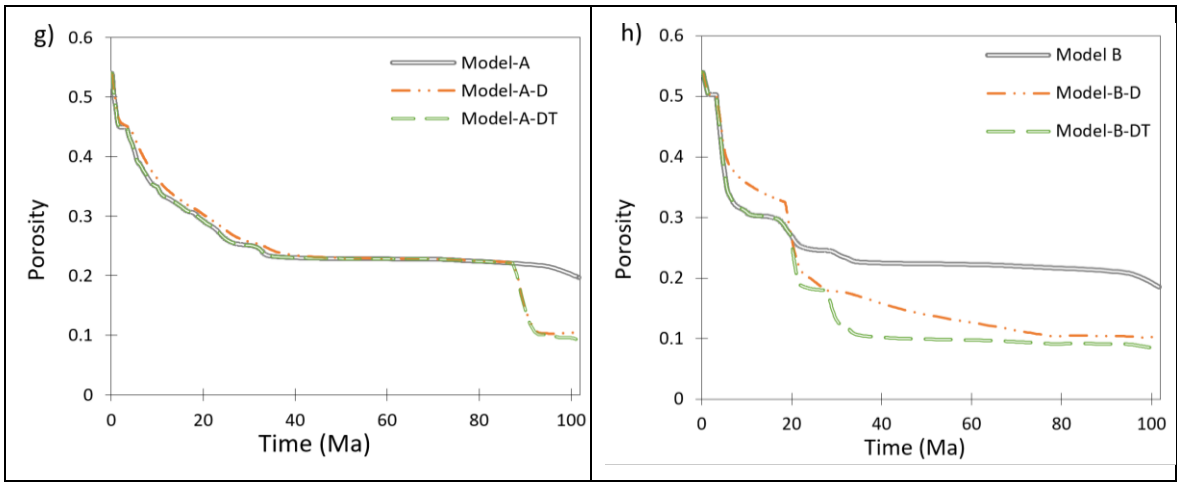

Figure 5.17.- Plots showing the evolution of porosity, permeability, and temperature through time. Plots a, c, e, and g show the results of the models constructed for Well A, while plots b, d, f, and h show the results of the models constructed for Well B. Models A and B investigated disequilibrium compaction and were used for comparison. a) and b) are sketches that represent the layers of each well that reached 80 °C at the monitored point.

Results from the four models (A-D, B-D, A-DT, and B-DT) show that high overpressures can be generated due to both disequilibrium compaction and the non-mechanical porosity reduction as a result of the clay mineral diagenesis, with a better match to the well data.

Model A-D (Well A), which used a low porosity-permeability relationship from the beginning of the sedimentation, generated higher pore pressure values than the registered data. This is the result of porosity and permeability reduction due to disequilibrium compaction and smectite to illite transformation when the sediments reached 80 °C (Figure 5.18b). On the other hand, model B-D (Well B) generated high pore pressures, which almost matched the registered data (Figure 5.18d). Porosity values also better matched the data in the intervals where smectite to illite transformation was set up to occur (Figures 5.18a and 5.18c). In the models A-D and B-D, porosity values were preserved as a result of the overpressure generated.

Model A-DT shows that pore pressure values can be matched (to registered well data) when the relatively high porosity-permeability relationship (Shale) is used from the beginning of sedimentation and then switched to a low porosity-permeability relationship (K-C Shale Ed.) when the sediments reach 80 °C (Figure 5.18b). In contrast, model B-DT shows that when the smectite to illite transformation begins, porosity is reduced, but this reduction does not result in the generation of high pore pressures. In this case, the model did not match pore pressure nor porosity values (Figures 5.18c and 5.18d). In both models, A-DT and B-DT, porosity values are too low in comparison to well data (Figures 5.18a and 5.18c).

The permeabilities in models A-DT and B-DT do not reach the low permeabilities reached in models A-D and B-D (Figures 5.17e and 5.17f). This is because the amount of permeability reduction due to first mechanical compaction and then clay diagenesis was dependent on the initial permeability curve (Shale) which is 40.5 times higher than the porosity-permeability relationship (K-C Shale Ed.; Figure 5.11a).

It is also observed that the low porosity-permeability relationship used from the beginning of the sedimentation in model B-D is required to match the high pore pressures of Well B, but this low relationship is not needed to match the pore pressure of Well A from the beginning of the sedimentation. The intervals above the smectite to illite transformation with low porosity data could indicate the possibility of an early smectite diagenesis with lower temperatures than 80 °C.

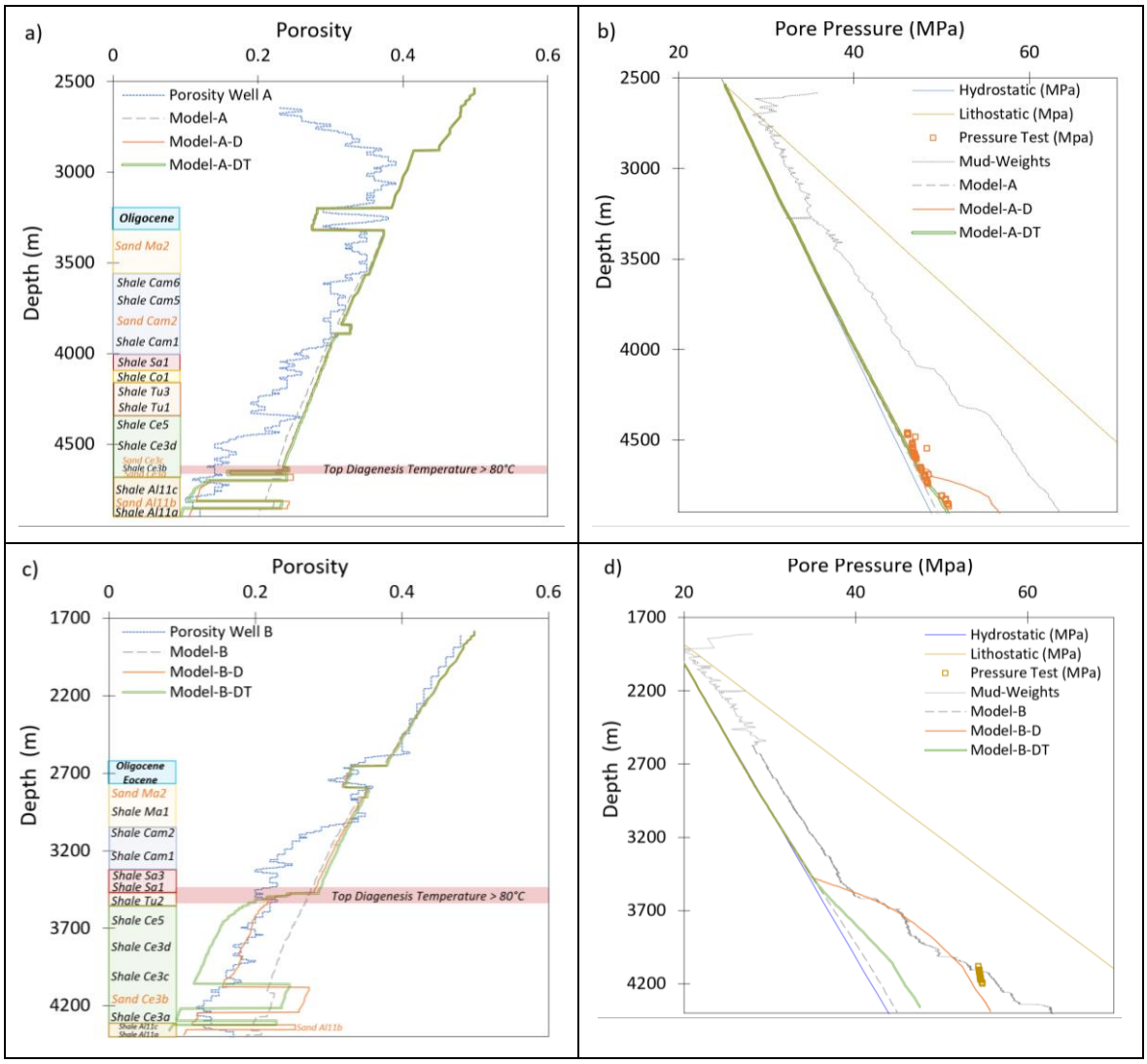

Figure 5.18.- a) Porosity-depth plot of Well A, models A, A-D, and A-D-T with sonic porosity. It has been highlighted the layers with the lithology used in the models, the period, and the depth where these sediments reached 80 °C. b) Pore pressure-depth plot of Well A, models A, A-D, and A-D-T with the measured pore pressure values. Lithostatic and hydrostatic gradients were also plotted for reference. c) Porosity-depth plot of Well B, models B, B-D, and B-D-T with sonic porosity. It has been highlighted the layers with the lithology used in the models, the period, and the depth where these sediments reached 80 °C. d) Pore pressure-depth plot of Well B, models B, B-D, and B-D-T with the measured pore pressure values. Lithostatic and hydrostatic gradients are also plotted for reference.

5.4.4 Pressure Transfer from Down-slope

Deep-water systems can in principle, allow both connectivity and compartmentalisation in all directions (Mayall et al., 2006). Any hydraulic connection between wells A and B was analysed to

determine the possibility of pressure transfer between these two locations. Due to the position of Well A in the basin (down-slope), higher fluid pressure in this well could in principle, be transferred to Well B.

Assessment of the seismic data suggests that there is no connection of likely high permeability units between these wells at the high-pressure interval observed in Well B (Figure 5.19b). Due to this analysis, no geomechanical models were used to assess the lateral transfer of pore pressure. Furthermore, the overburden thickness in Well B is greater than in Well A, so any lateral pore pressure transfer would be from Well B to Well A (Figure 5.19a).

To see the thickness variation through time in both wells, a flattened surface was applied to seismic data around 8,000 m depth. It is observed that the thickness at the Well B location is greater through time at all periods except during the Maastrichtian to the Turonian, where the thickness is higher at the Well A location (Figure 5.19c).

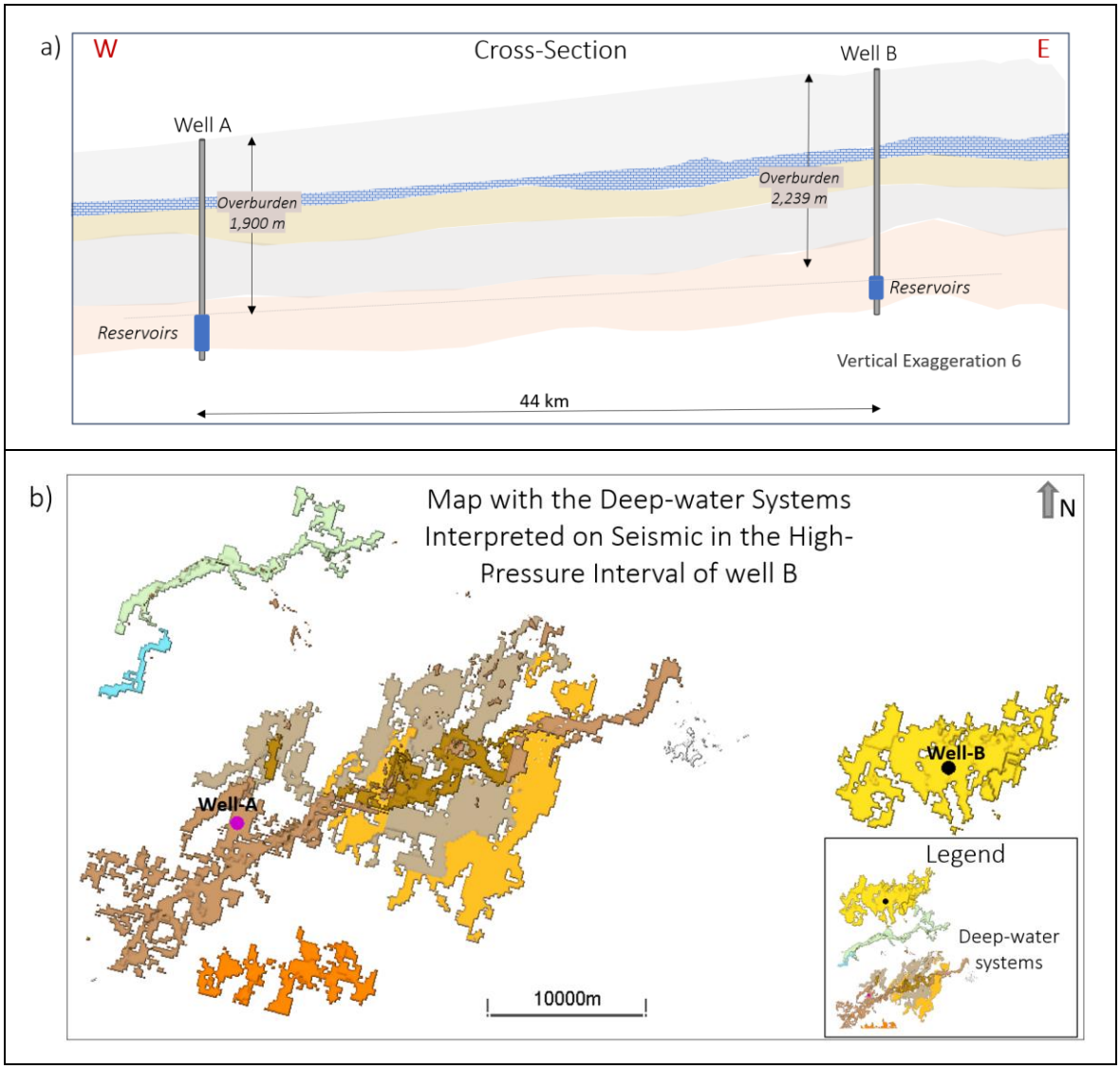

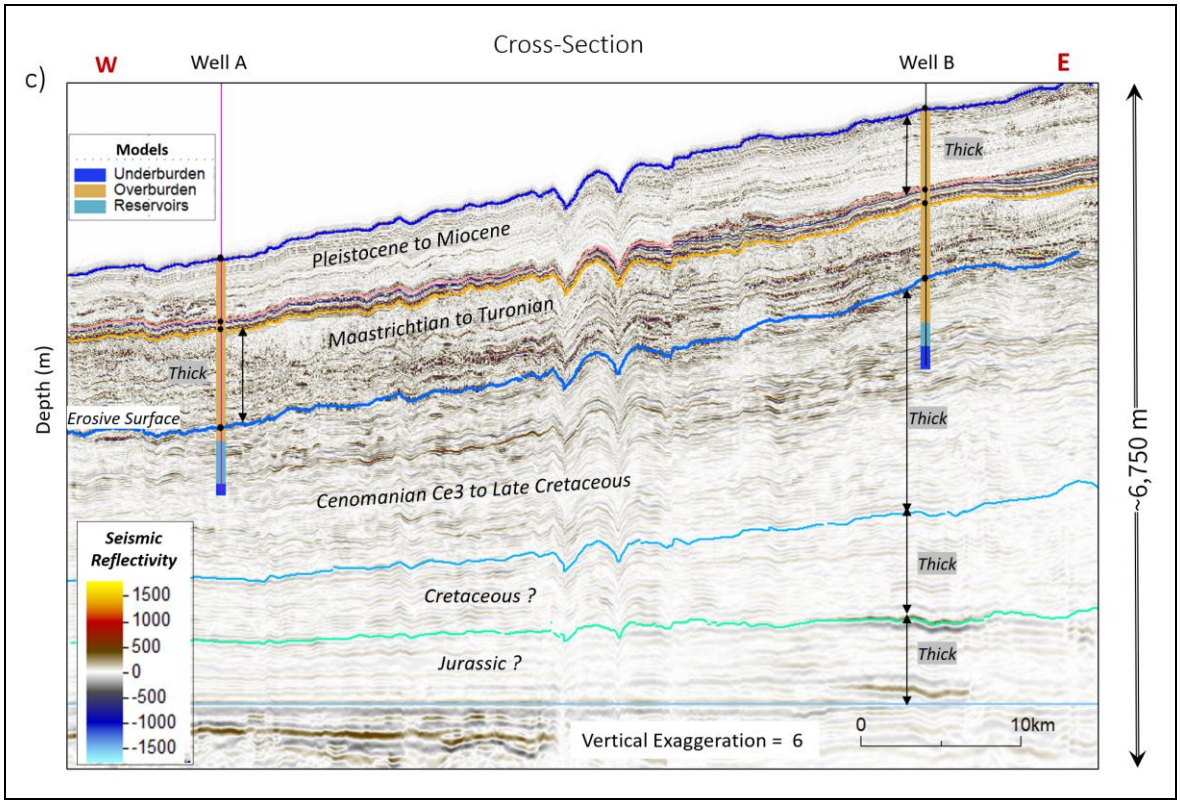

Figure 5.19.- a) Sketch showing the location of wells A and B and the overburden thickness. b) Map with the deep-water systems interpreted on seismic data for the high-pressure interval. c) Seismic-cross section between Well A and Well B showing the thickness variation through time and the main surfaces mapped during this study. The seismic section has been flattened at the base of the mapped interval named Jurassic.

5.4.5 Fluid Expansion due to Hydrocarbon Generation

This overpressure mechanism has been identified to generate overpressure from gas-prone, oil-prone source rocks and oil to gas cracking (Meissner, 1978; Barker, 1990; Swarbrick and Osborne, 1998; Swarbrick and Hills, 1990). From log-based interpretation and source rock samples, shale intervals above and below the reservoirs have been identified to have a variable but sometimes high organic matter content in both wells (A and B) (Figure 5.9).

The source rock analysis performed with the analytical equations (5.1 and 5.2) in wells A and B showed intervals with organic matter content above and below the reservoirs of both wells, having more intervals in Well B with a level of organic maturity 10 (LOM) than in Well A. However, the source rock data determined by the hydrogen index, which characterises the origin of the organic matter, is similar in both wells. The maturity of the rocks (Tmax) shows more intervals with early maturity and an oil window in Well B than in Well A. There are more intervals with total organic matter values (TOC) higher than 5% in Well B than in Well A (Figure 5.20).

In the Senegal-Mauritania Basins, TOC values between 5 and 28 for Aptian and Turonian shales have been described at sites 368 and 367 DSDP (Dean et al., 1978). However, neither of these two wells has those percentages in the Albian-Turonian shale intervals (Figure 5.20).

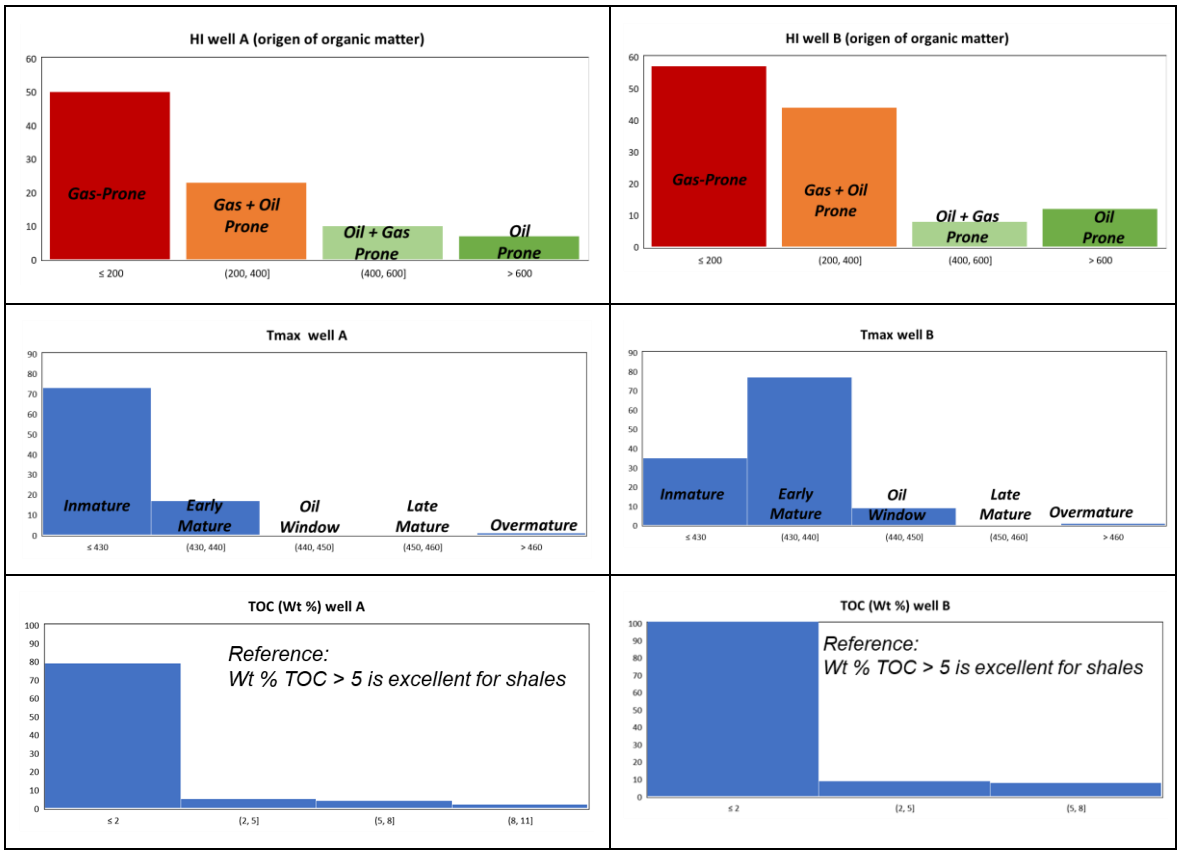

Figure 5.20.- Source rock data from wells A and B of the shale intervals above and below the reservoirs (for reference, see Figures 5.9a and 5.9b).

The amount of overpressure generated in the identified shale intervals was investigated with 1D basin models in both wells using the software Petrel-PetroMod. The models used the kinetics for Type II kerogen, which corresponds to aquatic, marine, and siliciclastic lithofacies with moderate sulphur for a marine environment (Pepper and Corvi, 1995). An organic matter content of 5% and a hydrogen index of 600 were considered in the models of both wells. The facies and well tops used in these models were interpreted during this project (see Figure 5.4 for references to the lithologies interpreted). The curves used in the models were Shale TOC 5% for the layers with organic-matter content (layers identified to have organic content in both wells, ~636 m for Well A and ~680m for Well B; Figure 5.9) and Typical Siltstone for the rest of the overburden layers. The reservoir intervals were represented by Typical Sandstone. These models were constructed from the seafloor to the Albian age (AL11). Thicknesses, well tops, lithologies, and time of each well used the same values as the values used in the geomechanical models (e.g., disequilibrium compaction and clay diagenesis).

Results agree with the source rock samples showing that these shale intervals are early-mature to mature, generating overpressures <1 MPa in these intervals (Figure 5.21).

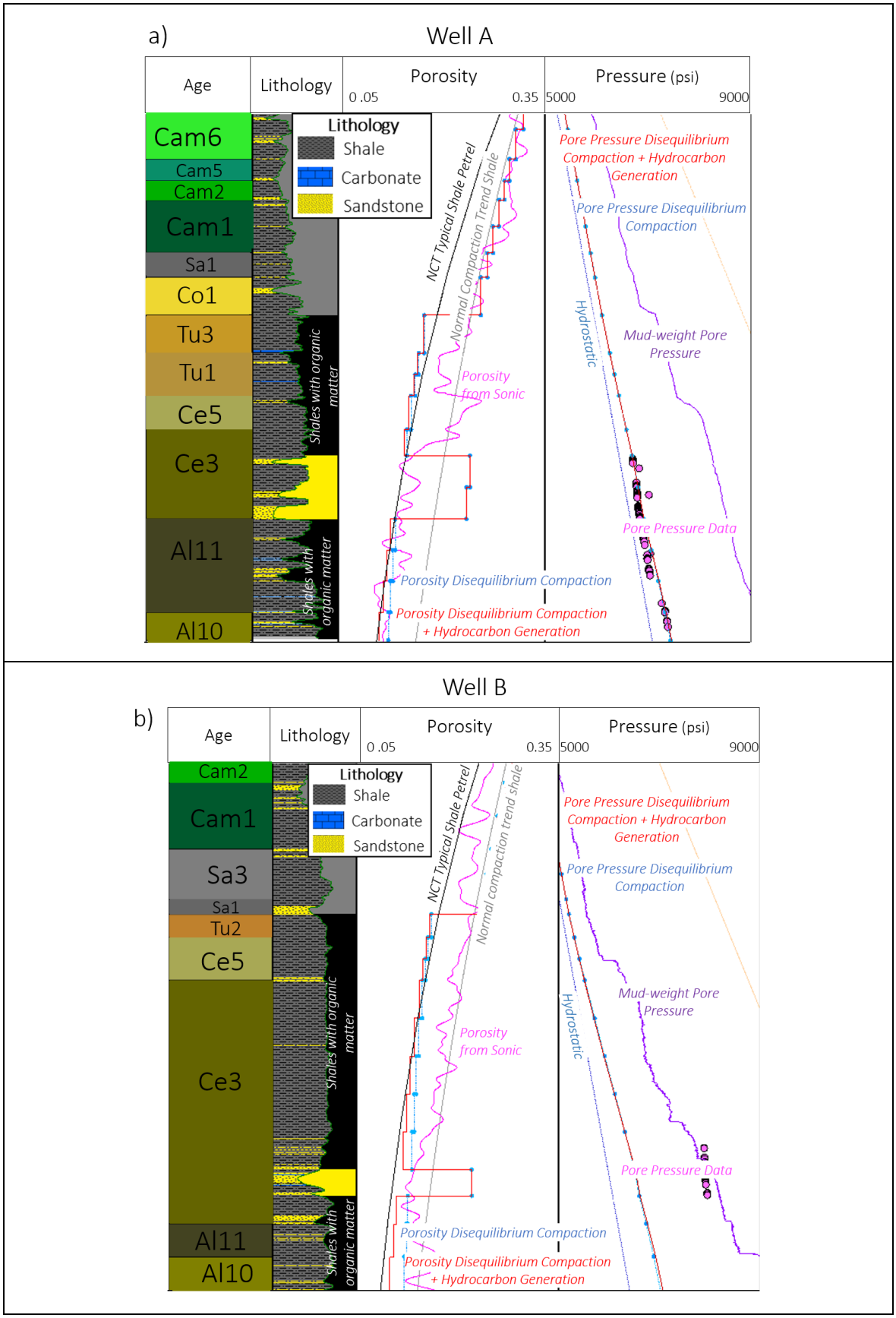

Figure 5.21.- 1D basin modelling for wells A and B showing period, lithology, porosity, and pressure of the two models generated for both wells. Disequilibrium compaction is shown in blue and disequilibrium compaction and hydrocarbon generation is shown in red.

5.5 Discussion

The objective of this project was to identify the factors and overpressure-generating mechanisms that contributed to the overpressure registered in Well B which is located 44 km apart from wells A and C at the continental slope. Methods previously determined or suggested were followed during this assessment, and the most relevant findings are discussed.

5.5.1 Log-based interpretation and overpressure

Even though Well B has ~12 MPa more overpressure than Well A, the analysis of the well logs (equivalent depth model; Bowers, 1995) could not determine this difference due to the similarities between these wells, such as similar overburden characteristics and similar well log responses. Log well analysis indicates that sonic and resistivity logs follow normal compaction trends in most of the sedimentary column, which indicate hydrostatic pore pressures in both wells. However, as suggested by Goulty et al. (2012), porosity-related well logs do not show any difference when overpressure is generated at the same time as shale intervals are experiencing chemical compaction. Therefore, the low porosity observed in the deep sections of both wells could indicate chemical compaction, as shown in the density-sonic plot (for reference, see Figure 5.10).

5.5.2 Disequilibrium Compaction and Overpressure

High sedimentation rates (2,000 m/Ma) of mud-rich lithologies have been identified as the main cause of overpressure in young basins (Swarbrick and Hillis, 1999; Osborne and Swarbrick, 1997; Swarbrick et al., 2002). On the other hand, erosive events and hiatus periods have been determined to dissipate overpressure that has been previously generated (Corbet and Bethke, 1992; Calderon et al., 2023). From the geological analysis, it was determined that both wells experienced relatively low sedimentation rates (<350 m/Ma) in addition to experiencing several erosive events and hiatus periods during the Late Cretaceous; both are consistent with limited overpressure generation. This was confirmed by the results of the 1D geomechanical models, where only slight overpressure was generated in both wells A and B.

To generate more overpressure similar to the data of Well B, a low porosity-permeability relationship (K-C Shale Ed.) 24 times lower than the one used in the rest of the shale layers (Shale) was applied from the beginning of the sedimentation in the geomechanical models of both wells (A2 and B2). As Well B has ~11 MPa more overpressure than Well A, it was necessary to apply this low porosity-permeability relationship to more intervals in Well B than Well A (e.g., ~1,155 m for Well B and 117 m for Well A; Figure 5.12). Although high pore pressure values similar to the registered data were generated, the porosity values of both wells A and B were too high in comparison to the well data. The reason for the high porosities is because the low permeability applied in those layers allowed pore pressure to be generated during sedimentation but not dissipated, so the high porosities are retained in those layers. These high porosities do not agree with the observed data, indicating that there is another factor or overpressure mechanism that contributes to the porosity reduction (e.g., clay diagenesis).

5.5.3 Temperature and Clay Diagenesis

Low porosity, for example, up to 10 percent lower than the expected at that depth (e.g., porosity of 0.14 at 4,500 m; Figure 5.22c), was observed in deep intervals of both wells, which can be related to either lithology changes or porosity reduction due to diagenetic processes. As suggested by Lothe et al. (2023), smectite to illite transformation alters the microstructure of the clays, reducing their permeability and flow properties. Lithology changes in these intervals could not be observed during the well-log assessment performed during this study.

The amount of smectite to illite in this area could be high and could also play an important role in the generation of overpressure due to mineral clay diagenesis. Ramdhan and O'Connor (2022) highlighted that the amount of smectite is associated with volcanic activity as determined in the Tertiary sedimentary basin of western Indonesia. As Well B is located closer to an area identified with more volcanic activity (Davison, 2005) and closer to the supply area (West Africa Craton and Mauritanides; Dean et al., 1978; Bonne, 2014) than Well A, Well B could have more smectite content (e.g., Mounteney et al., 2021) and result in further overpressure generation. Bellion and Crevola (1991), Goumbo Lô et al. (1992), and Davison (2005) have identified that volcanic activity occurred between the Cretaceous and Pleistocene with an intensification during the Late Eocene-Oligocene to Late Miocene.

There is a high level of uncertainty about the threshold temperature when the smectite to illite transformation begins in the project area. As suggested by Jennings and Thompson (1986), Dutta (1987), and Lahann and Swarbrick (2011), this process can begin at temperatures >70 °C. The present-day temperature of both wells at the reservoir intervals is >80 °C. As data on paleo-gradients in the study area were not available, the current geothermal gradients of 44 °C/km for Well B and 39 °C/km for Well A were used in the geomechanical models. There is also a high level of uncertainty about the smectite content along the sedimentary column of both wells A and B. Core data from the reservoir intervals of Well A show percentages between ~3 and ~55% of smectite and mix smectite and illite in the shale intervals within the reservoir (Figure 5.16b). These values suggest the possibility of the smectite transformation occurring on those intervals.

In this study, the results show that high overpressures can be generated from clay mineral diagenesis. However, the porosity from the 1D models and the data above the depth where the transformation began are still low in both wells. The possibility of this process beginning at lower temperatures was also addressed in this study. The approach used was similar to the models A-D and B-D, where the low porosity-permeability relationship (K-C Shale Ed.) was used from the beginning of the sedimentation (for reference, see Figures 5.17 and 5.18). In these models, the porosity reduction is the result of mechanical compaction until the sediments reach the defined threshold temperature, followed by both mechanical compaction and chemical compaction.

To better match the registered data in both wells, the temperature to start clay diagenesis was changed to 72 °C with a different value of the constant m. Models A-D, B-D, A-DT, and B-DT used a m value of 0.1 and the new model used a m value of 0.4. Additionally, the tight compaction trend for shale intervals was used from the shales Cam2 and Cam1 to the total depth of the wells. The

maximum imposed porosity reduction during clay diagenesis was changed from 0.12 to 0.09. These changes allow a better match between the porosity and pore pressure data of Well B (Figures 5.22c and 5.22d). However, the overpressure generated in Well A was too high, and the porosity reduction was too low in comparison to the registered data. Therefore, the low porosity-permeability relationship (K-C Shale Ed.) was replaced by the relatively high porosity-permeability relationship (Shale), and the imposed porosity reduction was changed to 0.05 in Well A (Figures 5.22a and 5.22b).

The changes performed to match the data indicate that these wells have different petrophysical characteristics or that clay diagenesis reduced permeability and porosity from the Cretaceous in Well B, while in Well A these two properties have not been totally changed as clay diagenesis started only during the Middle Miocene or that there is another overpressure mechanism acting locally at the Well B position (e.g., pressure transfer).

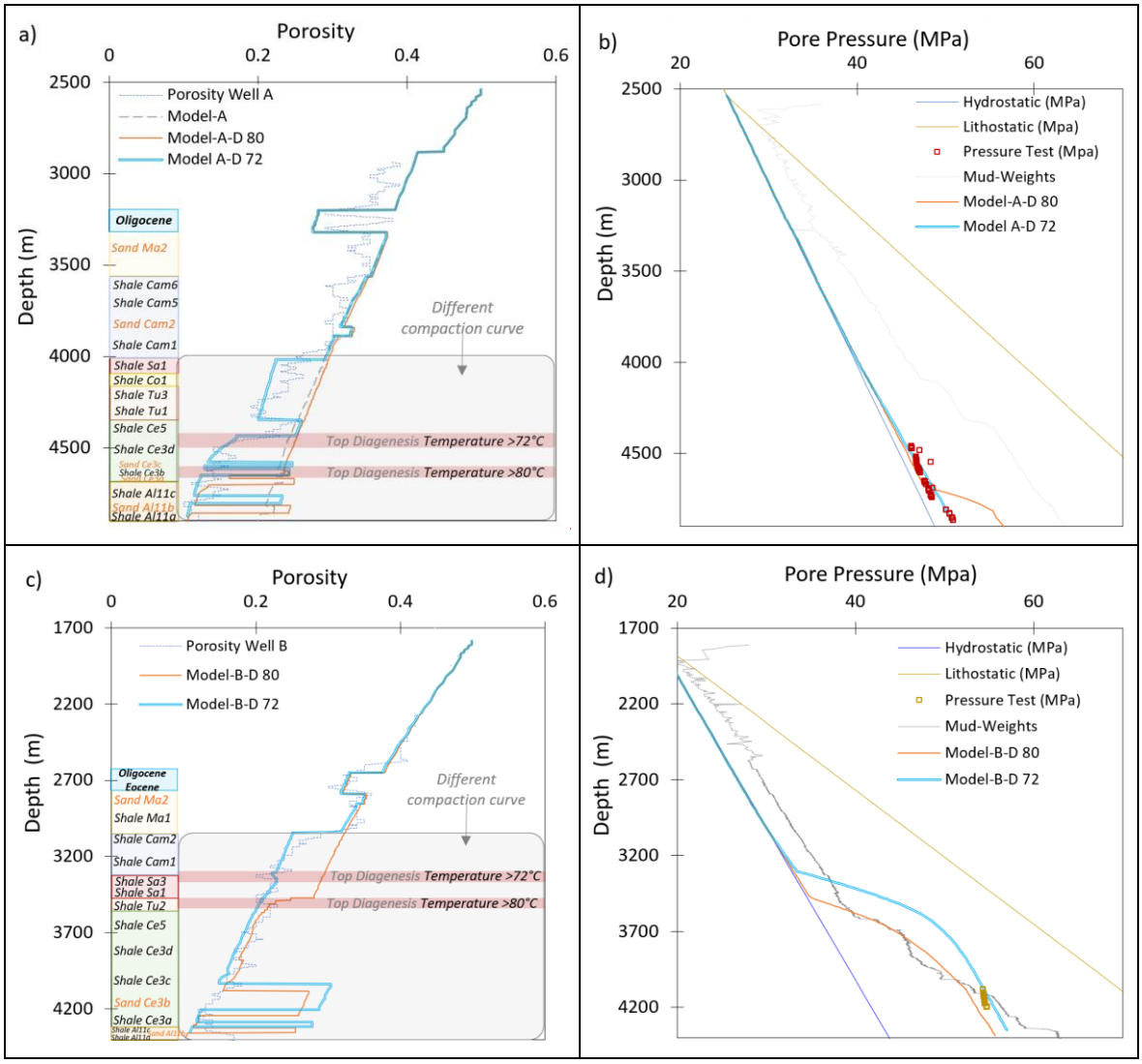

Figure 5.22.- Models A-D 72 and B-D 72 were created to investigate clay diagenesis at 72 °C. The settings used in the models A-D 72 and B-D 72 are the same as the models A-D and B-D presented in section 5.4.3 (Clay Mineral Diagenesis), with a temperature of 72 °C instead of 80 °C, a value of 0.4 for the variable m instead of 0.1, different compaction trends from the shale intervals Cam1 and Cam2, a maximum imposed porosity

reduction of 0.9 for Well B and 0.5 for Well A, and the porosity-permeability relationship Shale instead of K-C Shale Ed. in Well A.

Overpressure generation due to smectite dehydration was not investigated in this study, and it is recommended that this be taken into consideration in further studies as it has been suggested that smectite dehydration may contribute to up to 30% of total overpressure. Equations, models, and different approaches are presented in different studies such as Velde and Vasseur (1992), Cuadros (2006), and Tremosa et al. (2020).

5.5.4 Pressure Transfer.

The generation of high pore fluid pressure values similar to the registered in Well B using similar petrophysical properties as suggested by well logs and seismic data in both wells A and B has been a challenge during this study. Low-permeability layers are necessary to keep the overpressure registered in Well B through time. However, low-permeability layers could result in high porosity values when only disequilibrium compaction is acting or low porosities when disequilibrium compaction and clay diagenesis are acting together. These two mechanisms are proven to generate overpressure in both wells A and B, but to match the porosity and pore pressure data of both wells, different petrophysical properties are necessary in each well. Therefore, the possibility of pressure transfer affecting only Well B was analysed and could not be ruled out.

5.5.4.1 Vertical Pressure Transfer from Deep Intervals

Pressure transfer has been suggested to occur in this basin through vertical structures (Figure 5.23), and even though in early studies these structures were mapped on 2D seismic sections around the Dakar area (Figure 5.1) as igneous intrusions with saucer-shaped igneous sills and dykes (Rocchi et al., 2007; Hasen et al., 2008), these magmatic structures could not be identified in the studied area.

Recent studies performed in the western part of the Niger Delta interpret these structures as bypass structures (e.g., pipes, mud volcanoes, gas chimneys) where overpressures and fluids from deep layers are released (Løseth et al., 2011). Kirkham et al. (2022) also highlight how vertical structures interpreted on seismic sections in the Herodotus Basin, on the West Nile Deep-sea Fan, act as pathways that enable the release of overpressured intervals (source rocks) through salt and thick packages of shales. These events have been determined to occur every 0.050 to 0.150 Ma. Cartwright and Santamarina (2015) also relate these structures to hydrocarbon migration, with the structures able to develop during and post-sedimentation.

Another example is the present-day overpressure of the inner-shelf of the Tertiary Baram Delta province of Brunei, where vertical structures were identified to have transferred high overpressure from deep intervals (Tingay et al., 2009). In that study, analytical methods were able to identify the pressure transfer overpressure mechanism. However, when the same equations (Eaton's, 1972) were applied to the well data of wells A and B, the pore pressure values obtained did not match the registered data of these wells. The Eaton pore pressure curves presented in Figure 5.9 were

calculated with exponent 3, assuming disequilibrium compaction. A higher mismatch between the registered data and the equation results is observed with exponent 6, which is the value used in the Tertiary Baram Delta. These results could indicate that this overpressure mechanism does not have any influence on the present-day overpressure of Well B or that this mechanism cannot always be recognised through analytical methods.

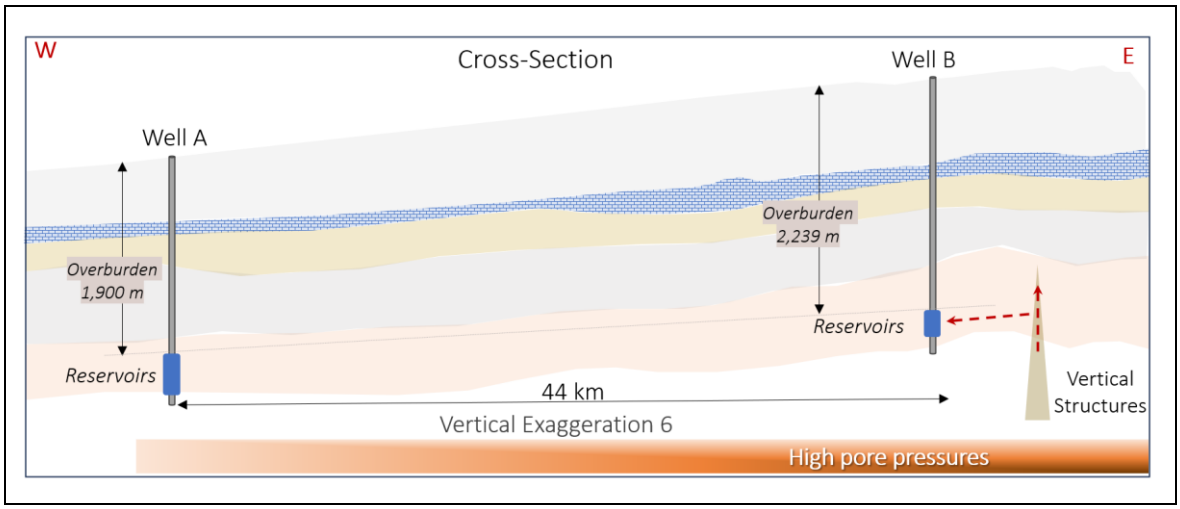

Figure 5.23.- Sketch showing the scenario of pressure transferred from deep layers by vertical structures.

In this study, vertical structures were interpreted using stacking reflectivity, acoustic impedance, and genetic inversion seismic cubes. These structures have low amplitude and blurry reflectors along them and a high amplitude at their ends. Most of the structures reached the Oligocene interval. Even though it was difficult to establish the origins of these structures, they seem to be connected to intervals older than Late Cretaceous sediments where source rocks could be located (Figure 5.24b). As these structures have been associated with overpressure release (Løseth et al., 2011; Cartwright and Santamarina, 2015; Karstens and Berndt, 2015; Karstens et al., 2017; Wangen, 2020; Robinson et al., 2021; Callow et al., 2021), the possibility of the high pore pressure registered in Well B being transferred by these structures was assessed.

Although it is uncertain where these structures commence, low amplitudes are observed from sediments older than Late Cretaceous on the seismic reflectivity cube (Figures 5.24a and 5.24b). The path of these structures is vertical and does not have a connection to any fault at the base. These structures have different sizes, with an average size of 1,500 m in width and 4,000 m in height. Most of them reached the Oligocene, and few crossed this succession (Figure 5.24b).

Two different sets of high-amplitude reflectors were observed in the stack reflectivity and acoustic impedance seismic cubes. The first is related to an erosive event during the Cenomanian, and the second is related to the vertical structures (Figure 5.24b). The closest vertical structure to Well B mapped on seismic data is located at ~3,000 m. This particular structure changes in its radius size from ~300 m at the south of Well B to ~3,000 m at the north side. It is observed, high amplitudes along the path of these structures from the Campanian to the Turonian. This structure was interpreted to have reached the Oligocene sediments (Figure 5.24b).

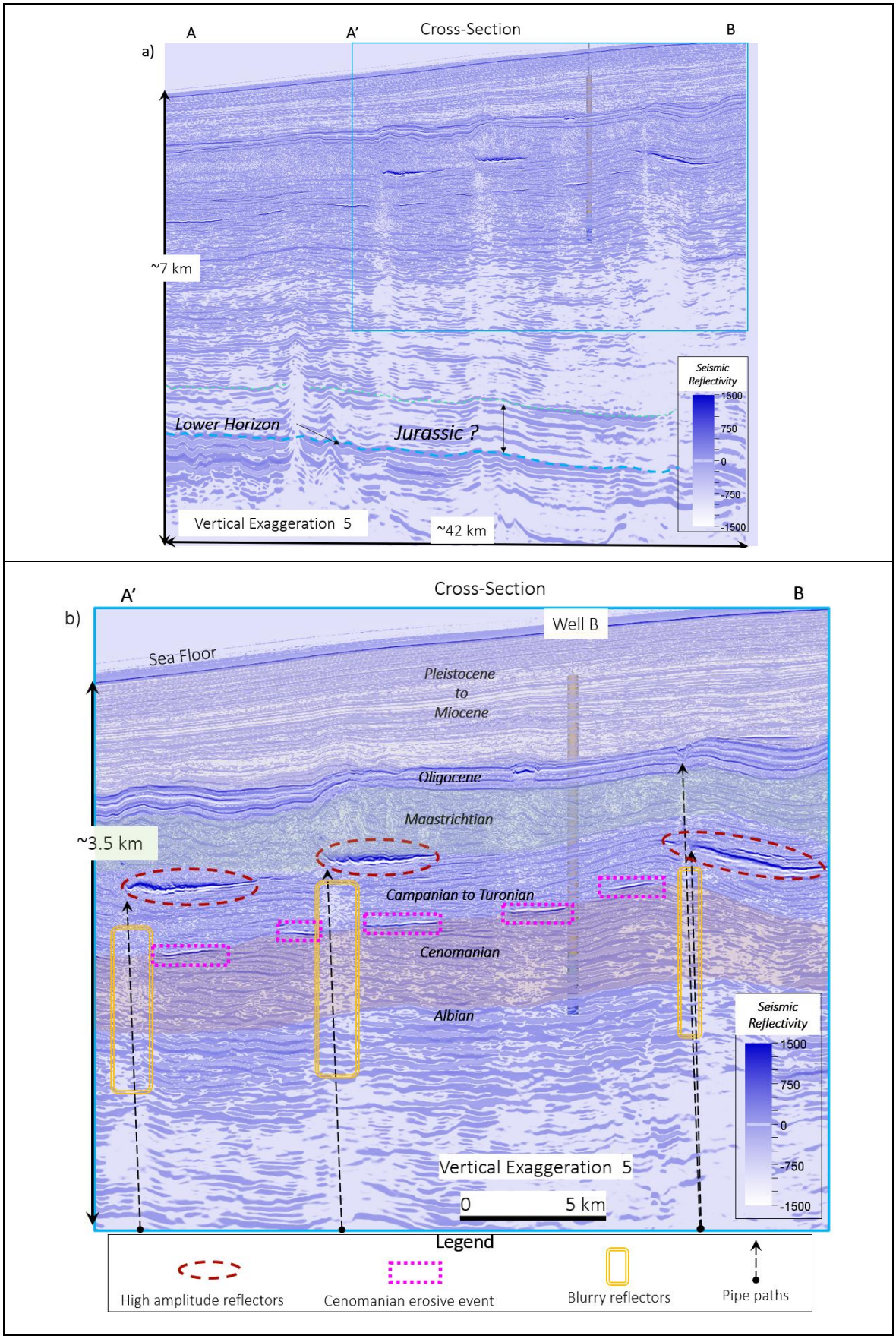

Figure 5.24.- a) Uninterpreted seismic cross-section of the reflectivity cube showing a squared, which was used for interpretation. B) Interpreted seismic cross-section showing the main periods of time, vertical structures, the Cenomanian erosive event, and the vertical structure paths.

While pressure transfer from deep layers through these structures cannot be accounted for with any certainty, they may, in part, be responsible for the overpressure encountered in Well B. During this study, no geomechanical models were created to investigate this possibility. However, it is recommended to model these structures as performed in other areas (e.g., Wangen, 2020; Robinson, 2021; Callow et al., 2021).

5.5.4.2 Lateral Pressure Transfer from Upslope

Thickness variations on the upper region of a slope are generated by the accumulation or erosion of sediments during geological times (Berg et al., 2005). This can generate fluid pressure instabilities, causing landslides (Strout and Tjelta, 2005; Berndt et al., 2012). The pressure generated in the upper part of the slope could also be transferred by permeable layers to other parts of the slope, which would be represented by high values (Dungan and Flemings, 2000).

Reports from a nearby region show that sediments from the Late Cretaceous to Miocene can be connected to deep layers (Jurassic and Early Cretaceous intervals) located below the slope area, opening the possibility of pressure transfer from these deep layers (Martin et al., 2010; Clayburn, 2017; ADEA, 2021). The pressure transfer was suggested to be transferred through an erosive event identified as being between Coniacian, Santonian, and Campanian (Martin et al., 2010; Hathon, 2018).

Well B is located close to the change of the slope; the upper-slope overburden is 1.8 km thicker than the overburden found at the location of Well B. In this case, the vertical effective stress will be higher where the overburden is thicker and, conversely lower where the overburden is thinner. If there is a connection to Well B through a permeable layer, the overpressure generated on the upper slope could be transferred to Well B. This hypothesis was based on the information available and needs to be explored. However, it could not be performed during this study with the available datasets.

5.6 Conclusions

Smectite clay diagenesis (load transfer process) investigated with 1D models shows that this process can contribute to overpressure generation in both wells A and B, and due to this process, porosity values can be reduced, increasing the contribution of disequilibrium compaction. This mechanism has acted first in Well B, which has a higher geothermal gradient and overburden thickness. The temperature for the smectite to illite transformation to be initiated and match better pore pressure and porosity data is 72 °C. The porosity-permeability relationship used in Well B when the smectite to illite transformation occurred was 24 times lower than the porosity-permeability relationship used before the transformation started.

Although small differences, such as a thick overburden with thick mud-rich lithologies are present in Well B and not in Well A, the log-based interpretation shows that sonic and resistivity logs follow normal compaction trends through most of the sedimentary columns of both wells A and B, suggesting hydrostatic pore pressures.

Unloading due to chemical compaction and/or clay diagenesis is interpreted based on the analysis of a density-velocity cross-plot in the shales of the reservoir intervals of both wells A and B. It is important to indicate that both wells have geothermal gradients >39 °C/km and smectite content.

Pressure tests show that Well B has ~12 MPa more overpressure than Well A. Therefore, it is concluded that simple approaches to overpressure evaluation are insufficient to explain the distribution of overpressure in this basin.

Even though the study area presents mud-dominated lithologies, disequilibrium compaction is unlikely to be the main overpressure mechanism due to the low sedimentation rates, erosive events, and hiatus periods that have occurred between the Cretaceous and present-day.

Pore pressure transfer from down-slope (Well A) to up-slope (Well B) is not possible as Well B has a thicker overburden than Well A, and if pressure were transferred, this would have occurred from Well B to Well A. Furthermore, it was also determined in the seismic assessment that there is a very limited hydraulic connection between the overpressured intervals of these two wells.

It is also concluded that overpressure generated from the organic-rich shales located above and below the reservoir intervals due to hydrocarbon generation is unlikely, as data show that these intervals are immature to early mature in the study area. However, overpressure generated from other source rocks (e.g., Jurassic, Permian, and Silurian) could not be ruled out. These intervals were not investigated during this study.

The 2D geomechanical models proved that the external structures, such as canyons or channels, did not generate the high pore pressure values encountered in Well B. The 1D models used to investigate disequilibrium compaction show that mechanical compaction cannot generate the overpressure encountered in Well B.

Finally, while there is no clear evidence of the main mechanism that generated the high overpressure registered in Well B, it does seem that it has acted locally rather than having a wider regional impact.

5.7 References

ADEA (2021). *Petrosen - Petroleum Potential Offshore Senegal*. Available at: https://www.energy-for-africa.fr/en/129/id/42 (Accessed: 03 June 2023).

Antobreh, A. A. and Krastel, S. (2006). Morphology, seismic characteristics and development of Cap Timiris Canyon, offshore Mauritania: A newly discovered canyon preserved-off a major arid climatic region. *Marine and Petroleum Geology*, 23(1), 37–59.

Aplin, A. C., Matenaar, I. F. and Van der Plujm, B. A. (2003). Influence of mechanical compaction and chemical diagenesis on the microfabric and fluid flow properties of Gulf of Mexico mudstones, *Journal of Geochemical Exploration,* 78-79, 449-451.

Athy, L. F. (1930). Density, porosity, and compaction of sedimentary rocks. *AAPG Bulletin*, 14(1), 1-24.

Audet, D. M. (1995). Mathematical modeling of gravitational compaction and clay dehydration in thick sediment layers, *Geophysics Journal International*, 122, 283–298.

Banik, N. C., et al. (2004). Seismic Pore-pressure Imaging in Deepwater Offshore West Africa, *Society of Petroleum Engineers,* SPE-89994-MS.

Baker, E. W., Palmer, S. E. and Huang, W. Y. (1978). Geochemical Studies: Intermediate and Late Diagenetic Tetrapyrrole Pigments, Leg 41: Cape Verde Rise and Basin. Available at: doi: 10.2973/dsdp.proc.41.123.1978

Barker, C. (1990). Calculated Volume and Pressure Changes During the Thermal Cracking of Oil to Gas in Reservoirs, *AAPG Bulletin*, 74, 1254-1261.

Beauchamp, W., Allmendinger, R.W., Baranzagi, M., Demnati, A., El Aliji, M., Dahmani, M. (1999). Inversion tectonics and the evolution of the High Atlas Mountains, Morocco, based on a geological/geophysical transect, *Tectonics,* 18, 163–184.

Bellion. Y. And Crevola, G. (1991). Cretaceous and Cainozoic Magmatism of the Senegal Basin (West Africa): A Review, in Bellion, Y., Kampunzu, A. B, Lubala, R. T and Bellion, Y. C. *Magmatism in Extensional Structural Settings*. Springer Berlin Heidelberg.

Berg, K., Solheim, A. and Bryn, P. (2005). The Pleistocene to recent geological development of the Ormen Lange area, *Marine and Petroleum Geology*, 22, 45-56.

Berndt, C., Costa, S., Canals, M., Camerlenghi, A., de Mol, B. and Saunders, M. (2012). Repeated slope failure linked to fluid migration: The Ana submarine landslide complex, Eivissa Channel, Western Mediterranean Sea, *Earth and Planetary Science Letters*, 65-74.

Bowers, G. L. (1995). Pore pressure Estimation from Velocity Data: Accounting for Overpressure Mechanisms Besides Undercompaction, *SPE Drilling and Completion*, 89-95.

Bowers, G. L. (2001). Determining an appropriate Pore-Pressure Estimation Strategy, *Paper presented at the Offshore Technology Conference,* Houston, Texas. April 2001. 1-14.

Bowers, G. L. and Katsube, T. J. (2002). The role of shale pore structure on the sensitivity of wire-line logs to overpressure, in Huffman, A. R. and Bowers, G. L. (eds.) *Pressure regimes in sedimentary basins and their prediction*. AAPG, 43-60.

Bonne, K. P. M. (2014). Reconstruction of the evolution of the Niger River and implications for sediment supply to the Equatorial Atlantic margin of Africa during the Cretaceous and the Cenozoic, in Scott, R. A., Smyth, H. R., Morton, A. C. and Richardson, N. (eds.) *Sediment Provenance Studies in Hydrocarbon Exploration and Production*. Geological Society. London, Special Publications, 386.

Brown, R. H. (1980). Triassic Rocks of Argana Valley, Southern Morocco, and Their Regional Structural Implications, *AAPG Bulletin*, 64(7), 988-1003.

Brownfield, M. E. and Charpentier, R. R. (2003). Assessment of the Undiscover Oil and Gas of the Senegal Province, Mauritania, Senegal, The Gambia, and Guinea-Bissau, Northwest Africa, *U. S. Geological Survey Bulletin 2207-A,* 1-15.

Brownfield, M. E. (2016). Assessment of undiscovered oil and gas resources of the Senegal Province, northwest Africa, in Brownfield, M.E., compiler (eds.), *Geologic Assessment of Undiscover Hydrocarbon Resources of Sub-Saharan Africa.* U. S. Geological Survey Digital Data Series 69-GG*,* 1-20.

Bruce, C. H. (1984). Smectite Dehydration – Its Relation to Structural Development and Hydrocarbon Accumulation in Northern Gulf of Mexico Basin, *AAPG Bulletin*, 68, 673-683.

Calderon, M.E. E., Obradors-Prat, J., Aplin, A. C., Jones, S. J., Rouainia, M. and Crook, A. J. (2023). 1D Hydro-Geomechanical Modelling of Pore Pressure on an Active Convergent Margin: East Coast Basin, New Zealand, *Paper presented at the Offshore Technology Conference*, Houston, Texas, USA, May 2023.

Callow, B., et al. (2021). Seismic chimney characterisation in the North Sea – Implications for pockmark formation and shallow gas migration, *Marine and Petroleum Geology*, 133, 1-18.

Cartwright, J. and Santamarina, C. (2015). Seismic characteristics of fluid escape pipes in sedimentary basins: Implications for pipe genesis, *Marine and Petroleum Geology*, 65, 126-140.

Casson, M., Calvès, G., Huuse, M., Sayers, B. and Redfern, J. (2021). Cretaceous continental margin evolution revealed using quantitative seismic geomorphology, offshore northwest Africa, *Basin Researcher*, *66*-90*.*

Clayburn, J. (2017). Realising the deepwater hydrocarbon potential of Senegal. *AAPG/SEG 2017 International Conference and Exhibition*, London, England. Search and Discovery Article 70345.

Corbet, T. F. and Bethke, C. M. (1992). Disequilibrium Fluid Pressures and Groundwater Flow in the Western Canada Sedimentary Basin, *Journal of Geophysical Research*, 97(B5), 7203-7217.

Couzens-Schultz, B. A. and Azbel, K. (2014). Predicting pore pressure in active fold-thrust systems: An empirical model for the deepwater Sabah foldbelt. *Journal of Structural Geology*, 69, 465-480.

Crevola, G. (1995). Cenozoic volcanism in Western Senegal and its relationship to the opening of the Central Atlantic Ocean – Comment, *Tectonophysics*, 246, 201-204.

Courtney, R. C. and White, R. S. (1986). Anomalous heat flow and geoid across the Cape Verde Rise: evidence for dynamic support from a thermal plume in the mantle, *Geophysical Journal International*, 87(3), 815-867.

Davison, I. (2005). Central Atlantic margin basins of the North West Africa: Geology and hydrocarbon potential (Morocco to Guinea), *Journal of African Earth Sciences*, 43 (1-3), 254-274.

Dean, W., Gardner, J. V., Jansa, L. F., Cepek, P. and Seibold, E. (1978). Lithological Studies: Cyclic Sedimentation along the Continental Margin of Northwest Africa. Available at: doi: 10.2973/dsdp.proc.41.103.1978

Dietz, R. S., Knebel, H. J. and Somers, L. H. (1968). Cayar Submarine Canyon, *Geological society of America Bulletin,* 79, 181-1828.

Dungan, B. and Flemings, P. B. (2000). Overpressure and fluid flow in the New Jersey continental slope: Implications for slope failure and cold seeps. *Science*, 289, 288–291.

Dutta, N. C. (1987). Shale compaction, burial diagenesis, and geopressures: a dynamic model, solution, and some results, in Burrus, J. (ed.) *Thermal Modeling in Sedimentary Basins.* Paris, 149-172.

Eaton, B. A. (1975). The Equation for Geopressure Prediction from Well Logs, *SPE,* 1-11.

Effimoff, I., Martin, L., Laughland, M. and Medou, J. O. (2010). Exploration of the Senegalese Portion of the Greater MSGBC Basin: a New Frontier Petroleum Province. *Annual Convention and Exhibition*,11th -14th April 2010. AAPG.

Fairhead, J. D., Green, C. M., Masterton, S. M., Guiraud, R. (2013). The role that plate tectonics, inferred stress changes and stratigraphic unconformities have on the evolution of the West and Central African Rift System and the Atlantic continental margins, *Tectonophysics*, 118-127.

Gardner, G. H. F., Gardner, L. W. and Gregory, A. R. (1974). Formation Velocity and Density- The Diagnostic Basics for Stratigraphic Traps, *Geophysics*, 39, 770-780.

Goulty, N. R., Ramdhan, A. M. and Jones, S. J. (2012). Chemical compaction of mudrocks in the presence of overpressure, *Petroleum Geoscience*, 18, 471-479.

Goumbo Lô, P. G., Dia, A. and Kampunzu, A. B. (1992). Cenozoic volcanism in Wester Senegal and its relationship to the opening of the Central Atlantic Ocean, *Tectonophysics*, 209, 281-291

Gradstein, F.M. and Ogg, J. G. (2012). The Chronostratigraphic Scale in Gradstein, F.M., Ogg, J. G., Schmitz, M.D. and Ogg, G. M. (eds.), *The Geologic Time Scale*, Amsterdam.

Hansen, S. (1996). A compaction trend for Cretaceous and Tertiary shales on the Norwegian Shelf based on sonic transit times. *Petroleum Geoscience*, 2, 159-166.

Hansen, D. M., Redfern, J., Federici, F., Biase, D. and Bertozzi, G. (2008). Miocene igneous activity in the Northern subbasin, offshore Senegal, NW Africa, *ScienceDirect*, 25, 1-15.

Hathon, E. (2018). The SNE Discovery Offshore Senegal – Moving a Frontier Basin to Emergent, *In 80th EAGE Conference and Exhibition 2018*, European Association of Geoscientists and Engineers.

Huang, Y. (2018). Sedimentary characteristics of turbidite fan and its implication for hydrocarbon exploration in Lower Congo Basin, *Petroleum Research*, 3, 189-196.

Jennings, S. and Thompson, G. R. (1986). Diagenesis of Plio-Pleistocene sediments of the Colorado River Delta, southern California, *Journal of Sedimentary Research*, 56, 89-98.

Jobe, Z. R., Lowe, D. R. and Uchytil, S. J. (2011). Two fundamentally different types of submarine canyons along the continental margin of Equatorial Guinea. *Marine and Petroleum Geology*, 28(3), 843–860.

Karstens, J. and Berndt, C. (2015). Seismic chimneys in the Southern Viking Graben – Implications for paleo fluid migration and overpressure evolution, *Earth and Planetary Science Letters*, 412, 88-100.

Karstens, J., Ahmed, W., Berndt, C., Holger, C. (2017). Focused fluid flow and the sub-seabed storage of CO_2: Evaluating the leakage potential of seismic chimney structures for the Sleipner CO2 storage operation, *Marine and Petroleum Geology*, 88, 81-93.

Kirkham, C., Cartwright J., James, D. and Kearney, L. (2022). Episodic venting of extreme subsalt overpressure through a thick evaporitic seal, *Marine and Petroleum Geology,* 142, 1-19.

Lahann, R. W. (2002). Impact of Smectite Diagenesis on Compaction Modeling and Compaction Equilibrium, in Huffman, A. R. and Bowers, G. L. (eds.), *Pressure regimes in sedimentary basins and their prediction*: AAPG Memoir, 76, 61–72.

Lahann, R. W. and Swarbrick, R. E. (2011). Overpressure generation by load transfer following shale framework weakening due to smectite diagenesis. *Geofluids*, 11, 362-375.

Lancelot, Y. and Bukry, D. (1978). Site 367: Cape Verde Basin. Available at: Initial Reports of the Deep-Sea Drilling Project, 41, 163–232. Available at doi: 10.2973/dsdp.proc.41.103.1978

Lancelot, Y. and Bukry, D. (1978). Site 368: Cape Verde Basin. *Initial Reports of the Deep-Sea Drilling Project*, 41, 233–326. Available at: doi: 10.2973/dsdp.proc.41.104.1978

Løseth, H., Wensaas, L., Arntsen, B., Hanken, N.-M., Basire, C. and Graue, K. (2011). 1000 m long gas blow-out pipes, *Marine and Petroleum Geology*, 28, 1047-1060.

Lothe, A. E., Grøver, A., Roli, O., Stenebråten, J. and Kristiansen, T. G. (2023). Simulations of the effect of smectite-to illite transformation on permeability and overpressures using a stochastic approach, a Norwegian margin case study, *Basin Research*, 1-25.

Guiraud, R., Bosworth, W., Thierry, J. and Delplanque, A. (2005). Phanerozoic geological evolution of the Northern and Central Africa: An overview, Journal of African Earth Sciences, 43, 83-143.

Mayall, M. Jones, E. and Casey, M. (2006). Turbidite channel reservoirs-key elements in facies prediction and effective development, *Marine and Petroleum Geology*, 23, 821-841.

Martin, L., Effimoff, I., Medou, J. and Laughland, M. (2010). Hydrocarbon prospectivity of offshore Senegal-unlocking the door to a new deepwater petroleum province. *Search and Discovery Article 10278*. Available at: (PDF) Hydrocarbon Prospectivity of Offshore Senegal - Unlocking the Door to a New Deepwater Petroleum Province (researchgate.net) (Accessed: 2023).

Mazzini, A. and Etiope, G. (2017). Mud volcanism: An updated review, *Earth-Science Reviews, 81*-112.

Mulder, T. (2011). Gravity Processes and Deposits on Continental Slope, Rise and Abyssal Plains, in HüNeke, H. and Mulder, T. (eds.) *Deep-Sea Sediments*, Oxford: Elsevier, 26-83.

McArthur, A. D. and McCaffrey, W. D. (2019). Sedimentary architecture od detached deep-marine canyons: Example from the East Coast Basin of New Zealand, *Sedimentary*, 66, 1067-1101.

McGuinness, D., Schneider, R., Colliton, J., Konings, S., Reed, J, Tomasso, M., Sow Deina, C. and Medou, J. O. (2021). The Greater Tortue/Ahmeyim Field Discovery: Opening the Mauritania-Senegal Deep Water Gas Basin, in Charles A. Sternbach, Robert K. Merrill, and John C. Dolson, (eds.), *Giant Fields of the Decade: 2010–2020.* AAPG Memoir, 125, 273–300.

Meissner, F. F. (1978). Petroleum Geology of the Bakken Formation Williston Basin, North Dakota, and Montana, in Demaison, D and Murris, R. J. (eds.) *Petroleum Geochemistry and Basin Evaluation.* AAPG Memoir, 159-179.

Morley, C. K., Promrak, W., Apuanram, W., Chaiyo, P., Chantraprasert, D. Ong., Suphawajruksakul, A., Thaemsirl, N. and Tingay, M. (2022). A major Miocene deepwater mud canopy system: the North Sabah-Pagasa Wedge, northwestern Borneo, *Geosphere*, 291-334.

Mounteney, I., Casson, M., Rushton, J., Millar, I., Dethie, N. and Redfern, J. (2021). Cenozoic to modern-day source to sink systems of Senegal: A record of provenance, transport, recycling and climate controls, *Journal of African Earth Sciences*, 178, 1-16.

Mourlot, Y., Calvès, G., Clift, P. D., Baby, G., Chaboureau, A. C. and Raisson, F. (2018). Seismic stratigraphy of Cretaceous eastern Central Atlantic Ocean: Basin evolution and palaeoceanographic implications. *Earth and Planetary Science Letters*, 499, 107–121.

Mourlot, Y., Roddaz, M., Dera, G., Calvès, G., Kim, J. H., Chaboureau, A. C. and Raisson, F. (2018). Geochemical evidence for large-scale drainage reorganization in Northwest Africa during the Cretaceous, *Geochemistry, Geophysics, Geosystems*, 19(5), 1690–1712.

O'Connor, S., Swarbrick, R. and Lahann, R. (2011). Geologically-driven pore fluid pressure models and their implications for petroleum exploration. Introduction to thematic set, *Geofluids*, 11 343-348.

Olsen, P. E., Kent, D. V., Et-Touhami, M. and Puffer, J. (2003). Cyclo-, Magneto-, and Bio-Stratigraphic Constraints on the Duration of the CAMP Event and its Relationship to the Triassic-Jurassic Boundary, in Hames, W., McHone, J. G., Renne, P. and Ruppel, C. (eds). *The Central Atlantic Magmatic Province Insights from Fragments of Pangea*. Washington: AGU Books Board.

Osborne, M. J. and Swarbrick, R. E. (1997). Mechanisms for Generating Overpressure in Sedimentary Basins: A Reevaluation, *AAPG Bulletin*, 81, 1023-1041.

Passey, Q. R., Creaney, S., Kulla, J.B., Moretti, F. J. and Stroud, J. D. (1990). A Practical Model for Organic Richness from Porosity and Resistivity Logs, *AAPG Bulletin*, 74(12), 1777-1794.

Pepper, A. S. and Corvit, P. J. (1995). Simple kinetic models of petroleum formation. Part I: oil and agas generation from kerogen, *Marine and Petroleum Geology*, 12(3), 291-319.

Petromod. Available at: www.software.slb.com/products/petromod

Powers, M. C. (1967). Fluid-Release Mechanisms in Compacting Marine Mudrocks and their Importance in oil Exploration, *AAPG Bulletin*, 51(7), 1240-1254.

Ramdhan, A. M. and O'Connor, S. (2022). Generation and estimation of overpressure from wireline logs using deterministic approaches in western Indonesia's Tertiary sedimentary basins, *Petroleum Geoscience*, 28, 2021-2062.

Raymer, L. L., Hunt, E. R. and Gardner, J. S. (1980). An improved sonic transit time-to-porosity transform, *OnePetro*, 1-13.

Reymond, A. and Negroni, P. (1989). Hydrocarbon occurrence in NW Africa's MSGBC area, *World Oil*, 208, 53–58.

Robinson, A. H., et al. (2021). Multiscale characterisation of chimneys/pipes: Fluid escape structures within sedimentary basins, *International Journal of Greenhouse Gas Control*, 106, 1-26.

Rocchi, S., Mazzotti, A., Marroni, M., Pandolfi, L., Costantini, P., Giuseppe, B., di Biase, D., Federici, F. and Goumbo Lô, P. (2007). Detection of Miocene saucer-shaped sills (offshore Senegal) via integrated interpretation of seismic, magnetic and gravity data, *Terra Nova*, 19(4), 232-239.

Rossen, C. and Beaubouef, T. (2007). Overview: Examples of slope to Basin Floor Reservoir Architecture, Brushy Canyon Formation, Texas, USA, in Gillis, M (ed.) *Atlas of Deep-Water Outcrops.* Tulsa: Geological Society, 425-428.

Schneider, F. Potdevin, J. L., Wolf, S. and Faille, I. (1996). Mechanical and chemical compaction models for sedimentary basin simulators, *Tectonophysics,* 263, 307-317.

Stow, D. A. V., Reading, H. G. and Collison, J. D. (2006). Deep seas, in Readings, H.G. (eds.) *Sedimentary Environments: Processes, Facies and Stratigraphy*, Oxford: Blackwell, 395-451.

Strout, J. M. and Tjelta, T. I. (2005). In situ pore pressures: What is their significance and how can they be reliably measured?, *Marine and Petroleum,* 22, 275-285.

Swarbrick, R. E. and Osborne, M. J. (1998). Mechanisms that Generate Abnormal Pressures: An Overview, in Law, B. E., Ulmishek, G. F. and Slavin, V. I. (eds.), *Abnormal pressures in hydrocarbon environments.*

Swarbrick, R. E. and Hillis, R. R. (1999). The Origin and Influence of Overpressure with Reference to the North West Shelf, Australia, *The APPEA Journal,* 39, 64-72.

Swarbrick, R. E., Osborne, M. O. and Yardley, G. S. (2002). Comparison of Overpressure Magnitude Resulting from the Main Generating Mechanisms, in Huffman, A. R. and Bowers, G. L. (eds.) *Pressure regimes in sedimentary basins and their prediction.* AAPG Memoir 76, 1-12.

Tingay, M. R. P., Hillis, R. R., Swarbrick, R. E., Morley, C. K. and Damit, A. R. (2009). Origin of overpressure and pore-pressure prediction in the Baram province, Brunei. *AAPG Bulletin,* 93, 51-74.

Tosaya, C. and Nur, A. (1982). Effects of diagenesis and clays on Compressional Velocities in Rocks, *Geophysical Research Letters*, 9, 5-8.

Tremosa, J., Gailhanou, H., Chiaberge, C., Castilla, R., Gaucher, E. C., Lassin, A., Gout, C., Fialips, C. and Claret, F. (2020). Effects of smectite dehydration and illitisation on overpressures in sedimentary basins: A coupled chemical and thermo-hydro-mechanical modelling approach, *Marine and Petroleum Geology*, 111, 166-178.

Vear, A. (2005). Deep-water plays of the Mauritanian continental margin, in Doré, A. G. and Vining, B. A. (eds.) *Petroleum Geology: North-West Europe and Global Perspectives.* Proceedings of the 6th Petroleum Geology Conference, 1217–1232.

von Rad U. and Einsele G. (1980). Mesozoic–Cainozoic subsidence history and palaeobathymetry of the Northwest African continental margin (Aaiun Basin to DSDP Site 397). *Philosophical Transactions of the Royal Society of London. Series A, Mathematical and Physical Sciences*, 294(1409), 37–50.

Wangen, M. (2020). A 3D model for chimney formation in sedimentary basins, *Computers and Geosciences*, 137, 1-10.

Wignall, P. B., Best, J. L. (2016). Basin Models, in Best, J. L. and Wignall, P. B. (eds.) *A field guide to the carboniferous sediments of the Shannon basin.* Western Ireland: Wiley-Blackwel, 35-47.

Yang, Y. and Aplin, A. C. (2010). A permeability-porosity relationship for mudstones, *Marine and petroleum Geology*, 27, 1692-1697.

Chapter Six: Summary and Discussion

This research sought to identify the overpressure mechanisms that generated the present-day overpressure in three projects: the East Coast Basin (ECB) of New Zealand, Magnolia Field in the Gulf of Mexico, and West Africa, located in three different basins with different geological histories. The distribution of overpressure in these three regions is very different; for example, the ECB has very high overpressures (almost to lithostatic) from shallow depths (300 m) to deep intervals (>3,000 m), whereas the overpressure in the West Africa and Magnolia Field projects reaches values of 13 MPa at depths higher than 2,000 m and increases with depth.

Initially, standard log-based methods were used to interpret pore pressures (e.g., Dickinson, 1953; Hottman and Johnson, 1965; Skempton, 1970; Eaton, 1975; Raymer et al., 1980; Raiga-Clemenceau et al., 1988; Issler, 1992; Bowers, 1995; Hart et al., 1995; Hansen, 1996; Osborne and Swarbrick, 1997; Harrold et al., 1999; Swarbrick et al., 2002; Bowers and Katsube, 2002; Tingay et al., 2009; Webster et al., 2011; Couzens-Schultz and Azbel, 2014). Whilst these methods can help to identify overpressure mechanisms due to the effects that fluid pressure exerts on the physical properties of the sediments and thus on log signatures, overpressure prediction and different overpressure mechanisms acting through time cannot be identified. Sophisticated 2D/3D geomechanical models can then provide further information on the evolution of stresses, pore pressures, and porosities and their areal distribution (e.g., Ge and Garven, 1992; Luo et al., 2012; Nikolinakou et al., 2014; Burgreen-Chan et al., 2016; Obradors-Prats et al., 2016; Obradors-Prats et al., 2017a and 2017b; Nikolinakou et al., 2017; Nikolinakou et al., 2018; Obradors-Prats et al., 2019; Nifuku et al., 2020; Brüch et al., 2021). However, these models produce results accompanied by high levels of uncertainty due to the number of assumptions that need to be made about a range of physical variables in order to construct the models. The generation of geomechanical models also requires significant time and processing power, meaning that results may not be as immediately accessible or available as through other methods.

To minimise the uncertainty of the results, this research used 1D geomechanical models, as they can provide an understanding of the effect of each variable separately, and more control can be exerted over the input data. 1D models are also more effective during data matching and minimise machine-time consumption. These models can be constructed with idealised geological settings or with well data (e.g., Audet, 1995; Darby and Ellis, 2001).

The approach used during this research is similar in all three projects and is based on established workflows used in the oil industry with a focus on pore fluid pressure. It consisted of a geological assessment with seismic and well data interpretation, the application of analytical equations to well data, and the analysis of measured data. 3D static models based on geological interpretation of seismic and log data were developed for each project. The depth of the geological assessment depends on the geological histories of each region. In the ECB Project, the 3D static model was used to identify potential regional compartmentalisation and the distribution of properties (e.g., lithofacies, formations, porosity, measured pore pressure) in space. In the Magnolia Field Project, the 3D static models were used to understand the salt wall shape variation in 3D and the proximity to the wells. In the West Africa Project, the 3D model was used to identify thickness variation along the sedimentary

successions and the connectivity between the wells. The results of the geological assessment were the input for the 1D and 2D geomechanical models of each project.

2D geomechanical models were constructed to investigate the effect of salt tectonics on pore pressure in the Magnolia Field Project and external structures such as canyons in the West Africa Project. While the input used to construct the 2D geomechanical models is more general and uses average values, the inputs used in the construction of the 1D geomechanical models represent well-locations with the geological histories of each region and project.

The geological assessment underpins the geomechanical models and allows to focus on the most likely or all the possible overpressure-generating mechanisms in each region and the factors that contributed to their maintenance or dissipation. For instance, the Magnolia Field Project is located in a relatively young basin (~3 Ma) in which low-permeability, mud-rich lithologies were deposited rapidly. This basin does not have multiple erosive events or hiatus periods, and the geothermal gradient is low (~23 °C/km), so that clay mineral diagenesis is not relevant. However, salt tectonics have been active from the Jurassic to the present-day creating the possibility of an overpressure contribution. The West Africa Project is located in a passive basin with high geothermal gradients (>39 °C/km), allowing the possibility of overpressure due to clay diagenesis. The successions, which consist of thick intervals of shales with intercalations of sands, were deposited at low sedimentation rates (~135 m/Ma) with different erosive events and hiatus periods from the Cretaceous to the present-day, which can result in overpressure dissipation. The East Coast Basin (ECB) has complex geological histories from the Cretaceous to the present-day (e.g., erosive events, hiatus periods, and different sedimentation rates that change along the geological time), as this project is located in an active tectonic basin (from the Oligocene to the present-day) during which the convergence of the tectonic plates has been modifying the structural frame of the basin, creating compartmentalised areas and the exposure of old intervals (e.g., Cretaceous sediments) to the surface. Therefore, the contribution of tectonic compaction is considered to be high in this project.

As disequilibrium compaction is regarded as a highly common overpressure-generating mechanism, investigation into the influence of this mechanism was conducted first within each project. As it has been previously established that disequilibrium compaction generates overpressure in basins with high sedimentation rates (>1,400 m/Ma) of mud-rich lithologies (Bredehoeft and Hanshaw, 1968; Harrison and Summa, 1991; Audet, 1996; Swarbrick et al., 2002; Nunn, 2012), understanding of the sedimentation rates of these low-permeability intervals in each region was required.

While the determination of sedimentation rates across the projects was straightforward (a sedimentation rate of ~1,600 m/Ma was calculated in the Magnolia Field in comparison to ~730 m/Ma in the East Coast Basin and ~135 m/Ma in West Africa), the challenge was to establish the permeability of the deposited intervals. The three projects have mud-rich intervals along the sedimentary column. However, as the permeability of these sediments was not available for any of the projects, porosity-permeability relationships that have previously been determined were used (e.g., Kozeny-Carmen; Yang and Aplin, 2010). The lowest permeability for mud-rich lithologies that were evaluated in the lab was between 10^{-21} and 10^{-23} m^2, as determined by Deming (1994) through their idealised mathematical models. The selected porosity-permeability relationship for shale was

based on the best match of porosity and pore pressure within several geomechanical models. For instance, the porosity-permeability relationship Shale at 0.15 porosity is 40.5 times higher than the classical K-C shale relationship and 9.65 times higher than the 0.6 clay fraction relationship determined by Yang and Aplin (2010). If lower permeability relationships were used in the geomechanical models, high porosity and thicknesses would have been preserved, which would not have aligned with the available well data. As the thicknesses of mud-rich intervals could also influence overpressure, these were also considered. The thickness of such intervals varies among the three projects. For instance, the Magnolia Field Project has around 4,000 m of mud-rich lithologies in comparison to approximately 1,000 m in the East Coast Basin and West Africa projects. These thicknesses correspond to the overburden sediments, which in the East Coast Basin Project are highly variable.

The results of this research indicate that while disequilibrium compaction is a common mechanism that contributes to overpressure within all three study regions, it is only within the Magnolia Field that it is the main overpressure mechanism. In both the West Africa and the East Coast Basin projects, the overpressure generated by disequilibrium compaction was dissipated due to erosive events and hiatus periods that occurred from the Cretaceous to the present-day. As suggested previously (e.g., Swarbrick and Osborne, 1998; Neuzil and Pollock, 1983; Field et al., 1997; Barnes, 1997; Nunn, 2012; Burgreen-Chan et al., 2016), erosive events and hiatus periods result in overpressure dissipation in the absence of an active overpressure mechanism.

Another overpressure mechanism that is common in both the East Coast Basin and the Magnolia Field projects, albeit with differing contributions in each region, is tectonic compression. Overpressure generated due to tectonic compression has been attributed to active basins similar to the East Coast Basin (Wang et al., 2022). In the East Coast Basin, this overpressure mechanism has been related to the active compression exerted by the convergence of the Pacific and Australian Plates, which has occurred from the Early Miocene to the present-day (e.g., Darby and Ellis, 2001 and 2003). In this basin, overpressures up to ~20 MPa have been registered at 2 km depth, and these high values were obtained when tectonic compression was applied to the 1D geomechanical models. In the Magnolia Field, tectonic compression is caused by salt wall growth. According to Luo et al. (2017) and Nikolinakou et al. (2018), salt tectonics can affect the overpressure on the sediments near the growing salt wall. This is because the salt wall pushes laterally, causing elevated horizontal stresses that can result in a significant overpressure increase. However, Obradors-Prats et al. (2023) identified a small overpressure contribution (~2 MPa at ~2 km depth) and highlighted that this difference can be related to the development of the salt wall and the location where the data were taken. This mechanism has not had any influence on the overpressure generated in the West Africa Project, as the study area is located in a passive basin without salt tectonics. However, in passive basins where salt tectonics are active, this mechanism can contribute to overpressure generation (Luo et al., 2017; Nikolinakou et al., 2018).

Another overpressure mechanism that was considered during the research was clay diagenesis. Overpressure due to clay diagenesis has been identified in hot basins (>39 °C/km) with smectite content, such as the Gulf Coast Basin, and the Niger Delta Basin. From the three projects assessed,

only the West Africa Project is located in a basin with relatively high geothermal gradients (>39 °C/km) and with mudstones with high smectite contents. The ECB and the Magnolia Field projects have geothermal gradients lower than 23 °C/km, and although the ECB has two thick intervals (Wanstead and Weber Formations) with high smectite content, there is no evidence of smectite to illite transformation (e.g., Darby and Funnell, 2001).

Temperatures between 50 and 120°C have been determined to be necessary to start the smectite to illite transformation, with the main reaction occurring between 70 and 100°C (Dutta, 1987). The overpressured intervals in the West Africa Project sit at temperatures between 80 and 120 °C. Even though three processes (release of water to the system, change of the arrangement of the clay mineral grains, and load transfer as the pressure of the grains is passed to the pore fluid) have been identified during smectite to illite transformation (e.g., Audet, 1995; Powers, 1967; Aplin et al., 2003; Lahann and Swarbrick, 2011; Goulty et al., 2012; Tremosa et al., 2020), this research only accounted for porosity loss and the related reduction of permeability due to chemical compaction.

The West Africa Project has different overpressures at the same reservoir intervals (Cenomanian) in two well locations separated by ~44 km. The data of this project show that Well B is located in an area with a higher geothermal gradient and greater overburden thicknesses than Well A (e.g., Well B 44 °C/km with an overburden thickness of 2,239 m and Well A 39 °C/km with an overburden thickness of 1,900m). These differences resulted in an early smectite to illite transformation in Well B (e.g., from the Cretaceous around 82 Ma ago), while in Well A the smectite to illite transformation is calculated to have occurred from the Oligocene or Middle Miocene, around 32 to 14 Ma ago. The early geological smectite transformation that occurred in Well B is interpreted to have reduced the porosity and permeability of the intervals where this transformation occurred, resulting in overpressure generation first due to chemical compaction and then by post-diagenesis sedimentation (mechanical compaction). If chemical compaction is not considered and instead low-permeability relationships are applied to these intervals, high overpressure would have been generated due to mechanical compaction, resulting in high porosity preservation. However, high porosity values are not observed in the registered data.

This research focused on the identification of the overpressure mechanisms that generated the present-day overpressure in three different regions, highlighting the factors and variables needed for overpressure maintenance and dissipation. In addition, it also presents how sediments behave mechanically when they are exposed to events such as different sedimentation rates, different erosive events with different thicknesses eroded, and different tectonic compaction shortenings through geological time. Analysis of sediment behaviour is important and perhaps increasingly necessary as it could reduce the uncertainty of seal failure due to fracturing, avoiding drilling hydrocarbon dry wells, and CO_2, H_2, and nuclear waste leakage. A tool to understand the sediment behaviour of any lithology interval and depth is the analysis of stress paths, which can be obtained as outputs of the geomechanical models. These stress paths display the mean effective stress, which is the average of the three principal stresses vs. deviatoric stresses, which is a 3D formulation of shear. In this research, stress paths were used for the parametric models and the East Coast Basin Project, as the overpressures encountered in this basin are near to lithostatic from shallow depths

(>300 m). The results show that the intervals selected for this analysis did not experience brittle behaviour; therefore, the risk of leaking is lower in these intervals. However, different behaviours could be obtained if the properties of the sediments (e.g., Poisson Ratio, Young's modulus, Bulk modulus, hardening modulus) and variables were changed (e.g., sedimentation rate, tectonic compression, erosive events with thicker intervals removed). For example, with the values used in this research, carbonate lithologies will fracture more readily than shale, siltstone, and sandstone lithologies, meaning that low permeability carbonates can reach the yield surface with a relatively small strength envelope and the shear side (plastic behaviour) with a small amount of stress.

6.1 References

Aplin, A. C., Matenaar, I. F. and Van der Plujm, B. A. (2003). Influence of mechanical compaction and chemical diagenesis on the microfabric and fluid flow properties of Gulf of Mexico mudstones, *Journal of Geochemical Exploration,* 78-79, 449-451.

Audet, D. M. (1995). Mathematical modeling of gravitational compaction and clay dehydration in thick sediment layers, *Geophysics Journal International*, 122, 283–298.

Audet, S. M. (1996). Compaction and overpressuring in Pleistocene sediments on the Louisiana Shelf, Gulf of Mexico, *Marine and Petroleum Geology*, *13*(5), 467-474.

Barnes, P. M. (1997). Rates and mechanics of rapid frontal accretion along the very obliquely convergent southern Hikurangi margin, New Zealand, *Journal of Geophysical Research,*102(B11), 24,931-24,952.

Bowers, G. L. (1995). Pore pressure Estimation from Velocity Data: Accounting for Overpressure Mechanisms Besides Undercompaction, *SPE Drilling and Completion,* 89-95.

Bowers, G. L. and Katsube, T. J. (2002). The role of shale pore structure on the sensitivity of wire-line logs to overpressure, in Huffman, A. R. and Bowers, G. L. (eds.) *Pressure regimes in sedimentary basins and their prediction*. AAPG, 43-60.

Burgreen-Chan, B., Meisling, K. E. and Graham, S. (2016), Basin and petroleum system modelling of the East Coast Basin, New Zealand: a test of overpressure scenarios in a convergent margin, *Basin Research*, 28, 536-567.

Bredehoeft, J. D. and Hanshaw, B.B. (1968). On the Maintenance of Anomalous Fluid Pressures: Thick Sedimentary Sequences, *Geological Society of America Bulletin*, 79, 1097–1106.

Brüch, A., et al. (2021). Coupling 3D geomechanics to classical sedimentary basin modeling: From gravitational compaction to tectonics, *Geomechanics for Energy and the Environment*, 28, 1-12.

Couzens-Schultz, B. A. and Azbel, K. (2014). Predicting pore pressure in active fold-thrust systems: An empirical model for the deepwater Sabah foldbelt. *Journal of Structural Geology* 69, 465-480.

Darby, D. and Ellis, S. (2001). Evaluating overpressure in Compressional Regimes using Geomechanical Modelling, *Petroleum Exploration Society of Australia*, 613-620.

Darby, D. and Funnell, R. H. (2001). Overpressure associated with a convergent plate margin: East Coast Basin, New Zealand. *Petroleum Geoscience*, 7, 291-299.

Darby, D. And Ellis, S. (2003). Contrasting pressure in sedimentary basins associated with a plate boundary, New Zealand, *Journal of Geochemical Exploration*, 78-79, 149-152.

Deming, D. (1994). Factors Necessary to Define a Pressure Seal, *AAPG Bulletin*, 78(6), 1005-1009.

Dickinson, G. (1953). Geological Aspects of Abnormal Reservoir Pressures in Gulf Coast Louisiana, *The American Association of Petroleum Geologist,* 37, 410-432.

Dutta, N. C. (1987). Shale compaction, burial diagenesis, and geopressures: a dynamic model, solution, and some results, in Burrus, J. (ed.) *Thermal Modeling in Sedimentary Basins.* Paris, 149-172

Harrison, W. J. and Summa, L. L. (1991). Paleohydrology of the Gulf of Mexico Basin, *American Journal of Science*, 291, 109-176.

Eaton, B. A. (1975). The Equation for Geopressure Prediction from Well Logs, *SPE,* 1-11.

Field, B. D., Uruski, C. I. and others (1997). Cretaceous-Cenozoic Geology and Petroleum System of the East Coast Region, New Zealand. *Institute of Geological and Nuclear Sciences monograph*, 19, p. 301.

Ge, S. and Garven, G. (1992). Hydromechanical Modeling of Tectonically Driven Groundwater Flow with Application to the Arkoma Foreland Basin, *Journal of Geophysical Research,* 97, 9119-9144.

Goulty, N. R., Ramdhan, A. M. and Jones, S. J. (2012). Chemical compaction of mudrocks in the presence of overpressure, *Petroleum Geoscience*, 18, 471-479.

Hansen, S. (1996). A compaction trend for Cretaceous and Tertiary shales on the Norwegian Shelf based on sonic transit times. *Petroleum Geoscience,* 2, 159-166.

Harrold, T. W. D., Swarbrick, R. E. and Goulty, N. R. (1999). Pore Pressure Estimation from Mudrock Porosities in Tertiary Basins, Southeast Asia, *The American Association of Petroleum Geologist,* 87(7) 1057-1067.

Hart, B. S., Flemings, P. B. and Desphpande, A. (1995). Porosity and pressure: Role of compaction disequilibrium in the development of geopressures in a Gulf Coast Pleistocene basin. *AAPG Bulletin,* 23, 45-48.

Hottmann, C. E. and Johnson, R. E. (1965). Estimation of Formation Pressures from Lo-Derived Shale Properties, *Journal of Petroleum Technology*, 17, 717-722.

Issler, D. R. (1992). A new approach to shale compaction and the stratigraphic restoration, Beaufort-Mackenzie Basin and Mackenzie Corridor, Northern Canada. *AAPG Bulletin, 76*(8), 1170-1189.

Lahann, R. W. and Swarbrick, R. E. (2011). Overpressure generation by load transfer following shale framework weakening due to smectite diagenesis. *Geofluids*, 11, 362-375.

Luo, G., Nikolinakou, M. A., Flemings, P. B. and Hudec, M. R. (2012). Geomechanical modelling of stresses adjacent to salt bodies: Part 1- Uncoupled models, *AAPG*, 96(1), 43-64.

Luo, G., Hudec, M. R., Flemings, P. B. and Nikolinakou, M. A. (2017). Deformation, stress, and pore pressure in an evolving suprasalt basin, *Journal of Geophysical Research: Solid Earth*, 122, 5663-5690.

Neuzil, C.E. and Pollock, D.W. (1983). Erosional unloading and fluid pressures in hydraulically tight rocks, *Journal of Geology*, 91, 179-193.

Nikolinakou, M. A., Flemings, P. B. and Hudec, M. R. (2014). Modeling stress evolution around a rising salt diapir. *Marine and Petroleum Geology*, 51, 230-238.

Nikolinakou, M. A., Flemings, P. B., Heidari, M. and Hudec, M. R. (2017). Initiation and growth of salt diapirs in tectonically stable settings: Upbuilding and megaflaps, *AAPG Bulletin*, 101(6), 887-905.

Nikolinakou, M. A., Heidari, M., Hudec, M. R. and Flemings, P. B. (2018). Stress and pore pressure in mudrocks bounding salt systems. *Rock Mechanics and Rock Engineering*, 51, 3883-3894.

Nunn, J. A. (2012). Burial and Thermal History of the Haynesville Shale: Implications for Overpressure, Gas Generation, and Natural Hydrofracture, *Gulf Coast Association of Geological Societies*, 1, 81-96.

Obradors-Prats, J., Rouainia, M., Aplin, A. C. and Crook, A. J. L. (2016). Stress and pore pressure in complex tectonic settings predicted with coupled, 3D geomechanical-fluid flow models. *Marine and Petroleum Geology*, 76, 464-477.

Obradors-Prats, J., Rouainia, M., Aplin, A. C. and Crook, A. J. L. (2017a). Assessing the implications of tectonic compaction on pore pressure using a coupled geomechanical approach. *Marine and Petroleum Geology*, 79, 31-43.

Obradors-Prats, J., Rouainia, M., Aplin, A. C. and Crook, A. J. L. (2017b). Hydromechanical modeling of stress, pore pressure, and porosity evolution in fold-and-thrust belt systems. *Journal of Geophysical Research: Solid Earth*, 122(11), 9383-9403.

Obradors-Prats, J., Rouainia, M., Aplin, A. C. and Crook, A. J. L. (2019). A diagenesis model for geomechanical simulations: formulation and implications for pore pressure and development of geological structures. *Journal of Geophysical Research: Solid Earth*, 124(5), 4452-4472.

Obradors-Prats, J., Calderon, M. E. E., Jones S. J., Rouainia, M., Aplin, A. C. and Crook, A. J. L. (2023). Integrating Petrophysical, Geological and Geomechanical Modelling to Assess Stress States, Overpressure Development and Compartmentalisation Adjacent to a Salt Wall, Gulf of Mexico, *Marine and Petroleum Geology*, 155, 1-22.

Osborne, M. J. and Swarbrick, R. E. (1997). Mechanisms for Generating Overpressure in Sedimentary Basins: A Reevaluation, *AAPG Bulletin,* 81, 1023-1041.

Powers, M. C. (1967). Fluid-Release Mechanisms in Compacting Marine Mudrocks and their Importance in oil Exploration, *AAPG Bulletin*, 51(7), 1240-1254.

Raiga-Clemenceau, J., Martin, J. P. and Nicoletis, S. (1988). The Concept of acoustic Formation for more Accurate Porosity Determination from Sonic Transit Time Data, *The log Analysis*, 29, 54-60.

Raymer, L. L., Hunt, E. R. and Gardner, J. S. (1980). An improved sonic transit time-to-porosity transform, *OnePetro*, 1-13.

Skempton, A. W. (1970). The consolidation of clays by gravitational compaction, *Quarterly journal of the Geological Society,* 125, 373-411.

Swarbrick, R. E. and Osborne, M. J. (1998). Mechanisms that Generate Abnormal Pressures: An Overview, in Law, B. E., Ulmishek, G. F. and Slavin, V. I. (eds.), *Abnormal pressures in hydrocarbon environments.*

Swarbrick, R. E., Osborne, M. O. and Yardley, G. S. (2002). Comparison of Overpressure Magnitude Resulting from the Main Generating Mechanisms, in Huffman, A. R. and Bowers, G. L. (eds.) *Pressure regimes in sedimentary basins and their prediction.* AAPG Memoir 76, 1-12.

Tingay, M. R. P., Hillis, R. R., Swarbrick, R. E., Morley, C. K. and Damit, A. R. (2009). Origin of overpressure and pore-pressure prediction in the Baram province, Brunei. *AAPG Bulletin,* 93, 51-74.

Tremosa, J., Gailhanou, H., Chiaberge, C., Castilla, R., Gaucher, E. C., Lassin, A., Gout, C., Fialips, C. and Claret, F. (2020). Effects of smectite dehydration and illitisation on overpressures in sedimentary basins: A coupled chemical and thermo-hydro-mechanical modelling approach, *Marine and Petroleum Geology*, 111, 166-178.

Wang, B., Qiu, N., Amberg, S., Duan, Y. and Littke, R. (2022). Modelling of pore pressure evolution in a compressional tectonic setting The Kuqa Depression, Tarim Basin, northwestern China, *Marine and Petroleum Geology,* 146, 1-21.

Webster, M., O'Connor, S., Pindar, B. and Swarbrick, R. (2011). Overpressures in the Taranaki Basin: Distribution, causes, and implications for exploration, *AAPG Bulletin, 95*(3), 339-370.

Yang, Y. and Aplin, A. C. (2010). A permeability-porosity relationship for mudstones, *Marine and Petroleum Geology*, 27, 1692-1697.

Chapter Seven: Conclusions, Implications, Further Work and Recommendations

7.1 Conclusions and Implications

The present-day overpressure encountered in the East Coast Basin, Magnolia Field, and West Africa projects is a result of the varying influence of different overpressure mechanisms acting at different periods of time. This has been established through the use of 1D geomechanical models in conjunction with more traditional geological assessment methods. While 1D geomechanical models have limitations as they cannot capture the complexity of basins, these models can investigate potential overpressure-generating mechanisms separately and thus allow for the development of more accurate 2D and 3D geomechanical models. It is therefore suggested that the use of 1D geomechanical models could be a cost-effective and efficient way to conduct assessments of pore pressure. This would in turn reduce the risk of drilling dry wells and seal failures during CO_2, H_2, and nuclear waste storage, as this would support more informed decision-making during the initial stages of development projects.

Sedimentation rates from 200 to 3,000 m/Ma can generate overpressure when the permeability of the sediments deposited is low (e.g., mudstones with a high content of clay or cemented carbonates with permeabilities <3.09 E-18 m^2). High sedimentation rates generate more overpressure as the pore fluid pressure is unable to dissipate at the same rate as it is generated by the sedimentation. The high overpressure generated during sedimentation results in porosity preservation. However, successions of sediments with exceptionally low permeability values (e.g., < 1.19 E-19 m^2) similar to mudstones with high clay content (e.g., >CF 0.8 based on Yang and Aplin, 2010) or carbonate intervals that have been cemented at early stages will preserve high porosities similar to the initial sedimentation porosity even with low sedimentation rates (e.g., 200 m/Ma; Figure 3.11). This means that the porosity-permeability relationship selected will play an important role in the overpressure generated, and therefore, not only do pore pressure values need to be matched during the evaluation to avoid erroneous interpretations, but also porosities and thicknesses.

Thin (< 85 m) and low permeability intervals of cemented carbonates or mudstones (e.g., >CF 0.6 based on Yang and Aplin, 2010) can act as overpressure seals, maintaining pore fluid pressures close to lithostatic values. This conclusion is based on the results of the geomechanical models created in this study and the measured data of two wells located in the ECB Project. However, the integrity of any hydrocarbon or overpressure seal could be compromised as lithologies experience stresses differently through time. To reduce the uncertainty of seal integrity, stress paths can be used to indicate if the properties of an interval or lithology have changed, which would suggest an increased risk of leakage during CO_2, H_2, and nuclear waste storage. This implies that analysis of stress paths could be beneficial when selecting sites for waste storage and also to avoid the drilling of dry wells. Although this technique adds little time to a geological assessment, as data need to be analysed, the results are highly dependent on accurate input data (e.g., porosity-permeability relationships, lithologies, sedimentation thicknesses, relative recent erosive and tectonic compression events) to be effective.

Overpressure dissipation can be the result of erosive events, hiatus periods, and lateral flow drainage, with the recent erosive events having a greater impact on overpressure dissipation. This

is because the overpressure dissipated during prior events can be overwritten by post-erosion sedimentation, while the overpressure generated during the most recent events will dissipate due to the mechanical unloading caused by the erosion and exhumation of sediments. For this reason, geological assessment prior to the construction of the geomechanical models can result in more accurate results, as the processes that contribute to overpressure dissipation or preservation can be applied to the geomechanical models.

Compartmentalisation is considered to play a crucial role in the maintenance and dissipation of overpressure as well as affecting the amount of the present-day overpressure, with overpressure distribution controlled by regional and local faults, low-permeability successions, and lateral pressure drainage. Measured pressure data can facilitate its identification, but as these data are not available along the whole sedimentary column, it is suggested that geological assessments (e.g., juxtaposition fault analysis and fault permeability prediction) be performed, and the findings then applied to geomechanical models. This can facilitate a pore fluid pressure evaluation of any basin and identify intervals or regions with possible lateral flow drainages.

Tectonic compression in active margin basins can generate high overpressures reaching almost lithostatic values from shallow depths (>300 m) when this overpressure-generating mechanism is acting within a recent period (e.g., ~6 Ma). This is because the sediments need time to dissipate the overpressure generated during sedimentation and the overpressure generated by tectonic loading. The amount of overpressure generated by this mechanism depends on the horizontal shortening, with high values of horizontal shortening (e.g., 12.5%) resulting in high overpressures. However, horizontal shortening values are scarce in active margin basins, which can compromise the results obtained through modelling. Although this overpressure mechanism can generate very high pore fluid pressures, the maintenance of these values depends on the properties of the sediments and geological processes (e.g., recent erosive events, lateral pressure drainage, compartmentalisation). This means that the identification of the factors that contribute to overpressure maintenance and dissipation, as well as the horizontal shortening applied, are essential.

Salt tectonics can generate overpressure due to the horizontal stress generated during salt wall growth. The contribution of this overpressure mechanism was observed to depend on the shape of the salt wall as well as the compartmentalisation and permeability of the sediments near the salt wall. Steep-slope salt walls are observed to generate more overpressure than gentle-slope salt walls. This conclusion is based on registered data in the wells of the Magnolia Field Project and the 2D geomechanical models created in this research. As the movement of the salt is unpredictable, a range of values of the overpressure contribution should be obtained through multiple geomechanical models. Although this can imply a delay in the decision taken as these models have a high machine time consumption and well data is necessary to calibrate the input data, these models can provide useful information during well planning.

Chemical compaction (porosity reduction due to smectite to illite transformation) can contribute to overpressure generation, with the timing of the chemical compaction shown to affect whether the overpressure values generated by mechanical compaction are high or low. If clay diagenesis had occurred during the early stages of the formation of a sedimentary column, as a result of a high

geothermal gradient, the permeability of the sediments where this process occurred would have been reduced due to chemical (clay diagenesis) and mechanical compaction (post-diagenetic sedimentation), resulting in an increase in pore fluid pressure. As this overpressure mechanism is related to the temperature of the sediments, the intervals that reach temperatures higher than ca. 72 °C were considered to go through smectite to illite transformation in the West Africa Project. As different processes have been determined to occur during clay diagenesis (e.g., water generation, load transfer), there is always going to be a degree of uncertainty about the impact of this overpressure unless it is mitigated by data collection (e.g., core samples and well logs of the overburden section) and more studies. In addition, the analysis of mechanical loading and chemical reactions in combined software could result in more reliable results. This means that this overpressure mechanism can be further studied so as to provide more certain results, which is beneficial not only for investigating this mechanism but also for chemical reactions due to changes in temperatures generated by CO_2, H_2, and nuclear waste storage.

Although simple approaches such as log-based interpretation and analytical methods provided an efficient way to gain information and insights into the overpressure-generating mechanisms acting within a location, these approaches were insufficient to explain the pore fluid pressure distribution in basins with complex geological histories. This uncertainty was reduced with geomechanical models, which are capable of replicating the physics involved in complex geological histories by capturing stresses, strain tensors, pore pressure, and temperatures to predict the evolution of sedimentary basins, providing more accuracy to the results. Crucial information used to identify intervals or areas with leakage risks was obtained through the analysis of the evolution through time of variables such as the present-day pore fluid pressure, mean stress, and porosity, as these variables evolve differently in each lithology and depth. The greater understanding of a specific lithology and its leakage risks, which is available via forward geomechanical modelling, suggests that the analysis of a lithology's current state alone is not sufficient when considering sites for waste storage.

This thesis shows that a combination of a detailed geological interpretation, input to the construction of geomechanical models, which are sophisticated techniques, is a way of understanding the development and distribution of overpressure through time. In addition, the geomechanical models provide information about the risk of mechanical seal failure through time and enable the quantification of the present-day overpressure in any basin.

7.2 Further Work and Recommendations

The results of this research can be applied to any basin (e.g., active and passive margins) as the methods applied and the geomechanical models constructed can investigate each overpressure-generating mechanism separately. It is recommended that the results of the 1D models should be used as input for the creation of 2D/3D geomechanical models where the complexity of the basin can be captured, and more accurate results obtained.

This research did not study deep intervals in the ECB which could have an influence in the present-day overpressure (e.g., clay diagenesis of deeper layers, lateral transfer from deep intervals, and gas generation), and it is suggested to be considered in further research.

The amount of horizontal compaction that different lithologies could experience in active tectonic basins should be accounted in future studies to reduce uncertainty in the results. The values used in this research are related to the restored displacements in the extensional and contractional domains on gravitational thrust belt systems of the Orange Basin, increasing a degree of uncertainty in the results obtained.

Data acquisition in low-permeability intervals should be considered, although the difficulty of this is acknowledged due to the known issues with data collection in shales and the expense that would likely be encountered. However, further understanding of these intervals would greatly add to the accuracy of the models. The lack of low permeability data adds considerable time to geological assessment due to the need for the construction and analysis of innumerable models, as previously established porosity-permeability relationships must be adjusted with well data.

The implementation of chemical reactions in the geomechanical models would be a plus, as these can provide information of the lithologies that could react to changes such as temperatures, different sedimentation rates, erosive vents, hiatus periods and tectonic compression.

With the rise of greenhouse gas emissions and their adverse impact on Earth's climate, it has become critical to store CO_2, H_2, and nuclear waste. Therefore, it is necessary that sites with the potential to store such waste are evaluated. To ascertain the feasibility of storage and reduce the uncertainty of leakage, 1D geomechanical models with stress paths can be used. This information could indicate when and which intervals have the potential of change the properties to become brittle which would result in fractures or faults and subsequent leakage.